

SYNTHESIS AND CHARACTERIZATION OF $\text{La}_2\text{Mo}_2\text{O}_9$ -BASED ELECTROLYTES FOR SOLID OXIDE FUEL CELL

Ph.D. THESIS

by

SIDDHARTH



**DEPARTMENT OF METALLURGICAL AND MATERIALS ENGINEERING
INDIAN INSTITUTE OF TECHNOLOGY ROORKEE
ROORKEE, INDIA (247667)
JULY, 2020**

SYNTHESIS AND CHARACTERIZATION OF $\text{La}_2\text{Mo}_2\text{O}_9$ -BASED ELECTROLYTES FOR SOLID OXIDE FUEL CELL

A THESIS

*Submitted in partial fulfilment of the
requirements for the award of the degree*

of

DOCTOR OF PHILOSOPHY

in

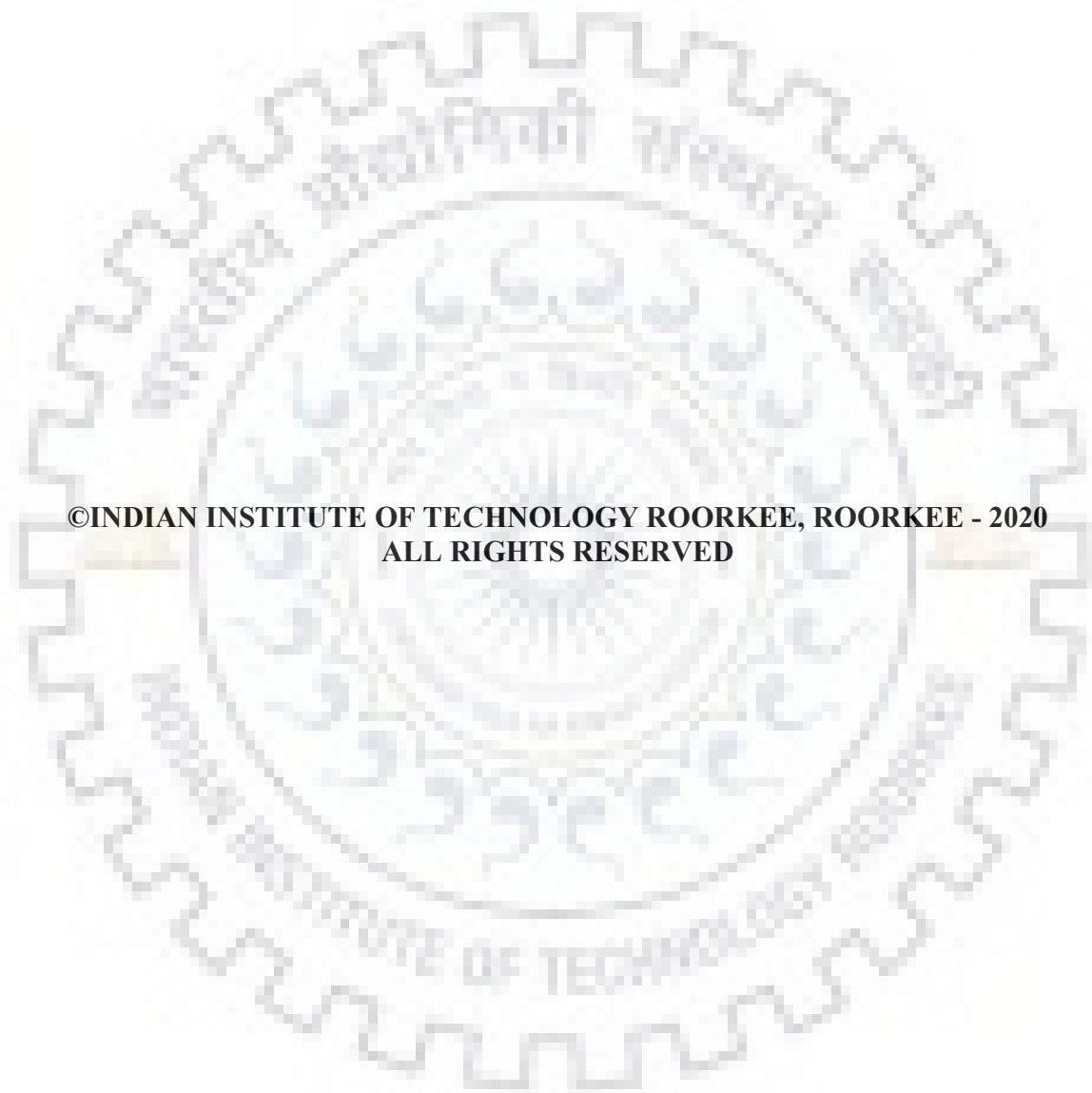
METALLURGICAL AND MATERIALS ENGINEERING

by

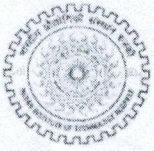
SIDDHARTH



**DEPARTMENT OF METALLURGICAL AND MATERIALS ENGINEERING
INDIAN INSTITUTE OF TECHNOLOGY ROORKEE
ROORKEE, INDIA (247667)
JULY, 2020**



**©INDIAN INSTITUTE OF TECHNOLOGY ROORKEE, ROORKEE - 2020
ALL RIGHTS RESERVED**




INDIAN INSTITUTE OF TECHNOLOGY ROORKEE

STUDENT'S DECLARATION

I hereby certify that the work presented in the thesis entitled "SYNTHESIS AND CHARACTERIZATION OF $\text{La}_2\text{Mo}_2\text{O}_9$ -BASED ELECTROLYTES FOR SOLID OXIDE FUEL CELL" is my own work carried out during a period from 08 January, 2013 to 07 February, 2020 under the supervision of Prof. Anjan Sil, Department of Metallurgical and Materials Engineering, Indian Institute of Technology Roorkee, Roorkee and Dr. Sandip Bysakh, Senior Principal Scientist, CSIR - Central Glass & Ceramic Research Institute, Kolkata, India.

The matter presented in the thesis has not been submitted for the award of any other degree of this or any other Institute.

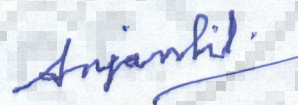
Dated: 06 July, 2020

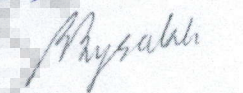

(Siddharth)

SUPERVISORS' DECLARATION

This is to certify that the above mentioned work is carried out under my supervision.

Dated: 06 July 2020


(Anjan Sil)


(Sandip Bysakh)

Abstract

The global energy demand is increasing at a very steep rate. To fulfill the energy requirements, non-conventional fossil fuels viz., coal, crude oil, petroleum products are significant contributors. But these traditional sources cause a lot of pollution in the past and even in the present and thus having a negative impact on ecology and society. Therefore, it is very much necessary to switch to clean energy sources. In this regard, it is required to develop alternative renewable and clean energy sources like solar, wind, and hydroelectric power and fuel cells intensively at a wide scale. Regarding clean energy sources or energy conversion devices, still, a lot of effort has to be made to make the clean energy generation economical. In the current scenario, progress is being made on a wide scale for a clean energy generation.

Solid oxide fuel cells (SOFCs) are considered to be one of the clean energy conversion devices. It has water as its by-product, which can be utilised again in the system to regenerate fuel. A SOFC unit mainly consists of two electrodes: anode, cathode, and a solid electrolyte. The fuel plays an important part in the cell operation and is independent of the SOFC unit as it is often converted into hydrogen through reforming process. The function of the SOFC relies mainly on O^{2-} (oxide) ion transport from cathode to anode side through the electrolyte. The main function of both the electrodes is to initiate the reaction between the reactants (fuel and oxygen) through the electrolyte, without being consumed or corroded during the reaction. The SOFC unit should also bring the three phases, i.e., the electrode, electrolyte, and the fuel into contact of each other.

The discovery of LAMOX based electrolytes in the year 2000 has attracted much attention in the SOFC area and may be seen as a potential competitive candidate to traditionally YSZ and GDC based electrolytes. It shows a superior oxygen ion conductivity of (0.06 S/cm and 0.4 S/cm for doped $La_2Mo_2O_9$ samples at 800 °C) as compared to yttria-stabilised zirconia (YSZ). However, its applicability is limited by its instability in reducing atmosphere, abrupt volume expansion due to the phase transition from monoclinic to cubic phase; high thermal expansion and chemical reactivity towards electrode components.

The first chapter of the thesis is dedicated to the introduction of fuel cell technology. The chapter includes an introduction to basic concepts of fuel cells, their history, and development through the years, various types of fuel cells classified according to the types of electrolyte used, and their operating temperatures, theory of fast oxide ion conductors, components of SOFCs viz., electrode, electrolyte, interconnects sealants and reforming agents. Materials used as

cathode/anode/electrolyte, the necessity of ($\text{La}_2\text{Mo}_2\text{O}_9$) LAMOX based electrolytes and its superiority over other electrolyte materials, structural study of LAMOX, limitations of $\text{La}_2\text{Mo}_2\text{O}_9$ as an electrolyte material, doped LAMOX members as a substitute for the parent compound for overcoming its limitations, suitable electrode material for LAMOX family members have also been discussed in the first chapter. Various kinds of electrolyte systems employed in solid oxide fuel cell systems have been studied in the past years. The most extensively researched electrolyte is yttria-stabilised zirconia (YSZ) and gadolinia doped ceria (GDC) electrolyte, which in the present time are still used commercially. The operation of YSZ at $1000\text{ }^\circ\text{C}$ makes it a very robust system for high-temperature applications, and the highest conductivity shown is 0.1 S/cm at $1000\text{ }^\circ\text{C}$.

The pristine LAMOX possesses some serious limitations viz., Mo reduction in reducing (Ar-H_2) atmosphere, low electrical conductivity at room temperature, large volume expansion at the phase transition temperature, and suitable compatible electrodes. Solutions in the form of doping at various elemental sites have been proposed in a way such that the limitations of pure $\text{La}_2\text{Mo}_2\text{O}_9$ could be overcome; then, it may very well serve as a potential candidate for electrolyte materials for intermediate temperature ($600\text{-}800\text{ }^\circ\text{C}$).

The second chapter of the thesis deals with the synthesis of the required compositions by solid-state synthesis route and details of various instruments required for characterisation of the samples prepared. Specifications of all the instruments and their standard reference data have been mentioned in this chapter.

The third chapter deals with the effect of air and reductive atmosphere treated $\text{La}_2\text{Mo}_2\text{O}_9$ at $900\text{ }^\circ\text{C}$, which has been studied by means of x-ray diffraction (XRD), scanning electron microscopy (SEM), x-ray photoelectron spectroscopy (XPS) and complex impedance spectroscopy studies (IS). The results revealed and validated with the previously published results and have shown detailed study on grain boundary resistance and XPS study of pristine LAMOX. The main purpose of the LAMOX study in this context is for electrolyte in fuel cells. However, the low value of electrical conductivity due to grain boundary resistance and monoclinic phase, Mo reduction in Ar-H_2 atmosphere, and high thermal expansion during the phase transition may lead to an overall degradation of the fuel cell.

The fourth chapter of the thesis is dedicated to the effect of various dopants in the LAMOX to overcome the disadvantages of pristine LAMOX like Mo reduction, thermal expansion coefficient mismatch due to phase change. The first section of the chapter deals with W doping

at Mo site, which has a solubility of around 60-80 mol percent at Mo site. The structural, morphological, x-ray photoelectron spectroscopy (XPS) and ion dynamics along with conductivity studies of $\text{La}_2\text{Mo}_{2-x}\text{W}_x\text{O}_9$ ($0.25 \leq x \leq 1.5$) both in air and reductive atmospheres have been presented and discussed. Though the W doping in LAMOX successfully stabilises the cubic phase at room temperature, it was not able to entirely suppress the Mo^{6+} reduction to its lower oxidation states as clearly revealed by comprehensive FE-SEM and x-ray photoelectron spectroscopic studies. No other elements in the doped LAMOX compositions were reduced.

The second section of the chapter deals with the effect of K doping in LAMOX. The composition $\text{La}_{1.9}\text{K}_{0.1}\text{Mo}_2\text{O}_{9-\delta}$ shows the stabilisation of the high-temperature cubic phase of $\text{La}_2\text{Mo}_2\text{O}_9$ at room temperature, as confirmed by XRD and Rietveld analysis. $\text{La}_{1.8}\text{K}_{0.2}\text{Mo}_2\text{O}_{9-\delta}$ composition shows the formation of K doped LAMOX phase with the appearance of K_2O as a secondary phase in both of the K doped LAMOX compositions. The microstructural analysis revealed some intra-granular pores suggesting incomplete sintering in the Ar- H_2 atmosphere of the doped compositions. X-ray photoelectron spectroscopic study has been done after microstructural characterisation and shows the Mo^{6+} stability in the reductive atmosphere.

The third and last part of the chapter has shown the effect of rare earth and W doping simultaneously in LAMOX at La and W site respectively. X-ray photoelectron spectroscopy study shows that there is not much stabilisation of the Mo^{6+} in the reducing atmosphere.

The fifth chapter of the thesis is dedicated to the compatibility study of cathode/anode material $\text{La}_2\text{NiO}_{4+\delta}$ (LN) and NiWO_4 , respectively, with pristine and W doped LAMOX as electrolyte in the air as well as reductive atmosphere. The XPS study is thoroughly exploited to study the effect of fuel (diluted hydrogen gas) on the electrode/electrolyte interface at elevated temperatures. Also, the cationic diffusion of the interspecies is also studied.

The sixth chapter of the thesis is concluding remarks of the present work, which shows the findings of the study. Future work and suggestions are also mentioned, which are required to carry out to make the present study more comprehensive and meaningful.



Acknowledgements

Perhaps, in my opinion, this is the toughest section in the thesis to write. I have to recall all my past moments and then find a suitable incident to stop and then say this moment is perfect to start the acknowledgement. But in fact, it is not that easy. To come till here in my academic career neither I have imagined nor my parents or anyone that I would come this far except a few persons. Two of them are my Uncle Mr. D. P. Upadhyay and Mr. G.P. Tripathi and other one is my Aunt Shiv Kumari Singh. They always used to say that your hard work won't go in vain. They had immense faith in me since I was in school.

Then comes the period of friends and without a doubt Vaibhav, Anubhav and Siddharth were my best friends and we did a lot of fun and studies only as a career emergency plan. After completing the school, we joined the colleges for our graduation degree. Vaibhav and Siddharth were not with me but fortunately Anubhav and I joined the same college in same trade. Being 900 kms away from home was proved to be a lot of fun and blessings for us. It was alike four years of holiday away from home but with a financial support. We learned a lot of things being away from home through hostel life. We cleared our papers in time but studies were the least priority at that time. Time passed and after four years we graduated with a first class degree. By that time also I was not aware that what I learnt in these four years. Some of my friends did get a job by that time. But, we were lucky enough not to get it.

I opted for higher studies after that and my friends got placed in good companies. After joining the higher studies my elder sister Rashmi Singh and Sunil uncle and Manju aunt helped me a lot in the initial phases of my course and being in the same campus I could not enjoy a lot in the campus because of my sisters' spying nature on me. I came to realize and got a glimpse of research field that too in area I was not even heard before. Welcome to the world of materials science and engineering where the concepts go beyond atomic level. Initially it was very tough but as the time progressed the concepts were becoming clear with the help of faculty members. I got the glimpse of research field through my project work and it was not a cake walk. Without the help of my Ph.D. seniors at IIT BHU, Late. Ravindra Singh Solanki Sir, Anar Singh Sir, and my classmates Ajay Sharma, Dayanand, Abhishek Singh, Pankaj Tripathi, this journey would not have been possible. Also, my M. Tech faculty members Dr. D. Pandey, Dr. P. Maity, Dr. C. Upadhyay and Dr. A Singh and Dr. C. Rath has helped me a lot in teaching the fundamentals of material science. My seniors helped me a lot to develop the research attitude and to analyse the data. Again after graduating without a job got me frustration because of the expectations. I

decided to quit this field and changed my trade to job sector. But there is a saying “*The thing you hate most is the one you are most likely to stuck up with*” and was very true in my case.

After spending some time jobless, I applied for Ph.D. and got call from some of the most prestigious colleges. One of them was IIT Roorkee. It was chilly winter when I came for interview at Roorkee. I had to appear for a written test before I get to the interview. I was second on the list to go before the panel for interview. This is where the funny story starts of my Ph.D. degree. As I entered in the room the chairman asked me to go to the blackboard with a piece of chalk in my hand. Questions after questions were showered upon me and I was desperately trying to answer them. Most of the questions were related to metallurgy so I was not very sure to answer them. But I did answer some of the questions very clearly and accurately and impressed the panel members. But the overall interview was not good and I decided to leave at the earliest. The letter came through e-mail of my selection which was quite unbelievable for me. After a series of discussions and meetings with Prof. Anjan Sil he decided to supervise me for my research work. This turned out to be a fantastic and excellent thing for me.

After one year of completion of my course I got selected in CSIR-CGCRI. This time was a little bit stagnation of my work because of the additional job responsibility I did not get much time to do my research. With the approval of the director I opted for a co-guide here as Dr. Sandip Bysakh. I express my sincere gratitude to our Director Dr.K. Muraleedharan for letting me to continue my research work from IIT Roorkee and letting me opting a co-guide at CGCRI.

Besides being a fine academician Prof. Anjan Sil is a very nice gentleman and above all a great person. No matter how much I write or say about him, can never be much. Because now at this stage I realize how much I owe him in this journey. He has got an excellent attitude towards research. He has always been available for discussion and guided me to achieve the objective of my study; he has been an inspiring and driving force during the course of this work. Without his timely help, intellectual input, constructive criticism and painstaking efforts, it would not have been possible for me to complete this thesis.

I would also like acknowledge and express gratitude towards my committee members Late Prof. Vijaya Agarwala, Dr. B.V Manoj Kumar, Prof. U. Prakash and Dr. S. Manhas whose valuable comments and suggestions helped me to improve my scientific aptitude and thinking. I am really indebted to Late Prof. V. Agarwala whose effort made this Ph.D. journey possible. She was the first person who suggested me not to leave my Ph.D. when I got the job offer letter.

I also express my gratitude to ex- head of department Prof. S.K. Nath for his help and providing the facilities in the department for the research work during my stay at IIT Roorkee. I would also like to extend my sincere thanks to Prof. R. Jayaganthan who taught us in the course work and helped me in developing scientific understanding for new subjects.

I also extend my sincere thanks to the technical and the administrative staff of the Department of Metallurgical and Materials Engineering especially to Mr. Dhan Prakash, Mr. R.K. Sharma, Mr. Kuldeep Sharma, Mr. Narendra, Mr. Ramveer Singh who have helped me during the course of my Ph.D.

There are several people who deserve special thanks for providing help in my research. Besides Dr. Bysakh, Dr. M. Sreemany, Dr. S. Mohanty helped me a lot in my research work through technical discussions. I express my sincere gratitude to Mr. Nitai Dey, Mr. Ashok Mondal, Mrs. S. Roy, Mr. Sukanta Mondal, Mrs. Titir Maity and Kajuri Dasgupta, Mr. S. Balaji, Mayur Shukla, Arnab. Mahato, Naresh Oraon, Ajitesh Kar, Dr. Mahesh Gagrai for providing all necessary help at CGCRI.

Now it is time to thanks my lab seniors and fellow colleagues at IIT Roorkee. First of all my thanks to Rajni Ma'am who was there to advise me whenever required. Then our most respected senior Mr. Sobhit Saxena whose charming personality has influenced me a lot. His non-stop chit chats in the lab mostly on non-technical topics were really helpful to kill the stress of Ph.D. He was of very jolly nature and I have never seen him worried except a last few days of his own research. What to say of juniors, they are exceptional. One wants to finish his Ph.D. in first year; Hari Raj, and other always busy upgrading some software and formatting others laptops and informing his guide after reaching home. This is Mr. Abhishek Gupta. But they have a very good presence of mind and are quite intelligent in their research work. Some of the new Ph.D scholars like Ayush Pundir, Bharat are also there to provide non-technical help.

This acknowledgement is still incomplete without mentioning my friends at IIT Roorkee and hostel life. I have spent some very fine moments of my life at Azad Bhawan. The guys who were responsible in making this moment unforgettable are Sandan Sharma, Gajendra Gaurav, Mr. Neeraj Srivastava, Dr. Sanjiv Rajpoot, Devasri Ma'am, Gaurav Singh, Shivam Verma, Kirandeep Singh, Vijay Sharma, Himanshu Sharma. I am also grateful to other hostel mates like Himanshu Panjiar Sir and Sankulp Goel Sir, Vijesh and Rajkumar for helping me out in my research work.

There is one person would like to express my deepest gratitude without whose guidance and motivation this research would not have been possible. Saurabh Chandra who is my friend since 2003 has always helped me in listened me whenever I got some genuine doubts. He is a very brilliant student and a very nice friend to me. Some credit also goes to Mr. Tanzeel Usmani the most daring person I have ever seen in my life. He never hesitated to take a step (whether right or wrong). I learnt a lot of from him. Also my good friend Siddharth Tripathi whom I have shared many good times.

I would also like to express my gratitude towards my CSIR CBRI colleagues. First of all, I would to express my sincere thanks to Dr. N. Gopalakrishnan, Director CSIR-CBRI my allowing me to complete my research work. I would also like to express my thanks to Dr. S. K. Panigrahi, Shri Sameer, R.S. Bisht, Soju Alexander, Dinesh Kumar, Anil Sharma, Gurucharan Singh, Narendra Sir, Chandrabhan Patel, Vikesh, Pawan, Saif, Saurabh, Naman, Utkarsh for helping with my office work.

Last but not the least I would like to express my deepest esteem to my parents, supreme divine power and brothers (Shrikant and Gautam and my friend from small town girl and Pratima) for morally and financially supporting me though I got the job well before. I know it was not easy. Without you I would never be standing where I am now. My brothers sucked every penny of my hard earned money out of my pocket and lived their life to the fullest. Thank you for making me bankrupt and nomad. I also like to pay respect towards my grandparents who are not here with me but their blessings are always there with me. I would also like to thanks my IIT BHU Colleagues Dr. Abhishek Singh and Dr. Pankaj Tripathi for their help and guidance in writing the thesis.

Special thanks to my wife Gargi, despite her best efforts I could not submit this earlier. She helped me with nothing except my daily routine, managing everything at home and weekend fights which helped me a lot to complete my dissertation on time. Deepest gratitude to my newest family member (my daughter) with whom this thesis now looks complete. Also a big thanks to my dearest Shumali and Pooja for being always non available.

There is also one person I would like to thank whose name I cannot mention but had an immense faith in me that I will surely do well in my Ph.D. work by making some breakthrough. Though I did not make any breakthrough but still able to complete this thesis. I would also like to thank everyone who supported me for completing this work successfully.

(Siddharth)

Contents

<i>Abstract</i>	i
<i>Acknowledgement</i>	v
<i>Contents</i>	ix
<i>List of Figures</i>	xv
<i>List of tables</i>	xxiii
<i>List of publications</i>	xxv
<i>List of abbreviations</i>	xxvii
Chapter 1: Introduction and literature review	1
1. Introduction	1
1.1. The energy challenge	1
1.2. Hydrogen and fuel cells	3
1.3. Fuel cell and its origin	5
1.3.1 Fuel cell status in India and foreign countries	6
1.3.2 Types of fuel cells	7
1.3.3 Theory of fast oxide ion conductors	10
1.3.4 Components of fuel cell	11
1.3.5 Solid oxide fuel cells and their necessity	12
1.4. Materials for solid oxide fuel cell	13
1.4.1 Electrolytes	13
1.4.2 Anode	14
1.4.3 Cathode	15
1.4.4 Fuel	15
1.4.5 Interconnects	15
1.4.6 Sealants	15
1.5. Design classification and operation of SOFCs	16
1.5.1. Thermodynamics of SOFCs	19
1.6. Various types of electrolytes for SOFC applications	21
1.6.1. Bismuth oxide based electrolytes	21
1.6.2. Zirconia based electrolytes	21
1.6.3. Ceria based electrolytes	21
1.6.4. Perovskite related systems	21

1.6.5.	LAMOX based systems	22
1.6.6.	Apatites	22
1.6.7.	Pyrochlores	22
1.7	Importance of LAMOX based electrolytes	23
1.8	La ₂ Mo ₂ O ₉ (LAMOX)	23
1.8.1	Structural analysis (α -La ₂ Mo ₂ O ₉)	24
1.8.2	β -La ₂ Mo ₂ O ₉	25
1.8.3	Conduction path in La ₂ Mo ₂ O ₉	27
1.9	Limitations of La ₂ Mo ₂ O ₉ as an electrolyte material	28
1.10	Doped LAMOX family	33
1.11	Chemical stability of LAMOX with various electrodes	35
1.12	Summary	37
Chapter 2:	Experimental procedure	39
2.1.	Introduction	39
2.2	Synthesis of powder samples	39
2.3	Green sample preparation	40
2.4	Sintering of pellets	40
2.5	Characterization techniques	42
2.5.1	X-ray diffraction and Rietveld analysis	42
2.5.2	Scanning electron microscopy	44
2.5.3	X-ray photoelectron spectroscopy	46
2.5.3.1	XPS instrumentation	48
2.5.3.2	Basic assumptions and general formulation in x-ray photoelectron spectroscopy	52
2.5.4	Impedance spectroscopy	53
2.5.4.1	Dielectric theory	54
2.5.4.2	Relaxation time and conductivity studies	54
2.5.4.3	Debye relaxation of dielectric materials	55
2.5.5	Fast diffusion path in ion conducting solids	58
2.5.6	Raman Spectroscopy	58
2.6	Summary	60
Chapter 3:	Study of La₂Mo₂O₉ electrolyte in air and reductive atmosphere	61
3.1.	Introduction	61
3.2	Structural analysis of air treated LAMOX	61

3.3 Microscopic study of air and Ar-H ₂ treated La ₂ Mo ₂ O ₉ by FE-SEM	64
3.4 Reduction mechanism of La ₂ Mo ₂ O ₉ treated under Ar-H ₂ atmosphere	67
3.5 X-ray photoelectron spectroscopic studies of air and Ar-H ₂ atmosphere treated LAMOX	68
3.5.1 La 3d core level analysis	70
3.5.2 Mo 3d and O 1s core level analysis	70
3.5.3 Core level XPS analysis of reduced LAMOX constituents	71
3.6 Conductivity studies of LAMOX sintered in air and Ar-H ₂ atmosphere	74
3.7 Summary	81
Chapter 4: Doping effects on La₂Mo₂O₉ treated in air and reductive atmosphere	83
4.1 Introduction	83
4.2 Effect of W doping at Mo site in La ₂ Mo ₂ O ₉	84
4.2.1 X-ray diffraction studies on La ₂ Mo _{2-x} W _x O ₉ sintered in air atmosphere	84
4.2.2 Diffraction studies of La ₂ Mo _{2-x} W _x O ₉ sintered in reductive atmosphere	93
4.3 Microstructure observation by Field-Emission Scanning Electron Microscope (FE-SEM) of air and diluted H ₂ treated W doped La ₂ Mo ₂ O ₉	94
4.3.1 FE-SEM study of air treated W doped La ₂ Mo ₂ O ₉	94
4.3.2 FE-SEM study of Ar-H ₂ treated W doped La ₂ Mo ₂ O ₉	96
4.4 Chemical state analysis by x-ray photo-electron spectroscopy (XPS) of air and Ar-H ₂ sintered W doped LAMOX samples	100
4.4.1 XPS studies of air treated W doped La ₂ Mo ₂ O ₉ samples	100
4.4.2 Core level analysis of La 3d spectrum of air treated LAMOX samples	100
4.4.3 Study of O 1s, Mo 3d and W 4f Spectra	102
4.4.4 X-ray photo-electron spectroscopy (XPS) of reduced W doped LAMOX samples	104
4.5 Oxygen ion diffusion studies in LAMOX	107
4.6 Ion dynamics and conductivity study of W = 0.25 doped LAMOX	108
4.7 Effect of K doping at La site in La ₂ Mo ₂ O ₉	113

4.7.1	Introduction	113
4.7.2	Structural study of K doped $\text{La}_2\text{Mo}_2\text{O}_9$ by x-ray diffraction	114
4.8	Microstructural study by field emission scanning electron microscope of K doped $\text{La}_2\text{Mo}_2\text{O}_9$ composition sintered in air and Ar-H_2 atmosphere	119
4.9	Chemical state analysis of air sintered and Ar-H_2 -reduced samples by x-ray photoelectron spectroscopy (XPS)	120
4.9.1	Survey analysis	120
4.9.2	Core level analysis of K = 5 mol % doped $\text{La}_2\text{Mo}_2\text{O}_9$ in air and Ar-H_2 atmosphere (K 2p, O 1s, La 3d, Mo 3d)	121
4.9.3	Core level analysis of K = 10 mol % doped $\text{La}_2\text{Mo}_2\text{O}_9$ (La 3d, Mo 3d, k 2p and O 1s)	122
4.10	Raman spectroscopy study of K = 10 mol % doped LAMOX	124
4.11	Conductivity studies of air sintered K = 10 mol% doped $\text{La}_2\text{Mo}_2\text{O}_9$	125
4.12	Relaxation dispersion studies of ionic conductivity in pristine and K doped LAMOX	129
4.13	Inter-atomic potentials, thermal energy and their relation to conductivity: A theoretical estimate	134
4.14	Effect of multiple doping at La and Mo site in LAMOX	135
4.14.1	Microstructural study of rare earth (Eu) and W doped LAMOX in Ar-H_2 atmosphere	135
4.14.2	XPS study of rare-earth doped (Eu, Sm, Tm, Y) and W doped $\text{La}_2\text{Mo}_2\text{O}_9$ in reductive atmosphere	136
4.15	Summary	149
Chapter 5:	Compatibility studies of $\text{La}_2\text{NiO}_{4+\delta}$ and $\text{La}_2\text{Mo}_{1.5}\text{W}_{0.5}\text{O}_9$ based electrode/ electrolyte for fuel cell application	151
5.1	Introduction	151
5.2	X- ray diffraction studies of LN/W-LAMOX system	152
5.3	X- ray photoelectron spectroscopic study of $\text{La}_2\text{NiO}_{4+\delta}$ / $\text{La}_2\text{Mo}_{1.5}\text{W}_{0.5}\text{O}_9$ system	154
5.4	X- ray photoelectron spectroscopic study of NiWO_4 anode/ $\text{La}_2\text{Mo}_2\text{O}_9$ (electrolyte) system in reductive atmosphere	155
5.5	Raman spectroscopy study of $\text{La}_2\text{NiO}_{4+\delta}$ / $\text{La}_2\text{Mo}_{1.5}\text{W}_{0.5}\text{O}_9$ system	156
5.6	Summary	157
Chapter 6:	Concluding remarks and future work scope	159
6.1	Concluding remarks on pristine LAMOX electrolyte	159
6.2	Concluding remarks on doped LAMOX	160
6.3	Concluding remarks on $\text{La}_2\text{NiO}_{4+\delta}$ (LN) and $\text{La}_2\text{Mo}_{1.5}\text{W}_{0.5}\text{O}_9$ (W-LAMOX) based electrode/electrolyte	161

6.4 Overall concluding remarks	161
6.5 Future scope of the work	162
Bibliography	163





List of Figures

<i>Figure No.</i>	<i>Title</i>	<i>Page No.</i>
Figure 1-1	Fossil CO ₂ emissions from major emitting countries.	1
Figure 1-2	Features of future energy system based on modern needs and ability to perform multi-functional task.	3
Figure 1-3	Hydrogen as a primary energy source, energy conversion and applications.	4
Figure 1-4	Various types of fuel cells and their applications.	5
Figure 1-5	Ionic conductivity of well-known electrolyte materials as a function of temperature.	14
Figure 1-6	A typical Westinghouse Tubular design SOFC.	17
Figure 1-7	A planar design of a SOFC unit.	18
Figure 1-8	Principle of operation of a typical SOFC showing anode and cathode side reactions.	19
Figure 1-9	Cell voltage/current characteristics of a fuel cell.	20
Figure 1-10	Conductivities of LAMOX and 8 mol % YSZ.	24
Figure 1-11	(a) Three Mo coordination geometry types observed in α -La ₂ Mo ₂ O ₉ . (b) Polyhedral representation of α -La ₂ Mo ₂ O ₉ : tetrahedral groups are shown in pink, trigonal bi-pyramidal in purple, octahedral in green.	25
Figure 1-12	Cationic environments in β -SnWO ₄ (left) and β -La ₂ Mo ₂ O ₉ (right). The environment of La is limited to the nearest neighbours. Hatched and open circles represent oxygen sites being partially occupied.	26
Figure 1-13	Neutron diffraction pattern of La ₂ Mo ₂ O ₉ collected below 533 °C and above 617 °C.	26
Figure 1-14	Crystallographic environment of La ³⁺ , Mo ⁶⁺ and all three O(1), O(2) and O(3) oxygen atoms in β -LAMOX.	27

Figure 1-15	x-ray Diffraction patterns collected at room temperatures of (a) LAMOX (b) 7730 phase and (c) amorphous phase.	28
Figure 1-16	Effect of H ₂ S concentration on open circuit voltage (OCV), output voltage, anodic and cathodic over-potential of a LAMOX/LDC/LSGM single cell observed at 800 °C.	30
Figure 1-17	Diffraction pattern of LAMOX powder treated in 100 ppm H ₂ S atmosphere at 800 °C for three days.	30
Figure 1-18	(a) Enhancement of cell parameters with temperature and (b) abrupt increase in volume at 580 °C and further increase of cell volume as a function of temperature of β- LAMOX.	31
Figure 1-19	Transition of monoclinic phase of LAMOX to cubic phase with (a) W, (b) Nd content.	34
Figure 1-20	Various phases of LAMOX and LWO with increase in W content on La ₂ Mo ₂ O ₉ at room temperature.	35
Figure 1-21	Plot of DTA curves for W doped LAMOX with W varying from 1.4 to 2.	35
Figure 2-1	Sintering mechanisms for a system of two particles.	41
Figure 2-2	Diagram of x-ray diffraction process by a single crystal.	42
Figure 2-3	Schematic of electron-matter interaction and resultant signals.	45
Figure 2-4	Simplified diagram showing the XPS process, (Right side) level of depth of photoelectrons which are detected from the surface.	46
Figure 2-5	Energy level diagram showing different work functions for binding energy measurements.	47
Figure 2-6	Illustration of the photoelectron emission phenomenon and related secondary process by the excitation of the material surface with a source of energy <i>hν</i> .	48
Figure 2-7	Detailed schematic analysis of electron energy analyser showing its components and concentric hemispherical analyser with different radii description.	50
Figure 2-8	Plot of IMFP of electrons for various elements.	51

Figure 2-9	Model of bulk (blue) and surface atoms (red) of a material.	52
Figure 2-10	Typical complex impedance plot and its equivalent circuit diagram.	54
Figure 2-11	Schematic of energy levels transition in case of I.R. and Raman spectroscopy.	59
Figure 2-12	Raman spectroscopy instrumentation.	60
Figure 3-1	XRD pattern of $\text{La}_2\text{Mo}_2\text{O}_9$ at room temperature. Inset: magnified view of 311 peak in the 2θ range of 41° to 42° .	62
Figure 3-2	FE-SEM images of (a) LAMOX powder sample calcined at 800°C for 6 hours, (b) sintered LAMOX in air at 900°C for 6 hours (c) formation of cracks as a result of H_2 interaction with grains at 500°C and (d) formation of intra-granular pores as last step of reduction process at 900°C .	65
Figure 3-3	FE-SEM images of LAMOX pellet sintered at 500°C for 6 hours in reducing atmosphere (a), (b), (c) and (d). The appearance of rod shaped branches between the grains indicated by arrow shows the mass transport process which ultimately leads to grain growth.	66
Figure 3-4	FE-SEM images of LAMOX pellet sintered at 500°C for 6 hours in reducing atmosphere (a), (b), (c) and (d). The appearance of rod shaped branches between the grains indicated by arrow shows the mass transport process which ultimately leads to grain growth.	67
Figure 3-5	FE-SEM images of (a), (b), (c) and (d) $\text{La}_2\text{Mo}_2\text{O}_9$ treated under diluted hydrogen for 6 hours at 900°C . All the images were captured without conductive coating on the sample. Features visible are as a result of appearance of electronic conductivity in the sample.	67
Figure 3-6	(a) Survey spectrum of LAMOX for detection of constituent elements, (b) core level spectra of La 3d, (c) Mo 3d spectra showing spin orbit splitting, (d) O 1s singlet peak.	69
Figure 3-7	(a) Survey spectrum (Su 1s), core level spectra of (b) La 3d spectrum (c) O 1s spectrum (d) Mo^{6+} spectrum with multiple valance states.	72

Figure 3-8	Complex impedance plot for LAMOX at (a) 573 K, (b) 623 K, (c) 673 K. (d) dc conductivity plot for LAMOX. The Y axis shows conductivity values in $\mu\text{S}/\text{cm}$.	76
Figure 3-9	Complex impedance plots for LAMOX at (a) 373 K, (b) 423 K, (c) 473 K (d) D.C conductivity plot for LAMOX sintered in diluted H_2 atmosphere at 900 °C.	80
Figure 4-1	Room temperature diffraction pattern of $\text{La}_2\text{Mo}_{2-x}\text{W}_x\text{O}_9$ in the range of $0.25 \leq x \leq 1.75$. The fewer reflection peaks correspond to higher symmetry, in this case cubic symmetry with space group $P2_13$.	85
Figure 4-2	Rietveld refinement of (a) $x = 0.25$ (b) $x = 0.75$ (c) $x = 1.0$ (d) $x = 1.25$ and (e) $x = 1.5$ W doped $\text{La}_2\text{Mo}_{2-x}\text{W}_x\text{O}_9$ compositions. The inset Figures are in (a), (b) and (c) shows the confirmation of cubic nature of W doped LAMOX along with the $K\alpha_2$ effect.	88
Figure 4-3	(a) Oxygen site occupancy of O(2) and O(3) atoms confirming the oxygen ion vacancies in the lattice and (b) Lattice parameter obtained from XRD data room temperature by Rietveld analysis considering $P2_13$ space group.	89
Figure 4-4	Fourier Map and 3-D electron density map of LAMOX.	93
Figure 4-5	Room temperature XRD of Ar- H_2 sintered W doped LAMOX compositions and their intermediate products formed as result of Mo reduction in Ar- H_2 atmosphere. The peaks of $\text{La}_2\text{Mo}_2\text{O}_9$ has not been shown because of overlapping of peaks.	94
Figure 4-6	Images of (a) W = 0.5 doped LMO sample treated in air (white) and Ar- H_2 atmosphere (black). (b) W = 1.75 doped. H_2 treated sample was less reduced in the latter due to high amount of W in the host lattice.	95
Figure 4-7	(a), (b), (c) and (d) Microstructures of air sintered W 0.25 doped LAMOX pellets for 4 hours. Arrows indicate the formation of pores at the grain boundaries.	95
Figure 4-8	Microstructures for W 0.25 doped LAMOX treated in Ar 90 % - H_2 10 %. The images clearly reveal the intra-granular porosity and formation of new products of reduced molybdates marked by arrows.	96

- Figure 4-9 Microstructures for W 1.0 doped $\text{La}_2\text{Mo}_2\text{O}_9$ treated in Ar 90 % - H_2 10 %. The images clearly reveal the intra-granular porosity and formation of new products of reduced molybdates marked by arrows. 97
- Figure 4-10 Microstructures for W 0.25 doped $\text{La}_2\text{Mo}_2\text{O}_9$ treated in Ar 90 % - H_2 10 % without conductive coating. The images clearly reveal the intra-granular pores at high magnification marked by arrows. 98
- Figure 4-11 Microstructures for W 0.5 doped $\text{La}_2\text{Mo}_2\text{O}_9$ treated in Ar 90% - H_2 10% without conductive coating. The images clearly reveal the intra-granular pore at high magnification marked by arrows and reduced molybdates. 98
- Figure 4-12 Microstructures for W 0.75 doped $\text{La}_2\text{Mo}_2\text{O}_9$ treated in Ar 90% and H_2 10% without conductive coating. The images clearly reveal the intra-granular pore at high magnification marked by arrows. 99
- Figure 4-13 Microstructures for W 1.75 doped $\text{La}_2\text{Mo}_2\text{O}_9$ treated in Ar 90% - H_2 10% without conductive coating. The images clearly reveal the charging effect due to accumulation of electrons on the sample surface from the beam. 99
- Figure 4-14 XPS Survey spectrum for $x = 0.25$ doped $\text{La}_2\text{Mo}_{2-x}\text{W}_x\text{O}_9$. 100
- Figure 4-15 Core level spectra of W (0.25) doped $\text{La}_2\text{Mo}_2\text{O}_9$ (a) La 3d, (b) O 1s, (c) W 4f, (d) Mo 3d of W doped LAMOX samples treated in air. The Mo 3d and W core level show natural splitting of the peak which indicates the presence of single $6+$ oxidation state. 101
- Figure 4-16 Nature of bonding based on O 1s peak values for (a) air treated and (b) Ar- H_2 treated W doped LAMOX samples in the W doping range of 0 to 2. 103
- Figure 4-17 Core level spectra of W doped $\text{La}_2\text{Mo}_2\text{O}_9$ (a) La 3d (b) O 1s (c) W 4f and (d) Mo 3d of W doped LAMOX samples treated in Ar- H_2 conditions. The Mo 3d core level shows the splitting of the spectrum which indicates the presence of multiple oxidation states of Mo. 105
- Figure 4-18 Plot of atomic concentration of various oxidation states of Mo in W doped LAMOX with varying concentrations. The graph clearly reveals that Mo^{6+} content has not been fully stabilised by W doping. 107

Figure 4-19	Complex impedance plot of $\text{La}_2\text{Mo}_{1.5}\text{W}_{0.5}\text{O}_9$ at (a) 613 K and (b) 653 K. (c) log-log plot of σ_{ac} vs. frequency at 593 K. (d) Frequency dispersion of real part of conductivity at 633 K, (e). Imaginary part of modulus of $\text{La}_2\text{Mo}_{1.5}\text{W}_{0.5}\text{O}_9$ at 633 K (blue) and 613 K (black) (f) Temperature dependence plot of dc conductivity σ_{dc} at various temperatures.	110
Figure 4-20	(a) Plot of σ_{dc} as a function of temperature ($1/T$). The slope of the graph yields activation energy (E_a) and follow the Arrhenius equation. (b) Plot of $\log\sigma_{ac}$ vs. \log frequency. The slope of the straight line gives the value of s , which represents the frequency dependent ac conductivity which follows the universal power law.	112
Figure 4-21	x-ray diffraction pattern for 5 mol % and 10 mol % for K doped $\text{La}_2\text{Mo}_2\text{O}_9$ obtained at room temperature.	115
Figure 4-22	Rietveld refinement of $x = 0.1$ mole fraction doped $\text{La}_2\text{Mo}_2\text{O}_9$. Inset shows the (321) peak, singlet in nature confirming the cubic nature of the composition.	115
Figure 4-23	Microstructures of $\text{La}_{1.9}\text{K}_{0.1}\text{Mo}_2\text{O}_9$ sintered in air (a) low magnification (b) high magnification, Ar- H_2 sintered (c) low magnification and (d) high magnification. Pore formation due to incomplete sintering in Ar- H_2 is indicated by arrow.	120
Figure 4-24	XPS spectra of K = 5 mol % doped LAMOX (a) survey and core level spectra of air sintered and Ar- H_2 sintered reducing atmosphere (b) K 2p, (c) La 3d, (d) O 1s, (e) Mo 3d and (f) Mo 3d reduced. The data were collected at room temperature.	122
Figure 4-25	XPS spectra of K = 10 mol % doped LAMOX. Core level spectra of air sintered and Ar- H_2 reduced sample (a) La 3d (b) O 1s, (c) Mo 3d air sintered and (d) Mo 3d reduced. All the spectra were collected at room temperature.	123
Figure 4-26	Raman spectra of (a) LMO and (b) K = 0.2 doped LMO. The difference in the intensities of band 1 and band 2 indicates the difference in crystallographic structure from monoclinic in LMO to cubic phase in K doped $\text{La}_2\text{Mo}_2\text{O}_9$.	125
Figure 4-27	Complex impedance plot of $\text{La}_{1.8}\text{K}_{0.2}\text{Mo}_2\text{O}_9$ at (a) 573 K (300 °C) and (b) 593 K (320 °C) (c) 613 K (340 °C) (d) 633 K (360 °C) (e) 653 K (380 °C) and (f) 673 K (400 °C).	126
Figure 4-28	(a) log dc conductivity plot for LMO vs. $1/T$ (b) dc conductivity variation with temperature.	128

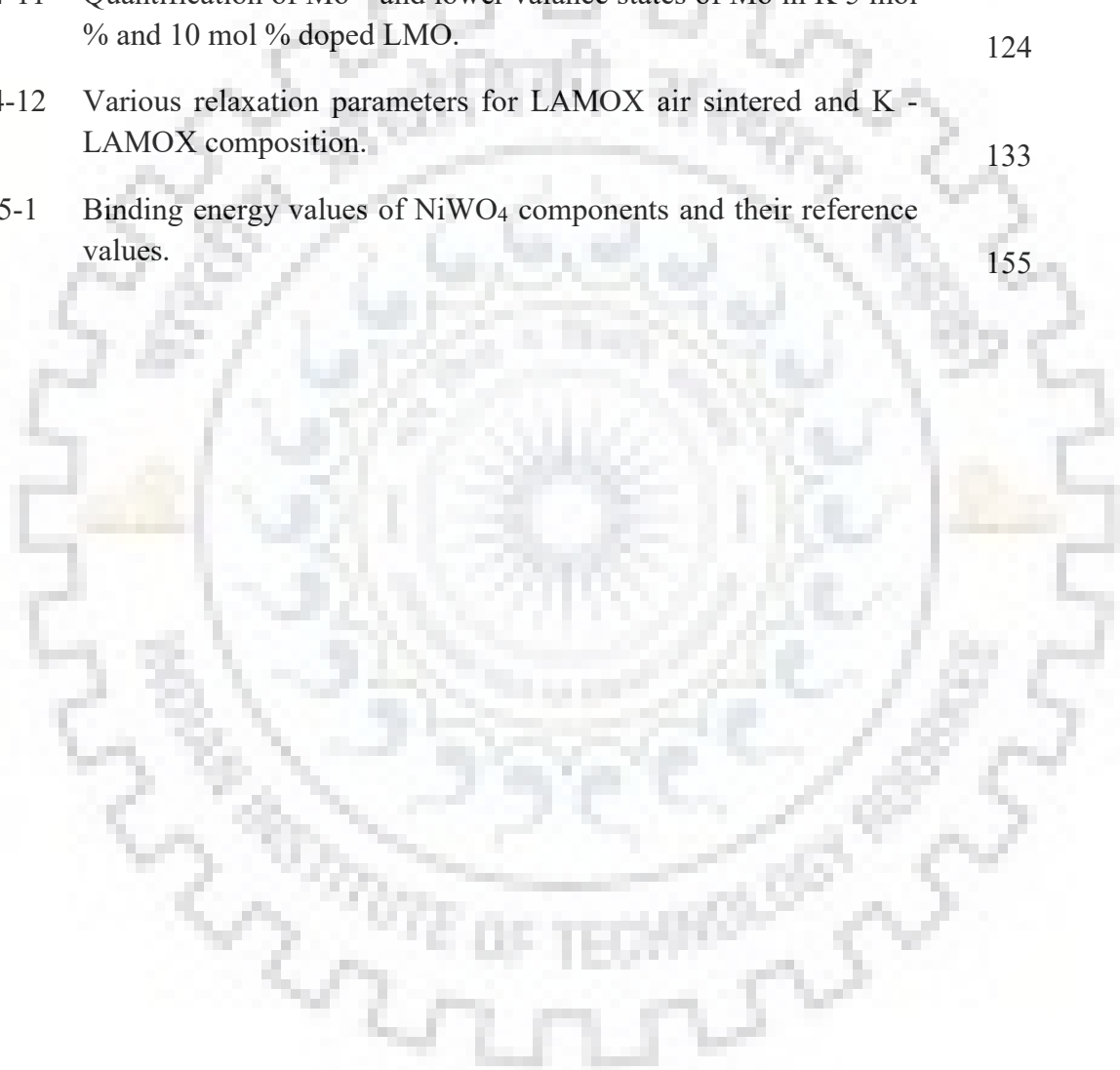
Figure 4-29	Frequency dependence of imaginary part (Z'') of complex impedance of (a) K doped LAMOX (b) LAMOX treated in air and (c) LMO treated in Ar-H ₂ at 900 °C.	130
Figure 4-30	Various polarisation processes with time.	131
Figure 4-31	Thermally activated diffusion process and energy barrier during migration of ions.	132
Figure 4-32	FE-SEM images of Eu and W doped La ₂ Mo ₂ O ₉ . Intra-granular pores are visible without carbon coating on the specimen due to reduction in Ar-H ₂ atmosphere.	136
Figure 4-33	Core level spectra of respective elements of Eu 10 mol % and W 50 mol % doped LAMOX treated in reductive atmosphere. (a) O 1s (b) La 3d(c) Eu 4d (d) W 4f (e) Mo 3d and (f) C 1s.	139
Figure 4-34	Core level spectra of respective elements of Sm 10 mol % and W 50 mol % doped LAMOX treated in reductive atmosphere. (a) La 3d (b) O 1s (c) Sm 3d (d) W 4f (e) Mo 3d and (f) C 1s.	142
Figure 4-35	Core level spectra of respective elements of Tm 10 mol % and W 50 mol % doped LMO treated in reductive atmosphere. (a) La 3d (b) O 1s(c) Tm 4d (d) W 4f (e) Mo 3d and (f) C 1s.	145
Figure 4-36	Core level spectra of respective elements of Y 10 mol % and W 50 mol % doped LMO treated in reductive atmosphere. (a) La 3d (b) O 1s (c) Y 3d (d) W 4f (e) Mo 3d and (f) C 1s.	148
Figure 5-1	(Left side) Room temperature diffraction patterns of equimolar mixtures of La ₂ Mo _{1.5} W _{0.5} O ₉ and La ₂ NiO _{4+δ} at 500 °C and 600 °C respectively. The pattern shows formation of new NiWO ₄ phase along with the parent phase, (Right side): Deconvoluted core level spectra of (a) O 1s peak (b) W 4f peak and (c) Ni 3p peak sintered at 600 °C for 4 hours for LN/W-LAMOX.	153
Figure 5-2	(Left side) Deconvoluted core level spectra of (a) O 1s peak (b) Ni 3p (c) Mo 3d peak and (d) La 3d and Ni 2p sintered at 600 °C of NW/LAMOX system for 4 hours, (Right side): Raman spectrum of LN / W-LMO showing the presence of NiWO ₄ peaks along with Mo-O bonding and oxygen vacancies existence.	156



List of Tables

Table No.	Title	Page No.
Table 1-1	Global emission of the top 15 nations by total CO ₂ volume in mega metric of tonnes.	2
Table 1-2	Evolution of fuel cell.	6
Table 1-3	Classification of fuel cells on the basis of electrolytes and their operating temperatures.	8
Table 1-4	Difference between various types of fuel cell.	9
Table 1-5	Structural information of β -LAMO _X 670 °C.	27
Table 1-6	Various substitutions at La and Mo sites with their respective solubility limits.	32
Table 1-7	Various cathode materials and their reaction with LAMO _X and the formation of secondary products as a function of temperature.	37
Table 3-1	Binding energies of various elements and their respective oxidation states.	73
Table 3-2	Respective oxidation state and quantitative analysis of respective phase of Mo in LAMO _X treated in Ar-H ₂ atmosphere.	74
Table 3-3	Values of Re (Z) and dc conductivity of air treated LAMO _X at various temperatures.	76
Table 4-1	Bond lengths between various elements and lattice parameters of W doped LAMO _X generated by Rietveld analysis using space group P2 ₁ 3.	90
Table 4-2	Refined crystal structure parameters (sp. gr. P 2 ₁ 3) of La ₂ Mo _{2-x} W _x O ₉ from XRD data obtained at room temperature.	91
Table 4-3	Unoccupied oxygen atom coordinates form difference Fourier analysis of La ₂ Mo _{2-x} W _x O ₉ .	92
Table 4-4	La 3d _{3/2} and 3d _{5/2} binding energy difference values of W doped LAMO _X compositions sintered in air and Ar/H ₂ atmosphere.	102
Table 4-5	Binding energies of O 1s peak of air and Ar-H ₂ sintered W doped LAMO _X compositions.	103
Table 4-6	Concentration values for Mo oxidation states obtained by heat treated in Ar-H ₂ atmosphere at 900 °C for 4 hours.	106

Table 4-7	Refined crystal structure parameters (sp. gp P 2 ₁ 3) of La _{1.9} K _{0.1} Mo ₂ WO ₉ from XRD.	117
Table 4-8	Determination of missing oxygen atom coordinates from difference Fourier analysis of La _{1.9} K _{0.1} Mo ₂ O ₉ .	118
Table 4-9	Calculated bond lengths between various elements in K 5 mol% doped La ₂ Mo ₂ O ₉ compositions by Rietveld analysis.	118
Table 4-10	Comparison of bond length of K doped LAMOX with β-LAMOX	119
Table 4-11	Quantification of Mo ⁶⁺ and lower valance states of Mo in K 5 mol % and 10 mol % doped LMO.	124
Table 4-12	Various relaxation parameters for LAMOX air sintered and K - LAMOX composition.	133
Table 5-1	Binding energy values of NiWO ₄ components and their reference values.	155



List of Publications

International Journals (Ph.D):

Siddharth, Sandip Bysakh and Anjan Sil “X-ray photoelectron spectroscopy and ion dynamics study of W^{6+} doped $La_2Mo_2O_9$ as SOFC electrolyte” Materials Research Bulletin, Volume 105 September 2018, Pages 36-44.

Siddharth, Anjan Sil and Sandip Bysakh “Effect of grain boundary and Ar- H_2 atmosphere on electrical conductivity of bulk $La_2Mo_2O_9$ studied by impedance and x-ray photoelectron spectroscopy” 2019. Materials Research Express 6 035505

Siddharth, Anjan Sil and Sandip Bysakh “Effect of K doping on Mo^{6+} stability and ionic conductivity study in $La_2Mo_2O_9$ as oxide-ion conductor” 2019. Materials Research Express 6 056203.

International Journals (Others):

Siddharth et al., “X-ray photoelectron spectroscopy study on adsorption property of harmful air pollutants on zeolite prepared from fly ash” Mater. Res. Express 2018, 5, 085507.

Hari Raj, **Siddharth**, Anjan Sil “ TiO_2 shielded Si nano-composite anode for high energy Li-ion batteries: the morphological and structural study of electrodes after charge-discharge process”. Electrochimica Acta, 2019, 326, 134981. (SCI, I.F.)

Conference(s):

1. International Conference (2017), International Conference on Advances in Materials and Processing Challenges and Opportunities (AMPCO 2017) organized by IIT Roorkee, Roorkee-247667 (U.K.)



List of Abbreviations

CCD	Charge Coupled Devices
DC	Direct Current
EIS	Electrochemical Impedance Spectroscopy
FE-SEM	Field Emission Scanning Electron Microscope
GDC	Gadolinium Doped Ceria
K - LAMOX	Potassium Doped $\text{La}_2\text{Mo}_2\text{O}_9$
LAMOX or LMO	$\text{La}_2\text{Mo}_2\text{O}_9$
LN	$\text{La}_2\text{NiWO}_{4+\delta}$
Ni-YSZ	Nickel- Yttria Stabilised Zirconia
NIO	Normal Ionic Oxide
NW	NiWO_4
OCV	Open Circuit Voltage
RS	Raman Spectroscopy
SOFC	Solid Oxide Fuel Cell
SCO	Semi Covalent Oxide
W-LAMOX	Tungsten Doped $\text{La}_2\text{Mo}_2\text{O}_9$
VIO	Very Ionic Oxide
XRD	X-Ray Diffraction
XPS	X-Ray Photoelectron Spectroscopy
XRF	X-Ray Fluorescence
YSZ	Yttria Stabilised Zirconia

Chapter 1

Introduction and literature review

1. Introduction

1.1 The energy challenge

The worldwide necessity for meeting energy demand is growing at a tremendous rate. According to a report by “World Energy Technology and Climate Policy Outlook” (WETO) has estimated an annual growth rate of 1.8 % in primary energy sources globally from 2000 to 2030. This growing demand for energy is currently primarily fulfilled by fossil fuel reserves, which emit not only greenhouse gases but also other harmful pollutants, thereby causing an ecological imbalance. These fossil fuel reserves are depleting at a very fast rate and thus becoming costlier. By 2030, the CO₂ emission from developing nations will account for more than half of the world's CO₂ emission, with China being the principal contributor of CO₂ emission. [Jos et al., 2015; J.R.C., Crippa et al., 2019; Palacio E.U. Report 2003].

Figure 1-1 depicts the CO₂ emission from the major countries of the world. China due to its fast-growing economy is the major contributor in CO₂ emission followed by United States of America (USA), India, countries of European Union (E.U.) and Japan. Majority of CO₂ emission is due to burning of fossil fuels in various sectors viz. energy, transport, industry etc., To minimise some of the effects caused by burning of fossil fuels, clean energy approaches are being adopted. In this context, a fuel cell may definitely be considered as a green energy source that produces electricity by chemical reaction of hydrogen and oxygen, which has water as its by-product.

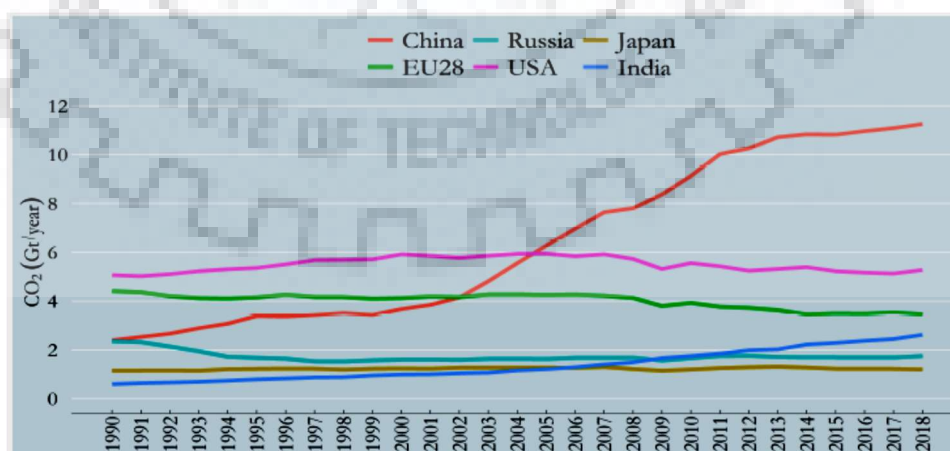


Figure 1-1 Fossil CO₂ emissions from major emitting countries (Source; Crippa et al., 2019).

As of current times, global warming is taking place because of gas emissions viz. CO₂, NO_x, SO_x, and CO gases. According to a survey conducted by Intergovernmental Panel on Climate Change (IPCC), the average global surface temperature for the period 2006-2015 was 0.87 °C higher than last century [IPCC 2018; Eurobarometer Climate Change Report 2017; NCAR 2001]. Table 1-1 shows the CO₂ emissions of the top 10 nations. According to the latest energy review by the United States Energy Information Administration (EIA) and international energy agency (IEA) [UCUSA, IEA 2019], China has surpassed the United States of America (USA) in CO₂ emission with India as currently ranked third in CO₂ emission. The sulphur emissions from marine ships are also a major source of marine life pollution, causing a huge ecological imbalance. A reduction of 85 percent in sulphur emission is proposed from 2020 [Annual energy Outlook 2019; Annual energy review 2011]. One of the main concerns associated with these primary energy usages is related to air pollution. But it has also been extended to environmental concerns such as acid precipitation, depletion of the ozone layer, forest destructions, and overall ecological imbalance resulting in global warming.

Table 1-1 Global CO₂ emissions of the top 10 nations in mega metric of tonnes (Source; USA Today 2019, Crippa et al., 2019).

Rank	Nation	CO ₂	Rank	Nation	CO ₂
1	China	9838.8	6	Germany	799.4
2	USA	5269.5	7	Iran	672.3
3	India	2466.8	8	S. Arabia	635.0
4	Russia	1692.8	9	S. Korea	616.1
5	Japan	1205.1	10	Canada	572.8

It is known that energy security is a major concern for each country. Fossil fuel reserves, particularly crude oil, is confined to very few areas in the world. The continuity of these energy resources is often governed by political, economic, and ecological factors. The world population keeps increasing at 1.2 – 2 % per year and is expected to reach 12 billion in the year 2050. Economic development will also continue to grow. Due to the increase in energy demand by the growing population, the use of primary energy needs is expected to increase by three times [Annual energy Outlook 2019; Annual energy review 2001]. Therefore, there is an urgent demand for such energy systems that can fulfill the needs of society without harming the

ecosystem. Figure 1-2 below shows a future energy system that will have the following characteristics.

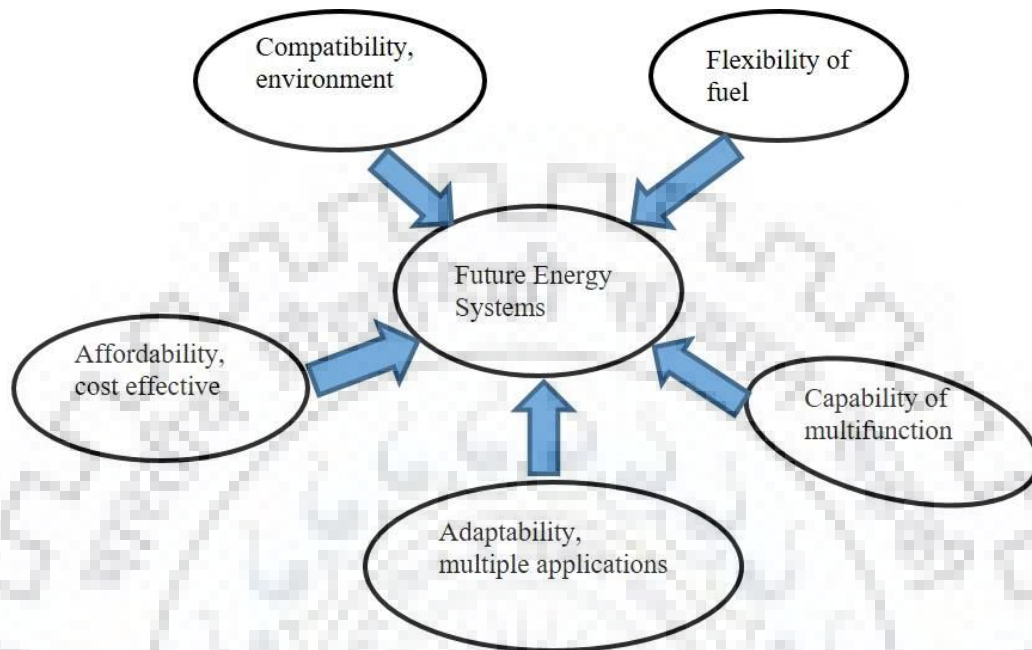


Figure 1-2 Features of future energy system based on modern needs and ability to perform multi-functional task.

As the global oil supply is decreasing day by day, the development of new power generation technologies is becoming paramount. As a matter of fact, energy is one of the prime factors that is considered for the sustainable development of any society. In response to clean energy approach, many efforts have been made to reduce fossil fuel consumption and improving energy efficiency. In response to fossil fuel-based technology, the solid oxide fuel cell (SOFC) technology is one of the most efficient and eco-friendly technologies currently being researched and developed for power generation from hydrogen and other natural gases. Many large scales, utility-based power generation systems, have already been implemented in the U.S.A., Europe, Japan, Canada and Australia, and other developed countries.

1.2. Hydrogen and fuel cells

To provide a clean, safe, reliable and secure energy supply, the energy systems must meet the following criteria to

- a) weaken the effects of climate change

b) reduce harmful pollutants

c) develop a secondary plan to overcome rapidly diminishing reserves of oil and natural gases.

If the above criteria are not fulfilled, the above will have a negative impact on:

1) economy

2) the environment; and

3) public health.

Therefore, for creating a clean, reliable, safe, and secure source of energy, one must promote efficient use of energy and its supply from a growing proportion of carbon-free sources. As we all know, the potential effects of fuel combustion products on climate change are very serious, and above all, the effects are irreversible.

Hydrogen can be an option as a carbon-free energy source. However, it is not a primary energy source like coal and gas, but it is an energy carrier. In longer-term, renewable energy sources will be the key to the production of hydrogen. Producing hydrogen in large quantities and its transportation beyond a certain limit could become a barrier to the progress. Storage of hydrogen is achieved by adsorption or chemisorption process. Maroudas and co-workers, has explored the possibilities of hydrogen storage through the chemisorption process on carbon nanotubes mentioned elsewhere in detail [Maroudas et al., 2009a; 2009b]. Figure 1-3 and figure 1-4 illustrate the application of hydrogen and fuel cell energy systems.

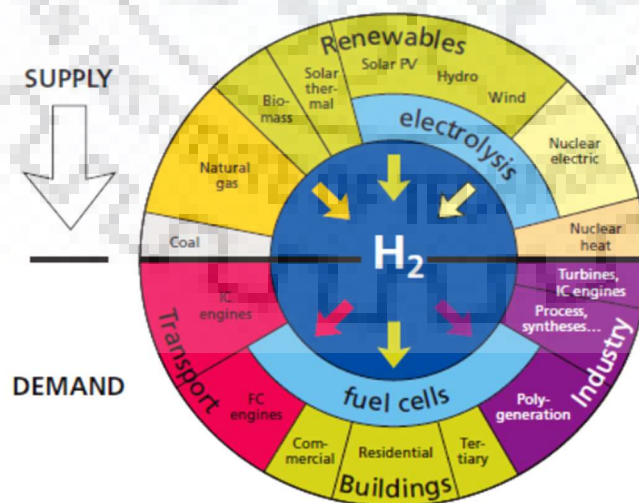


Figure 1-3 Hydrogen as a primary energy source, energy conversion and applications (Source; Palacio 2003).

The advantages of hydrogen-based fuel cells are very broad, but they will not be fully utilised until the awareness of green energy sources, and its commercial applications are widespread in society. Hydrogen used in fuel cell systems has negligible/zero emission of harmful gases like NO₂, SO₂, and CO. Because of their low noise and high quality of power, the fuel cell systems are suitable for use in hospitals, IT sectors and even in mobile communication tower applications.

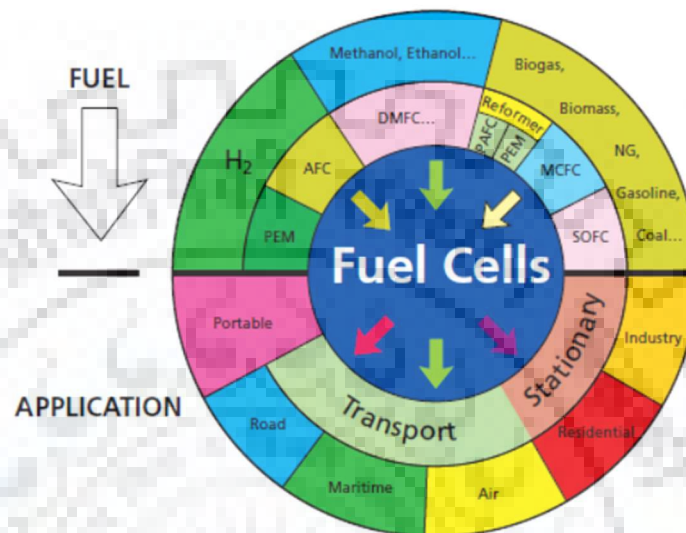


Figure 1-4 Various types of fuel cells and their applications (Source; Palacio 2003).

The following abbreviations are used in fuel cell technologies. AFC: Alkaline Fuel Cell; DMFC: Direct Methanol Fuel Cell; MCFC: Molten Carbonate Fuel Cell; PEM: Proton Exchange Membrane; SOFC: Solid Oxide Fuel Cell.

1.3. Fuel cell and its origin

Basically, a fuel cell is a device that converts the chemical energy (of hydrogen or natural gas as fuel) directly into electrical energy and heat without any requirement of fuel combustion as an intermediate step. As a result, higher efficiency is obtained for fuel cells as compared to conventional thermo-mechanical methods, which involve the burning of primary fuels. In case of the fuel cells, electricity is generated through the combination of hydrogen or any natural gas, e.g., methane or propane, as a fuel supplied at one electrode and oxygen from the air at the other electrode via an ion-conducting electrolyte. However, unlike a battery, the fuel cells neither get exhausted nor require recharging. It works as long as both fuel and oxygen supplies are maintained at the respective electrodes.

Many attempts are being made to develop the fuel cells as power sources, but initially, their usage was restricted mainly to space and defense applications. In space applications, the shuttles have

pure hydrogen (H₂) and liquid oxygen (O₂) tanks as fuel supplies to propel them in space. With these two as fuel sources, the cells can generate power on board, and the by-product water (H₂O) can be used by astronauts for their survival.

Due to their strong influence on society, the fuel cells have been known for more than 160 years. It is a subject of intense research since World War II. Table 1-2 shows the evolution of fuel cell made by the researchers [Grove 1839; Nernst 1899 and Bezian 1998]. Almost all the fuel cells were discovered before 1939.

Table 1-2 Evolution of fuel cell (Source; Bezian 1998).

Scientist	Year	Contribution
Alessandro Volta	1795	Electrical phenomena
J W Ritter	1803	Founder of electrochemistry
Sir Humphrey Davy	1802	Simple fuel cell
Christan Friedrich Schonbein	1829-1868	First principle of fuel cell
Sir William Grove	1838	Wet cell battery
Friedrich Wilhelm Ostwald	1899	Ceramic fuel cells
Francis Thomas Bacon	1930	Alkali type electrolyte fuel cells
Emil Baur	1937	Solid Oxide Fuel Cells

Fuel cells have played a vital role in many space programs in the past years. In 1960, space Apollo program hydrogen-powered fuel cells were extensively used to power on-board electrical systems of the spacecraft on the Apollo journey to the moon [Warshay 1989]. Today fuel cells are very important accessories in space flight, transportation for making portable power, stationary and large power generation in various systems.

1.3.1 Fuel cell status in India and foreign countries

Nowadays fuel cell-based industry is gaining massive attention worldwide, including in India. The fuel cells are being utilised in stationary power sources like data centres, buildings, hospitals etc. According to the U.S. Department of Energy report, more than 235 MW stationary fuel cell power installations have been done in nearly 43 states of America. Recent emerging applications of fuel cells include forklifts at airports, public transport buses, and heavy-duty trucks. Recently

Germany has launched a world's first fuel cell-powered train, the first fuel cell cargo trucks at U.S. airport and stadium lights are now being powered for the very first time to widen the potential applications of fuel cells [Satyapal 2018].

Westinghouse and Siemens are the two major companies for SOFC development. Besides these two companies Lockheed Martin, Versa Power (U.S.A.), L.G. Fuel Cell Systems (South Korea), Ceres (U.K.), Mitsubishi (Japan), ApA (Italy), Staxera-Sunfire (Germany), Toposoe (Denmark) and Ceramic Fuel Cells Limited (Australia) are among the key players for SOFC development and commercialisation. Sumitomo and Acumetrics (Japan) have developed 1 kW fuel cell system for home applications. Whereas, Bloom energy has installed 100 kW planar SOFC design in stationary applications. In developed nations like the U.S.A., U.K., Australia, Canada, Germany, and Denmark, they have advanced in SOFC research and commercialisation of fuel cell technologies [Report on fuel cell 2016].

As far as the fuel cell research status in India is concerned, a significant jump is noticed. Premier academic institutes in India like CSIR-CGCRI Kolkata, CSIR-NCL Pune, CSIR- NAL Bangalore, Indian Institute of Technology Delhi, Indian Institute of Technology Madras, Indian Institute of Technology Kanpur, Indian Institute of Technology Mumbai and recently Indian Institute of Technology Roorkee are actively engaged in SOFC research, development and their commercialisation in India. Till now, 500 W of fuel cell planar system with hydrogen as a fuel has been demonstrated by CSIR-CGCRI with glass-based sealants developed indigenously by them. However, some challenges like the absence of unified program involving academic institutes and industries either public or private, relating SOFC technology as an alternate source of energy, competition from the global manufacturers especially from China and necessary funding requirement for R&D is likely to create a delay in the overall development and commercialisation of fuel cell technology in India. Hydrogen production, its storage, and distribution are other problems that need to be addressed since it is used as fuel in all fuel cell systems [Report on fuel cell 2016; Rao 2003].

1.3.2 Types of fuel cells

Generally, the fuel cells are characterised by the chemical features of the electrolyte being used as an ionic conductor and its operating temperature. The classification of the various fuel cells is shown in table 1-3. It is evident from the table that earlier developed fuel cells had a low operating temperature, but the liquid electrolyte poses the space and portability problem. Whereas, the SOFC, despite having higher operating temperatures, requires less space and does not have any portability issues. Moreover, they have the advantage of solid electrolytes sandwiched between

two electrodes. Since their discovery, there had been a lot of research works on developing high efficiency and economical fuel cells. The most common commercialised electrolytes being employed in the SOFCs are yttria-stabilized zirconia (YSZ) and gadolinia doped ceria (GDC) based oxide ceramics. A detailed explanation has been given in subsequent sections. Table 1-4 shows the major differences between various fuel cells and their descriptions.

Table 1-3 Classification of fuel cells on the basis of electrolytes and their operating temperatures (Source; Stambouli and Traversa 2002).

Types of fuel cell	Electrolyte	Operating Temp. (°C)	Fuel	Oxidant	Efficiency (%)
Alkaline	KOH	50-200	Pure H ₂ or hydrazine	O ₂ /Air	50-55
Direct Methanol	Polymer	60-200	Liquid methanol	O ₂ /Air	40-55
Phosphoric acid	Phosphoric acid	160-210	H ₂ from hydrocarbon or alcohol	O ₂ /Air	40-50
Sulphuric acid	Sulphuric acid	80-90	Alcohol or impure H ₂	O ₂ /Air	40-50
Proton exchange membrane	Polymer, proton exchange membrane	50-80	Less pure H ₂ form hydrocarbon or methanol	O ₂ /Air	40-50
Molten Carbonate	Nitrate salts such as nitrates and sulphates	630-650	H ₂ , CO ₂ or Natural gas	CO ₂ /O ₂ /Air	50-60
Solid Oxide	YSZ, perovskite	600-1000	Natural gas or propane	O ₂ /Air	45-60
Protonic Ceramic	BaCeO ₃ film	600-700	Hydrocarbons	O ₂ /Air	45-60

Table 1-4 Difference between various types of fuel cell (Source; Ravella 2012).

	PEFC	PAFC	MCFC	SOFC
Electrolyte	Ion Exchange Membrane	Immobilised Liquid Phosphoric acid	Immobilised Liquid Molten Carbonate	Ceramic
Operating Temperature (°C)	80	205	650	600-1000
Charge Carrier	H ⁺	H ⁺	CO ₃ ²⁻	O ²⁻
External Reformer for CH₄	Yes	Yes	No	No
Prime Cell Components	Carbon- based	Graphite-based	Stainless-steel	Ceramic
Catalyst	Platinum	Platinum	Nickel	Perovskites
Product Water Management	Evaporative	Evaporative	Gaseous Product	Gaseous Product
Product Heating Management	Process Gas + Independent Cooling Medium	Process Gas + Independent Cooling Medium	Internal Reforming + Process gas	Internal Reforming + Process gas

The low-temperature fuel cells such as proton exchange and alkaline types are mainly utilised for transport purposes. According to the current literature proton exchange membrane fuel cell have shown to exhibit superior properties by incorporating nano-clay in its hybrid structure. This also helps in fabricating novel membranes for the PEM fuel cells [Maiti 2016; Maiti 2017a; 2017b]. The phosphoric acid fuel cell, being a medium temperature range fuel cell, is considered as a first-generation fuel cell developed. Molten carbonate fuel cell (MCFC), which usually operates at higher temperatures of 650 °C and above is considered as a second-generation fuel cell at an operating capacity of 100 kW range.

The solid oxide fuel cell is the third generation fuel cell, which is gaining much interest because of its efficiency and versatility in power generation systems. The operating temperature is around 1000 °C, but efforts are being made to develop SOFC requiring lower operating temperatures of 800-900 °C. A 140 kW power supply SOFC manufactured by Siemens Inc. has been under operation in the Netherlands, and 1 MW SOFC facility has also been commissioned by the department of energy (DOE) U.S. and Siemens Westinghouse [Chalk 2002; Stambauli 2002]. Apart from the above-mentioned fuel cells, research on new kinds of fuel cells is under progress. This new fuel cell system is known as microbial fuel cell, which involves certain kinds of bacteria as catalysts to oxidise the organic/inorganic materials and CO₂ for the production of the green fuel which may be fed to fuel cells to generate electric current. The details have been mentioned elsewhere [Verma 2017a; 2017b].

1.3.3 Theory of fast oxide ion conductors

Fast ionic conductors play an important role in a clean energy source. Out of these ionic conductors, oxide ion conductors are the most studied ones because of their wide range of applications viz. in oxygen sensors, oxygen separating membranes, membranes for oxygen catalysis, and electrolytes for the solid oxide fuel cells (SOFCs). The oxide ion conducting property was discovered by Nernst [Nernst 1899]. The oxide ion can be defined as a negatively double charged ion with an ionic radius of 1.40 Å [Shannon 1976]. It can interact with its host cationic network in the structure. Being such a large ion, it requires high operating temperatures in order to attain high mobility in a particular crystallographic structure which can support its movement inside the structure through the vacant sites for the ion transport. A material can support the oxide ion conduction provided it has vacant sites within the structure [Jacquens et al., 2010]. Therefore, most of such electrolytes have cubic or near cubic structures which support oxide ion conductivity. For some electrolyte materials, the structure may be non-cubic, in which the ion conduction occurs through the conducting planes, which is an example of anisotropic conductivity [Steele 2001a; 2001b; Arai 1992].

As stated earlier, to achieve high ionic conductivity, a material should have vacant oxygen sites through which oxide ions can move. These vacant positions can be obtained in two ways. Firstly, that the material should have enough intrinsic vacancies for oxide ion migration and secondly can be generated by doping with suitable aliovalent cations [Liu 2011].

1.3.4 Components of fuel cell

A fuel cell unit mainly consists of two electrodes, namely: anode, cathode and a solid electrolyte. The fuel is an important part of the SOFC unit, and it is converted into hydrogen. The function of the SOFC relies mainly on O^{2-} (oxide ion) or H^+ (proton) transport from cathode to anode side or vice-versa through the electrolyte.

The main function of both the electrodes is to initiate the reaction between the reactants (fuel and oxygen) through the electrolyte, without getting damaged or corroded during the reaction. The fuel cell unit should also bring the three phases, i.e., the electrode, electrolyte, and the fuel into contact with each other. Of the two electrodes, the anode is the negative electrode of the cell, which disperses the hydrogen gas over its whole surface and conducts electrons freed from hydrogen gas molecules and are used in the external load application.

The cathode, being the positive electrode of the fuel cell unit, distributes the oxygen supplied to it and conducts the electrons coming from external circuit where they recombine with oxygen atoms which are converted into oxide ions which pass through the electrolyte and combines again with hydrogen to form water molecules as a secondary product along with the heat.

The electrolyte of a fuel cell determines the temperature of operation. It also acts as an insulator between the two electrodes, which prevents them from short-circuiting and restrict the flow of electrons through itself. It allows the flow of charged ions within its structure and maintains the overall electrical charge balance. Based on the ion conductors, electrolytes for fuel cells can be categorised into:

- a) oxide ion conductor: a typical example is YSZ electrolyte in which O^{2-} ion migrates from cathode to anode side to combine with H^+ ion and results in the formation of H_2O at anode side.
- b) hydrogen ion (proton) conductor: a typical example is $BaZr_{0.8}Y_{0.2}O_{3-\delta}$ perovskite structure. The H^+ ion migrates from anode to cathode side resulting in the formation of H_2O at cathode side.

Each part of the fuel cell has various functions to perform. Therefore, they must meet the following necessary requirements [Minh 1993]:

- 1) should have chemical, phase, morphological and dimensional stability
- 2) should have high ionic conductivity

- 3) should have chemical compatibility with other fuel cell components
- 4) should have similar thermal expansion between electrode and electrolyte to avoid any cracks during the operation
- 5) should have dense and thick electrolyte prohibiting any gas mixing
- 6) should have porous anode and cathode material at the microstructural level to allow gaseous transport to the respective reaction sites
- 7) should have high strength and toughness of individual components
- 8) should have ease of fabrication of SOFC components
- 9) should have compatibility at elevated temperatures at which ceramic structures are fabricated
- 10) should have low cost for fabrication and commercial production

Among the various types of fuel cells based upon their charge carriers, the temperature of operation, nature of the electrolyte, the most robust are SOFC based electrolytes which will be reviewed in detail.

1.3.5 Solid oxide fuel cells (SOFCs) and their necessity

SOFCs are potential candidates in high-temperature fuel cell technology. They are very much useful in full-scale industrial stations and large scale electricity generation. Some of them are being used in motor vehicles also. A SOFC system comprises a solid-state ceramic as an electrolyte which usually operates at higher temperatures (600-1000 °C). The high operating temperature promotes the internal reforming (production of H₂ from hydrocarbons) and enhances the electro-catalysis activity. The efficiency of these types of fuel cells can reach up to 70 percent [Singhal 2000]. SOFC technology is most demanding from a material point of view. Following are the points worth noting for SOFCs:

- a) SOFCs are considered to be the most reliable electricity generators currently being used across the world.
- b) SOFC is very effective in the distributed electric power generation because of its high efficiency.

- c) SOFCs are flexible in fuel selection such as hydrogen and natural gas (e.g., methane and propane, etc.)
- d) SOFCs consist of solid-state design part and have all fixed or stationary parts, therefore, can be installed indoors.
- e) SOFCs have a longer operating period of 40000 to 80000 hours.

The origin of solid oxide fuel cells is quite old. Initial research was conducted in the late 1930s by Swiss scientist Emil Baur and his colleague H Preis on various ceramic materials viz., zirconium, yttrium, lanthanum, and tungsten oxides, etc. The operation of the first ceramic fuel cell was demonstrated in 1937 at a temperature of 1000 °C. In the 1940s, O.K Davtyan of Russia studied the effect of addition of monazite sand in sodium carbonate, tungsten trioxide to enhance the ionic conductivity and mechanical strength of the doped composition.

1.4 Materials for solid oxide fuel cell

1.4.1 Electrolytes

The electrolytes in the SOFCs are usually of solid-state ceramics. A variety of oxide combinations has been used to prepare the electrolytes. One of the most common examples is 8 mol % yttria stabilised zirconia (YSZ), a highly commercialised electrolyte because of its superior properties. This type of electrolyte is purely based on the oxide ion conductivity with negligible electronic conduction. Some of the common dopants in ZrO_2 are CaO, MgO, Y_2O_3 , Sc_2O_3 and certain rare earth oxides like Nd_2O_3 , Sm_2O_3 , Yb_2O_3 . Other doped oxide-based ceramic electrolytes being used in SOFCs includes:

- Samarium doped cerium oxide (SDC), $(Ce_{0.85}Sm_{0.15})O_{1.925}$
- Gadolinium doped cerium oxide (GDC), $(Ce_{0.90}Gd_{0.10})O_{1.95}$
- Yttrium doped cerium oxide (YDC), $(Ce_{0.85}Y_{0.15})O_{1.925}$
- Calcium doped cerium oxide (CDC), $(Ce_{0.88}Ca_{0.12})O_{1.88}$
- Lanthanum Gallate ceramic that includes lanthanum strontium gallium magnesium (LSGM), $(La_{0.80}Sr_{0.20})(Ga_{0.90}Mg_{0.10})O_{2.85}$ or $(La_{0.80}Sr_{0.20})(Ga_{0.80}Mg_{0.20})O_{2.80}$
- Bismuth yttrium oxide (BYO), $(Bi_{0.75}Y_{0.25})_2O_3$

Figure 1-5 shows the comparison of ionic conductivity as a function of operating temperature for various electrolyte materials.

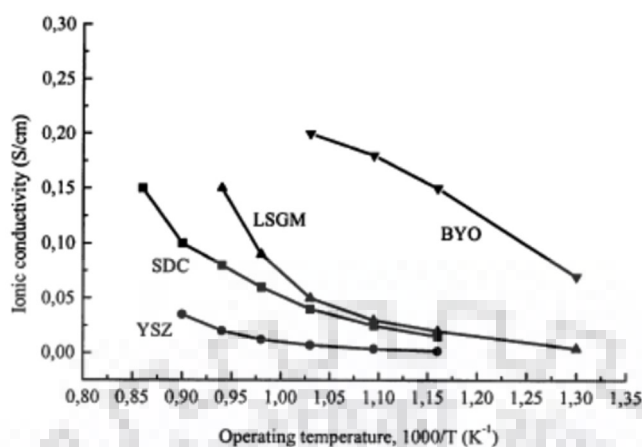


Figure 1-5 Ionic conductivity of well-known electrolyte materials as a function of temperature (Source; Fuel cell materials 2001).

1.4.2 Anode

The anode materials of SOFC are fabricated from composite powder mixtures of electrolyte material e.g., YSZ, GDC, or SDC with nickel (Ni) or nickel oxide (NiO). These composite powder mixtures are also known as cermets. The main use of the cermet is to match the thermal expansion coefficients of electrode and electrolyte. Nickel being a fine catalyst, is used in hydrogen oxidation and steam reforming. Ni is highly sensitive to sulphur which is a contamination of various fuel gas sources. It kills the active site for hydrogen oxidation. Other drawbacks include the formation of carbon fibres on the anode surface [Gerke and Willert 1999]. This issue was solved by inserting an additional layer of yttria doped ceria (CYO) between the YSZ and Ni/YSZ layer to avoid carbon deposition on the anode surface, which helps in maintaining active sites for hydrogen oxidation [Keep 1977; Murray 1999].

Some examples of conventional anode materials employed with electrolytes are:

- Ni/YSZ anode material is well suited for the applications with YSZ material.
- NiO/SDC and NiO/GDC material are best suited with ceria based electrolytes

The anode material is prepared with a porosity of 20-40 % to allow the transfer of reactant fuel and air.

1.4.3 Cathode

Due to the high operating temperature of the solid oxide fuel cells, noble metals like Pt, Pd, and Au or electronic conducting oxides are used as cathode materials which can withstand the high temperatures. Noble metals are not suitable for commercial applications due to their high cost and long term instability. Various metallic oxide compounds have been studied in this regard. Such oxides have perovskite structures like LaSrO_3 , LaCaMnO_3 , and are used at an operating temperature above 800°C . Some typical examples of the cathode materials include:

- Lanthanum doped strontium ferrite (LSF), $(\text{LaSr})\text{FeO}_3$
- Lanthanum doped strontium cobaltite (LSC), $(\text{LaSr})\text{CoO}_3$
- Samarium doped strontium cobaltite (LSF), $(\text{SmSr})\text{CoO}_3$
- Lanthanum nicklate (La_2NiO_4)

1.4.4 Fuel

Fuel to SOFCs can vary from hydrogen to a range of hydrocarbons. The use of hydrocarbon has an advantage over hydrogen. They are much easier to transport and easy to store due to their stable state. Methane, for example, yields four electrons per molecule, whereas hydrogen yields only two electrons per molecule. This advantage can be magnified by the use of complex hydrocarbons such as pentane and higher hydrocarbons to yield a large number of electrons [Galdo 2001].

1.4.5 Interconnects

Interconnects are used to make interconnections between the cells. Usually, for the tubular type modules, the interconnections are made from $\text{La}_{1-x}(\text{Sr}, \text{Mg})\text{CrO}_3$ layers and are connected by Ni pads. These type of ceramic interconnects are also used in the monolithic design. For the planar design, ceramic materials, as well as cermets options, are also possible. Metals provide good thermal and electrical conductivities, which reduce the temperature gradients and are easy for fabrication. But they also require a corrosion-resistant layer while their thermal expansion coefficient is also quite large. Siemens Company has developed a Cr based alloy in collaboration with Planese AG to overcome this problem [Badwal 1996].

1.4.6 Sealants

Sealants are required in SOFC (in planar and monolithic designs) to prevent the fuel gas and air from mixing with each other. Such an event can cause the direct combustion of fuel at an elevated

temperature that will lead to decreased power generation efficiency and may cause local overheating. The sealant materials must be stable in both oxidising as well as reducing atmospheres. Usually, the sealants used are glass-based, doped with Bismuth, or Boron.

1.5 Design classification and operation of SOFCs

SOFCs differ from other fuel cell technologies in many ways, such as:

1. they are composed of all solid-state materials.
2. they can operate at temperatures as high as 1000 °C, significantly higher than required in any other categories of fuel cells.
3. there is no limitation on the cell configuration due to the solid-state characters of all the SOFC components.

Normally hydrogen or natural gas as a fuel is supplied to the anode side of the fuel cell, and oxygen from the air is fed through the cathode side. For achieving the desired power outputs, the single unit of fuel cells is combined into multiple cell units, called a stack. Various configurations that differ in geometry, power density, and methods of sealing have been reported. Apart from their stacking methods, they also vary in their design aspects. There are two types of fuel-cell design, namely: i) self-supporting ones, where the electrolyte thickness ranging from 80-250 μm forms the structural element of the design, ii) supported structures, where the electrolyte (less than 50 μm) is deposited on a porous substrate. There are three main designs of the solid oxide fuel cells (SOFCs) on stack basis:

a) The Tubular design: This type of design is a supported base concept. In this type of configuration, a single tube represents a single cell. The Westinghouse Corporation has developed an advanced and highly efficient design of 25 kW units. The two cell units are connected by Ni felt pads. A Ca- stabilised zirconia forms a supporting structure sealed at one end on to which active parts like cathode, anode, and interconnects are placed. This type of model does not require a sealant. A typical tubular design is shown in figure 1-6. One of the disadvantages of these designs is low power density, which makes them less popular in commercial systems. The tubular SOFCs have dimensions from needle-like shapes to lengths of about 1.5–2 m for rapid start-up times and high gross power, respectively.

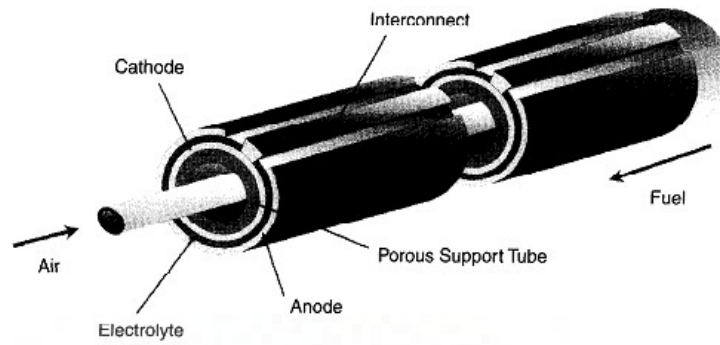


Figure 1-6 A typical Westinghouse Tubular design SOFC (Source; Badwal 1996).

b) Planar design: This design methodology is considered to be the most effective and cheapest one in the fabrication of the multiple fuel cell stacks. In this fabrication technique, the electrodes are mounted on both sides of the electrolyte in green form and co-fired simultaneously. The interconnect plates having gas channels made either from ceramics or high-temperature metal alloys are fabricated separately and stacked together and sealed with a high temperature sealing material. Figure 1-7 shows a typical planar type SOFC stack unit. These designs have the advantages of lower processing costs and a shorter current path, which helps in achieving high power density. The planar designs can be categorised in stacks containing metallic or ceramic interconnect material as well as into cells with thick (electrolyte-supported) or thin (electrode-supported) membranes with thicknesses usually of 150–250 μm and 5–20 μm , respectively [Teitz 2008].

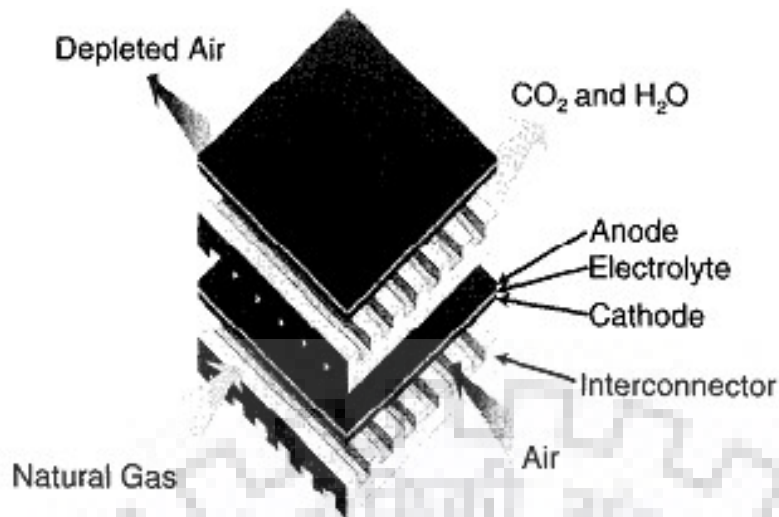


Figure.1-7 A planar design of a SOFC unit (Source; Badwal 1996).

c) Monolithic design: This new concept is under development and has not been fully commercialised. This concept involves the flow of fuel and oxidant, either in the same direction or counter direction. A third way, which involves cross-flow of fuel and oxidant, is also proposed. This design concept has the potential for high power density stacks, which would be well exploited in aerospace applications.

When fuel is burnt in the porous anode, the oxygen concentration is reduced on one side of the electrolyte that is in contact with the anode. Oxide ions will leave the cathode-side across the electrolyte and react with the hydrogen on the other side, which is in contact with the porous anode, resulting in the release of electrons at the anode. If there is an external electrical connection between anode and cathode, the electrons will flow in the outer circuit. The supply of oxide ions is always maintained by oxygen flow within the porous cathode and assuring the overall electrical charge balance, which in turn generates the useful power. The by-product of this process is water molecule (H_2O) and heat, as shown in figure 1-8.

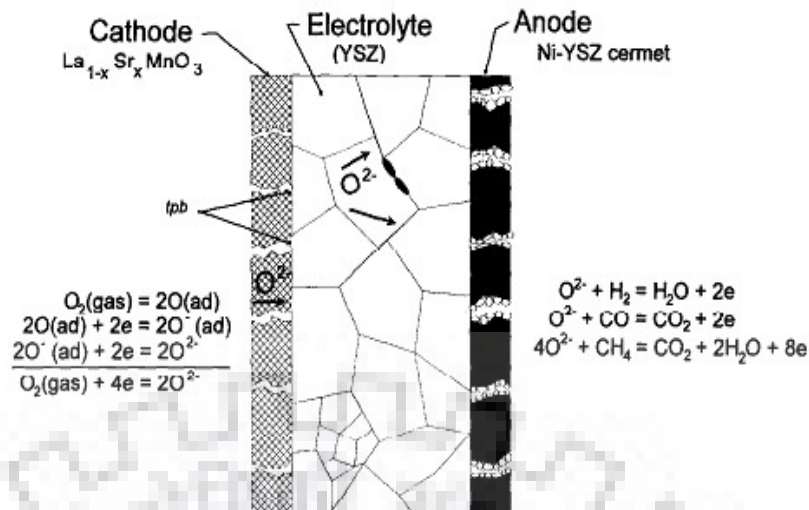


Figure 1-8 Principle of operation of a typical SOFC showing anode and cathode side reactions (Source; Badwal 1996).

1.5.1 Thermodynamics of SOFCs

The open-circuit voltage (OCV) or reversible voltage E_r , is given by the free energy of the fuel oxidation reaction and may be written as $-\Delta G/nF$, where n is the number of electrons transferred and F is the faraday constant. The OCV values generally lie between 1.1 to 1.2 V for a single solid oxide fuel cell. Under loading conditions, this voltage reduces to 0.6 - 0.9 V, and current densities of 800 mA/cm² can still be achieved. There are internal losses (I.R.) associated with fuel cells that are resistive in nature while the over-potential (η) at electrode/electrolyte interface can decrease the cell efficiency so that the effective voltage E from a fuel cell can be stated as $E_{cell} = E_r - I.R - \eta$. Electrical efficiency is given by the ratio of E and E_r , i.e. (E/E_r) , where $E_r = E_{cathode} - E_{anode}$ [Hirschenhofer 1998]. Figure 1-9 shows the cell voltage and current density characteristics in the presence of losses, namely polarisation, and over-potentials, which ultimately leads to the degradation of cell potential. A detailed open circuit measurement of different SOFC materials has been done and mentioned elsewhere by Chiodelli and Malavasi [2013].

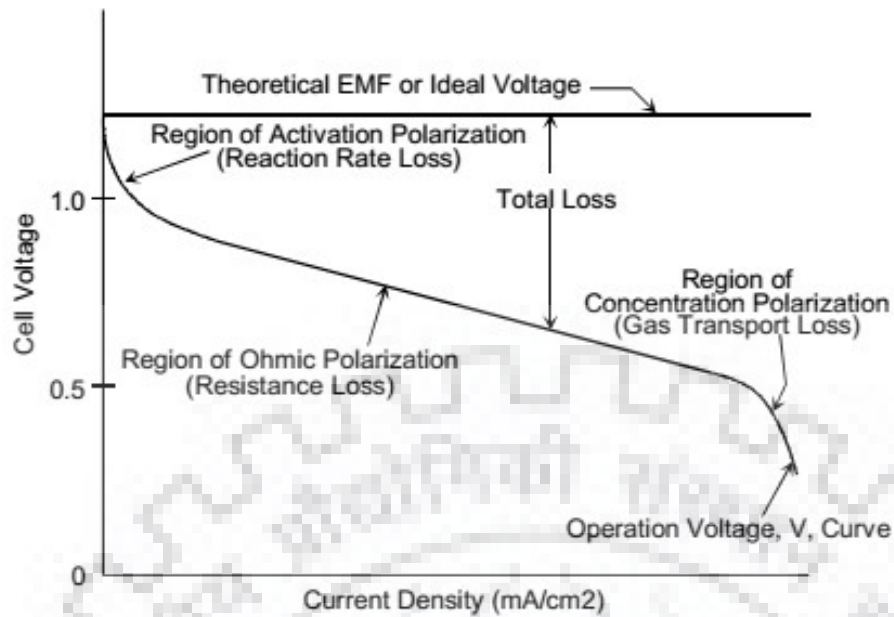


Figure 1-9 Cell voltage/current characteristics of a fuel cell (Source; Hirschenhofer 1998).

The losses generally originate from the three sources namely i) activation polarisation, ii) ohmic polarisation and iii) concentration polarisation

i) **Activation polarisation:** This type of loss occurs due to slow rate of electrode kinetics governing the electrochemical reaction, which involves an activation barrier to be overcome by the reactant species.

ii) **Ohmic polarisation:** This kind of loss occurs due to resistance in the flow of ions in electrolytes. These losses can be minimised by reducing the electrode separation (i.e., decreasing the electrolyte thickness) and increasing the ionic conductivity of the electrolyte.

iii) **Concentration polarisation:** This type of loss occurs due to slow diffusion of the gas in the electrode pores or the diffusion of reactants/products through the electrolyte to/from the electrochemical reaction sites.

1.6. Various types of electrolytes for SOFC applications

1.6.1 Bismuth oxide-based electrolytes

Bismuth oxide-based ion conductors (δ -Bi₂O₃) show the highest conductivity > 1 S/cm among all the electrolytes. The only drawback is that it is stable only in between 730 to 800 °C and its melting point is 804 °C. This phase has got a fluorite related structure. At temperature below 730 °C the oxygen vacancies are ordered, but on heating above 730 °C, a first-order vacancy order-disorder transition takes place, and the conductivity increases by three orders [Takahashi 1972; 1975].

1.6.2 Zirconia based electrolytes

Zirconia based electrolytes are well established in the field of SOFCs with divalent and trivalent dopants studied for several years. Yttria stabilized zirconia (YSZ) is a preferred electrolyte in SOFC application. At 8 mol % of Y₂O₃ doping, high-temperature cubic phase of the ZrO₂ stabilises down to room temperature. The conductivity is the order of 0.1 S/cm at 1000 °C. This high temperature gives rise to thermal stresses generated in the SOFC components. But it also offers a good chemical and mechanical stability over a wide range of high temperatures and oxygen partial pressures [Sammes 1997]. Other applications for YSZ ceramic include thermal barrier coatings (TBCs) in gas turbines, where low thermal conductivity is required for insulation [Gandhi 2017].

Scandia stabilized zirconia (ScSZ) is an alternative to YSZ electrolyte for application in SOFC at intermediate temperatures because of its higher conductivity. ScSZ compositions with 8-12 mol % scandia show the highest ionic conductivity among all the zirconia-based electrolytes.

1.6.3 Ceria based electrolytes

Gd or Sm doped ceria electrolytes are interesting candidates for the intermediate temperature of operation (550-650 °C) due their high ionic conductivity and compatibility with high-performance electrode materials. A typical disadvantage of ceria based electrolytes is that they become n-type semiconductors under reducing conditions, and the cell output voltage reduces [Eguchi 1992; Wang 1997; 2000; Andersson 2005; Adham 1983; Gerhardt et al., 1986].

1.6.4 Perovskite related systems

The perovskite Brownmillerite Ba₂In₂O₅ is another type of electrolyte system. This phase can be classified as an oxygen-deficient perovskite. At room temperature, the oxygen vacancies are

ordered, resulting in alternate layers of tetrahedral and octahedral indium oxide. This phase undergoes an order-disorder transition above 900 °C to yield a tetragonal perovskite, resulting in a drastic increase in oxide ion conductivity (0.1 S/cm at 900 °C) [Goodenough 1990].

1.6.5 LAMOX based systems

LAMOX ($\text{La}_2\text{Mo}_2\text{O}_9$) based oxide ion conductor was first reported by P. Lacorre and his group in the year 2000. It shows that oxide ion conductivity is greater in LAMOX than in yttria-stabilised zirconia (YSZ) at 800 °C [Takahashi 1975; Lacorre 2000a; 2000b; Goutenoire U. S. Patent 2003; Lopez 2005]. Prior to this research Lacorre and his group have studied the effect of high energy ball milling of Lanthanum molybdates based compounds [Lacorre 1997]. The LAMOX compound exhibits a structural phase transition from a non-conducting monoclinic (α) phase to a highly conducting (β) cubic phase at a temperature of about 580 °C and above. The conductivity of the cubic phase increases by two orders of magnitude as compared to the monoclinic phase and is 0.06 S/cm at 800 °C. Due to the phase transition and reducibility of molybdenum, various substitutions have been attempted to stabilise the cubic phase at a lower temperature and also to suppress the phase transition as well as improve the stability in reducing conditions.

1.6.6 Apatites

Rare earth apatite materials have general formula $\text{M}_{10}(\text{XO}_4)_6\text{O}_{2+y}$, where M is a rare earth or alkaline earth metal, and X is P, Si, or Ge. The apatite materials have high oxide ion conductivity at a moderate temperature as well as at low oxygen partial pressure [Islam 2003; Kendrak and Islam 2007]. They have been targeted as potential solid electrolytes alternatives by the initial work of Nakayama et al., 1995 on the silicate-based systems.

1.6.7 Pyrochlores

Pyrochlores are the potentially attractive solid electrolytes having general formula $\text{Ln}_2\text{M}_2\text{O}_7$, where $\text{Ln} = \text{Sm}, \text{Lu}$ and $\text{M} = \text{Ti}, \text{Hf}, \text{Zr}$. They belong to the system of $\text{Ln}_2\text{O}_3\text{-MO}_2$ which is expected to possess intrinsic ionic conductivity. $\text{Ln}_2\text{Zr}_2\text{O}_7$ type pyrochlores, which are also called as zirconate pyrochlores where $\text{Ln} = \text{Nd}, \text{Sm}, \text{and Gd}$; with the structure of fluorite having defects (order-disorder) were the first studied. The $\text{Ln}_2\text{Hf}_2\text{O}_7$ ($\text{Ln} = \text{Nd}, \text{Sm}$ and Gd) hafnates and $\text{R}_2\text{Ti}_2\text{O}_7$ ($\text{R} = \text{Y}, \text{Gd}, \text{and Lu}$) and rare earth pyrochlore structure are much less studied [Kramer 1994].

1.7 Importance of LAMOX based electrolytes

In the year 2000, when LAMOX based electrolytes were discovered attracted much attention in SOFC field. They fall under the category of fast oxide ion conductors. These electrolytes show superior oxide ion conductivity as compared to yttria-stabilised zirconia at lower temperatures [Lacorre 2000a; 2000b]. LAMOX is subjected to a structural phase transition from a non-conducting monoclinic phase to conducting the cubic phase at temperature 580 °C and above.

With ceria based electrolytes, their main disadvantage is that they become n-type conductors under reducing conditions, and the cell voltage is also reduced. Another disadvantage of ceria based electrolytes is that they have silica as a common impurity which has a detrimental effect on the ionic conductivity by blocking at the grain boundaries. YSZ based electrolytes, which are most extensively studied, have good chemical and mechanical stability over a wide range of oxygen partial pressures and temperatures. The only drawback is that the desired conductivity is achieved at a higher temperature of about 1000 °C at which conductivity is 0.1 S/cm, which ultimately leads to high operation temperature and manufacturing cost by the use of noble metal interconnects and cathode as current collectors. Therefore, by reviewing all the factors, one can conclude that LAMOX based system is more effective than all other electrolyte systems though it has some of the drawbacks mentioned in the subsequent sections.

1.8 $\text{La}_2\text{Mo}_2\text{O}_9$ (LAMOX or LMO)

As mentioned in section 1.6.5, the synthesis of the LAMOX compound was done by Lacorre et al., in 2000 [Lacorre 2000b], but it was initially synthesised by Fournier et al., 1970. At that time, its electrolytic properties were not studied in detail. The compound exhibits higher order oxide ionic conductivity of 0.06 S/cm at 800 °C or above, which is higher as compared to that of 8 mol % yttria-stabilised zirconia (YSZ) as shown in figure 1-10. The higher temperature phase of LAMOX exhibits two to three orders higher ionic conductivity than that of the low-temperature monoclinic phase. This high value of conductivity was observed in 8 mol % YSZ electrolyte at a temperature around 970 °C, suggesting that LAMOX can be a potential candidate for intermediate temperature solid oxide fuel cell (IT-SOFC) application [Lopez et al., 2005].

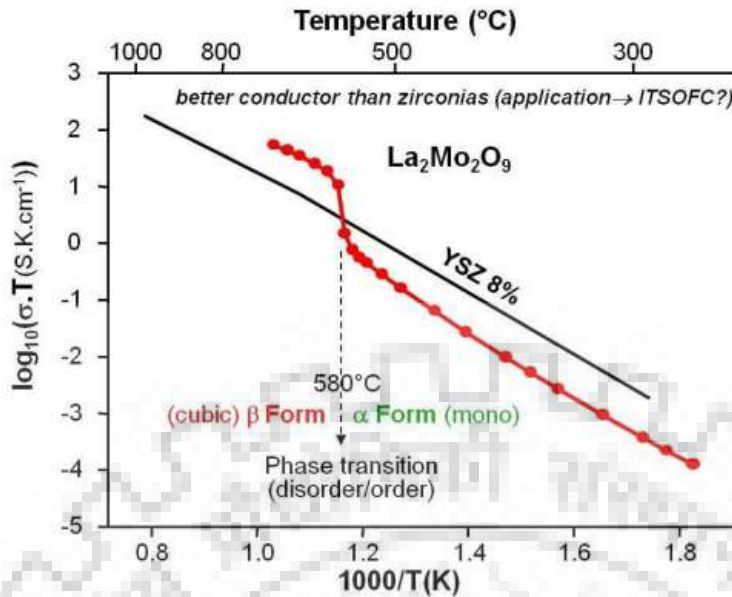


Figure 1-10 Conductivities of LAMOX and 8 mol % YSZ (Source; Lacorre et al., 2000a).

These LAMOX compounds are based on the new concept called lone pair substitution (LPS). This LPS concept is based upon the volume of a lone pair electron gets substituted by an oxygen or fluorine atom due to their similar ionic radius. The $\text{La}_2\text{Mo}_2\text{O}_9$ composition is derived from $\beta\text{-SnWO}_4$ with Sn in 2^+ state and with a lone pair of electrons. In $\beta\text{-SnWO}_4$ the lone pair of Sn^{2+} distorts its octahedral environment. A lone pair of electron occupies a volume similar to that of oxide ion in a given structure. This assumption allows one to propose the mechanism of the oxide ion conductivity in $\text{La}_2\text{Mo}_2\text{O}_9$. Initiating from Sn^{2+} and considering the lone pairs, the stoichiometry can be reformulated as $\text{Sn}_2\text{Mo}_2\text{O}_8\text{L}_2$ (L denotes the lone pair). Substitution of Sn^{2+} by La^{3+} , a cation of approximately the same size but without a lone pair, creates two extra oxygen vacancies. For charge balancing purposes, one vacancy is occupied by the extra oxygen, and another vacancy participates in oxide ion conduction. The new formula thus becomes $\text{La}_2\text{M}_2\text{O}_{8+1(\text{vacancy})}$ [Lacorre 2000b].

1.8.1 Structural analysis ($\alpha\text{-La}_2\text{Mo}_2\text{O}_9$)

As mentioned in the previous section, the $\text{La}_2\text{Mo}_2\text{O}_9$ exists in two phases. The room temperature form of LAMOX is non-conducting (less conducting) monoclinic phase with the unit cell parameters; $a = 14.325 \text{ \AA}$, $b = 21.482 \text{ \AA}$, $c = 28.585 \text{ \AA}$ and $\beta = 90.40^\circ$ having space group P2_1 . The crystal structure of $\alpha\text{-La}_2\text{Mo}_2\text{O}_9$ contains 312 independent crystallographic atoms, namely: 48 La atoms, 48 Mo atoms and 216 O atoms. It is the second-largest oxide structure solved by single crystal methods [Karlsruhe 2004]. The Mo atoms in $\alpha\text{-La}_2\text{Mo}_2\text{O}_9$ are found in three

different types of co-ordination. These are: 15 tetragonal, 15 trigonal bipyramidal and 18 octahedral [Georges 2003; Evans 2005; Emery 2005; Malavasi 2007]. The three coordinations are shown in figure 1-11 (a), whereas; figure 1-11 (b) represents the room-temperature structure of $\text{La}_2\text{Mo}_2\text{O}_9$.

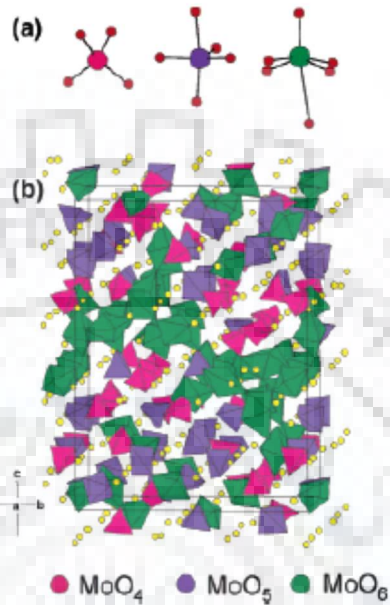


Figure 1-11 (a) Three Mo coordination geometry types observed in α $\text{La}_2\text{Mo}_2\text{O}_9$. (b) Polyhedral representation of α - $\text{La}_2\text{Mo}_2\text{O}_9$; tetrahedral groups are shown in pink, trigonal bi-pyramidal in purple, octahedral in green (Source; Evans et al., 2005).

1.8.2 β - $\text{La}_2\text{Mo}_2\text{O}_9$

In β - $\text{La}_2\text{Mo}_2\text{O}_9$, alternate La and Mo cations form a lattice of slightly distorted parallelepipeds. This phase has a cubic structure which crystallises in the space group $P2_13$. The β - $\text{La}_2\text{Mo}_2\text{O}_9$ structure is similar to β - SnWO_4 structure and has a similar cationic arrangement. Figure 1-12 shows atomic arrangement of β - $\text{La}_2\text{Mo}_2\text{O}_9$ and β - SnWO_4 [Lacorre 2000b; Georges 2003; Goutenoire 2000; Hou 2007; 2008; Lacorre 2006].

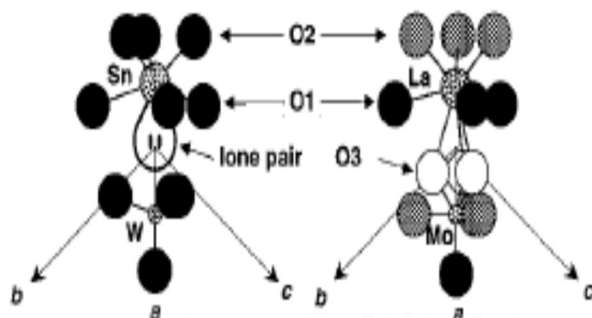


Figure 1-12 Cationic environments in β - SnWO_4 (left) and β - $\text{La}_2\text{Mo}_2\text{O}_9$ (right). The environment of La is limited to the nearest neighbours. Hatched and open circles represent oxygen sites being partially occupied (Source; Lacorre 2000b).

The cell parameters calculated by neutron and x-ray diffraction patterns are $a = b = c = 7.2014 \text{ \AA}$. Both La and Mo occupy 4a Wyckoff positions. Oxygen O(1) is also at 4a position, which is fully occupied, whereas oxygen at O(2) and O(3) sites which are at 12b Wyckoff positions are partially occupied with 78 % and 38 % occupancies respectively. These O(2) and O(3) oxygen-deficient sites facilitate oxide ion migration. The thermal factors (B_{iso}) of these oxygen atoms are high, suggesting three-dimensional oxide ion conduction through the vacancies. Figure 1-13 shows a neutron diffraction pattern of LAMOX at $533 \text{ }^\circ\text{C}$ and $617 \text{ }^\circ\text{C}$. The atomic arrangement and the table shows the cell parameters of the two different phases of LAMOX. Figure 1-14 shows the crystallographic environment of La, Mo, and O in β -LAMOX at elevated temperatures. Table 1-5 shows the structural information of the β -LAMOX at $670 \text{ }^\circ\text{C}$.

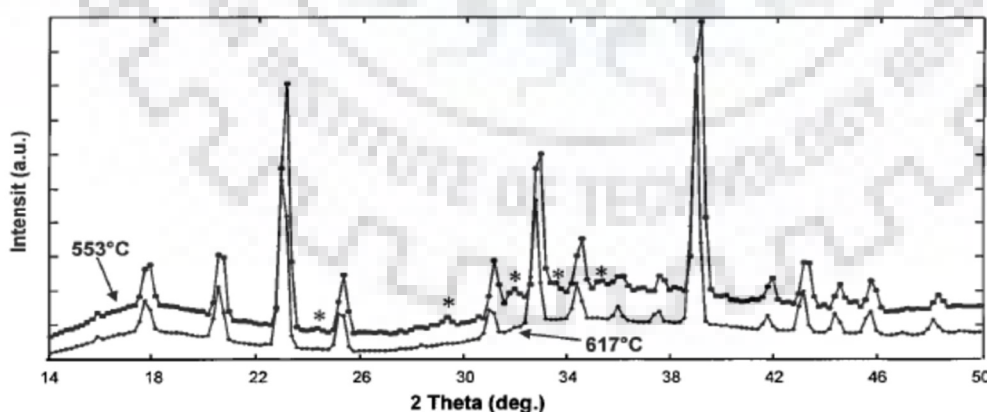


Figure 1-13 Neutron diffraction pattern of $\text{La}_2\text{Mo}_2\text{O}_9$ collected below $533 \text{ }^\circ\text{C}$ and above $617 \text{ }^\circ\text{C}$. The star points the extra peaks in α - $\text{La}_2\text{Mo}_2\text{O}_9$, which corresponds to superstructure reflections (Source; Evans et al., 2005).

Figure 1-14 (Right side) Crystallographic environment of La^{3+} , Mo^{6+} and all three O(1), O(2) and O(3) oxygen atoms in β -LAMO₂O₉ (Source; Goutenoire et al., 2000).

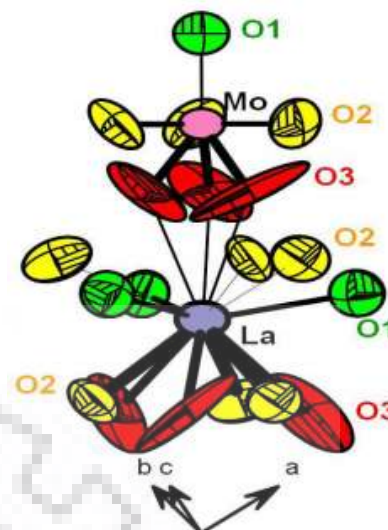


Table 1-5 Structural information of β -LAMO₂O₉ 670 °C (Source; Malavasi et al., 2007).

Atomic site	La (4a)	Mo (4a)	O(1) (4a)	O(2) (12b)	O(3) (12b)
x	0.8528(3)	0.1697 (5)	0.3165(6)	0.9928(7)	0.911(3)
y	0.8528(3)	0.1697 (5)	0.3165(6)	0.181(2)	0.642(5)
z	0.8528(3)	0.1697 (5)	0.3165(6)	0.336(2)	0.551(2)
Occ	1	1	1	0.78(2)	0.38(2)
$B_{eq} (\text{\AA}^2)$	5.6(2)	4.5(1)	6.9(2)	7.7(4)	19(2)

1.8.3 Conduction path in $\text{La}_2\text{Mo}_2\text{O}_9$

From the previous discussion, it is evident that oxide ion is responsible for conduction in LAMO₂O₉ based systems. Goutenoire et al., 2001) have solved the crystal structure of β - $\text{La}_2\text{Mo}_2\text{O}_9$ and has shown that there are three different sites being occupied by O atom, namely 4a, 12b, and 12b. The O(2) and O(3) sites are altogether 50 percent occupied, and O(3) sites less than 50 percent occupied. Some of the O(2)-O(3) and O(3)-O(3) bond distances are of the order of 2.5 Å. In these cases, one of the two sites is not occupied by oxygen atoms, and oxygen atoms on the other site is close to vacancy. These shortest distances between O(2)-O(3) and O(3)-O(3) are an indication of the conduction path for the oxide ions [Goutenoire et al., 2001].

1.9 Limitations of $\text{La}_2\text{Mo}_2\text{O}_9$ as an electrolyte material

High chemical reactivity and Mo reduction to lower oxidation states under diluted H_2 (reducing) condition pose a serious drawback of LAMOX to be utilised as electrolyte material. As a result, the material becomes electronically conducting (n-type) in nature, which may ultimately lead to failure of the fuel cell unit. Goutenoire et al., 1999, had shown that when LAMOX is treated under diluted H_2 condition at 760°C , the compound loses 1.5 wt % amount of oxygen from its lattice site and forms $\text{La}_7\text{Mo}_7\text{O}_{30}$ (7730) phase which upon further reduction lead to total amorphisation of the compound. The similar result was obtained by J. Vega Castillo et al., 2010, when they treated LAMOX at 608°C in 10 % H_2 and 90 % Ar with a flow rate of 6 l/h but did not observe any intermediate 7730 phase. Even Lopez et al., [2005c] found the same result as that of Goutenoire et al., 1999, after annealing LAMOX at 650°C for 24 hours in 5 % diluted H_2 atmosphere. Figure 1-15 shows XRD patterns of degraded LAMOX material in the presence of reducing atmosphere at 700°C , respectively [Goutenoire et al., 1999].

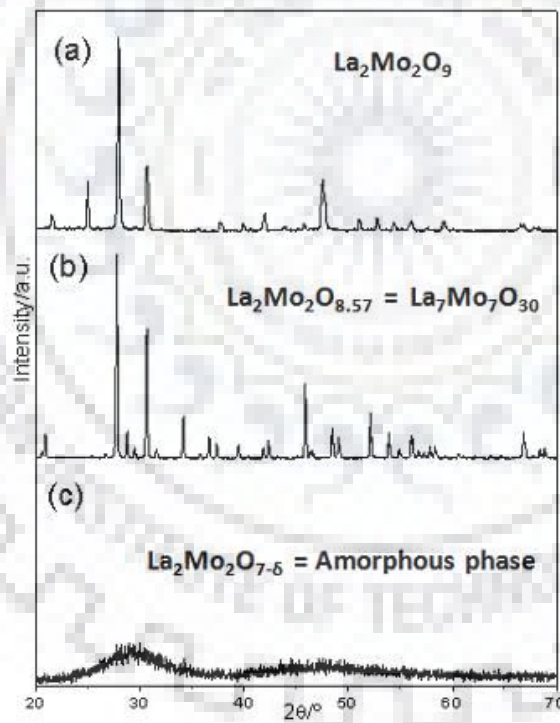


Figure 1-15 X-ray Diffraction patterns collected at room temperatures of (a) LAMOX (b) 7730 phase and (c) amorphous phase (Source; Ravella 2012).

Since the reduction of LAMOX in reducing atmosphere introduces the electronic (n-type) conductivity along with the ionic conductivity, an enhancement in overall conductivity is observed which has been reported by many researchers [Goutenoire et al., 1999; Castillo et al.,

2010; Lopez et al., 2005b]. It has also been found that reduced LAMOX in the amorphous phase has shown excellent anodic properties, especially as a sulphur tolerant material up to 20 ppm level opening a new possibility of anode materials in LAMOX family. The amorphous electrolyte materials have been studied in structural, magnetic, and other functional applications, especially in Li-ion batteries and solar cell applications [Lu and Zhu 2008; Guha 1997]. But they are not well studied and tested in fuel cell areas. The amorphous materials are well-known to exhibit the highest structural disorder and have the most unsaturated sites on their surface, which may provide excellent catalytic properties. The solar cells and battery storage materials have similar device fabrication techniques, which include electrolyte materials sandwiched between electrodes. The solar cell materials comprising of Indium-doped zinc oxide (IZO) and CdTe based thin films are described in detail elsewhere [Dutta et al., 2015; 2004]. The amorphous LAMOX synthesised under diluted H₂ (reducing, Ar-H₂) condition which may possess high catalytic power to dissociate H-H bond and also possess good electrical conductivity because of the n-type nature induced by reduced Mo to lower valance states. According to the literature, up to 20 ppm level of sulphur in the hydrogen-containing gas is acceptable for solid oxide fuel cells to operate without any degradation. Above this level of sulphur there is a significant degradation of cell performance. Figure 1-16 shows the effect of sulphur gas on the output voltage of the cell. More information on sulphur tolerant levels in fuel gases is described elsewhere in detail [Williams; Fuel cell handbook; EG&G 2004]. Figure 1-17 shows the XRD pattern of a LAMOX sample treated in 100 ppm H₂S atmosphere for three days and shows the formation of multiple by-products which is the ultimate cause of degradation of the cell performance [Williams; Fuel cell handbook; EG&G 2004].

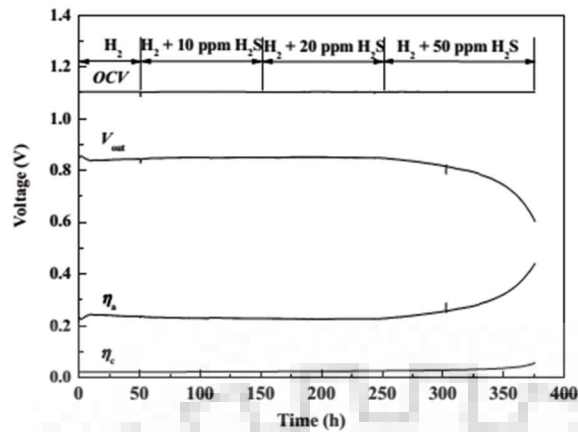


Figure 1-16 Effect of H₂S concentration on open-circuit voltage (OCV), output voltage, anodic and cathodic over-potential of a LAMOX/LDC/LSGM single-cell observed at 800 °C. (V_{out} is output voltage; η_a and η_c are anodic and cathodic over-potentials) (Source; Fuel cell handbook; EG&G 2004).

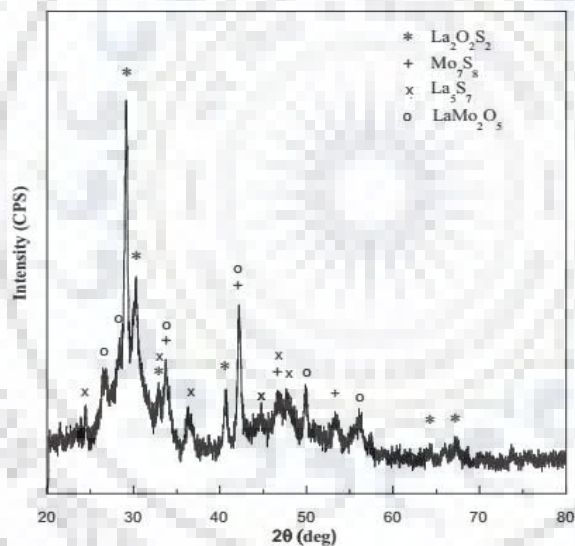


Figure 1-17 Diffraction pattern of LAMOX powder treated in 100 ppm H₂S atmosphere at 800 °C for three days (Source; Fuel cell handbook; EG&G 2004).

The verification and stability of LAMOX under reducing conditions were studied by x-ray photoelectron spectroscopy (XPS) by a few researchers. In an XPS study done by T.Y. Jin et al., 2007, it was shown that substitution by Dy at La site and W at Mo site successfully suppresses the Mo reduction to 100 percent. In another study carried out by Amar Khaled et al., 2012, it was shown that the doping of Ba and Ca at La site tends to increase the conductivity but has no effect on Mo stability. The W substitution at Mo site proved to stabilise the high conducting cubic phase up to room temperature but does not effectively suppress the Mo reduction.

The high thermal expansion coefficient of LAMOX makes it quite difficult to find suitable electrode materials. During the phase transition of $\alpha \leftrightarrow \beta$, the material undergoes an abrupt volume change of about 0.46 percent, as shown in figure 1-18(b) and subsequent enhancement of cell parameters, as shown in figure 1-18(a). This kind of abrupt volume and lattice parameters change can possibly induce mechanical stress at the electrode/electrolyte interfaces, which may lead to failure of the fuel cell. Also, the thermal analysis shows a hysteresis loop during heating and cooling, which is of the first-order type. [Wang et al., 2001; Khadasheva et al., 2002; Hayward and Redfern, 2004]. Many substitutions have been successfully tried out at La and Mo sites to suppress the phase transition and to suppress the crack formation at the electrode and electrolyte interface. Table 1-6 given below, gives an estimation of the solubility limit at La and Mo sites.

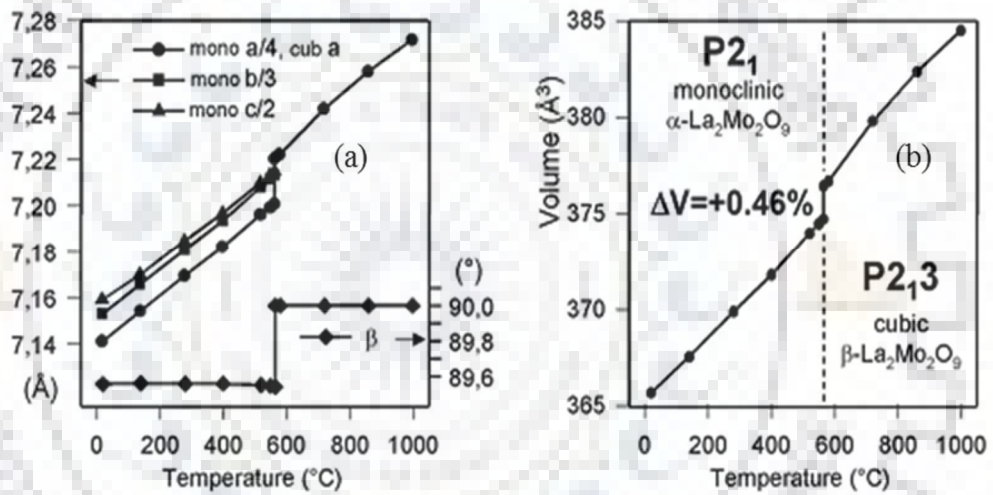


Figure 1-18 (a) Enhancement of cell parameters with temperature and (b) abrupt increase in volume at 580 °C and the further increase of cell volume as a function of the temperature of β-LAMOX (Source; Lacorre 2000b).

Table 1-6 Various substitutions at La and Mo sites with their respective solubility limits (Source; Ravella 2012).

<i>Substituted element</i>	<i>Solubility limit (mol %)</i>	<i>References</i>
Bi ³⁺	3-15	Li 2007; He 2005
Pr ³⁺	10-35	Li 2007
Nd ³⁺	65-75	Horita 1998
Sm ³⁺	10	Corbel 2005
Eu ³⁺	12.5-20	Taimatsu 1992
Gd ³⁺	10-25	Basu 2005
Dy ³⁺	-	Li 2008
Er ³⁺	-	do
Y ³⁺	5-10	Basu 2005
Ca ²⁺	~2	Subasri 2004; Takahashi 1972
Sr ²⁺	-	Jin 2007
Ba ²⁺	-	Subasri 2004
K ⁺	~2-3	Takahashi 1972; Pinet 2007
Rb ³⁺	-	Kishimoto 2007
W ⁶⁺	12.5-70	Marozau 2005
Re ⁶⁺	-	He 2005
Cr ⁶⁺	5-25	do
V ⁵⁺	-	do
Dy ³⁺ and W ⁶⁺	-	Li 2009

- Data not available.

1.10 Doped LAMOX family

Several aliovalent and isovalent dopants on La and Mo sites have been incorporated and studied with respect to the LAMOX family. Various dopants on La and Mo sites have been doped in order to improve the conductivity and stability of the electrolyte at room temperature of the parent compound. At the La site, the rare earth and transition elements, e.g., Nd, Gd, Y, Ca, Ba, K, Nb, Ta, Hf, and other elements, have been used as dopants and studied [Georges 2003; Khadasheva 2002; Corbel 2007]. Simultaneously, doping at both sites has been studied to increase the conductivity and stability of the cubic LAMOX structure at room temperature. In other literature, an attempt was made to substitute the oxygen atom by fluorine [Arulraj et al., 2002]. The conductivity of a doped LAMOX is thus increased by creating more number of oxide ion vacancies. Doping of tungsten is done to stabilise the cubic structure of LAMOX at room temperature [Georges 2006; Lopez et al., 2005b; 2005c]. As shown in figure 1-14, the diffraction pattern is accompanied by extra low-intensity peaks, which validate the formation of a superstructure. The extra peaks observed in the α -polymorph disappear with the introduction of the W at the Mo site. With W contents higher than 0.25-mole fraction, the reflections observed correspond to β - polymorph of LAMOX, which seems to favour stabilisation of the cubic phase at room temperature. Figure 1-19 shows the effect of various dopants on the crystal structure of LAMOX. It can be clearly observed that multiple splitting of (231) peak of LAMOX has been suppressed to one single peak, which corresponds to the cubic phase with space group $P2_13$. In the W doping case, the (231) peak evolved is singlet in nature but is not symmetric, implying that some kind of distortion in the unit cell is caused by doping. The various effects of doping at respective La, Mo and O sites have been studied by many researchers in detail and can be found in literature [Selmi et al., 2010; 2006; Goutenoire et al., 2001; Georges et al., 2005; 2006; 2003a; 2003b; 2002; Corbel et al., 2005; 2007; 2009; Lopez et al., 2004a; 2004b; 2005; 2006; 2007a; 2007b; Fang et al., 2003;2004; 2008; Wang et al., 2002; 2006; Liang et al., 2006; Collado et al., 2002; Basu et al., 2005; 2006; 2009; 2010; Li et al., 2010; Li et al., 2008; Bo et al., 2003; Tealdi et al., 2004; Yang et al., 2005; Yoo and Jacobson 2005; 2010; Arulraj et al., 2002; Corbel et al., 2007; Subasri et al., 2003]. The effect of doping on dielectric relaxation and ionic conductivity of LAMOX based compounds has been carried out by various researchers [Wang et al., 2006; Wang et al., 2001; 2006; 2002; Tsai et al., 2005; Zhang et al., 2003; Georges et al., 2008; Li et al., 2007; 2009; Voronkova et al., 2008, 2010].

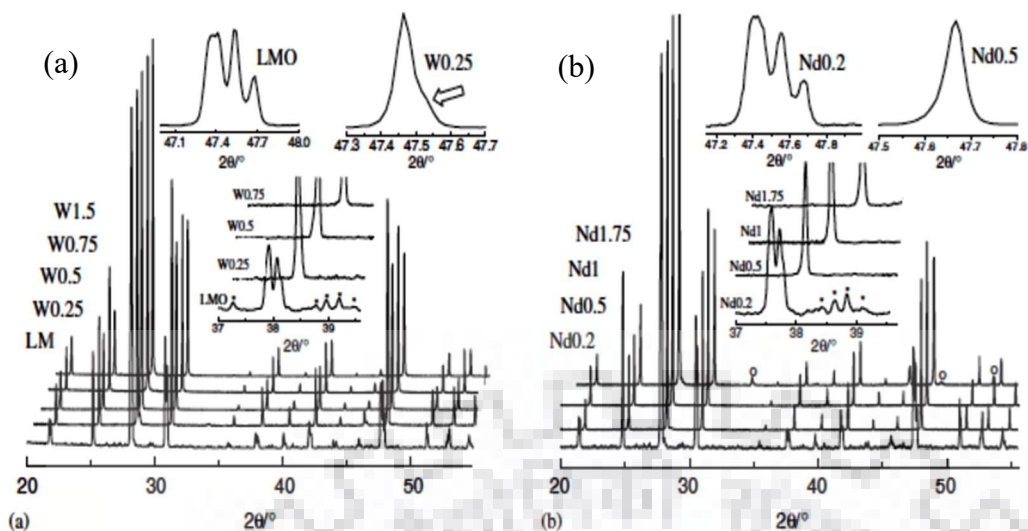


Figure 1-19 Transition of monoclinic phase of LAMOX to cubic phase with (a) W, (b) Nd content. The evolution of single peak suggests the stabilisation of the cubic phase (Source; Lopez et al., 2005c).

α - $\text{La}_2\text{Mo}_2\text{O}_9$ and the cubic or β -LAMOX members have some peculiar atomic level differences. The cubic LAMOX has a very mobile oxygen sub-lattice above the phase transition temperature. However, when cooled down, the freezing of the oxide ions in $\text{La}_2\text{Mo}_2\text{O}_9$ occurs through an ordering between the oxide ions and the vacancies that are mainly responsible for symmetry breaking and formation of the superstructure is observed at a temperature less than 580°C [Georges et al., 2006]. Such a phenomenon is not possible for substituted LAMOX systems because the random cationic distribution suppresses the ordering of oxide ion/vacancy. The oxide ion sub-lattice is frozen in a random way without symmetry breaking; hence no superstructures are formed in cases of doped LAMOX. Figure 1-19 shows the effect of continuous doping of W and Nd in LAMOX and subsequent stabilisation of cubic phase. Figure 1-20 shows a generalised phase boundary diagram [Li et al., 2008] of various phases formed with the varying W content in LAMOX. It is evident from the figure that 10 mol % of W in LAMOX stabilises the β (cubic) phase of LAMOX up to 65 mol %. Further doping of W leads to the $\alpha+\beta$ phase of LAMOX up to 90 mol % of W content. Beyond that, the appearance of the α - $\text{La}_2\text{W}_2\text{O}_9$ phase happens until the Mo is fully replaced by W. Also DTA studies in figure 1-21 reported on LAMOX compounds with W doping in the range of $x \geq 1.3$ ($\text{La}_2\text{Mo}_{1-x}\text{W}_x\text{O}_9$) shows an endothermic reaction above 950°C for $y = 70$ mol % doping.

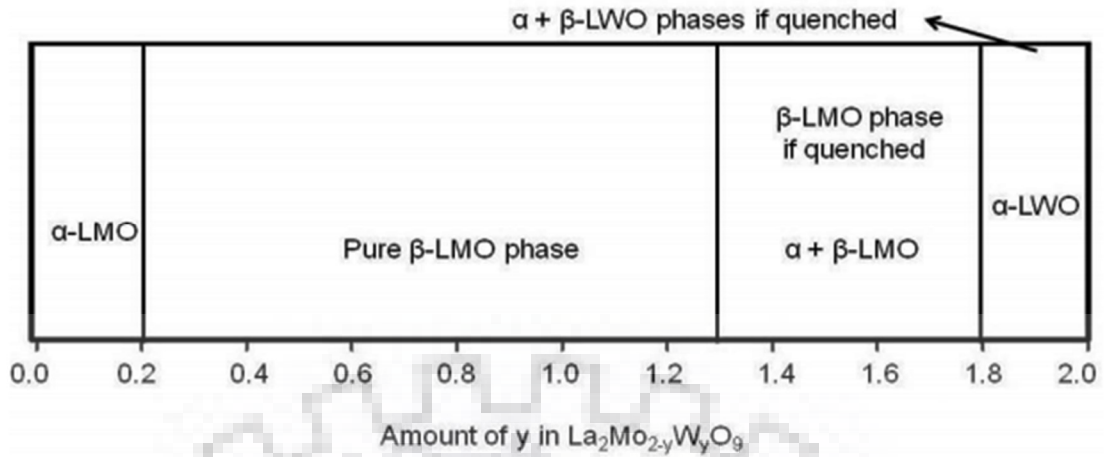


Figure 1-20 Various phases of LAMOX and LWO with an increase in W content on $\text{La}_2\text{Mo}_2\text{O}_9$ at room temperature (Source; Li et al., 2008)

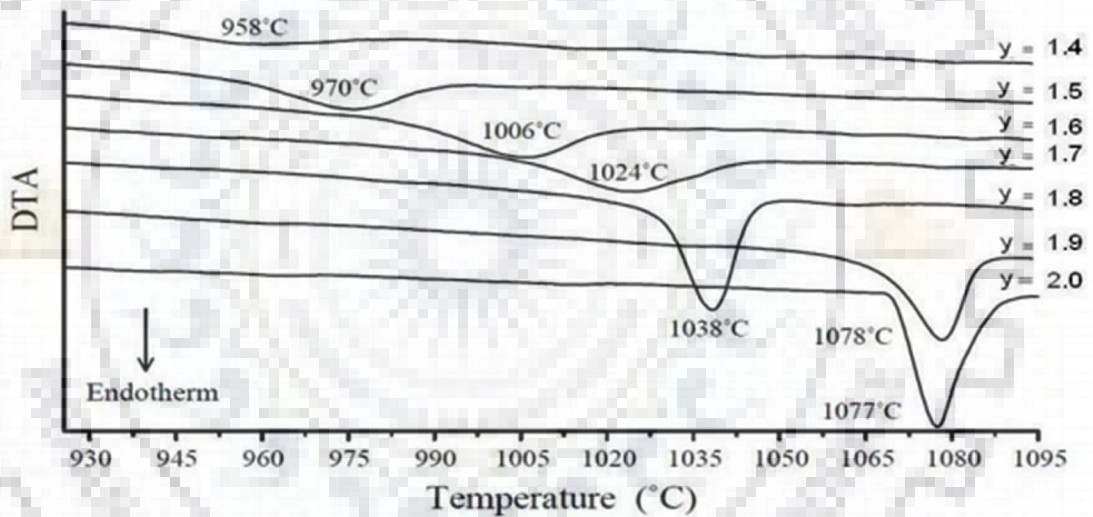


Figure 1-21 Plot of DTA curves for W doped LAMOX with W varying from 1.4 to 2 (Source; Li et al., 2008).

1.11 Chemical stability of LAMOX with various electrodes

Designing of electrolyte material alone is not sufficient as far as fuel cell application is concerned. One must also look for compatible electrodes that can withstand the mechanical strength under high temperatures, reducing conditions and should have chemical inertness with the electrolyte material. Undesirable reactions at electrode and electrolyte interface may lead to the formation of phases which may degrade or result in complete failure of the fuel cell.

Many of the cathode materials, when tested with LAMOX at various temperatures, e.g., in the temperature range of 500 – 1000 °C, have shown inter-cationic diffusion reactions between

electrode and electrolyte and such reactions are listed in the table 1-7. Only $\text{Ce}_{0.9}\text{Gd}_{0.1}\text{O}_{1.95}$ (CGO) when mixed with LAMOX and annealed together at 600 – 1000 °C for 72 hours, no inter-cationic diffusion reactions were found to occur. This study shows that LAMOX is compatible with CGO as cathode material [Corbel et al., 2005]. In another study carried out by Corbel et al., 2006, they have studied $\text{La}_2\text{NiO}_{4+\delta}$ as a new kind of cathode material, which reacts with LAMOX at 600 °C and results in the formation of La_2MoO_6 and NiO as by-products. Any kind of inter-cationic diffusion products which may degrade the overall cell performance is highly undesirable.

Unlike the cathode materials which are perovskite in nature, the anode materials are usually metals or cermets of Ni, NiO, or Ni-YSZ and have been in the commercial use for a long time with YSZ type of electrolytes. Since it has been shown that Ni-CGO based cermets do not react with LAMOX type electrolytes, they can be a potential anode material for this electrolyte [Corbel et al., 2006]. Some studies have shown that 75 mol % W doped LAMOX when annealed with NiO, leads to the formation of α -LWO phase, which is a poor conductor of oxide ions. A similar kind of study was done by C. Tealdi et al., 2010, which has shown stability of NiO with W doped LAMOX compositions [Lopez et al., 2007a; Tealdi et al., 2010; Le 2018]. The synthesis of electrode materials along with the electrolytes is of great importance in any energy storage device. Their ease of fabrication, compatibility with electrolyte, and most importantly, its non-toxicity plays a vital role in large amount production. These properties of an electrode material should be matched with its electrochemical properties, which will enhance the performance of energy storage systems [Mitra et al., 2016; 2014; Ghosh et al., 2015; 2009].

Table 1-7 Various cathode materials and their reaction with LAMOX and the formation of secondary products as a function of temperature (Source; Corbel et al., 2005; 2006)

Cathode	500 °C	600 °C	700 °C	1000 °C
$(\text{La}_{0.85}\text{Ca}_{0.15})\text{FeO}_3$		Stable		+CaMoO ₄ for T ≥ 1000 °C
$(\text{La}_{0.75}\text{Ca}_{0.25})(\text{Co}_{0.8}\text{Fe}_{0.2})\text{O}_2$		Stable		+CaMoO ₄ +La ₂ MoO ₆ for T ≥ 1000 °C
$(\text{La}_{0.8}\text{Sr}_{0.2})\text{MnO}_3$		Stable	+SrMoO ₄ for T ≥ 700 °C	
$(\text{La}_{0.6}\text{Sr}_{0.4})(\text{Co}_{0.2}\text{Fe}_{0.8})\text{O}_3$	Stable		+SrMoO ₄ +La ₂ MoO ₆ for T ≥ 700 °C	
$\text{La}_2\text{NiO}_{4+\delta}$	Stable		NiO + La ₂ MoO ₆ for T ≥ 600 °C	

1.12 Summary

The literature review has shown that there exists a need for finding a suitable replacement for fossil fuel-based energy sources. Due to the increased consumption of non-renewable based energy sources, the amount of CO₂, NO_x, SO_x, and other greenhouse gases are increasing and causing a negative impact on the ecosystem. Hydrogen based fuel cell systems are definitely a viable solution for substituting fossil fuel-based systems. Fuel cell-based driven transport systems, stationary power generations have been successfully tested and are being implemented on a commercial basis by various companies in western countries, and in India, TATA motors are planning to introduce hydrogen-powered fuel cell buses.

Various kinds of electrolyte systems employed in solid oxide fuel cell systems have been studied in the past years. The most extensively researched electrolyte is yttria stabilised zirconia (YSZ) and gadolinia doped ceria (GDC) electrolyte, which in the present time are still used commercially. The operation of YSZ at 1000 °C makes it a very robust system for high-temperature applications, and the highest conductivity shown is 0.1 S/cm at 1000 °C. The GDC based electrolytes have also shown a potential application in the SOFC systems. Other systems like perovskite Brownmillerite electrolyte systems have also been studied by various researchers.

Apart from the advantages, some of the limitations, like the use of noble metal current collectors at a high temperature of operation, increase the overall cost of YSZ fuel cell systems. For GDC

based SOFCs the appearance of electronic conductivity under reducing conditions results in reduced cell output voltage. Similarly, the volatilisation of In_2O_3 in perovskite Brownmillerite electrolyte systems restricts its commercial application in SOFC. Bismuth oxide-based electrolytes despite having excellent ionic conductivity of 1 S/cm is stable over 730 – 800 °C and melts at 804 °C, which also restricts its application in SOFC application.

Among all the electrolyte systems, the recently discovered $\text{La}_2\text{Mo}_2\text{O}_9$ based electrolyte can be considered as a potential electrolyte as compared to YSZ and CGO (GDC) ceramics, which are commercially used in the fuel cells industry. Though, the basic LAMOX possesses some serious limitations on its applicability like the reduction of Mo in reducing atmosphere, low electrical conductivity at room temperature, large volume expansion at the phase transition temperature, and finding suitable compatible electrodes. Doping at various sites in LAMOX is among one of the solutions to overcome the limitations of pure $\text{La}_2\text{Mo}_2\text{O}_9$, then it may very well serve as a potential candidate for electrolyte materials for intermediate temperature (600-800 °C) fuel cell applications. This is also the objective of the thesis. The main focus is laid on the tailoring the properties of pure $\text{La}_2\text{Mo}_2\text{O}_9$ to make it suitable for fuel cell applications. Apart from the electrolyte development, the focus has been on the design of new electrode materials and new electrolytes. The next chapter of the thesis deals with the synthesis route for various LAMOX based materials and electrodes by the solid-state route. A brief overview of the instruments used for characterisation of samples has also been presented.

Chapter 2

Experimental procedure

2.1 Introduction

After reviewing the literature on various electrolytes, examining their advantages and disadvantages, mechanism of oxide ion conduction, LAMOX has been selected as a suitable electrolyte material for the present study. This chapter actually provides the background and working of all the instruments used in the present research work. This chapter also describes the synthesis, characterisation of pristine $\text{La}_2\text{Mo}_2\text{O}_9$, W doped $\text{La}_2\text{Mo}_2\text{O}_9$, K doped $\text{La}_2\text{Mo}_2\text{O}_9$, co-doping at La and Mo site, and compatibility study of $\text{La}_2\text{NiO}_{4+\delta}$ (LN) as cathode material with W doped LAMOX and NiWO_4 (NW) as anode material with LAMOX as electrolyte powder by solid-state route has been discussed. The compaction and densification of the powder mixtures have also been discussed in this chapter. The analysis of the powder and sintered pellets was done by various characterisation techniques viz. x-ray diffraction (XRD) for structural study, field emission scanning electron microscope (FE-SEM) for microstructural analysis, electrochemical impedance spectroscopy (EIS) for conductivity analysis and x-ray photoelectron spectroscopy (XPS) for chemical state analysis. A brief instrumentation overview has also been discussed in this chapter.

2.2 Synthesis of powder samples

The synthesis route of $\text{La}_2\text{Mo}_2\text{O}_9$, W doped $\text{La}_2\text{Mo}_2\text{O}_9$, K doped $\text{La}_2\text{Mo}_2\text{O}_9$ is a well-established process. So far, different processing techniques like conventional solid-state route, Pechini method [Pechini 1967], sol-gel process, precipitation method, microwave synthesis, chemical vapour deposition (CVD), or physical vapour deposition (PVD) are well known and have been employed extensively in ceramic synthesis route. The synthesis process allows us to vary input parameters which will affect the final properties of the sample.

In the present chapter, for the synthesis of LAMOX (or LMO) and its derivatives, $\text{La}_2\text{NiO}_{4+\delta}$ as a cathode material, NiWO_4 , the traditional solid-state route is employed. The commercially available powders La_2O_3 , MoO_3 , WO_3 and K_2CO_3 , NiO , SnO_2 , rare earth oxides like Eu_2O_3 , Sm_2O_3 , Tm_2O_3 , and Y_2O_3 , were used in stoichiometric amounts as raw materials. The appropriate amounts of all the starting materials for the desired composition were mixed using an agate mortar and pestle in acetone medium to ensure the uniform mixing and avoiding agglomeration. After the hand mixing, the mixture was further mixed in a ball mill (Retsch corp. Germany) in

acetone medium to ensure the uniform mixing of the samples. All the compositions, including LAMOX and its doped compositions, were initially calcined at 800 °C for 6 hours in a muffle furnace. The heating and cooling rates were 10 °C / min for all the samples. The calcined powder mixtures were again grinded in a mortar and pestle to obtain fine powders and were kept at a temperature of 400 °C for annealing.

2.3 Green Sample preparation

After the confirmation of the pure phase of the samples through initial XRD analysis, these samples were moulded into a defined shape in the form of cylindrical pellets. Some of the analysis techniques require a definite shape of the powder samples for various characterisation purposes such as electrochemical impedance spectroscopy (EIS) and x-ray photoelectron spectroscopy (XPS) measurements. The sample in the form of cylindrical pellets is prepared in three steps: 1) grinding and ball milling of the powder, 2) moulding and uniaxial pressing, 3) sintering.

2.4 Sintering of pellets

After compacting the fine powders of LAMOX and its doped compositions into pellets of diameter 10 mm with the polyvinyl alcohol (PVA) of 10 percent as a binder, these pellets were pre-sintered at 500 °C for 12 hours for binder removal and then finally sintered at 900 °C for 4 hours. Basically, the sintering process is accompanied by grain growth and reduction in surface energy. The sintering mechanism for two particles (for illustration purpose) has been shown in figure 2-1. The vapour transport, lattice diffusion, and surface diffusion from the surface of the particle to the neck lead to the growth and coarsening of the particle without densification. The grain boundary diffusion to neck leads to densification as well as coarsening of the particles during the sintering process [Rahaman 2003].

The whole preparation of the undoped and doped LAMOX samples (pellets) was done in two atmospheres viz. air and reduced (Ar-90 % and H₂ 10 %) for various characterisation studies like XRD, FE-SEM, XPS, EIS, etc. The air treated LAMOX, and doped LAMOX samples correspond to cathode/electrolyte interface, and dilute H₂ treated LAMOX samples corresponds to the anode/electrolyte interface. From LAMOX (electrolyte) point of view, the reducing conditions are most important from the characterisation and study point of view since they give similar results when the SOFC is operated under the fuel conditions.

Basically, there are three stages of sintering. The initial stage corresponds to the beginning of atomic mobility in which sharp concave necks formed between the adjacent particles in contact. The amount of densification is very less at this stage. The second stage is an intermediate stage where the sharp curvature of necking begins to disappear, and most of the densification takes place during this stage. The formation of channel-like pores is also seen in this stage. In the last stage, the grain growth starts to become significant, and these channel-like pores become isolated and form closed isolated voids.

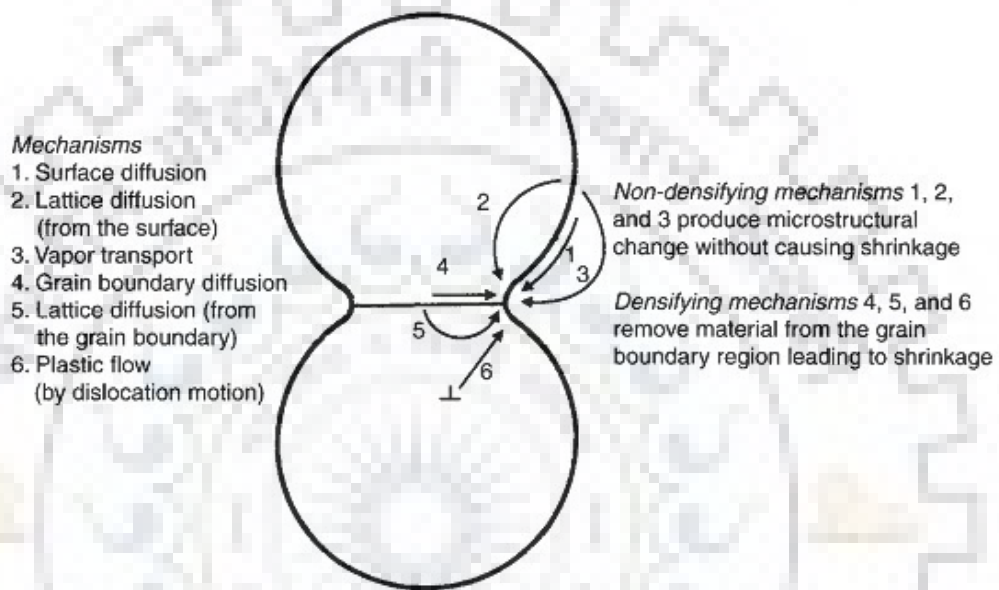


Figure 2-1 Sintering mechanisms for a system of two particles [Rahaman 2003].

The reduction in the surface energy during the sintering process occurs due to the elimination of internal surface area associated with the pores, which provides the sufficient driving force for sintering.

The specific energy and the curvature of a grain surface provide resultant stress on the atoms under the surface. For a curved surface with curvatures r_1 and r_2 , the stress is given by Young and Laplace:

$$\sigma = \gamma_{sv} \left(\frac{1}{r_1} + \frac{1}{r_2} \right) \quad 2.1$$

where γ_{sv} denotes specific surface energy. The diffusion potential μ , which is the driving force for the matter transport, calculated by equating the mechanical work done by the stress to the thermodynamic work actually required by the system for the reduction of the surface energy, is given by:

$$\mu = \sigma\Omega$$

2.2

where Ω is atomic/molar volume. This diffusion potential is more complex for polycrystalline materials where some pores are in contact with grain boundaries.

Relative density is a measure of sample densification, which represents the ratio of experimental density to theoretical density. The relative densities of the LAMOX pellets treated in air were found to be ~90-94 percent. Whereas the relative density of the reduced LAMOX sample treated for 4 hours in Ar-H₂ atmosphere was ~70-75 percent.

2.5 Characterisation techniques

2.5.1 X-Ray Diffraction (XRD) and Rietveld analysis

X-ray diffraction (XRD) is a well-known technique used to determine the phase and phase composition of a compound. Apart from the main phase present in the compound, it can also check the presence of any impurity phase(s). When x-ray beams sufficient energy hit the samples (powder or single crystal), the monochromatic x-rays are diffracted by the crystal lattices. This diffraction is the typical case of scattering (coherent) by the successive planes formed by an array of atoms, which is defined by Bragg's law. If θ is the angle between the incident beam and the lattice planes, d is the spacing between the planes and λ is the wavelength of the incident x-ray beam, then the Bragg's law may be written according to equation 2.3:

$$n\lambda = 2d \sin\theta \quad 2.3$$

n is an integer (generally taken as 1). Figure 2-2 shows a schematic of the x-ray diffraction phenomenon by a single crystal.

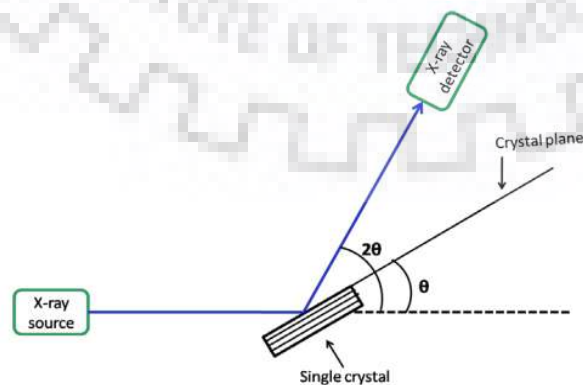


Figure 2-2 Diagram of x-ray diffraction (XRD) process by a single crystal (Source, Rigaku).

For the phase purity and finding of various phases present in the synthesised LAMOX compounds, x-ray diffraction (XRD) of the powder samples was carried out at room temperature using a x-ray diffractometer Smart Lab (Rigaku, 40 kV, 30 mA) with Cu $k\alpha$ radiation in the range of $10^\circ \leq 2\theta \leq 70^\circ$ range with a 2θ step of 0.02° and scanning speed $4^\circ/\text{min}$. The XRD pattern was matched with JCPDS and ICSD data files for phase identification.

Further analysis and information about the crystal structure can be obtained by combining the XRD data by software like [Le Bail 1969] fitting and Rietveld refinement [Rietveld 1969] to study the structure of any given composition in detail. The structural analysis of the powder x-ray diffraction patterns was done using Rietveld analysis by x'pert high score plus software. The whole pattern was refined with the constant scale factor and by pseudo-Voigt function. Overall, a large number of parameters were refined in order to get a good fit for the obtained XRD data. The peak FWHM analysis was done by following pseudo-Voigt profile function and can be defined by Caglioti et al., [1958]:

$$H_k^2 = U \tan^2 \theta + V \tan \theta + W = F_{instr} \quad 2.4$$

where H_k is full width at half maximum (FWHM) of the k^{th} Bragg reflection, and U , V and W are refinable parameters related to peak shape. The crystallite size β can be calculated by the Scherrer equation after considering instrumental correction

$$\beta = \frac{0.9\lambda}{\cos \theta \sqrt{F_{obs}^2 - F_{instr}^2}} \quad 2.5$$

where λ is the radiation of the wavelength used, F_{obs} and F_{instr} are full width and half maximum (FWHM) of sample and instrumental reflections. The F_{instr} was calculated by using the equation 2.5.

The basis of Rietveld refinement is the least square procedure which minimises the error described by the equation

$$S_y = \sum_i w_i (Y_i^2 - Y_{ci}^2) \quad 2.6$$

where Y_i is the observed intensity at a point i of the powder pattern, and Y_{ci} is the calculated intensity. The weight w_i can be defined as $w_i = Y_i^{-1}$, which is based on counting statistics. The calculated Y_{ci} can be written as

$$Y_{ci} = s \sum_H L M_H |F|^2 \Phi (2\theta_i - 2\theta_H) P_H A + Y_{bi} \quad 2.7$$

where s is the overall scale factor, H represents the Miller indices for the Bragg reflection,

L contains the Lorentz and polarization factors, M_H is the multiplicity, F is the structure factor for H^{th} Bragg reflection, $\phi(2\theta_i - 2\theta_H)$ is a profile function, $2\theta_i$ is corrected for the 2θ zero error,

P_H is a preferred orientation function, A is the absorption factor, Y_{bi} is the background intensity at step i .

The Bragg reflections contained in the summation at each point of the powder pattern are determined from a sorted list of the possible reflections and their profile widths at $2\theta_i$. The structure factor which contains the structural information can be defined by the equation:

$$F = \sum f_j g_j \exp - 2\pi i(hx_j + ky_j + lz_j) \exp(-B_j \sin^2 \theta / \lambda^2) \quad 2.8$$

where f_j is the scattering factor, or in the case of neutron data the scattering length, of atom j , g_j is the occupancy factor, x_j , y_j and z_j are the fractional coordinates, and B_j is the temperature factor coefficient.

2.5.2 Scanning Electron Microscopy and Energy Dispersive Spectroscopy

Scanning electron microscopy (SEM) is a characterisation technique for the study of the microstructure of sectioned or fractured surfaces of any sample. The surface morphology like grain, grain boundaries, the formation of pores or voids, and any other information about the physical structure can be studied. In SEM, basically, a beam of accelerated electrons of the order of 100 V to 20 kV is focused as a fine spot onto the sample surface. As a result of interaction between the electron beam and sample under study, various types of signals are produced in the form of x-rays and electrons. Usually, secondary electrons (SE) and backscattered electrons (BSE) are the most prominent signals, which are commonly used for image capturing. Field emission (FE) electron gun has an advantage over W filament or LaB₆ thermionic emission gun because of more coherency producing images with a better resolution to reveal finer details of sample microstructure. Figure 2-3 presents a schematic showing the image of the electron beam and matter interaction as well as the production of various signals from the material.

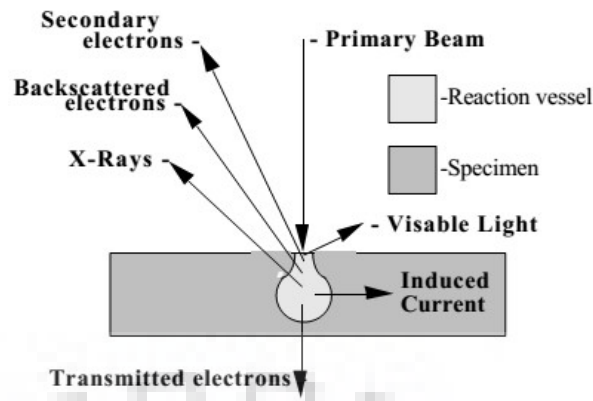


Figure 2-3 Schematic of electron-matter interaction and resultant signals (Source, Zeiss).

The magnification achieved by the FE-SEMs is of the order of 100 kx and this magnification can be defined as the ratio of display screen area to scan area on the sample surface by the focused electron beam. Smaller the scan area higher will be the ratio and hence the magnification. For imaging purposes, the aperture area is kept between 10 to 30 μm . Small aperture area or beam diameter implies low signal but better resolution while a higher accelerating voltage produces a greater interaction volume of the samples.

The FE-SEM used in the present study is Carl-ZEISS-Sigma model with a high voltage of operation from 100 V to 30 kV. For energy-dispersive x-ray spectroscopy (EDX) analysis, Oxford detector was used with an active area window of 50 mm^2 . The resolution of the EDX detector is 127 eV with a working distance of 5.8 mm, and a beam diameter greater than 60 μm was used for detecting x-ray signals for EDX composition analysis.

The ultimate goal of the EDX technique is to provide the quantification analysis with the error limits. Usually, the detection limit of the EDX instrument is greater than atomic number 6 i.e., $Z > 6$ in the periodic table. The commonly used windows to separate the EDX detector and the SEM chamber are Beryllium window and super-ultra-thin Al-coated polymer window, which absorb the X-rays of the elements below the atomic number 5. The quantification of the various elements by EDX by introducing ZAF correction [Russ 1984] is given as

$$[Z * A * F] = \frac{C_i}{C_i^{std}} = \frac{I_i}{I_i^{std}} = k_i \quad 2.9$$

where Z, A, and F are atomic number, absorption, and fluorescence correction factors. C_i and C_i^{std} are the weight percentage of test and standard element. I_i and I_i^{std} are the intensity of i^{th} and standard element, respectively. Z. A. F. correction is automatically taken care by the EDX software *INCA*.

2.5.3 X-ray photoelectron electron spectroscopy (XPS)

This characterisation is one of the important tools for surface chemistry analysis. Basically, the technique is based on x-rays as an input excitation source and electrons ejection as a result of the interaction of the x-rays with matter [Agarwal 1979]. This technique analyses the kinetic energies of the ejected electrons to reveal the chemical information, e.g., oxidation state, nature of bonding in the compound. Figure 2-4 shows x-ray interaction with the core level electrons, thus demonstrating the XPS phenomenon. The figure also shows the depth of penetration of these soft monochromatic x-rays in the sample.

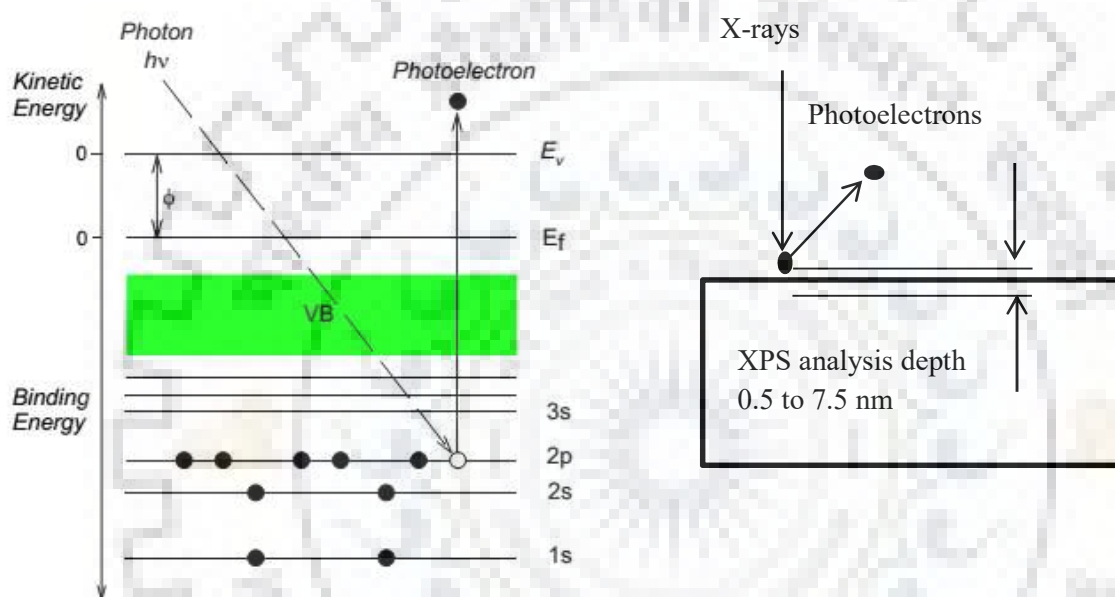


Figure 2-4 (Left side) Simplified diagram showing the XPS process, (Right side) level of depth of photoelectrons which are detected from the surface (Source, Moulder 1995).

The x-ray photoemission is a phenomenon that involves photoelectric effect and uses x-rays as a primary source of excitation. These x-rays, when incident on the sample, produces photoelectrons of discrete energy which has the information of the particular (elements) surface to be analysed.

In the present study, the surface analysis of LAMOX and its derivative compounds was done by means of irradiating the sample with monochromatic soft x-rays and analysing the energy of ejected electrons. Al $K\alpha$ (1486.7 eV) was used as an excitation source. The incident x-ray beam has a limited penetrating power of 1-10 μm in the solid. But the electrons which manage to reach the detector were emitted from a depth up to 7.5 nm of the sample surface and are elastically scattered. While other electrons that are ejected from a depth greater than 7.5 nm suffer an inelastic collision losing their energy, resulting in background noise along with the instrumental

noise. The ejected electrons from the sample surface have the kinetic energies which can be described by:

$$K.E = h\nu - B.E - \phi \quad 2.10$$

where $h\nu$ is the photon energy, B.E is the binding energy of the atomic orbital from which the photoelectrons originate, and ϕ is the work function of the spectrometer. Figure 2-5 shows the energy level diagram of a photoelectron ejected from a material when bombarded with a specific energy.

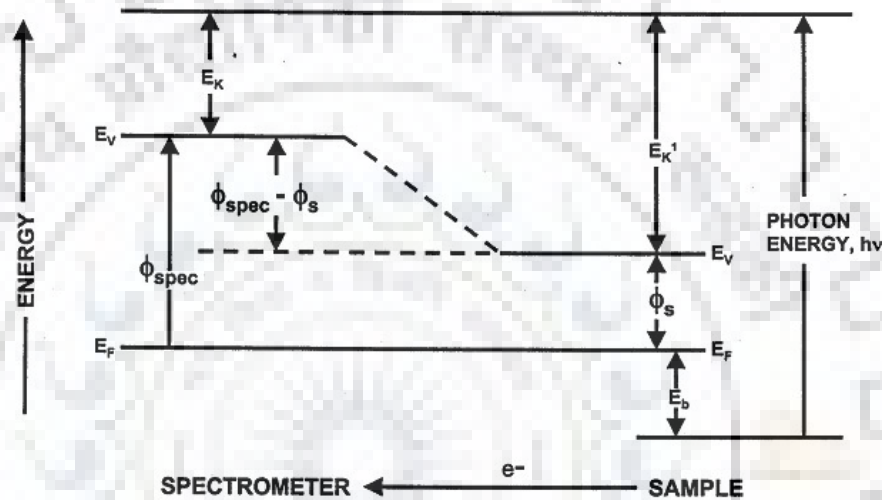


Figure 2-5 Energy level diagram showing different work functions for binding energy measurements (Source, Chusuei 2002).

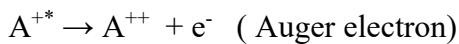
The binding energy of the ejected electrons is measured indirectly from the kinetic energy of the ejected electrons, which are retarded while ejecting from the sample surface.

The equations describing the generation of a photoelectron from a core level excited by a photon source are given below:



where A is the neutral atom or molecule, A^{+*} is the excited ion, and e^- is the ejected photoelectron. Other secondary processes that happen along with the ejection of the photoelectron are x-ray fluorescence and auger electron emission. These secondary processes are represented in the figure 2-6 given below along with the equations:





2.13

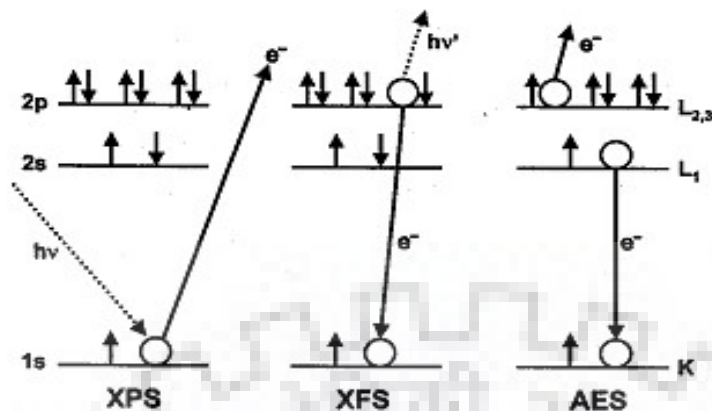


Figure 2-6 Illustration of the photoelectron emission phenomenon and the related secondary process by the excitation of the material surface with a source of energy $h\nu$ (Source, Chusuei 2002).

For the present study, the chemical states of the elements on the sample surface of various compositions sintered in air and reductive atmospheres were analysed by using PHI Versa Probe 5000 II (ULVAC- PHI) x-ray photoelectron spectroscopy (XPS). In XPS analysis, basically, a set of survey and core level spectra were collected in ultra-high vacuum (UHV) conditions of about 10^{-10} Torr for oxidation state analysis of the constituent elements. The survey spectra of respective compositions were recorded at 187.5 eV pass energy rating for detection of all possible elements with atomic concentration limit above one atomic percent. To confirm the oxidation state of the various elements present in the compound, the core level spectrum was acquired at 11.75/23.5 eV pass energy and at a step size of 0.1 eV with an x-ray probe beam of 100 μm diameter. The electron neutraliser and Ar ion gun were used for charge loss compensation, which occurred as a result of photoelectrons emission from the sample surface during the data collection process. Prior to the collection of data, Z alignment (optimum height between detector and sample surface for maximum photoelectron collection) of each data acquisition point was done with 200 μm 25 W and 15 kV x-ray settings. The adventitious carbon C 1s spectrum was recorded for reference from the sample surface, and then the surface of the sample was sputtered by Ar ion gun with a rating of 2 kV 2 mm x 2 mm at a sputter rate of 10 nm/min of SiO₂ standard. After the sputtering process, core level data were acquired for oxidation state analysis [Moulder 1995].

2.5.3.1 XPS instrumentation

The various parts of an XPS system are mentioned below:

Ultra-high vacuum chamber, sample manipulator (4 degrees of movement: x, y, z, tilt), sample stage, sample mounts, source of x-rays/UV rays/electrons, an electron collection lens, an electron energy analyser, an electron detector system, computer interface for data acquisition and processing, surface cleaning: ion gun, scrape, cleave and electron source for neutralising extra positive charge accumulated by photoemission, sample introduction chamber.

One of the most important parts of the XPS instrument is its electron energy analyser as its energy resolution is of paramount importance which can be described by the equation:

$$\Delta E_{instrument}^2 = \Delta E_{analyzer}^2 + \Delta E_{Xray}^2 \quad 2.14$$

where $\Delta E_{analyzer}$ is given by

$$\Delta E_{analyzer} = E_p \left(\frac{W}{2R} + \frac{\alpha^2}{2} \right) \quad 2.15$$

where E_p is the pass energy of the analyser

W is the slit width, and α is the acceptance angle of the analyser, which is $\pm 20^\circ$ and R is the radius of the concentric hemispherical analyser with a value 279.2 mm.

The slit width of the PHI Versa probe 5000 II analyser is 4 mm x 12 mm, and the x-ray line width of Al $K\alpha$ is about 0.2 eV to 0.3 eV.

Putting the above values in equation (2.14) and then in equation (2.15), one can get the resolution of the XPS instrument as 0.4 eV to 0.6 eV depending upon the pass energy used to collect the photoelectrons.

In addition to chemical state analysis the x-ray photoelectron spectroscopy can be used to determine the atomic concentration of various constituent elements which can be described by the equation:

$$\alpha_i = \frac{I_i}{ASF} / \sum_i I / ASF \quad 2.16$$

for all i . I_i is the intensity/area under the curve for the i^{th} element, I is intensity/area under the curve and ASF is the atomic sensitivity factor of the individual element.

The figure 2-7 given below shows a basic internal schematic of an analyser of an XPS for a detailed understanding of the instrument.

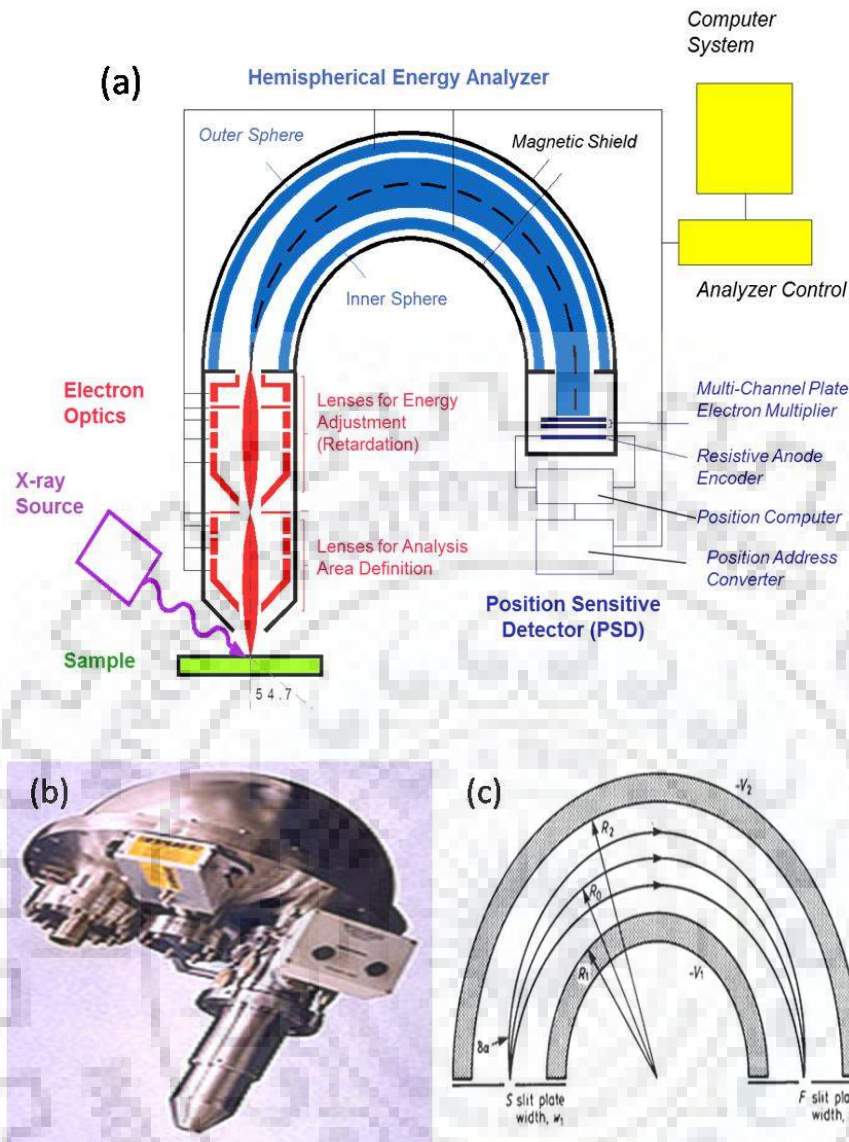


Figure 2-7 Detailed schematic analysis of electron energy analyser showing its components and concentric hemispherical analyser with different radii description (Source, PHI electronics).

Another important part of the instrumentation of the XPS is the ultra-high vacuum condition. A pressure of 10^{-10} Torr is maintained in the main chamber with a series of the pumps like rotary, turbo molecular, ion pump, and titanium sublimation pump (TSP) which are used in order to maintain ultra-low pressure. It is necessary to keep such low pressures to provide a sufficient inelastic mean free path for the photoelectrons to escape the solid surface and reach the detector without being lost in inelastic collisions.

$$\text{Gas molecule impingement flux rate: } I = \frac{P}{\sqrt{2\pi mk}} \quad 2.17$$

$$\text{Mean free path of the electrons: } \lambda = \frac{kT}{\sqrt{2}P\sigma} \quad 2.18$$

$$\text{and monolayer of contamination formation may be written as } \tau = \frac{n_o}{I} = \frac{n_o \sqrt{2\pi mk}}{P} \quad 2.19$$

P is the pressure inside the chamber, k the Boltzmann const., n_o surface atomic density, m the molecular weight and T is the absolute temperature.

The universal curve of inelastic mean free path (IMFP) of various elements w. r. t. binding energy (B.E.) has been shown in **figure 2-8** below.

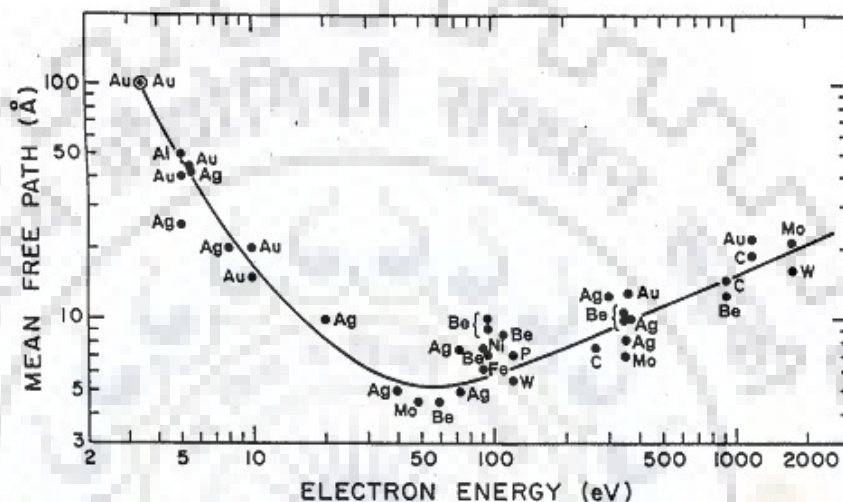


Figure 2-8 Plot of inelastic mean free path (IMFP) of electrons for various elements (Source, Chusuei 2002; Pratt 1973).

The basic purpose of keeping such ultrahigh vacuum in the main chamber is to make sure that the x-ray source, ion gun filament, electron neutraliser (E-neut) and other filaments are free from any contamination. Another important reason is to make surface analysis free from impurity. According to the kinetic theory of gases, high pressure can cause an enhancement in the surface bombardment of the gas (contamination) molecules. Pressure of 760 Torr will cause the deposition of contamination layer in just 3 ns causing a huge problem in analysing the sample surface under investigation. As the pressure is decreased to 10^{-6} Torr, the time for layer formation is about 2 sec and further decrease in pressure to 10^{-10} Torr will lead this time to around 3600 seconds which give sufficient time to analyse the sample surface.

Figure 2-9 shows a diagram of bulk and surface atoms of a material. Surface is a term which is of great importance in XPS characterisation due to the following reasons:

- i) all the materials interact with their surroundings through their surface.

ii) surface atoms determine the reactivity of the materials in a chemical reaction like corrosion, catalysis, etc.

iii) surface atoms control the mechanism of wear and tear.

Also, they differ from the bulk in various ways:

i) atomic environment of surface usually differ from that of bulk.

ii) breaking of three-dimensional periodicity of surface atoms leads to strong atomic modification of the surface structure.

iii) redistribution of the charge density and formation of new electronic states.

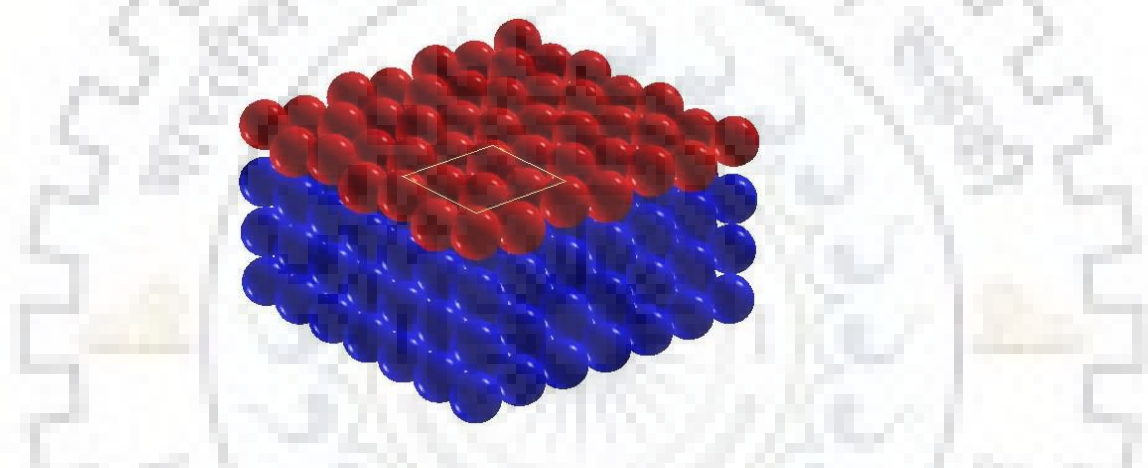


Figure 2-9 Model of bulk (blue) and surface atoms (red) of a material.

2.5.3.2 Basic assumptions and general formulation in x-ray photoelectron spectroscopy

Basic assumptions: The absorption of photons of energy $h\nu$ by a material leads to the ejection of electrons. This complex process includes numerous effects. For the ease of understanding, the interaction of only one photon and one isolated atom, resulting in the ejection of one electron has been considered [Pratt 1973]. Once this cross-section area of ejection of this electron has been determined, the other additional effects can be included. The simplifying assumptions which were used in the above theory are as follows:

1. the target material is a single isolated atom.
2. the target material is neutral and in its ground state.
3. the central model describes the atom.

4. the process is treated as one photon - one electron interaction.

The first assumption concerns the neglect of crystal structure and energy band effects in the photoelectron emission process. Usually, these effects are more pronounced for the loosely bound electrons of the outer shells. The direct contribution of the outer electrons to the total cross-section is minimal as compared to tightly bound core level electrons, which are ejected with the available energy. Often during the photoelectric process, the secondary electrons are more pronounced, which complicates the photoelectric cross sections measurement.

The second assumption states that the atom is neutral and in its ground state, eliminating the consideration of temperature and pressure effects, which may excite/ ionise the atom. At a finite temperature not all the states are filled; the Fermi-Dirac distribution suggests the probability that a state of given energy (E_i) is occupied. This can be described by the formula:

$$f(E_i) = \frac{1}{\exp(E_i - E_f)/kT} + 1 \quad 2.20$$

where E_f is the Fermi energy level, K is Boltzmann constant and T is absolute temperature.

The third assumption is based on the fact that the whole atomic system may be regarded as a central field in which the given electron to be ejected moves. Many atomic properties (e.g., binding energies) based on this assumption matches very well with experimental results.

2.5.4 Impedance spectroscopy

For measurement of the dielectric constant, impedance, modulus formalism, dc and ac conductivity of the LAMOX and its derivatives, NOVOCONTROL Alpha-A high-frequency impedance analyser was used. This analyser is suitable for the measurement of the various physical parameters at different frequencies simultaneously. Complex impedance data, a.c. conductivity modulus formalism were measured directly. The frequency range used in the complex impedance measurement is 1 Hz - 3 MHz with 1 V of applied sinusoidal voltage. The d.c. conductivity and other parameters were calculated indirectly by taking the logarithm of quantities. Figure 2-10 shows a typical complex impedance plot and its equivalent circuit diagram.

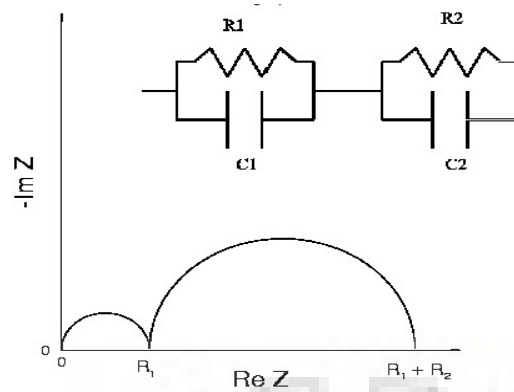


Figure 2-10 Typical complex impedance plot and its equivalent circuit diagram.

2.5.4.1 Dielectric theory

A material is said to be dielectric if it has got the ability to store electrical energy when an external electric field is applied to the material. A dielectric material can be very well exploited in the capacitor application. A high value of a dielectric constant is exploited in supercapacitor applications with minimum volume occupied on the device. The capacitance of a material and its dielectric constant are related by the equation $C = \epsilon A / d$, where ϵ is the permittivity of the material, A and d are the area and thickness between the plates of parallel plate capacitor respectively.

If a d.c. voltage is applied across a capacitor, then all the dipoles of the dielectric material are aligned in the direction of the field. It may be ions or electron clouds which upon the application of strong electric field displaced from their position and results in the formation of dipole. If a sinusoidal voltage is applied across the same plates of the capacitor then the resulting current will be the sum of charging current and loss current.

2.5.4.2 Relaxation time and conductivity studies

Relaxation time τ may be defined as the time required for a one hundred percent polarised material to return to a value of $1/e$ times of its random equilibrium value. The relaxation frequency and relaxation time are related by the equation $\tau = 1/\omega c$ [Bottcher 1978; Debye 1912]. The relaxation study has been done in chapters III and IV in pristine and doped LAMOX compositions, respectively, in detail. Also, the ion dynamics study through the modulus formalism (inverse of dielectric permittivity) and conductivity study have been done in chapter IV of the thesis.

Regarding ionic conductivity (d.c.), the impedance (Z) plots of the real and imaginary parts of Z at various temperatures have been plotted in the form of Nyquist plot. The variation of dc conductivity can be defined as

$$\sigma_{dc} = \sigma_0 \exp\left(-\frac{E}{kT}\right) \quad 2.21$$

where σ_0 is the pre-exponential factor, E is the activation energy, k is the Boltzmann constant, and T is the absolute temperature.

For impedance spectroscopy, dense sintered pellets are coated with the silver paste on flat surface and heated to a temperature of 500 °C for proper binding of silver paste on the pellet surface. The impedance data were collected at 10 °C interval from room temperature up to 400 °C in the range of frequencies from 1 Hz to 3 MHz. The data includes complex impedance, conductivity and modulus formalism. The imaginary, as well as the real part of Z values, are plotted against each other at a particular temperature. The appearance of a wide semi-circle shape plot reveals the presence of non-debye type relaxation. The value of the real part of the impedance is obtained by extrapolating the semi-circle to intercept the x-axis. Hence, resistivity or conductivity is calculated by the formula $R = \rho l/A$, where R is the real part of the impedance, ρ is the resistivity, l and A are the thickness and flat surface area of the pellet respectively.

2.5.4.3 Debye relaxation of dielectric materials

The Debye relaxation analysis predicted that if a material is under the influence of a constant dc electric field, the orientation of permanent dipoles along the electric field takes place. This phenomenon is called as orientation polarisation P_o . This polarisation rises exponentially to a steady-state value P_s with a time constant τ . Once the \vec{E} field is removed, the polarisation decays exponentially with the same time constant. This τ is termed as relaxation time of the process. Instead of dc field if a sinusoidal electric field is applied with an angular frequency ω the polarisation will lag behind the \vec{E} by an angle of δ , where $\tan\delta = (\omega\tau)$ which corresponds to a loss in the material [Calderwood 1989; Turik et al., 2011].

This behaviour can be explained on the basis of the complex susceptibility \hat{X} possessed by the material that varies with ω in accordance with the equation

$$\frac{\hat{X}}{X_s} = \frac{1}{1+j\omega\tau} \quad 2.22$$

where X_s is the value of \hat{X} at very low frequency. \hat{X} leads to origin of complex orientational polarisation \hat{P} , which can be described as $\hat{P} = \epsilon_0 E \hat{X}$, ϵ_0 being the permittivity of free space.

All the above explanations are valid only for materials that display the ideal Debye behaviour. This theory was developed by Debye on the basis of the following assumptions:

- i) the molecular inertia in solid is negligibly small.
- ii) effect of field created by other dipoles on any dipole is considered as zero.

The first assumption means that if the inertia of the dipoles is taken as zero, then the total torque acting on any dipole is zero, and the second assumption implies that the field acting on any dipole is zero by other dipoles. Thus the equation of torque becomes:

$$T_E - T_F - T_P = 0 \quad 2.23$$

where T_E is the torque applied by the electric field, T_F is frictional torque exerted by other dipoles on any dipole of interest that experiences a retarding torque by random collisions with other dipoles, and T_P is the elastic polarisation torque.

When a field is applied to dielectric specimen between two parallel plate electrodes, at $t = 0$ the energy density between the plates is $\frac{1}{2} \epsilon E^2$ ignoring the fast polarisation process. At $t = t_1$ when polarisation has reached some value P , the value of energy density is $\frac{1}{2} PE$. This increase in energy density is by virtue of the fact that the dipoles themselves are in higher energy state which have been displaced through an angle ψ against the torque T_P provided by the polarisation field.

If we consider that all the dipoles are oriented within the angle between ξ to $d\xi$ of two cones. Now if we consider that ψ is so small and ξ may be taken to be effectively constant so that for a given dipole T_E is given by:

$$T_E = \mu E \sin \xi \quad 2.24$$

The frictional torque T_F may be written as

$$T_F = K_F \frac{d\psi}{dt} \quad 2.25$$

The elastic polarization torque T_P is proportional to the angular displacement so that

$$T_P = K_P \psi \quad 2.26$$

Thus the equation of motion becomes

$$T_E - K_F \frac{d\psi}{dt} - K_P \psi = 0 \quad 2.27$$

The solution of the equation leads to

$$\tau = \frac{K_F}{K_P} \quad 2.28$$

But usually, the case is not the ideal one as considered in the Debye phenomenon. The dielectric constant as a function of frequency can be generally described as:

$$\varepsilon_r(\omega) = \varepsilon_r(\infty) + \frac{\varepsilon_r(0) + \varepsilon_r(\infty)}{1 + (1\omega\tau)^{1-\alpha}} \quad 2.29$$

And also the dielectric frequency peak can be described as

$$\tan \delta = \frac{\left(\frac{1}{2}\right)\Delta \sin(\beta\pi/2)}{\cosh(\beta z) + \cos(\beta\pi/2)} \quad 2.30$$

where Δ is the relaxation strength, $z = \ln(\omega\tau)$, $\beta = 1-\alpha$, and α (lies within 0 and 1) is the width parameter leading to a symmetric broadening of the Debye relaxation. $\alpha = 0$ corresponds to standard Debye relaxation $\varepsilon_r(\infty)$. The above equation can also be reformulated as

$$\varepsilon' = \varepsilon_\infty + (\varepsilon_s + \varepsilon_\infty) \int_0^\infty \frac{f(\tau)d\tau}{1 + \omega^2\tau^2} \quad 2.31$$

and

$$\varepsilon'' = (\varepsilon_s - \varepsilon_\infty) \int_0^\infty \frac{\omega\tau f(\tau)d\tau}{1 + \omega^2\tau^2}, \quad \int_0^\infty f(\tau)d\tau = 1. \quad 2.32$$

In the case of single-component dielectric where $f(\tau)$ is delta function, the equation is reduced to Debye formula [Turik 2011].

The non-debye behaviour can be postulated in terms of considering a single dielectric component with a rectangular distribution function $f(\tau) = h$ and the relaxation times within the interval of $\tau_1 \leq \tau \leq \tau_2$ according to equation 2.32 and 2.33.

Another way of writing the complex dielectric constant using the Debye model is

$$\varepsilon_r^* = \varepsilon_\infty + \frac{(\varepsilon_s - \varepsilon_\infty)}{1 + i\omega\tau} \quad 2.33$$

The equation implies low values of ε at high frequencies. This equation may be modified to the following equation and separating the real and imaginary part:

$$\frac{(\varepsilon_s - \varepsilon_\infty)}{1 + \omega^2\tau^2} - i\omega\tau \frac{(\varepsilon_s - \varepsilon_\infty)}{1 + \omega^2\tau^2} \quad 2.34$$

2.5.5 Fast diffusion path in ion-conducting solids

The diffusion in ion-conducting solids is rather a typical phenomenon as compared to lattice ion diffusion, which occurs either by vacancy or interstitials. The diffusion of atoms in grain boundary present in the microstructure is higher as compared to the lattice or bulk diffusion. In polycrystalline materials, the diffusion along the grain boundaries is very common and exists in many materials. Therefore, the overall or effective diffusion in these materials is contributed by both grains as well as grain boundaries. That is why it is very important to understand these two aspects while considering the oxygen diffusion into the vacancies either by lattice or by grain boundaries.

The overall diffusion coefficient D_{eff} may be written as

$$D_{eff} = gD_{gb} + (1 - g)D \quad 2.35$$

where g is the atomic fraction site in the grain boundaries and can be written as

$$g = \frac{q\delta}{d} \quad 2.36$$

where q is a numerical factor depending upon the grain shape and δ is the grain boundary width. In the micron range of polycrystalline materials, the grain boundary volume is very small as compared to bulk volume, and hence the g parameter can be ignored in this case [Liu 2009].

2.5.6 Raman Spectroscopy

Like FTIR, Raman spectroscopy technique also gives the structural information based on vibrational, rotational modes of the molecules in a system. In case of Raman spectroscopy technique, the photons of particular energy from a laser source interacts with molecular vibrations, phonons, and other excitations resulting in scattering of laser photons elastically and inelastically. In the first case, the absorbed photon has the same wavelength as that of the emitted one (Rayleigh scattering), but in the second case, some photons have lost or gained an amount of energy-related to the vibrational energy spacing in the molecule as shown in figure 2-11. This

difference in the energy levels corresponds to the wavelength of the Stokes and anti-Stokes lines which are equally displaced from the Rayleigh line in the Raman spectrum.

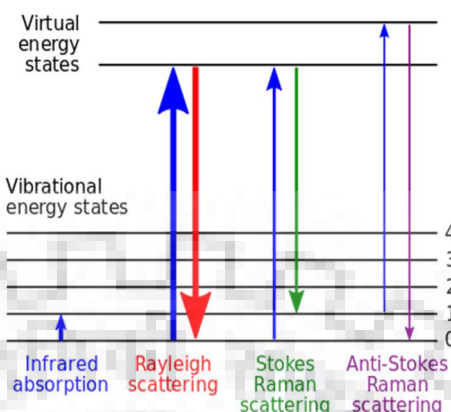


Figure 2-11 Schematic of energy levels transition in case of I.R. and Raman spectroscopy (Source, Smith 2005).

The basic difference between the IR and Raman technique lies in their respective molecular transitions taking place when the molecules are excited by a photon of energy $h\nu$. For a transition to be Raman active, there should be a noticeable change in the polarisability of the molecule during the vibration. This implies that the electron cloud of the molecule must be displaced from its initial position. On the other hand, for an IR transition to occur, the molecules should show a dipole moment change during vibration. Therefore, when a molecule is symmetrical, one cannot detect any IR absorption spectra, since the molecules cannot change its dipole moment. Therefore, together with FTIR and Raman one can get complete information on the structural entity of the material under consideration.

In this work, the Raman Spectrum of the LAMOX and doped LAMOX samples have been recorded using 488 nm Argon ion laser on confocal Laser Raman Spectrometer (Model: LabRam HR 800 EV, HORIBA Jobin Yvon, France).

The instrument equipped with TE cooled charge couple device (CCD) detector (Model: Synapse CCD), air-cooled CW 488 nm Argon ion laser with variable power up to 20 mW and air-cooled CW 785 nm diode laser with fixed power of 100 mW. Further source laser power can be varied using density filters as low as 0.1 percent through 'Labspec 6' software used for running the instrument. The schematic for explaining working principle of the Raman instrument has shown below in figure 2-12.

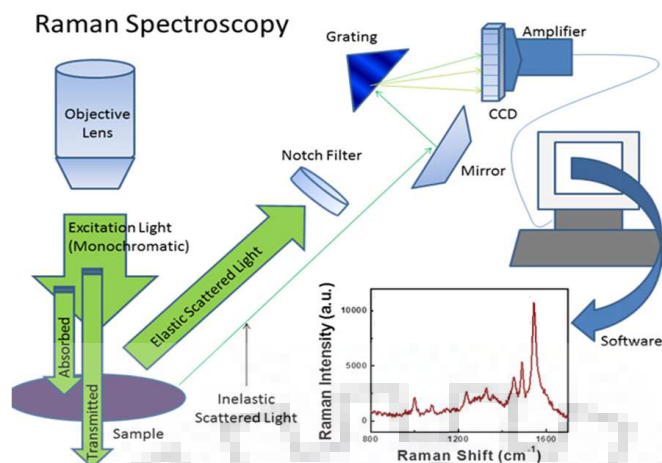


Figure 2-12 Raman spectroscope instrumentation (Source, Analytical Techniques).

The excitation wavelength-specific ‘Notch filter’ will cut down the high intensity elastically scattered (Rayleigh scattering) monochromatic light. Raman useful inelastically scattered laser light would pass through the holographic grating before reaching the CCD detector where the signals would be detected and amplified for its software processing in obtaining Raman spectrum of the sample. The instrument has been calibrated for crystalline ‘silicon’ Raman signal at 520.7 cm⁻¹ every time before proceeding to the sample analysis.

2.6 Summary

The synthesis route for pristine LAMOX, doped LAMOX materials, has been discussed in the present chapter. Calcination and sintering of the green pellets for various characterisation techniques have been discussed in detail. In the present study, the LAMOX has been synthesised by solid-state processing for the various investigations. Various characterisation techniques that are extensively used in the analysis of LAMOX compositions have been described in detail along with their instrumentation and principle of operation. Some basic formulae have also been discussed in brief to give an understanding of the respective characterisation technique. After preparing all the necessary LAMOX and its doped compositions, the respective characterisation study was done to reveal the information of the particular composition to be studied in detail.

The next chapter is devoted to the synthesis and analysis of pristine LAMOX sample treated in air and Ar-H₂ atmosphere. The effect of the atmosphere under which the LAMOX is treated is of great importance, which will focus on some important properties of LAMOX and its constituent elements. These properties will help us in evaluating the merits and demerits of LAMOX as an electrolyte.

Chapter 3

Study of $\text{La}_2\text{Mo}_2\text{O}_9$ electrolyte in air and reductive atmosphere

3.1 Introduction

This chapter focuses on the study of $\text{La}_2\text{Mo}_2\text{O}_9$ (LAMOX or LMO) synthesised by solid-state process in air and reductive atmosphere. The details of the synthesis and the instrumentation have been mentioned in chapter 2. In the present chapter, some of the studies viz. XRD, FE-SEM done on LAMOX have been presented and were also done by various researchers, and some of the new studies viz., XPS, and grain boundary conductivity have been done and found interesting. The XRD, XPS, SEM and impedance spectroscopy data were analysed for LAMOX samples treated both in air and Ar-H_2 (reducing) atmospheres. The results obtained were in agreement with the literature published by the various researchers. The XPS study has been done presently in this chapter as well as in the subsequent chapters to study the effect of reducing atmosphere (Ar-H_2) on Mo in LAMOX. The results show that Mo in LAMOX has a strong tendency to get reduced, which may damage the fuel cell performance. The ionic conductivity data show that grain boundary resistance plays an important role in low ionic conductivity for monoclinic LAMOX systems.

3.2 Structural analysis of air treated LAMOX

Figure 3-1 shows the diffraction pattern at room temperature of the $\text{La}_2\text{Mo}_2\text{O}_9$ calcined at 800°C in air. The peaks present in the XRD pattern of $\text{La}_2\text{Mo}_2\text{O}_9$ corresponds to JCPDS file no. 00-028-0509. The XRD pattern shows the existence of a large number of small XRD peaks corresponding to lower symmetry (monoclinic) crystallographic phase. The inset in figure 1 shows the enlarged view of the (311) peak in 41.4° to 42.1° 2θ range. The multiple splitting of the peaks reveals that $\text{La}_2\text{Mo}_2\text{O}_9$ is monoclinic phase at room temperature, which is in accordance with the literature by Evans et al., [2005], and Lacorre [2000b]. At higher angle side, few peaks are observed, which corresponds to La_2MoO_6 and are subsequently verified with the JCPDS data file 24-0550.

A monoclinic unit cell system can be defined as $a \neq b \neq c$; $\alpha = \gamma = 90^\circ$ and $\beta \neq 90^\circ$. The relation between d spacing and lattice parameters may be written as

$$\frac{1}{d^2} = \frac{1}{\sin^2\beta} \left(\frac{h^2}{a^2} + \frac{k^2 \sin^2\beta}{b^2} + \frac{l^2}{c^2} - \frac{2hl \cos\beta}{ac} \right) \quad 3.1$$

The lattice parameters and unit cell volume of $\text{La}_2\text{Mo}_2\text{O}_9$ were calculated and given as: $a = 7.161 \text{ \AA}$, $b = 7.135 \text{ \AA}$, $c = 7.144 \text{ \AA}$, $\gamma = 89.94^\circ$ and cell volume = 365.063 \AA^3 .

The crystallite size of $\text{La}_2\text{Mo}_2\text{O}_9$ sample was calculated using the Debye Scherer formula

$$0.9\lambda/\beta \cos(\theta) = 71.16 \text{ nm.}$$

where λ is the wavelength of the x-ray used (Cu $K\alpha$), and β is the full width at half maximum (FWHM).

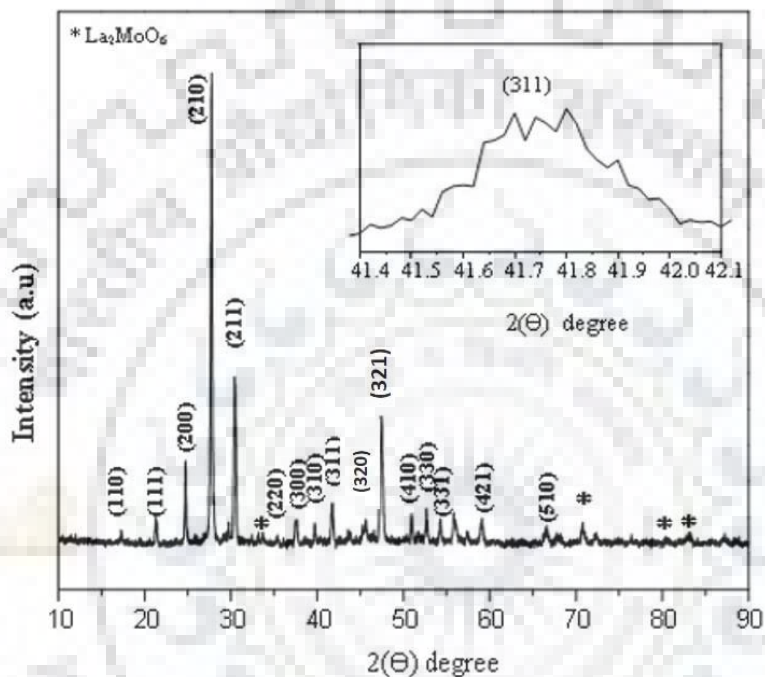


Figure 3-1 XRD pattern of $\text{La}_2\text{Mo}_2\text{O}_9$ at room temperature. Inset: magnified view of (311) peak in the 2θ range of 41° to 42° .

At higher 2θ value, small peaks of La_2MoO_6 were observed. This phase is possibly formed by the 1:1 reaction of La_2O_3 and MoO_3 . Previous studies on this compound have reported that it crystallizes in tetragonal symmetry with space group $I\bar{4}_2m$. However, some other studies have shown that it is very difficult to index the peaks into the earlier space group because of the too low peak intensity obtained from the diffraction pattern. Later, it was confirmed that it could be better indexed in $I4_1/a\ c\ d$ (space group no. 142). The neutron diffraction study has revealed the crystal structure of the compound, which consists of puckered sheets of $\text{La}_2\text{O}_2^{2-}$ and isolated layers of MoO_4^{2-} tetrahedra. The potential application of the compound is in selective oxidation of hydrocarbons and dehydrogenation of organic compounds [Rocha and Muccillo 2005].

One of the disadvantages of room temperature LAMOX is its low ionic conductivity, which may be attributed to confinement of oxide ions at the respective sites. To facilitate the oxide ion conductivity, disordering of oxide ions/vacancies in the lattice is required. This theory is well established for yttria-stabilised zirconia (YSZ) [Goffet et al., 1999; Predith et al., 2008], and one can also correlate that with LAMOX electrolyte. The mechanism of oxide ion conduction is common for both cases. The α -LAMOX structure has ordered vacancies-ions. Therefore, the conductivity was nearly two to three orders less than that of β - LAMOX phase, which exists at 600 °C or above which has disordered cation/vacancy arrangements. In β -LAMOX two out of three O atoms sites (three separate sites) are partially occupied O(2), and O(3) Wyckoff position 12b) and contribute to conductivity. The O (1) atom at 4a site is fully occupied site according to the literature and thus barely contributes to conductivity [Evans et al., 2005].

As already described in chapter I, the LAMOX is derived from SnWO_4 . The Sn has a lone pair of electrons which has been substituted by La^{3+} which is a non-lone pair cation. To balance the overall charge in the compound, oxide ion incorporation takes place in the lattice and subsequently creating the vacancies in the oxide lattice. In this case La has been doped at Sn site. There exists an interaction between cation and vacancy, which can be explained on the basis of repulsive and attractive forces [Xia et al., 2009]. If the interaction between the cation and the vacancy is significant, then the mobility of vacancy is restricted, which results in reduced ionic conductivity. This may be treated as the condition prevalent in α - LAMOX which has a very low electrical conductivity.

The ordering can be either short-range or long-range (20-50 Å), which influences the ionic conductivity of the material. Short-range ordering ($\sim 5 - 15\text{Å}$) restricts the vacancies/oxide ions to hop freely in the structure [Cohen and Fine 1962]. This effect is even more severe in the long-range ordering since the ordering of vacancies /ions is extended up to the larger distance. This implies that the oxide ions have to hop on to a large distance which requires a high value of energy. To break this arrangement, ions have to cross a barrier or has to make a transition from ordered to a disordered phase which occurs at 600 °C and above in LAMOX for $\alpha \leftrightarrow \beta$ transition giving rise conductivity enhancement of three orders of magnitude.

This $\alpha \leftrightarrow \beta$ transition can be stabilised with the disordered phase of vacancies at lower or room temperature by suitable dopants. Hence, to increase the low-temperature conductivity, it is highly recommended to decrease the ordering or the interaction among the cations and vacancies.

The detailed diffraction study of LAMOX under reducing conditions has been discussed by many researchers in detail elsewhere [Lu and Zhu 2008; Goutenoire et al., 1999; Ravella 2012]. The photoelectron spectroscopy, scanning electron microscopy, and electrical conductivity studies have been done in detail to understand the effect of sintering atmosphere. The first initial observation of the reduction of the samples sintered in reductive atmosphere was the change in colour of the LAMOX pellets from creamy white to grey. As reported in the literature above 700 °C the LAMOX is reduced to an amorphous phase of $\text{La}_2\text{Mo}_2\text{O}_{7.8}$ and below 700 °C this compound is reduced to a perovskite-related phase with a composition of $\text{La}_7\text{Mo}_7\text{O}_{30}$ (also known as 7730 phase) under reducing conditions. The structure of $\text{La}_7\text{Mo}_7\text{O}_{30}$ is built up from a hexagonal array of cylinders or rods of a perovskite-type arrangement along its three-fold axis. The reduction of LAMOX in 7730 phase was due to the reduction of Mo^{6+} in LAMOX to multiple oxidation states of Mo^{5+} , Mo^{4+} , Mo^{3+} , and Mo as reported elsewhere [Lopez et al., 2005; Goutenoire et al., 1999; Jin et al., 2007; Khaled et al., 2012]. This 7730 phase can be obtained from the $\text{A}_7\text{B}_7\text{O}_{21}$ perovskite phase. The Mo^{6+} was reduced to lower oxidation states leading to the formation of other higher-order oxides of lanthanum and molybdenum. The amorphous phase of LAMOX formed above 700 °C can also be exploited as the anode material for the LAMOX based electrolytes since the amorphous phase is sulphur tolerant and is a part of hydrocarbon gas source used as fuel in SOFC applications [Lu 2008].

3.3 Microscopic study of air and Ar-H₂ treated $\text{La}_2\text{Mo}_2\text{O}_9$ by FE-SEM

The LAMOX powder samples treated in air and Ar-H₂ atmospheres for an appropriate time period are examined by scanning electron microscope for morphological analysis to explore the effect of various atmospheres. The calcined powder of LAMOX is compacted in the form of green pellets and calcined in air and Ar-H₂ atmosphere. The details have been covered in the experimental section. Here only phenomena related to the treatment of LAMOX in both atmospheres are presented.

The morphological study of LAMOX pellets sintered in air and reducing atmospheres as well as of the powder samples was carried out by FE-SEM, and the micrographs are shown in figure 3-2. As evident from figure 3-2(a) the calcined powders have the average grain size of 200-500 nm. Upon the sintering of the compacted powders, the grain size has been increased to 1 µm as depicted in figure 3-2 (b). This clearly indicates the minimisation of the surface energy and merging of grains to bigger grains.

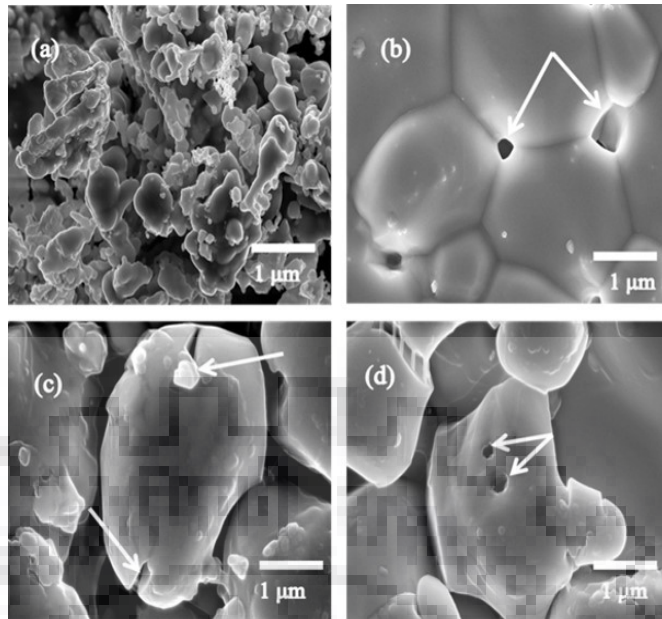


Figure 3-2 FE-SEM images of (a) LAMOX powder sample calcined at 800 °C for 6 hours, (b) sintered LAMOX in air at 900 °C for 6 hours (c) formation of cracks as a result of H₂ interaction with grains at 500 °C and (d) formation of intra-granular pores as the last step of reduction process at 900 °C.

The FE-SEM micrographs in figure 3-2(b) show a similar situation where a pore is formed at the grain boundary. The relative density of the air treated LAMOX samples is found to be 90-94 percent. The densification and coarsening occur simultaneously during sintering. Figure 3-2(b) clearly shows the FE-SEM images of the LAMOX air sintered composition where most of the grain growth phenomenon has occurred due to abnormal grain growth process, where some grains grow rapidly at the expense of other grain giving rise to a bimodal grain size distribution in the final grain structure [Rahaman 2003]. From figure 3-2(b), it is quite evident that the coarsening mechanism dominates the densification and grain growth mechanisms. Generally, in the coarsening mechanism, an increase in average grain size is accompanied by the increase in the average pore size. This has an effect on the reduced driving force for sintering and increased diffusion distance for matter transport. This results in a reduced sintering rate.

The FE-SEM analysis of the LAMOX samples sintered at 500 °C and 900 °C in reductive atmosphere are shown in figure 3-2(c) and 3-2(d). It is evident from the figure that the formation of intra-granular pores has been observed at a sintering temperature of 900 °C. The formation of the intra-granular pores is not a straight forward process. During the exposure of Ar-H₂ gas to the sample, the series of cracks is formed, which leads to pore formation. The detailed discussion has been provided in the next section. Figures 3-3 and 3-4 give an insight into intermediate stages

of the sintering process at 500 °C. Before the grain growth, the mass transport phenomenon is observed where the masses are diffused from one grain to another to form bigger grains and dense samples [Schulmeyer and Ortner 2001; Park and Levenspiel 1975]. As earlier mentioned, the relative density of reduced LAMOX samples is 70-75 percent.

The Ar-H₂ treated samples of LAMOX can be studied by the reduction mechanism. This mechanism is more complex as compared to that of air treated samples. In the literature, it is well established that LAMOX under reducing conditions loses oxygen from the lattice site, and molybdenum gets reduced among all the LAMOX members [Lacorre 2000b]. Also, the loss of oxide ion from the lattice site makes the LAMOX system to exhibit electrical conductivity. The appearance of electrical conductivity on the sample surface is shown in figure 3-5, where the images of the LAMOX sample are captured by FE-SEM without any conductive coating. The image reveals all the features visible even at high magnification. This clear images may be due the presence of electronic conductivity shown by the LAMOX pellet under reducing atmosphere. The figures clearly reveal the formation of rod-shaped structures suggesting the mass transport and necking process during sintering [Demirskyi 2012]. This necking process ultimately leads to grain growth at the end stage of the sintering.

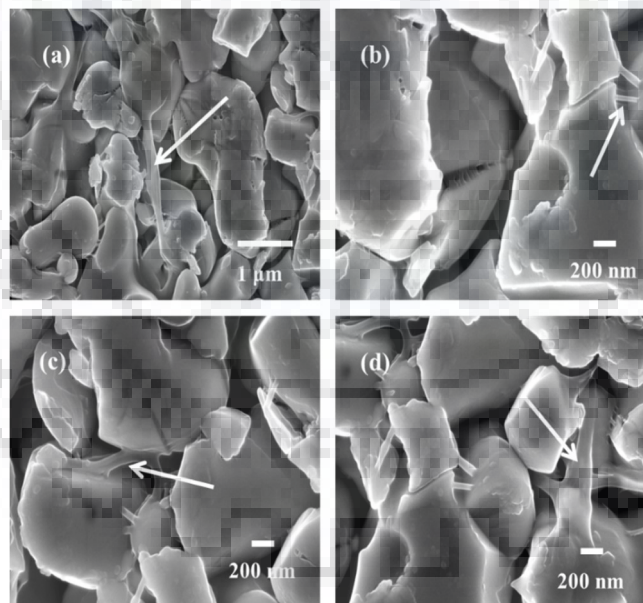


Figure 3-3 FE-SEM images of LAMOX pellet sintered at 500 °C for 6 hours in reducing atmosphere (a), (b), (c), and (d). The appearance of rod-shaped branches between the grains indicated by arrow shows the mass transport process, which ultimately leads to grain growth.

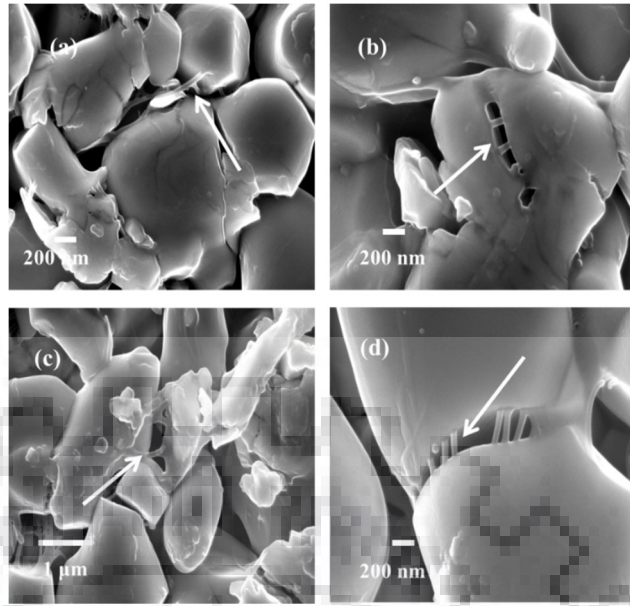


Figure 3-4 FE-SEM images of LAMOX pellet sintered at 500 °C for 6 hours in reducing atmosphere (a), (b), (c), and (d). The appearance of rod-shaped branches between the grains indicated by arrow shows the mass transport process, which ultimately leads to grain growth.

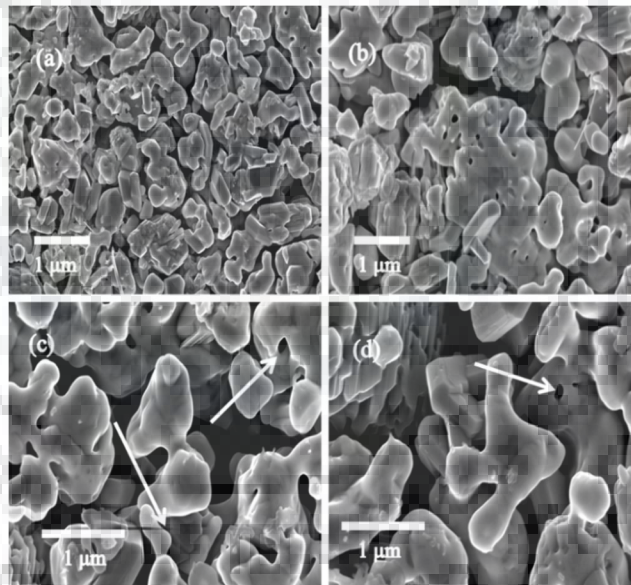
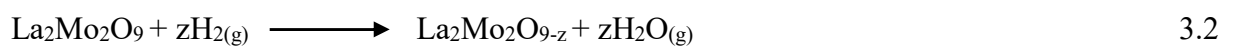


Figure 3-5 FE-SEM images of (a), (b), (c), and (d) $\text{La}_2\text{Mo}_2\text{O}_9$ treated under diluted hydrogen for 6 hours at 900 °C. All the images are captured without conductive coating on the sample. Features visible are a result of the appearance of electronic conductivity in the sample.

3.4 Reduction mechanism of $\text{La}_2\text{Mo}_2\text{O}_9$ treated under Ar- H_2 atmosphere

The equation describing the reduction of $\text{La}_2\text{Mo}_2\text{O}_9$ under reductive atmosphere can be written as



where $9-z$ represents the oxygen loss from the host lattice responsible for electronic conductivity [Buvat 2016].

Another model for the reduction mechanism of Mo oxides in Ar-H₂ atmospheres has been postulated by Schulmeyer et al. [2001] for the reduction of molybdenum oxides in diluted hydrogen atmosphere. According to this, two models were developed to explain the cause of reduction of Mo in reductive atmosphere which can be described by

- a) The shrinking core model (SCM) and
- b) The crackling core model (CCM)

Both of the models explain the exposure of LAMOX in reductive atmosphere and have been explained in detail elsewhere Schulmeyer et al., [2001].

3.5 X-ray photoelectron spectroscopic studies of air and Ar-H₂ atmosphere treated LAMOX

Detailed structural and morphological (FE-SEM) based studies on α -LAMOX, as well as on β -LAMOX, can be seen in the literature. But very few authors have reported x-ray photoelectron spectroscopic (XPS) studies of LAMOX treated under different atmospheres, which is of paramount importance in this context. Here we explore the XPS advantage in analysing the various aspects of LAMOX constituents for electrolyte application. Both XPS and secondary ion mass spectroscopy (SIMS) studies the surface of organic/inorganic materials. XPS study of LAMOX has been presented in this section for air and reductive atmosphere.

Figure 3-6(a) shows the survey spectrum (Su 1s) of the LAMOX sintered in the air atmosphere. The survey spectrum shows the photoelectron peaks and Auger electron peaks of the respective elements in the range of 0 to 1150 eV. The survey spectrum was collected to confirm the presence of various elements present in the sample with concentration greater than one atomic percent (theoretically). Some auger peaks are visible in the spectrum because the photoelectric process and auger emission occur at a small interval of time of about 10^{-15} seconds after the photoelectric process [Moulder 1995]. These auger peaks have the usual nomenclature as KVV. The symbol V represents the final vacancies in the valence band levels. The survey spectrum shows O KLL peak at near about 1013 eV with the source as Al K α . Along with the most prominent photoelectron peak, other core level peaks are also present in the spectrum. Shallow core levels and valance levels are present near the fermi edge i.e., 0 to 15 eV of the binding energy scale.

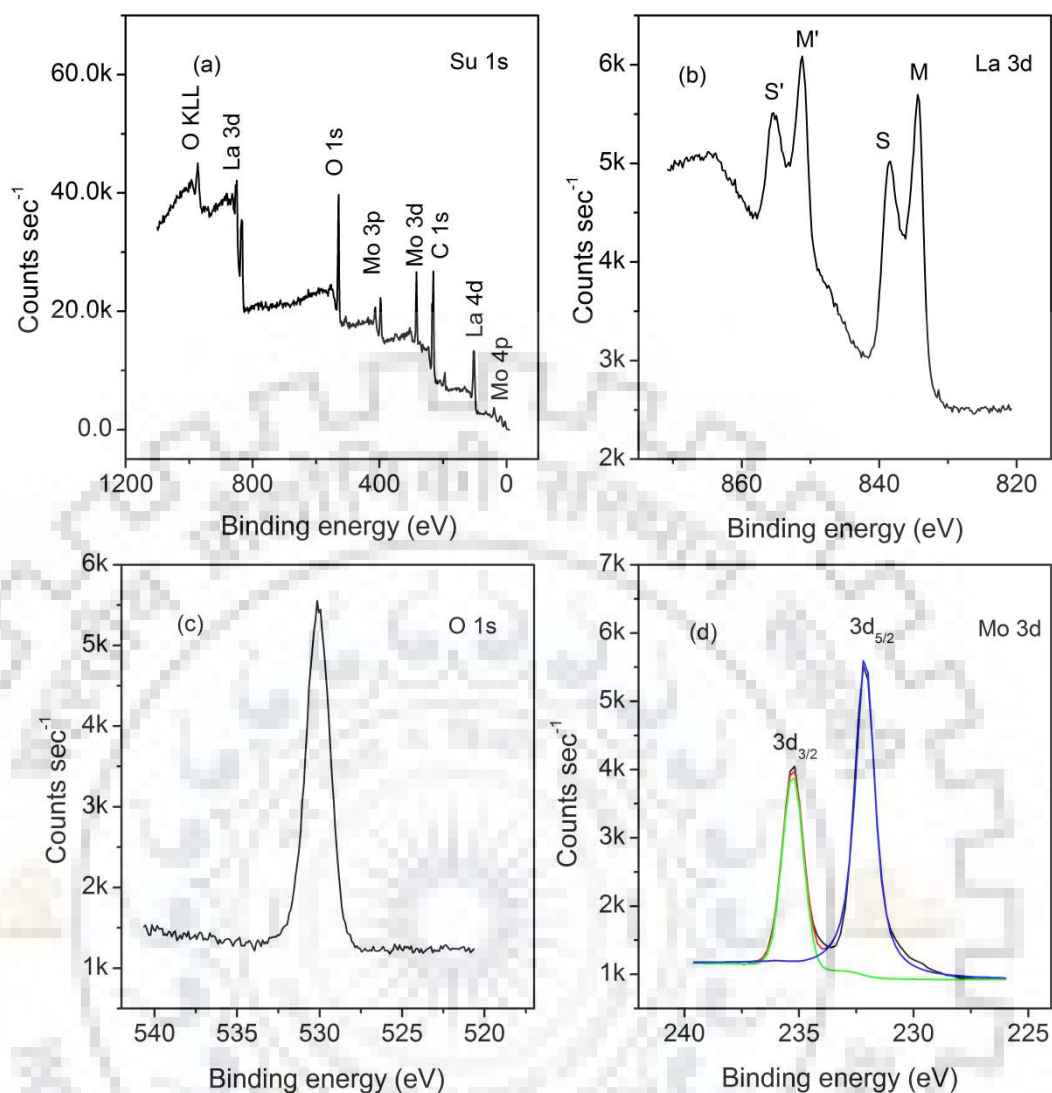


Figure 3-6 (a) Survey spectrum of LAMOX for detection of constituent elements, (b) core level spectra of La 3d, (c) Mo 3d spectra showing spin-orbit splitting, (d) O 1s singlet peak. All the spectra were taken at room temperature for the sample treated at 900 °C in air for 4 hours.

Figure 3-6 also shows the XPS core level spectra of La 3d, O 1s, and Mo 3d in figure 3-6 (b), (c), and (d), respectively. All the spectra were collected at a slow scan rate with a pass energy of 11.750 eV and at 0.1 eV step size. Except for O 1s, all the other core level peaks show natural splitting. The *s* level generally cannot have splitting because of the absence of orbital quantum number and same angular momentum number according to the formula $j = |l \pm s|$, where *l* being orbital quantum number and *s* is spin. The peak splitting ratio is given by: $|2j + 1|$. The emission of an electron during a photoelectric process from a core level that itself has a spin i.e., unpaired electron in the valence shell may create a vacancy in two or more ways. The coupling of the unpaired electron left after the photoemission from an *s*-type orbital with other unpaired

electrons results the ion/atom in several possible final states with many energies. As a consequence, an asymmetrical peak splitting occurs. In p, d, and f- type orbital, the ionisation of these levels are much more complex and difficult. Usually, in these types of levels, the separation between the spin doublet increases.

3.5.1 La 3d core level analysis

At first, La 3d core level is analysed and the spectrum is shown in figure 3-6(b). The spectra show four peaks for 3d level. Usually, 3d level splits into two peaks. But the main peaks $3d_{5/2}$ and $3d_{3/2}$ also split into two peaks in the spectra. These peaks are referred to as satellite peaks which results from two different screening processes of the initial empty 4f orbital as a consequence of the creation of 3d core hole. For the unscreened state, namely M and M', the 4f level is predominantly filled by the electrons belonging to the outermost shell of the La atom. Whereas, for the screened state, the peaks S and S' the 4f level is filled by the electrons of a ligand atom (O 2p) to fill the 3d hole. The two states, namely screened M and M' has $3d^9 4f^0$ as final state and screened orbital has $3d^9 4f^1 L$ as the final state [Khaled et al., 2012]. The binding energy evidence for $3d_{5/2}$ peak and $3d_{3/2}$ peak (834.6 eV and 851.2 eV) and deconvolution of La 3d spectra confirm the presence of La in 3+ state. No other peaks are observed during the deconvolution of the spectra. Therefore, it can be concluded that apart from the natural splitting no more splitting was observed, which shows the absence of any further oxidation peaks in the La 3d spectrum.

3.5.2 Mo 3d and O 1s core level analysis

The Mo 3d spectrum of the air treated LAMOX has been shown in figure 3-6(d). It also shows the splitting of the peak in $3d_{5/2}$ and $3d_{3/2}$. The binding energy for Mo^{6+} for $3d_{5/2}$ and $3d_{3/2}$ are 232.5 eV and 235.8 eV, respectively, which upon deconvolution shows a good fit on the spectrum obtained. The spectrum shows no other peaks merged with the main peak, which confirms the absence of other lower oxidation states of Mo. The O 1s peak of the LAMOX in figure 3-6(c) shows singlet component but which corresponds to all metal oxides ranging from 528 eV to 532 eV.

Therefore, one can conclude that air treated LAMOX sample has no adverse effect on any of the constituent elements and the properties remain the same in air-treated atmosphere as evident by crystal structure analysis, morphological analysis, and XPS analysis.

3.5.3 Core level XPS analysis of reduced LAMOX constituents

The spectroscopic study of reduced LAMOX samples treated in Ar-H₂ atmosphere has been explained in detail in this section. Figure 3-7 shows the core level spectra of the respective elements of the LAMOX composition. From the figure, it can be seen that Mo core level spectrum shows clear splitting into multiple peaks at various level of binding energies which upon deconvolution confirms the reduction of Mo⁶⁺ oxidation state to lower oxidation states like 5+, 4+, 3+ and even Mo 0 sintered in reductive atmosphere as can be clearly seen in figure 3-7 (d). No other spectrum in figure 3-7(a-c) shows splitting apart from its natural 3d splitting, which has no effect of reducing atmosphere when compared to air-treated sample spectrum. In the curve-fitting procedure both Gauss and Lorentz type of functions are used to obtain a better fit and the background treatment was done by Shirley function to the original data. MULTIPAK software is used for deconvolution, which takes care of background noise during deconvolution. Therefore, even if the background is subtracted manually from the data and then deconvoluted, that will produce no change in the data as compared to automatically done by MULTIPAK software.

The reference binding energy values for the respective elements and their states can be found in the XPS handbook [Moulder 1995]. This reduction of Mo to lower oxides and oxygen loss from the lattice site contributes to electronic conductivity in the sample along with the ionic conductivity. Though the overall conductivity of the sample increases but the presence of electronic conductivity in the sample is highly undesirable because it may degrade the performance of the fuel cell operation. Therefore, to get the optimum performance of LAMOX as an electrolyte, one has to work at a lower temperature regime. This Mo reduction in the Ar-H₂ atmosphere is the main drawback that restricts the potential of LAMOX as an electrolyte, which can be overcome by lowering the operating temperature but a cost of lower conductivity.

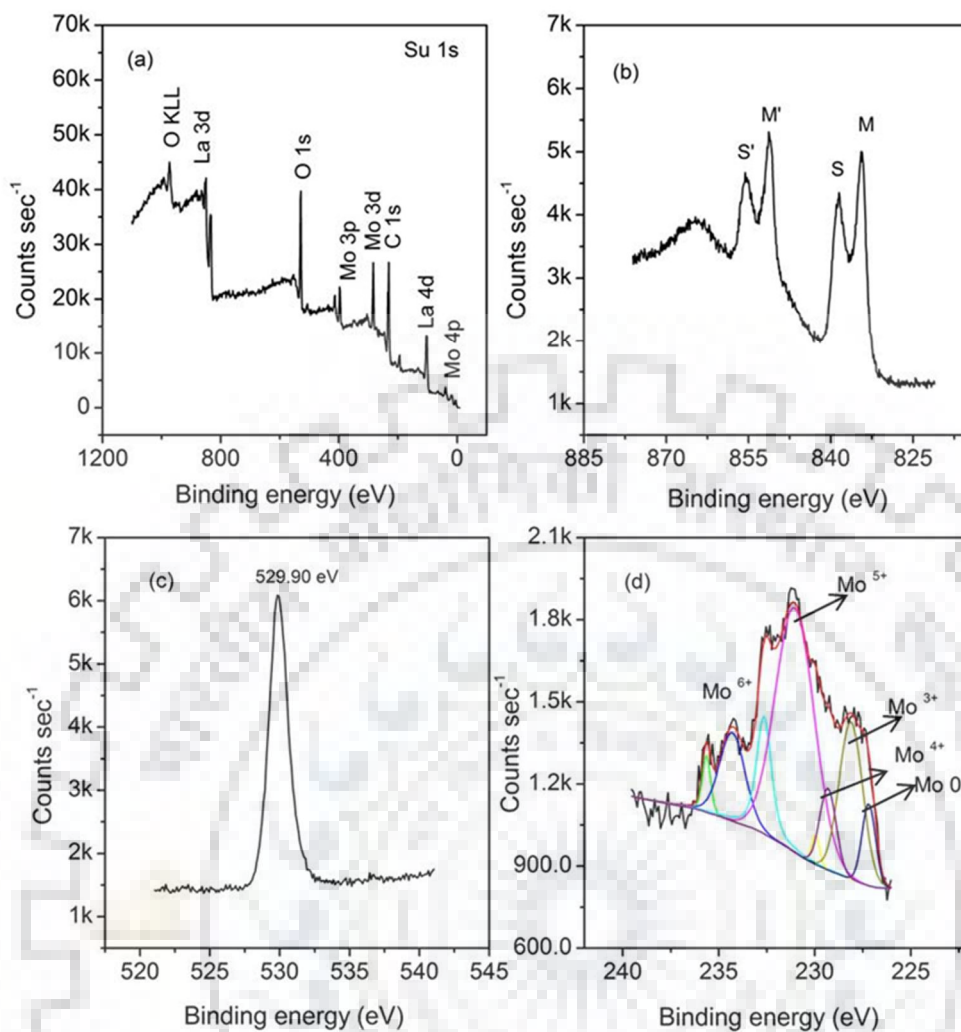


Figure 3-7 (a) Survey spectrum (Su 1s), core level spectra of (b) La 3d spectrum (c) O 1s spectrum (d) Mo⁶⁺ spectrum with multiple valance states. All the data are collected at room temperature treated in Ar-H₂ atmosphere for 4 hours and sintered at 900 °C.

The standard binding energy values in eV of various elements in their respective oxidation states are listed in table 3-1. For the deconvolution of a single core level spectrum, the FWHM parameter should be kept constant (fixed) and then the atomic concentrations should be calculated. In the present study, the FWHM is varied during Mo spectrum deconvolution. The multiple chemical states of Mo has been listed in table 3-2. The variation in FWHM is over the range of 1.77 to 1.25 for Mo spectrum curve fitting. The changes observed in the atomic concentrations upon curve fitting of the Ar-H₂ treated Mo spectrum are minimal. Therefore, the values are kept the same. The variation FWHM during the deconvolution process has been adopted throughout the thesis. But for more accurate results, the FWHM parameter should be fixed during the curve fitting process for a single spectrum.

Table 3-1 Binding energies of various elements and their respective oxidation states.

Elements	Peak names	Binding energy (eV)	Reference
La ³⁺	3d _{5/2} , 3d _{3/2}	834.6, 851.2	Moulder 1995
O ²⁻	1s	530.2	do
C	1s	284.5	do
Mo ⁶⁺	3d _{5/2} , 3d _{3/2}	232.7, 235.8	do
Mo ⁵⁺	3d _{5/2} , 3d _{3/2}	231.7, 234.9	Jin 2007
Mo ⁴⁺	3d _{5/2} , 3d _{3/2}	229.1, 232.3	do
Mo ³⁺	3d _{5/2} , 3d _{3/2}	228.3, ---	do
Mo 0	3d _{5/2} , 3d _{3/2}	227.7, 230.9	do

The amount of Mo in various oxidation states in atomic percent is calculated through MULTIPAK software. The same Mo concentration can be calculated based on the formula:

$$a_i = \frac{I_i}{ASF} / \sum_i I_i / ASF \quad 3.3$$

Where a is the atomic concentration, I is intensity or more precisely area under the curve and $A.S.F.$ is the atomic sensitivity factor of the respective element.

The atomic concentrations of various reduced Mo states treated at 900 °C are listed in table 3-2.

Table 3-2 Oxidation state and quantitative analysis of respective phases of Mo in LAMOX treated in Ar-H₂ atmosphere at 900 °C.

Sintering temp. (°C)	Mo atomic concentration (%)				
	6+	5+	4+	3+	0
900	23.66	42.09	18.27	10.83	5.15

The table clearly shows that at sintering temperature 900 °C, the Mo⁶⁺ stabilisation has not been achieved. Good percentages of other reduced Mo have been found, and they are sufficient enough to cause electronic conductivity in the compound apart from the ionic conductivity. Unfortunately, this electronic conductivity is highly undesirable for the fuel cell operation which may degrade the cell performance. The stability of Mo⁶⁺ may be achieved by lowering the operating temperature of the cell, but the ionic conductivity will be reduced. Therefore, one has to compromise between the operating temperature and conductivity value. Thus, the effect of reductive atmosphere on LAMOX has been successfully studied through XPS analysis and the results obtained here are in agreement with the previous literatures on LAMOX [Khaled et al., 2012; Jin et al., 2007].

3.6 Conductivity studies of LAMOX sintered in air and Ar-H₂ atmosphere

Figure 3-8 shows the complex impedance plot of LAMOX treated in air atmosphere at 300 °C, 350 °C, and 400 °C. The plot clearly shows three distinct parts in the curve. The first segment is due to the grain interior part, second segment of grain boundaries, and the third part is due to the electrode.

The complex impedance can be written as

$$Z^* = Z' + jZ'' \quad 3.4$$

where $Z' = R$ and $Z'' = 1/j\omega C$ are real and imaginary parts of the impedance.

This depressed semi-circular plot of complex impedance can be shown in terms of the RC parallel circuit. The overall impedance for one RC parallel circuit can be estimated following the equivalent circuit configuration given in figure 2-10 of chapter 2. The overall complex impedance may be written as:

$$\frac{1}{Z^*} = \frac{1}{R} + \frac{1}{X_c} \quad 3.5$$

$$|Z^*| = \frac{RX_c}{\sqrt{R^2 + X_c^2}} \quad 3.6$$

The semi-circular plots between Z'' vs. Z' in figure 3-8 represent the depressed semi-circle showing non-debye type relaxation behaviour [Paul 2014]. A non-debye relaxation may be defined as a dielectric component having more than one relaxation time represented as τ . The relaxation time may be defined as the time taken by the dipoles to orient them in the direction of the applied electric field. More detailed analysis and explanation on this aspect are presented in the subsequent chapters of the thesis. At lower frequencies of applied ac voltage, the oxide ion and vacancies have sufficient time to migrate through the electrode-electrolyte interface. As a result, the oxide ions-vacancies which are migrated across the interface get accumulated, creating a space charge barrier. This resistance appears in the form of a linear curve at the lower frequency side of the applied ac voltage. Also, at the electrode/electrolyte interface, cross ion diffusion occurs which leads to the formation of resistive phases across the interface eventually blocking the transport of oxide ions. This blocking of oxide ions-vacancies can be seen in Nyquist plot in figure 3-9 and 3-10. The blocking effect and interfacial resistance are more dominant in the case of reduced LAMOX sample, as seen in figure 3-10. This can be explained by large extent of the electrode and porous LAMOX interface which may have resulted in resistive layer formation [Mei et al., 2018; Pornprasertsuk et al., 2007; Kumar 2018].

The short and long-range hopping of oxide ions through the vacant sites and their jump probability can be explained on the basis of modulus formalism. The imaginary part of modulus formalism explains the nature of oxide ion hopping (short or long-range) with the variation in temperature. The detailed analysis has been presented in section 4.6 of the next chapter.

After the calculation of the conductivity from the impedance plot, the dc conductivity values have been plotted as a function of temperature and are shown in figure 3-9(d). The conductivity values obtained are of α - LAMOX which has low conductivity as reported by other researchers [Lacorre 2000b]. It shows the ordering of the vacancies leads to low conductivity, as evident from the figure 3-9(d). The dc ionic conductivity at 400 °C is 16 μ S/cm. Therefore, the room temperature phase of LAMOX has a poor conductivity and cannot be utilised as an electrolyte in fuel cell application. The ionic conductivity (dc) was calculated with the help of intercept of the curve on the x-axis by the formula $R = \rho l/A$, where R is the real part of the impedance, ρ the

resistivity, l and A is the thickness and area of the pellet respectively. The inverse of the resistivity is the conductivity.

The real part of complex impedance $Re(Z)$ for the three different temperatures and respective dc conductivity values are listed in **table 3-3**.

Table 3-3 Values of $Re(Z)$ and dc conductivity of air treated LAMOX at various temperatures.

Temperature ($^{\circ}C$)	$Re(Z)$ (Mega ohms)	σ_{dc} (S/cm)
300	0.3511	$06.866 \cdot 10^{-7}$
350	0.6781	$3.553 \cdot 10^{-6}$
400	0.1532	$1.5725 \cdot 10^{-5}$

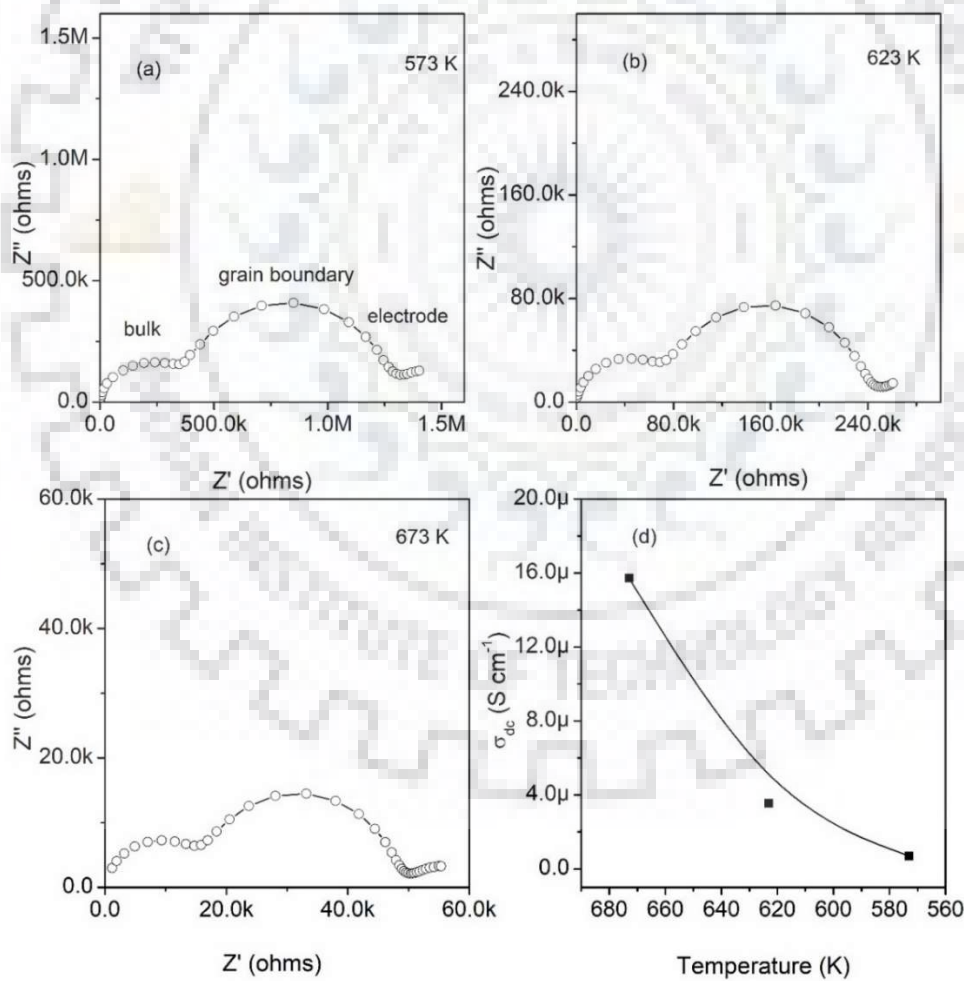


Figure 3-8 Complex impedance plot for LAMOX at (a) 573 K, (b) 623 K, (c) 673 K. (d) dc conductivity plot for LAMOX. The Y-axis shows conductivity values in $\mu S/cm$.

The value of activation energy E_a calculated on the basis of the following formula can be written as

$$\sigma_{dc} = \sigma_0 \exp\left(-\frac{E_a}{kT}\right) \quad 3.7$$

where σ_0 is the pre-exponential factor, E_a is the activation energy, k is the Boltzmann constant and T is the absolute temperature. By applying logarithm on both sides of the equation, it can be treated as a straight line of which negative slopes give activation energy, and y-intercept gives the σ_0 value. E_a and σ_0 can be estimated from the plot of $\ln \sigma_{dc}$ vs. $(1/T)$.

The activation energy E_a is around 1 eV. The logarithmic plot has not been shown here because of less number of points but yields the approximate value of E_a in this case.

Grain boundary conductivity plays a vital role in the overall electrical conductivity in ceramic electrolytes [Guo 1995; 2001a; 2001b; 2003; 2006; Lin et al., 2015]. According to Baurele [1969], the application of impedance spectroscopy of YSZ electrolytes has provided a very useful technique to analyse grain interior and grain boundary conductivities. According to the theory, the grain boundary is considered to act as a barrier for oxide ion migration. The enhanced resistance offered by the grain boundaries to oxide ion movement is called as grain boundary blocking effect. Impurities such as dopants at the grain boundary, the large volume fraction of grain boundaries contribute to the grain boundary resistance. The grain boundary consists of two adjacent space charge layers along the grain boundary core. The depletion of the oxide ions in the space charge region contributes to large ionic resistance in the material.

As previously mentioned, the total resistivity of the LAMOX is the sum of two arcs of the Nyquist plot which represents the grain interior and grain boundary resistivity, respectively. According to the bricklayer model, grain boundary thickness and specific grain boundary conductivity can be calculated. The specific grain boundary conductivity which is an average conductivity of the grain boundary, can be expressed as [Martin and Mecartney 2003]:

$$\sigma_{sp.gb} = \left(\frac{\delta}{d}\right)\sigma_{total gb} \quad 3.8$$

where δ is the grain boundary width, d is the grain size, and $\sigma_{total gb}$ is the total grain boundary conductivity.

The grain boundary width (δ) can be calculated as

$$\delta = d \left(\frac{C_1}{C_2} \right) \left(\frac{\epsilon_{gb}}{\epsilon_{interior}} \right) \quad 3.9$$

where C_1 and C_2 are the capacitances of grain interior and grain boundary obtained from impedance values, ϵ_{gb} and $\epsilon_{interior}$ are the permittivity values of grain boundary and grain interior, respectively. In the present study, it is assumed that ϵ_{gb} and $\epsilon_{interior}$ are similar, i.e., $\epsilon_{gb} \sim \epsilon_{interior}$.

According to the previous studies, the $\epsilon_{interior \text{ or } bulk}$ value of LAMOX and K= 2.5 mol % doped LAMOX is approximately 100 [Sandler 2010; Wang et al., 2005]. The similar values of permittivity of K doped LAMOX and pristine LAMOX show that dielectric value is composition independent. Therefore, ϵ_{gb} and $\epsilon_{interior \text{ or } bulk}$ are considered similar for grain boundary width calculation [Steil et al., 1997].

Permittivity implies the ease of polarisation of a medium. Since the grain volume is much larger than the grain boundary volume in the polycrystalline LAMOX, it implies large numbers of dipoles are present in the grain interior as compared to that in the grain boundary. Therefore, the effective polarisation (dipole moment per unit volume) and correspondingly permittivity of the grain and grain boundary of LAMOX material are justified to be considered nearly the same.

Polarisation is defined as dipole moments per unit volume. The relation between polarisation and permittivity may be written as

$$P = \epsilon_0 \cdot \chi \cdot E \quad 3.10$$

where ϵ_0 is the permittivity of free space, χ is the dielectric susceptibility of the material and E is the electric field applied.

$$\chi \text{ may be written as } \epsilon_r - 1. \quad 3.11$$

The validation of this approximation has also been experimentally proved for acceptor doped SrTiO₃ in which ϵ_{gb} was calculated as 0.95 $\epsilon_{interior \text{ or } bulk}$ values [Steil 1997; Vollman 1994].

From the FE-SEM images, the value of grain size is approximately 1000 nm. The C_1/ C_2 ratio obtained is 0.0146. Using equation 3.9, the value of δ comes out to be 14.6 nm. This value is in agreement with the results obtained and mentioned elsewhere [Martin and Mecartney 2003]. Putting the values of δ in equation 3.8, the value of $\sigma_{sp. gb}$ equals to 0.014 $\mu\text{S/cm}$. All the calculations have been done for complex impedance data obtained at 300 °C (573 K). The obtained grain boundary conductivity is two orders less than the total ionic conductivity. The low value of electrical conductivity is the main drawback of the monoclinic phase of La₂Mo₂O₉.

According to the grain boundary easy path model, there are two paths for the oxide ions to pass through a grain boundary. Firstly, they can migrate through the grain boundary, which requires higher activation energy than the bulk values. Secondly, the oxide ions can migrate through the paths known as easy paths that have the same activation energy as that of the bulk [Lilley 1979].

The effect of grain boundaries on conductivity can also be explained on the basis of the '*Brick Layer Model*.' In this model, the grains are assumed in the form of cubes with edge length '*D*' and grain boundary thickness as '*d*'. The total volume fraction of the grain boundaries may be written as $3d/D$. The applied sinusoidal current is perpendicular to the electrode faces at both ends giving rise to two plausible paths for ion conduction, namely: either through the grain interior and through one of the horizontal grain boundaries or through the vertical grain boundaries [Macdonald 1987].

After studying the conductivity of LAMOX treated in air, the effect on the conductivity in the presence of Ar-H₂ atmosphere has been discussed. The LAMOX sample has been treated in diluted H₂ atmosphere for the conductivity measurement. Figure 3-9 shows the complex impedance plots at 100 °C, 150 °C, and 200 °C under reducing atmosphere. The curves are of depressed semi-circular and intercept the real *Z*-axis giving the real part of the resistance. The electrode impedance in figure 3-10 has shown some irregular trend which may be due to the diffusion of electrode paste in the porous LAMOX material. From the real part of impedance value and geometry of the pellet (*d* = 11.65 mm and *t* = 1.47 mm), the conductivity can be calculated by using the formula: $R = \rho t/A$, where ρ is the resistivity, *t* is the thickness, and *A* is the surface area of the pellet.

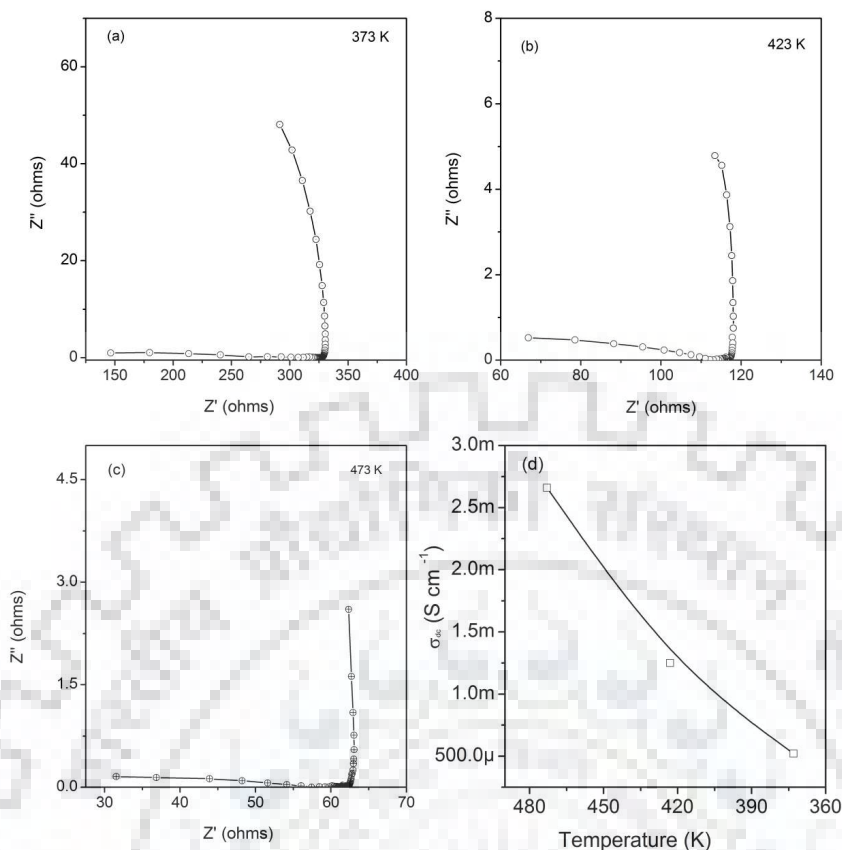


Figure 3-9 Complex impedance plots for LAMOX at (a) 373 K, (b) 423 K, (c) 473 K (d) D.C conductivity plot for LAMOX sintered in diluted H_2 atmosphere at 900 °C.

From figure 3-8(d) and figure 3-9(d) it is evident that the LAMOX sample sintered under $Ar-H_2$ (diluted) atmosphere shows three orders of higher conductivity than the air treated LAMOX samples. The reason for such a high electrical conductivity may be attributed to the introduction of electronic conductivity due to Mo reduction to lower oxidation states. This reduction of Mo leads to loss of oxygen from the lattice site.

The porosity of the reduced LAMOX samples has an important effect on electrical conductivity. With an increase in sintering temperature in the air atmosphere, the porosity of the pellets reduces, thereby giving high values of electrical conductivity. But for the reduced LAMOX samples, the conductivity is much higher as compared to air treated LAMOX samples because of the contribution of a high electronic conductivity from Mo reduction. The higher the porosity is, the higher is the conductivity. This is due to the higher ceramic/gas interface in the case of porous LAMOX samples [Goel et al. 2011].

Basically, the enhancement of the conductivity is the combined effect of ionic and electrical conductivities. The amorphous LAMOX has a disordered structure and hence the vacancies are also disordered. This combined effect gives rise to a high value of overall conductivity.

3.7 Summary

The effect of air and Ar-H₂ (reductive) treated La₂Mo₂O₉ at different sintering temperature has been studied by means of x-ray diffractometer (XRD), field emission scanning electron microscope (FE-SEM), x-ray photoelectron spectroscopy (XPS) and impedance analyser (spectroscopy) (IS) studies.

The XRD pattern at room temperature reveals that the crystal structure has monoclinic symmetry with space group P2₁. This room-temperature phase is of low ionic conductivity. The LAMOX sample treated under Ar-H₂ atmosphere turned out to be amorphous at 700 °C, though not verified here in the chapter. At this temperature, the LAMOX gets converted into (La₇Mo₇O₃₀)₇₇₃₀ phase in which oxygen loss from the lattice site occurs.

The electron microscopy data reveals dense and coarse grain morphology of air treated samples. Some pores are observed at the grain boundary. The reduced samples show intra-granular pores as a result of the interaction of the LAMOX particle and H₂ gas atmosphere. This porous nature of the samples can be exploited in the anodic application, as mentioned in the literature [Goutenoire et al., 1999] since they are sulphur tolerant and provide excellent catalytic properties.

The XPS analysis of LAMOX sample treated in Ar-H₂ atmosphere reveals Mo⁶⁺ reduction to a large extent at 900 °C. It gives a good insight of the compound whether to be used as an electrolyte in solid oxide fuel cells at high/intermediate temperatures but at the cost of electronic conductivity. This high temperature plays a significant role in the degradation of the fuel cell performance caused by the Mo reduction to lower oxidation states. Whereas, the sample treated in air shows no oxidation state change of the respective elements in LAMOX. The Mo⁶⁺ content is found to be almost 25 atomic percent when the sample is treated at 900 °C in Ar-H₂ atmosphere. The reduction of Mo to lower oxidation states is the critical factor in limiting the LAMOX electrolytes in commercial SOFC applications.

The complex impedance spectroscopy data of air and Ar-H₂ atmosphere treated LAMOX samples show a huge difference in ionic conductivity. This is attributed to the introduction of the electronic conductivity of the sample in the Ar-H₂ treated sample. The observed value for the Ar-H₂ treated sample is around 3 x 10⁻³ S/cm as compared to air-treated sample which is 16 x 10⁻⁶

S/cm. The ionic conductivity enhancement is of three orders magnitude. The impedance spectroscopy data for the LAMOX compound treated in air shows two semi-circles corresponding to the grain interior and grain boundary region. The impedance plots of LAMOX treated in Ar-H₂ condition shows a highly depressed semi-circle and low resistance due to electronic conductivity in the sample. The width of grain boundary and specific grain boundary conductivity obtained from the EIS study of air treated LAMOX samples equals 14.6 nm and 0.014 μS/cm, respectively. Specific grain boundary conductivity obtained is almost two orders of magnitude less than the grain interior conductivity. The existence of grain boundary resistivity is responsible for low value of ionic conductivity of the monoclinic phase of LAMOX.

The primary purpose of LAMOX in this context is of electrolyte in fuel cells. However, the low value of electrical (ionic) conductivity due to grain boundary resistance, Mo reduction in Ar-H₂ atmosphere, and high thermal expansion coefficient during the phase transition may lead to the overall degradation of the fuel cell. Therefore, to overcome all these drawbacks encountered in LAMOX, the strategy of doping has been introduced and studied extensively in subsequent chapters to make the LAMOX as an electrolyte material more useable and practical in solid oxide fuel cell application.

Chapter 4

Doping effects on $\text{La}_2\text{Mo}_2\text{O}_9$ treated in air and reductive atmosphere

4.1 Introduction

As discussed in the previous chapter, the drawbacks of pure LAMOX is very likely to affect the working of the fuel cell under its normal (reducing) operating condition. In this chapter, hexavalent dopants viz. W^{6+} at Mo^{6+} site, rare earth elements like Gd, Y, Sm, Eu, and K^{1+} at La site have also been doped to tailor the properties of $\text{La}_2\text{Mo}_2\text{O}_9$ for better electrolyte performance. The basic purpose of these dopants is to eliminate the drawbacks like phase transition which causes the abrupt volume change, Mo reduction stabilisation under reductive atmosphere and enhancing the ionic conductivity of the electrolyte along with the reduction in the operating temperature.

The effect of these dopants has been studied by x-ray diffraction, field emission-scanning electron microscopy, x-ray photoelectron spectroscopy, and complex impedance spectroscopy. Though many authors have reported the effect of doping in LAMOX and studied the structural effects, the reduction study by XPS analysis has not done in detail which reveals a lot of information [Corbel et al., 2005; Goutenoire et al., 2001; Georges et al., 2005; 2006; Lopez et al., 2005; Wang et al., 2008; Jin et al., 2007; Voronkova et al., 2009]. Therefore, the main focus of this chapter is on Mo stabilisation in reductive condition and its study by means of x-ray photoelectron spectroscopy and the ion dynamics study along with XRD, Rietveld analysis, microstructural analysis.

T.Y. Jin and co-workers have shown that Mo reduction has been successfully suppressed by doping of Dy and W at La and Mo sites, respectively. Later in the chapter, it has been shown that the results obtained by same doping composition are different from that of the result obtained by Jin et al., 2007. The Mo stabilisation result obtained by W doping at Mo site which has been able to suppress the Mo reduction though not fully, but to an extent which is believed not sufficient for normal operation of the fuel cell. On the other hand, doping of K^{+} at La site has been proved to be very effective in suppressing Mo reduction in the presence of Ar- H_2 atmosphere.

We can broadly classify the chapter into three following subsections:

- i) effect of W doping at Mo site.

ii) effect of K doping at La site.

iii) effect of rare earth elements doping at La site and W doping at Mo site.

The structural stability of $\text{La}_2\text{Mo}_{2-x}\text{W}_x\text{O}_9$ is well reported by many researchers but its photoelectron spectroscopy studies, structural study of W doped LAMOX treated in Ar-H₂ atmosphere on and ion dynamics is not reported in detail. Here, these studies have been done on W doped $\text{La}_2\text{Mo}_2\text{O}_9$ composition in the temperature range of 300 – 400 °C. $\text{La}_2\text{Mo}_2\text{O}_9$ is doped with W^{6+} in the range of $0.25 \leq x \leq 1.5$ (x being the mole fraction of W) at Mo^{6+} site. One such study of W doped LAMOX has been done by G. Corbel and team members [Corbel et al., 2005]. They have successfully stabilised the high-temperature cubic phase at room temperature, but they have not shown the effect of W doping on the stabilisation of Mo^{6+} in reductive atmosphere. Here the W has been doped at 0.25-mole fraction (12.5 mol %) increment starting from LAMOX to 1.75-mole fraction.

4.2 Effect of W doping at Mo site in $\text{La}_2\text{Mo}_2\text{O}_9$

4.2.1 X-ray diffraction studies on $\text{La}_2\text{Mo}_{2-x}\text{W}_x\text{O}_9$ sintered in air atmosphere

Figure 4-1 shows the room temperature x-ray diffraction pattern of $\text{La}_2\text{Mo}_{2-x}\text{W}_x\text{O}_9$ (W-LAMOX). From the figure, it is evident that with the increased W doping, the crystal structure remains cubic and the cell parameter increases for the doping level up to 25 mol % W and reduces thereafter up to 75 mol % W doping. The W- LAMOX maintains a cubic phase up to 62.5 mol % of W doping. Further addition of W at Mo site yields a two-phase product which is identified as β - $\text{La}_2\text{Mo}_2\text{O}_9$ and α - $\text{La}_2\text{W}_2\text{O}_9$, which are also confirmed by the presence of the large number of multiple peaks in XRD pattern. The W has a good solubility of about 75-80 percent in the LAMOX at Mo site because of their similar ionic radii and valency. The ionic radii of W^{6+} and Mo^{6+} are 0.6 Å and 0.59Å, respectively [Shannon 1976]. Since the difference in the radii is very small, they form a complete solid-solution. For W content up to 1.25, the formation of La_2MoO_6 as a minor impurity phase may be observed at 32.5°. This impurity phase is also observed in pure LAMOX phase mentioned in chapter 3.

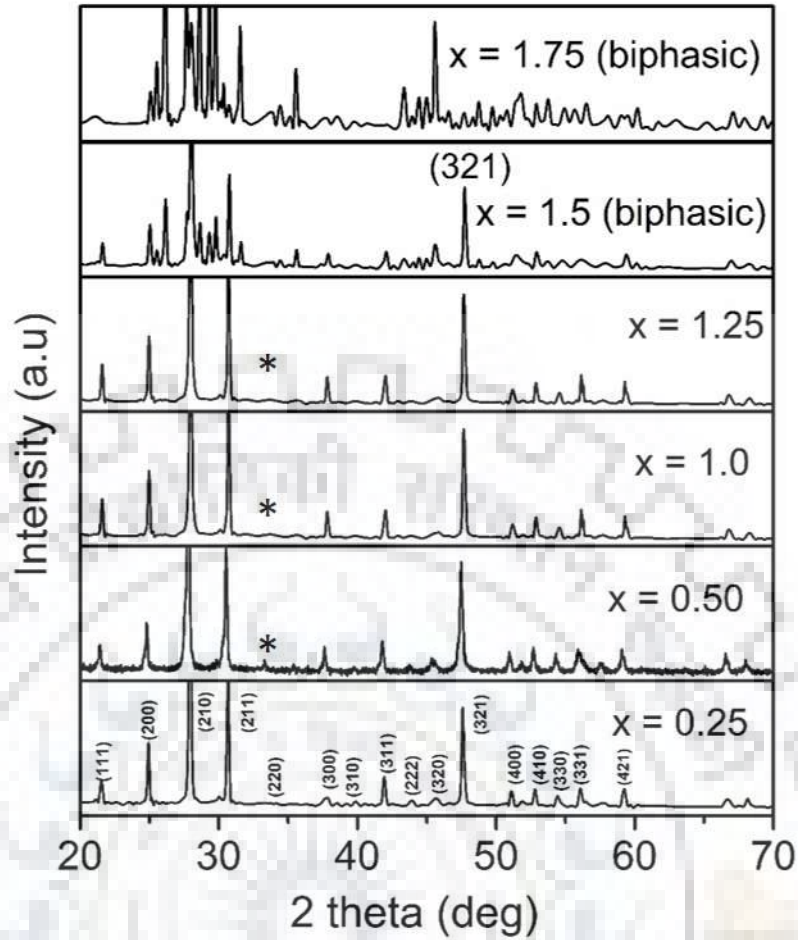


Figure. 4-1 Room temperature diffraction pattern of $\text{La}_2\text{Mo}_{2-x}\text{W}_x\text{O}_9$ in the range of $0.25 \leq x \leq 1.75$. The fewer reflection peaks correspond to higher symmetry, in this case, cubic symmetry with space group $P 2_13$. The impurity phase marked at 32.5° represents the La_2MoO_6 phase.

To further establish the existence of the cubic phase in W doped LAMOX, Rietveld analysis was done using X'pert high score plus software. The basis of Rietveld refinement [Rietveld 1967] is a least-square procedure which minimises the error that can be described by the following equation

$$S_y = \sum_i w_i (Y_i^2 - Y_{ci}^2) \quad 4.1$$

where Y_i is the observed intensity at a point i of the XRD pattern and Y_{ci} is the calculated intensity. The weight w_i can be defined as $w_i = Y_i^{-1}$, which is based on counting statistics.

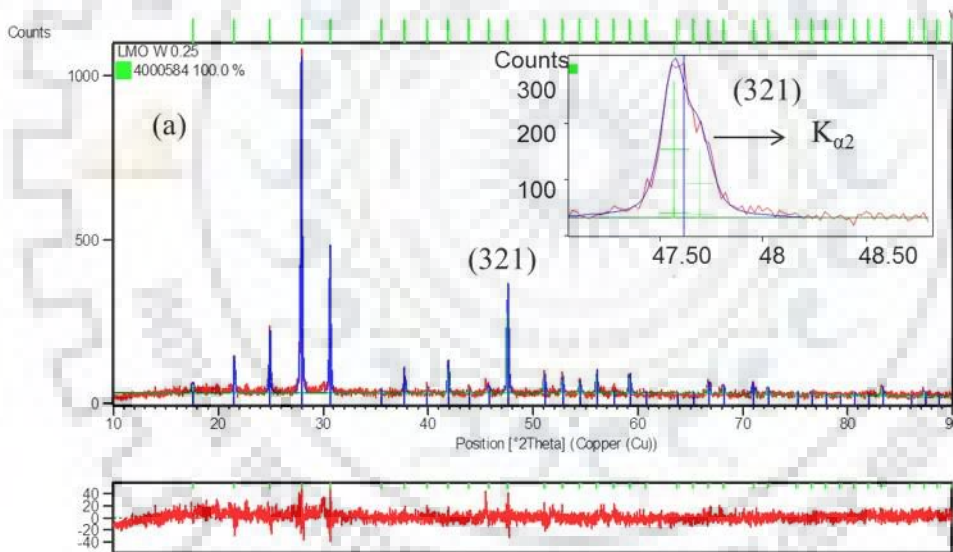
The pattern is refined with a constant scale factor and by pseudo-Voigt function. A large number of parameters are refined in order to obtain a good fit for model structure with the experimental pattern. According to the pseudo-Voigt profile function, the peak FWHM can be defined as

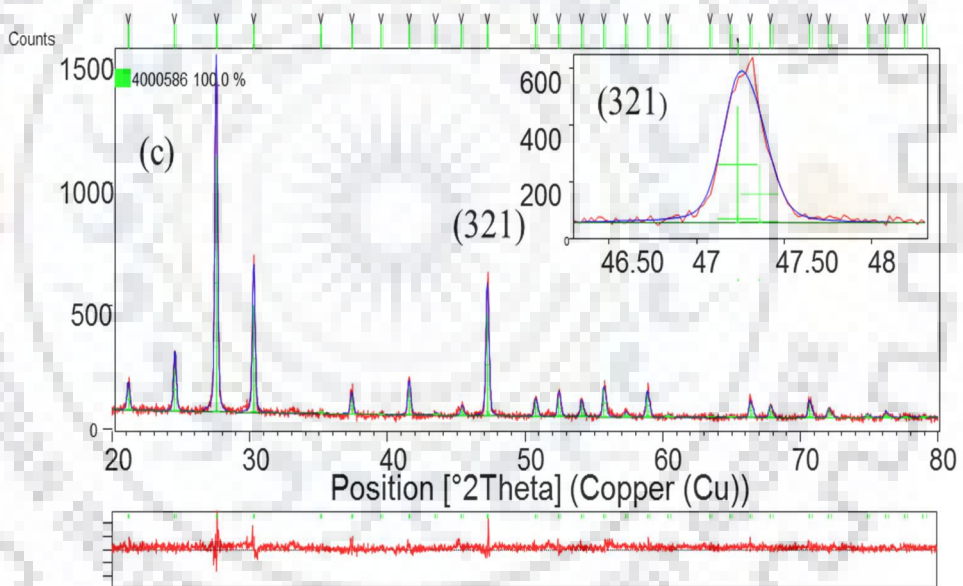
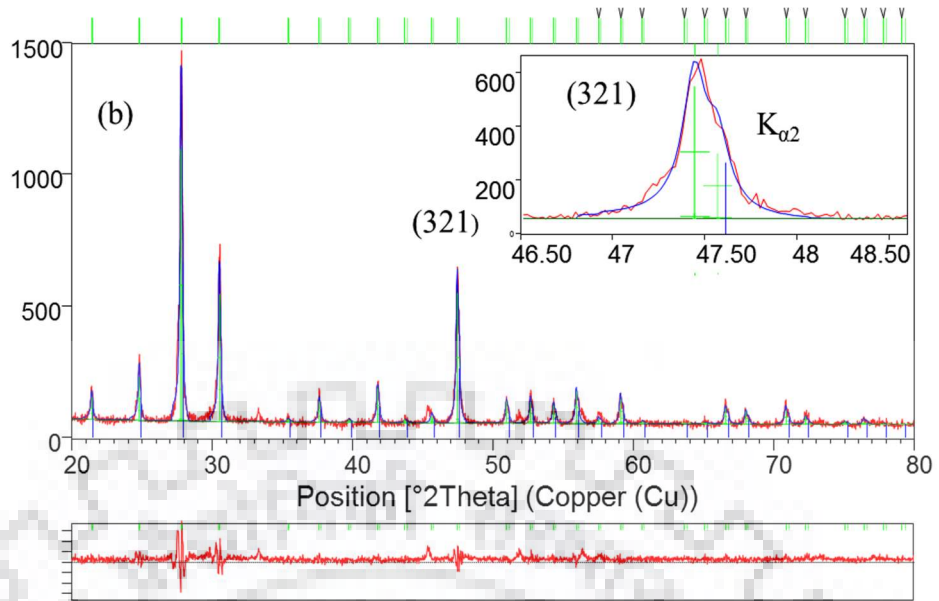
according to Caglioti [1958]. The goodness of fit for figure 4-2 was found to be less than two, indicating good profile fitting.

$$H_k^2 = U \tan^2 \theta + V \tan \theta + W \quad 4.2$$

where H_k is full width at half maximum (FWHM) of the k^{th} Bragg reflection and U , V and W are refinable parameters related to peak shape.

The Rietveld analysis in figure 4-2(a) shows that the (321) peak in the inset is slightly asymmetrical. This clearly suggests the distortion of the unit cell based on the changes in the bond length between its constituent ions. Inset of figure 4-2(a) also shows the $K\alpha_2$ effect on the peak as a hump on the right-hand side of the (321) peak. The reason for the asymmetric nature of (321) peak is that when W^{6+} ($r = 0.6 \text{ \AA}$) becomes dominant at the Mo^{6+} ($r = 0.59 \text{ \AA}$) site, due to bigger ionic radius it imposes a change in the hexavalent cation atmosphere which distorts the perfect cubic symmetry.





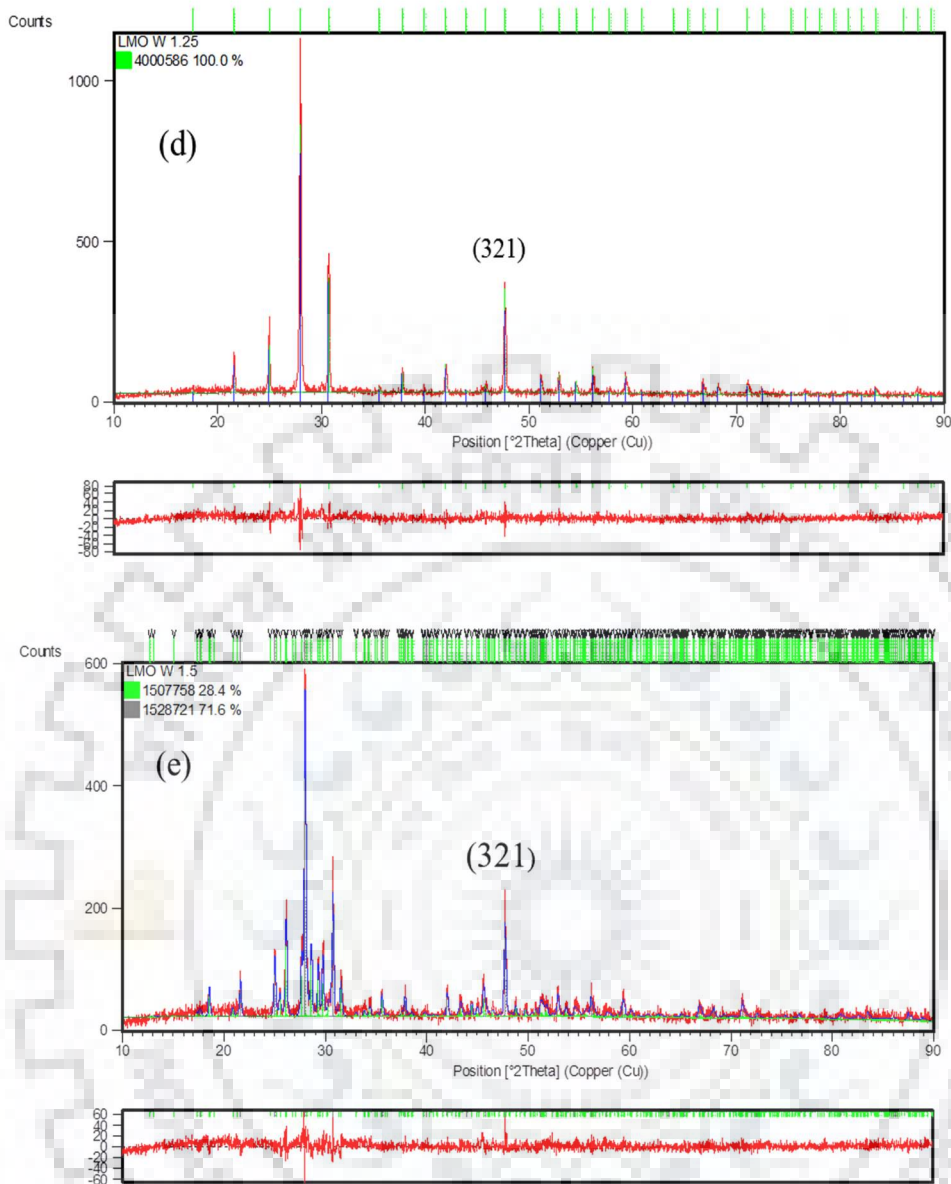


Figure 4-2 Rietveld refinement of (a) $x = 0.25$ (b) $x = 0.75$ (c) $x = 1.0$ (d) $x = 1.25$ and (e) $x = 1.5$ W doped $\text{La}_2\text{Mo}_{2-x}\text{W}_x\text{O}_9$ compositions. The inset figures in (a), (b), and (c) show the confirmation of the cubic nature of W doped LAMOX along with the $K\alpha_2$ effect.

In figure 4-2(e) at W content of 1.5-mole fraction and above the two-phase region is obtained. The second phase is found to be $\alpha\text{-La}_2\text{W}_2\text{O}_9$ (LWO), which is triclinic in nature. This second phase can be clearly understood from the XRD data which shows the extra peaks for W - LAMOX samples with $W > 1.25$.

The various parameters like oxide ion occupancy and lattice parameters obtained as the refinement result are plotted in figure 4-3. For refinement purposes, crystallographic information file (CIF) was used. From the various bond length data as shown in table 4-1, it is evident that

with the increasing amount of W doping in LAMOX, the various bond lengths have an average decreasing trend which ultimately has a similar consequence on lattice parameters.

Table 4-1 shows the various La-O bond lengths and lattice parameters of W doped LAMOX. For the addition of W = 1.5-mole fraction, LAMOX becomes biphasic in structure due to the formation of $\text{La}_2\text{W}_2\text{O}_9$ as the second phase, which gives rise to multiple peaks in the XRD pattern as confirmed. From the refinement of higher W doped LAMOX, the LWO phase is around 71.6 % as compared to β -LAMOX phase which is 28.4 %. Table 4-1 also shows that upon the refinement of the entire composition, one can find a regular variation trend of structural parameters with W content. The lattice parameters, oxygen site occupancy obtained from the refinement are plotted in figure 4-3. It is evident that with the increasing amount of W doping in LAMOX, the La-O bond length has an increasing trend (up to 0.5 mol fraction) firstly and further an average decreasing trend which corresponds to reduction in the La-O polyhedra which in turn has a similar consequence on lattice parameters. Another reason for the reduction of lattice parameters is that the introduction of W in the host lattice causes the nature of bonding to be slightly shifted from covalent to ionic oriented as compared to undoped LAMOX. The nature of bonding can be explained by the peak position of O 1s peak of W doped LAMOX compounds. Details have been outlined in section 4.3.2.

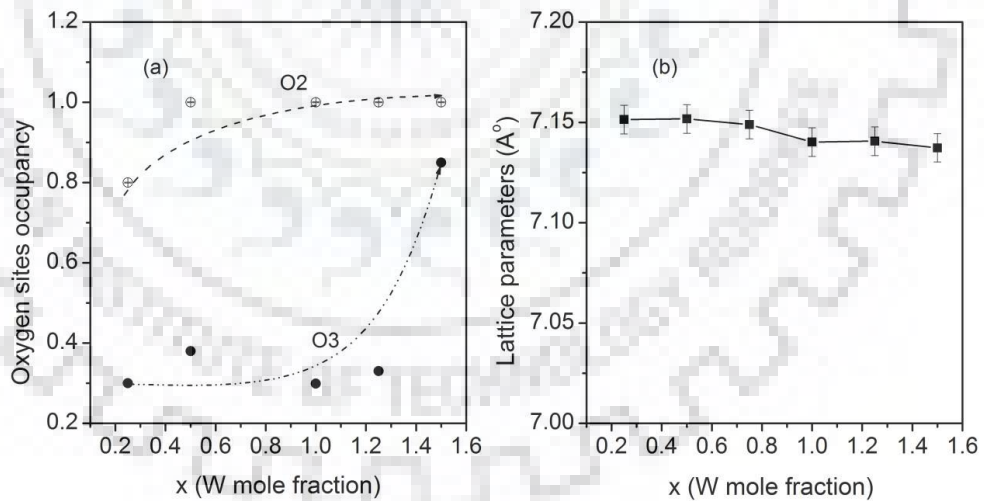


Figure 4-3 (a) Oxygen site occupancy of O(2) and O(3) atoms confirming the oxide ion vacancies in the lattice and (b) Lattice parameter obtained from XRD data room temperature by Rietveld analysis considering $P2_13$ space group.

Table 4-1 Bond lengths between various elements and lattice parameters of W doped LAMOX generated by Rietveld analysis using space group P2₁3. The standard uncertainty for bond lengths and lattice parameter has been shown in parenthesis.

x	0.25	0.50	0.75	1.0	1.25	1.5 (Bi phasic)
Bond length (Å)						
La-O3	2.942(4)	2.694(2)	2.417(3)	2.890(6)	2.111(3)	2.556(5)
La-O2	2.367(4)	2.506(6)	2.542(4)	2.356(7)	2.445(2)	2.573(4)
La-O1	2.614(7)	2.730(3)	2.676(8)	2.750(5)	2.550(5)	2.540(3)
Lattice parameters (Å)	7.1514(3)	7.1516(9)	7.1489(2)	7.1403(1)	7.1408(7)	7.1370(9)

Table 4-2 shows the different refined parameters by X'pert high score plus software of W doped LAMOX compositions. The parameters like fractional atomic coordinates, Wyckoff positions, oxygen atom occupancies, their coordinates have been refined and presented. The unoccupied oxygen atom coordinates, electron density, and closest atoms of the oxygen have been calculated from the difference Fourier analysis and is presented in table 4-3. A similar kind of study was done by Corbel et al., [2005] on the doping of W and Cr in LAMOX compositions. The results obtained by W doping in LAMOX are well in agreement with that obtained by Corbel and his co-workers. The lattice parameter did not match exactly but shows the similar decreasing trend along with increased W doping. Above x = 0.5-mole fraction doping at Mo site, the lattice parameter has a decreasing trend and O(1) site being fully occupied are some of the peculiar observations that are found to be in agreement with the above authors' results [Corbel et al., 2005]. Table 4-3 shows the position of unoccupied oxygen atom coordinates, electron density and Wyckoff positions of different oxygen atoms.

Table 4-2 Refined crystal structure parameters (sp. gr P 2₁3) of La₂Mo_{2-x}W_xO₉ from XRD data obtained at room temperature.

x		0.25	0.5	0.75	1.0	1.25	1.5
a (Å)		7.1514(3)	7.1516(9)	7.1489(2)	7.1403(1)	7.1408(7)	7.1370(9)
La (4a)	x	0.396(9)	0.385(9)	0.396(8)	0.393(6)	0.396(5)	0.404(4)
	Occupancy	1.00	1.00	1.00	1.00	1.00	1.00
	B _{iso}	0.5	0.5	0.5	0.5	0.5	0.5
Mo(4a)	x	0.081(1)	0.089(3)	0.087(2)	0.095(1)	0.092(4)	0.126(6)
	Occupancy	0.875	0.75	0.625	0.5	0.375	0.25
	B _{iso}	0.5	0.5	0.5	0.5	0.5	0.5
W (4a)	x	0.081(1)	0.089(5)	0.087(2)	0.093(9)	0.091(5)	0.098(4)
	Occupancy	0.125	0.25	0.375	0.5	0.625	0.75
	B _{iso}	0.5	0.5	0.5	0.5	0.5	0.5
O1(4a)	x	0.958(6)	0.986(9)	0.922(3)	0.993(5)	0.996(5)	1.009(1)
	Occupancy	1.00	1.00	1.00	1.00	1.00	1.00
	B _{iso}	0.5	0.5	0.5	0.5	0.5	0.5
O2(12b)	x	0.129(5)	0.152(8)	0.134(4)	0.140(8)	0.131(7)	0.133(7)
	y	0.529(5)	0.577(0)	0.575(2)	0.542(1)	0.540(9)	0.232(6)
	z	0.249(8)	0.244(0)	0.244(0)	0.243(4)	0.234(2)	1.0
	Occupancy	0.80	1.0	0.69	1.00	1.00	0.5
	B _{iso}	0.13	0.5	0.5	0.5	0.5	
O3(12b)	x	0.112(4)	0.129(7)	0.167(9)	0.065(3)	0.126(5)	0.055(2)
	y	0.166(1)	0.310(5)	0.303(8)	0.256(7)	0.249(1)	0.118(7)
	z	0.255(8)	0.135(2)	0.056(4)	0.137(1)	0.117(8)	0.391(5)
	Occupancy	0.30	0.38	0.47	0.299	0.33	0.850
	B _{iso}	1.971	1.7	1.53	1.0	1.0	1.0
R_{exp}		15.87	4.21	11.180	11.076	16.679	17.382
R_{wp}		20.193	6.77	15.383	13.053	18.750	19.859
G.O.F		1.618	2.578	1.892	1.388	1.263	1.305

Table 4-3 Unoccupied oxygen atom coordinates from difference Fourier analysis of $\text{La}_2\text{Mo}_2\text{O}_9$.

x	0.25	0.5	0.75	1.00	1.25	1.5
Unoccupied atom	O(2)/O(3)	O(3)	O(2)/O(3)	O(3)	O(3)	O(3)
x	0.408(4)	0.551(2)	0.399(4)	0.550(4)	0.395(6)	0.382(3)
y	0.408(4)	0.418(7)	0.404(9)	0.412(7)	0.398(9)	0.373(8)
z	0.408(4)	0.056(5)	0.059(9)	0.059(9)	0.417(6)	0.372(6)
Wyckoff position	12b	12b	12b	12b	12b	12b
Electron density	0.962	2.515	0.593	0.813	0.591	0.349
Closest atoms	2 La:0.119, 1 La :0.126	1Mo: 0.349 2 O3: 0.405	2 O3: 0.051 2 La :0.068	1 W: 0.984 1Mo: 0.984	1 La :0.111 2 La: 0.121	1W:0.349 2 O3 .096 1 La .238

The electron density in LAMOX crystal is shown in figure 4-4. Basically, the electron density in a crystal represents the structure of the crystal. Since the crystal has a three-dimensional periodicity, the electron distribution density $\rho(r)$ can be described by the Fourier series:

$$\rho(r) = V^{-1} \sum_h^{\infty} F_h \exp(-2\pi i h r) \quad 4.3$$

where V is the volume of the unit cell, r is a vector whose components locate a point inside a unit cell and h is a vector whose integral components points an imaginary plane that cuts through the crystal and F_h is the structure factor which may be written as:

$$F_h = |F_h| \exp(i\phi_h) \quad 4.4$$

The angle ϕ_h is the phase associated with F_h and $|F_h|$ is the maximum scatted amplitude of x ray wave from a segment of the crystal lying inside a unit cell [Karle 1991].

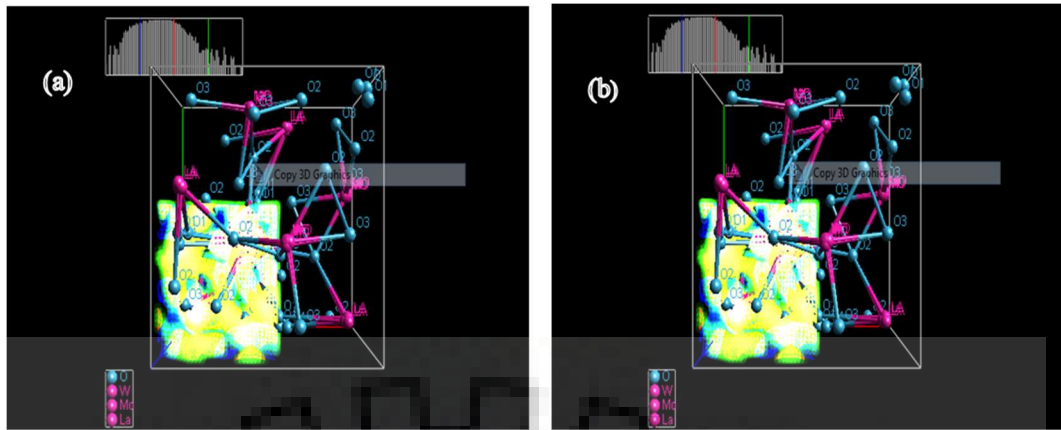


Figure 4-4 3-D electron density map of LAMOX.

4.2.2 Diffraction studies of $\text{La}_2\text{Mo}_{2-x}\text{W}_x\text{O}_9$ sintered in reductive atmosphere

This section deals with the diffraction studies under the effect of reductive atmosphere on W doped LAMOX. Diffraction studies of three W doped LAMOX compositions namely $W = 0.25$, $W = 1.0$ and $W = 1.25$ are presented along with the phase identification. Figure 4-5 shows the room temperature x-ray diffractogram of the three compositions mentioned above treated under Ar 90 % - H_2 10 % atmosphere at 900 °C for 6 hours in a tubular furnace with a flow rate of 2.8 l/h.

The XRD patterns of samples sintered in Ar- H_2 atmosphere are shown in figure 4-5. A large number of minor peaks clearly suggests the presence of intermediate phases. These intermediate phases or, so-called mixed molybdates are $\text{La}_5\text{Mo}_3\text{O}_{16}$ (PDF no. 04-006-4779), $\text{La}_5\text{Mo}_6\text{O}_{21}$ (PDF no. 04-011-9451), $\text{La}_{16}\text{Mo}_{21}\text{O}_{56}$ (PDF no.04-010-9577), which consist of mixed valance states of Mo further verified by XPS analysis in the later sections. The reason for the reduction of Mo^{6+} to lower states may be attributed to the intercalation of H atom at high temperatures between the layers comprising of MoO_6 octahedral that increases the interatomic distances between the octahedral layers [Sloczynski 2002]. This results in the formation of H_xMoO_3 bronzes, which in turn results in reduction of MoO_3 to MoO_2 . The reduction of Mo^{6+} to lower states and formation of secondary phases can be supported on the basis of oxygen loss from the host lattice and therefore, contribution to electronic conductivity in the material is explained.

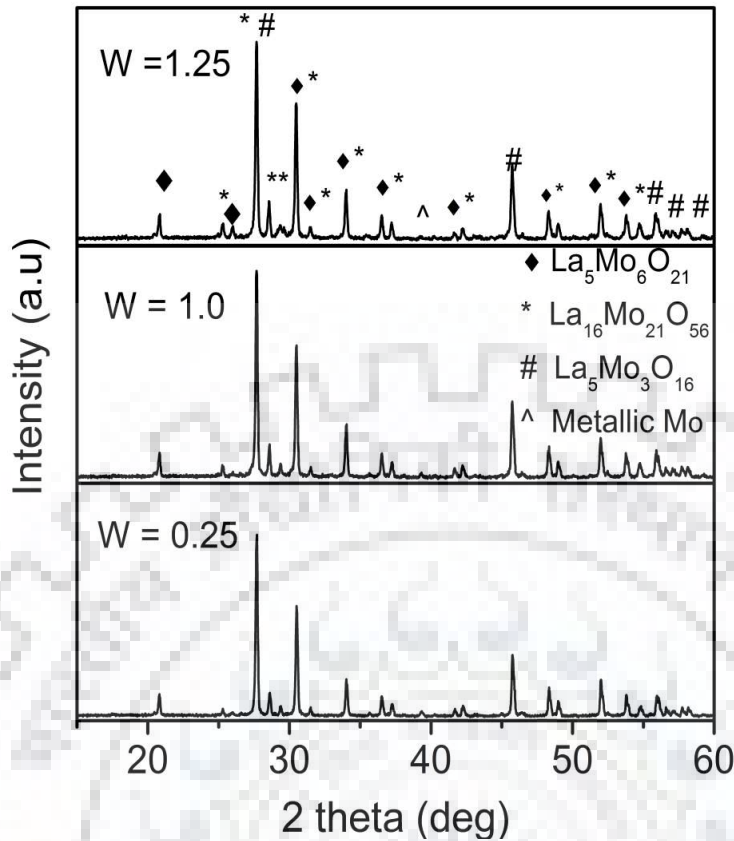


Figure 4-5 Room temperature XRD of Ar-H₂ sintered W doped LAMOX compositions and their intermediate products formed as a result of Mo reduction in Ar-H₂ atmosphere. The peaks of La₂Mo₂O₉ have not been shown because of the overlapping of peaks.

4.3 Microstructure observation by Field-Emission Scanning Electron Microscope (FE-SEM) of air and diluted H₂ treated W doped La₂Mo₂O₉

4.3.1 FE-SEM study of air treated W doped La₂Mo₂O₉

The physical appearance and microstructures of W doped LAMOX samples sintered in air are investigated by field emission scanning electron microscope (FE-SEM) and are shown in figures 4-6 and 4-7. The air sintered pellets show a reasonably dense packing of the grains. The air treated samples do not show any intra-granular pores, but show pores at grain boundaries. Before going in details of the microstructural analysis, figure 4-6 shows the images of the pellets of W doped LAMOX samples treated in air and reductive atmosphere. The air treated pellets can be seen as white or cream in colour, whereas Ar-H₂ treated samples were black or grey in colour. This change in colour of the pellets may be treated as physical verification of reduction of the Mo in the sample. The W = 1.75-mole fraction doped LAMOX sample sintered in Ar-H₂ atmosphere shows light grey colour suggesting a very less amount of Mo reduction in the composition.

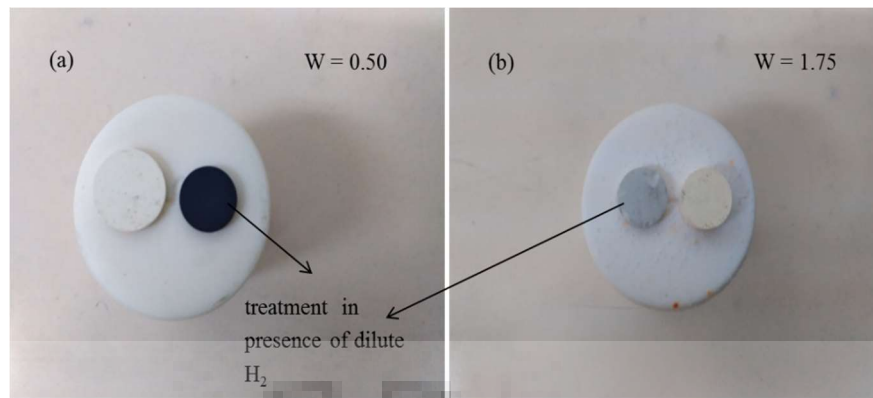


Figure 4-6 Images of (a) $W = 0.5$ doped LMO sample treated in air (white) and Ar- H_2 atmosphere (black). (b) $W = 1.75$ doped. H_2 treated sample was less reduced in the latter due to high amount of W in the host lattice.

The microstructural images in figure 4-7 (b), (c), and (d) show some pores at the grain boundaries indicating that coarsening mechanism dominates the densification and grain growth mechanisms. Generally, in coarsening, an increase in average grain size is accompanied by an increase in the average pore size. A detailed explanation has been provided in chapter III.

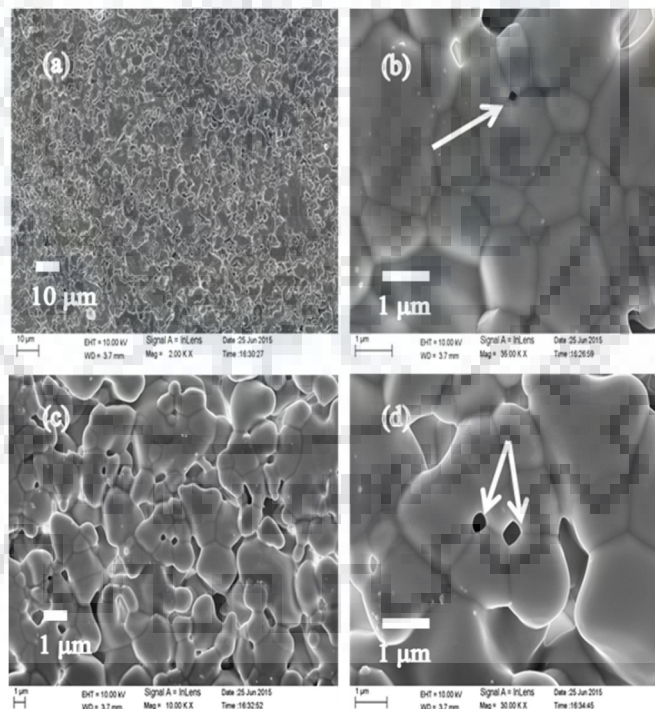


Figure 4-7 (a), (b), (c), and (d) Microstructures of air sintered $W 0.25$ doped LAMOX pellets for 4 hours. Arrows indicate the formation of pores at the grain boundaries.

4.3.2 FE-SEM study of Ar-H₂ treated W doped La₂Mo₂O₉

The microstructure of the Ar-H₂ heat-treated pellet in figures 4-8 and 4-9 show a significant amount of porosity as clearly revealed at the high magnification. The appearance of pores at the grain boundary and grain interior can be explained on the basis of gas-solid reaction models. One of the models introduced by Park and Levenspiel is described elsewhere [Schulmeyer 2001; Park 1975] and also a detailed explanation has been provided in chapter III. The first sign of reduction of samples can be verified by the colour change of samples from cream-yellow to dark grey, as shown in figure 4-6. The reduced samples are identified by the change of colour but this does not indicate the extent of reducibility.

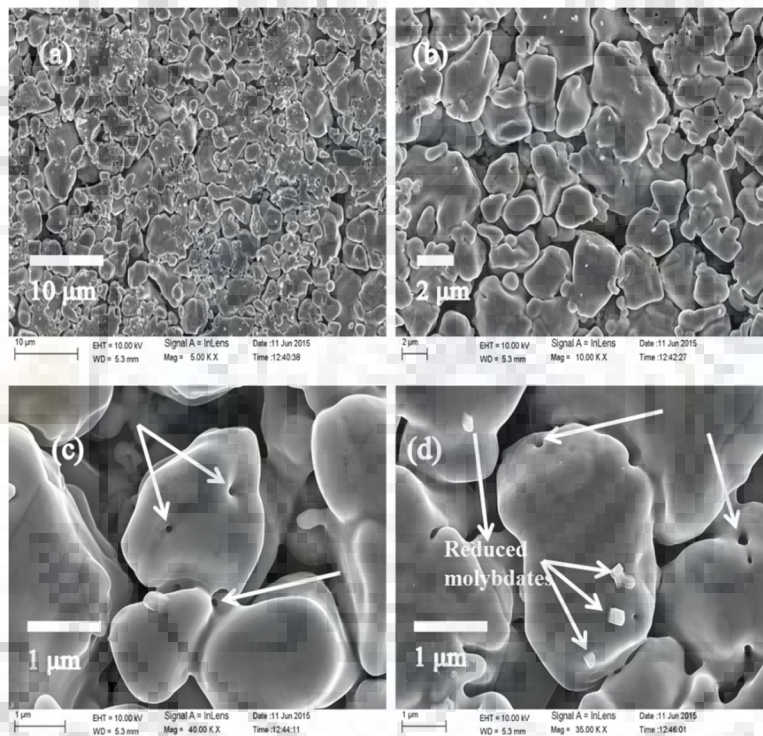


Figure 4-8 Microstructures for W 0.25 doped LAMOX treated in Ar 90 % - H₂ 10 %. The images clearly reveal the intra-granular porosity and formation of new products of reduced molybdates marked by arrows.

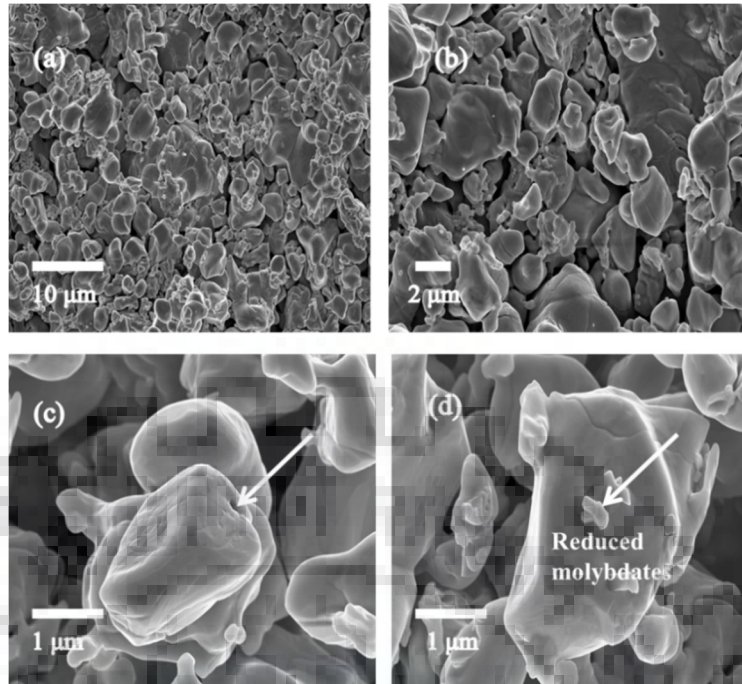


Figure 4-9 Microstructures for W 1.0 doped $\text{La}_2\text{Mo}_2\text{O}_9$ treated in Ar 90 % - H_2 10 %. The images clearly reveal the intra-granular porosity and formation of new products of reduced molybdates marked by arrows.

Also, from the morphological point of view, significant changes can be noticed by the microscopic studies as seen from the figure 4-8 and 4-9. Latter images show intra-granular pores which may be exploited in anode applications with $\text{La}_2\text{Mo}_2\text{O}_9$ type of electrolytes because of the gas permeation feature is present inherently. To confirm the electrical conductivity in these reduced compositions, the microstructures were captured by FE-SEM without carbon coating, as shown in figure 4-10 to 4-13. The samples which are conducting in nature have shown quite clear images whereas, the images of high W doped in figure 4-13 of W doped LAMOX show very low-quality images due to charge accumulation on the surface due to electron beam, since they do not get a continuous conducting path to dissipate the electrons.

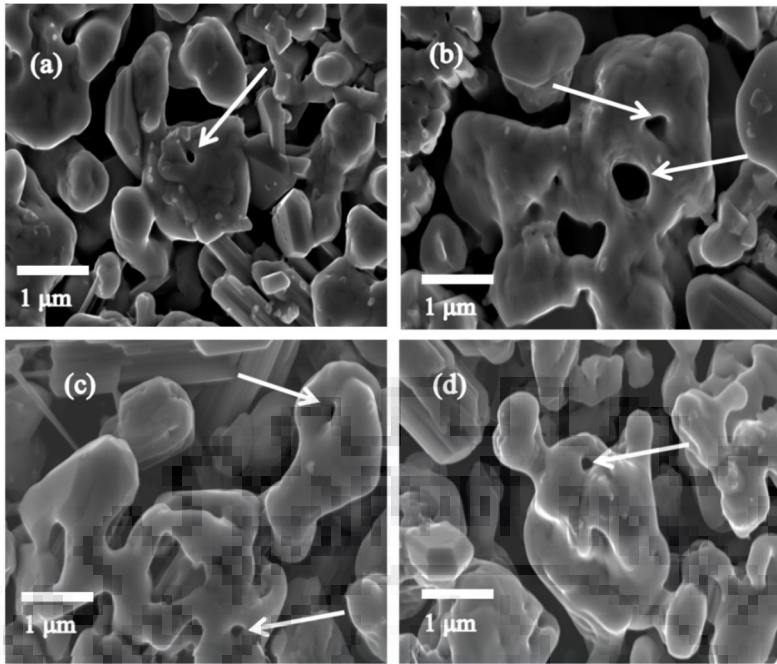


Figure 4-10 Microstructures for W 0.25 doped $\text{La}_2\text{Mo}_2\text{O}_9$ treated in Ar 90 % - H_2 10 % without conductive coating. The images reveal the intra-granular pores at high magnification marked by arrows.

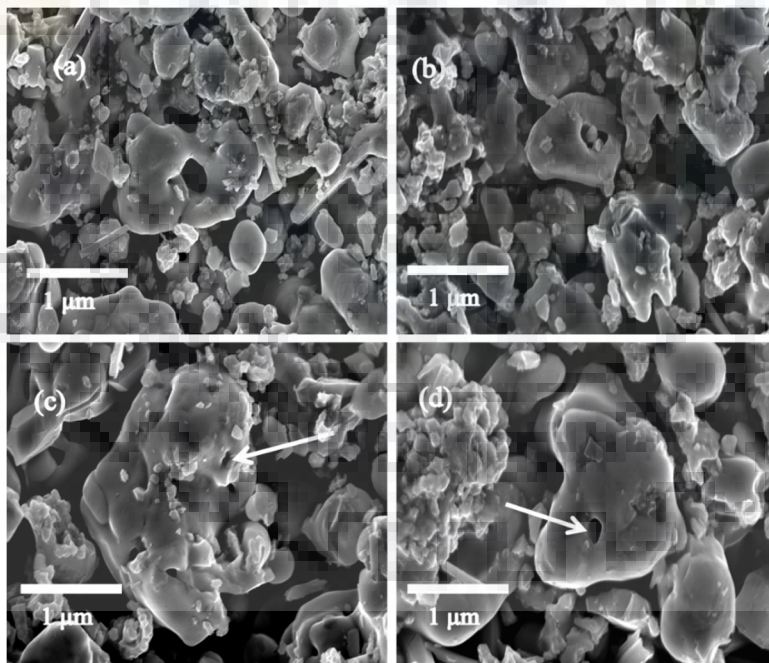


Figure 4-11 Microstructures for W 0.5 doped $\text{La}_2\text{Mo}_2\text{O}_9$ treated in Ar 90% - H_2 10% without conductive coating. The images reveal the intra-granular pore at high magnification marked by arrows and reduced molybdates.

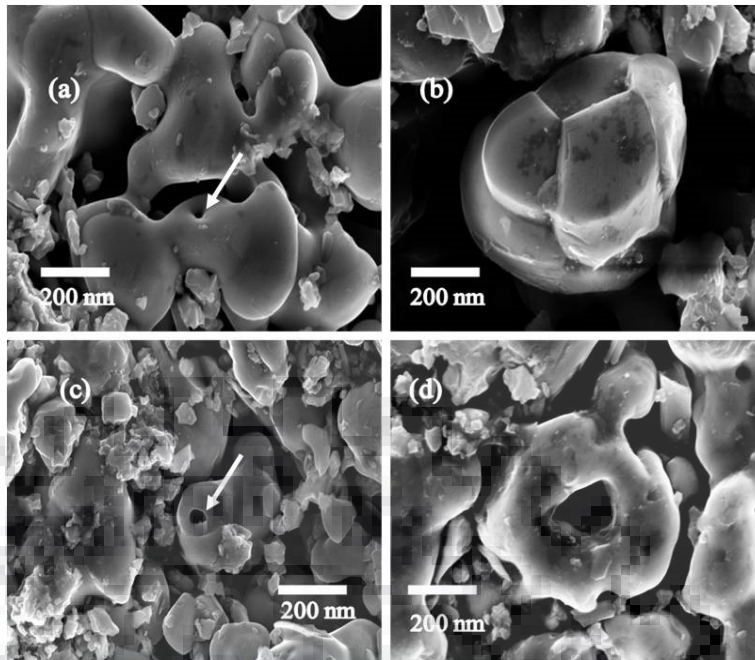


Figure 4-12 Microstructures for W 0.75 doped $\text{La}_2\text{Mo}_2\text{O}_9$ treated in Ar 90% and H_2 10% without conductive coating. The images reveal the intra-granular pore at high magnification marked by arrows.

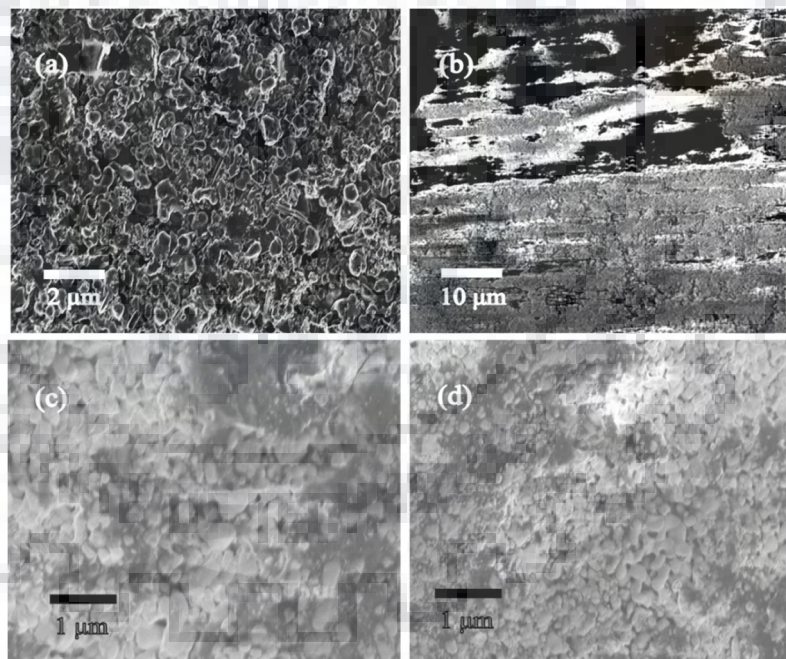


Figure 4-13 Microstructures for W 1.75 doped $\text{La}_2\text{Mo}_2\text{O}_9$ treated in Ar 90% - H_2 10% without conductive coating. The images reveal the charging effect due to the accumulation of electrons on the sample surface from the beam.

The microstructural aspect of Mo reduction in the W doped LAMOX has been verified by FE-SEM analysis. It has been confirmed from the XRD study that W doping in LAMOX is not

effective in stabilising the Mo^{6+} states in reductive atmospheres, which still is a problem for the operation of fuel cell utilising LAMOX kind of electrolytes. The next sub-section deals with the XPS study of W doped LAMOX treated in air and Ar-H_2 atmosphere.

4.4 Chemical state analysis by x-ray photoelectron spectroscopy (XPS) of air and Ar-H_2 sintered W doped LAMOX samples.

4.4.1 XPS studies of air treated W doped $\text{La}_2\text{Mo}_2\text{O}_9$ samples

As discussed in chapter I, the effect of the atmosphere on W doped LAMOX samples has been studied and analysed by means of x-ray photoelectron spectroscopy (XPS) for both air and reductive atmosphere treated samples. Figure 4-14 shows the survey spectrum of air sintered and Ar-H_2 sintered of $W = 0.25$ -mole fraction doped LAMOX composition collected at 187.5 eV pass energy over the binding energy range of 0 to 1100 eV with an x-ray probe diameter of 100 μm for elemental identification in the sample with adventitious carbon as reference C 1s at 284.5 eV [Moulder 1995].

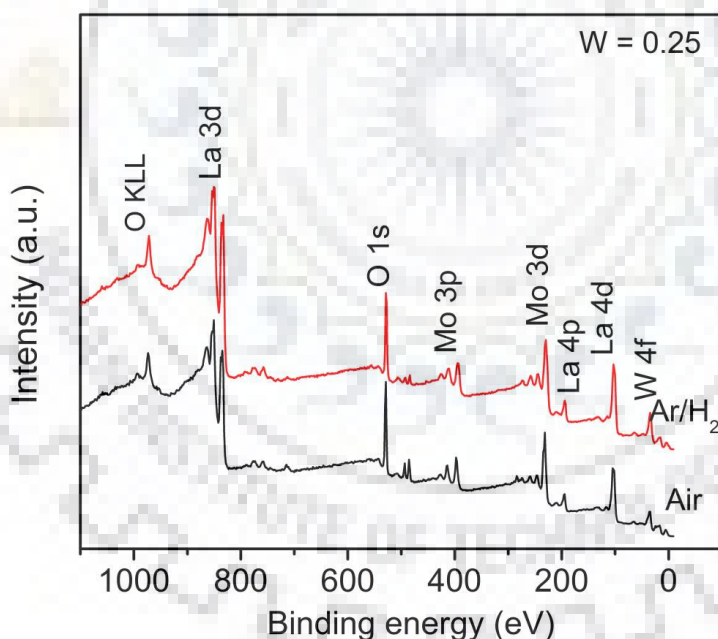


Figure 4-14 XPS Survey spectrum for $x = 0.25$ doped $\text{La}_2\text{Mo}_{2-x}\text{W}_x\text{O}_9$.

4.4.2 Core level analysis of La 3d spectrum of air treated LAMOX samples

Figure 4-15 shows the core level analysis of all the constituent elements of W doped LAMOX (x varying from 12.5 mol % to 100 mol %) collected at 11.750 eV pass energy for a better energy resolution. All the plots are presented in one set of the axis of individual elements for a better understanding of the doping effect.

From figure 4-15(a) it is evident that all La 3d spectra show a spin-orbit splitting giving rise to La 3d_{5/2} and 3d_{3/2} constituent peaks. The difference in energy of La 3d_{5/2} and 3d_{3/2} (ΔE) varies from 16.5 eV to 16.9 eV for all W doped compositions. Both La 3d_{5/2} and 3d_{3/2} peaks show clear doublet peaks due to multiple splitting. When compared with the standard La₂O₃ the La³⁺ in LAMOX does not show any further splitting which confirms the La³⁺ oxidation state in LAMOX. The energy gap values of E 3d_{5/2} - E 3d_{3/2} (spin-orbit splitting) for W doped LAMOX compositions sintered in Ar-H₂ atmosphere have been listed in the table 4-4. A detailed explanation of La 3d spectrum is provided in section 3.3.3 of chapter 3.

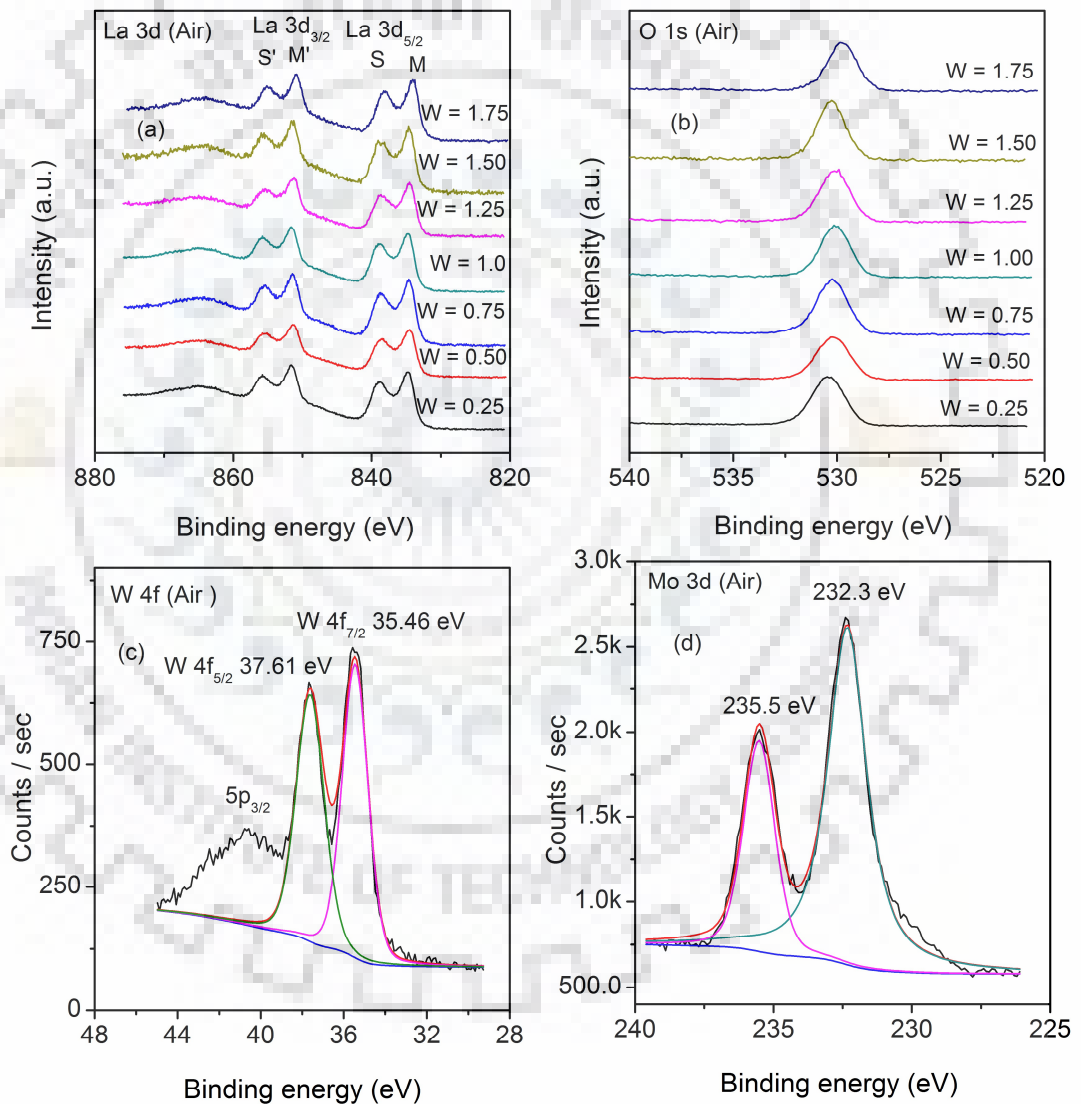


Figure 4-15 Core level spectra of W (0.25) doped La₂Mo₂O₉ (a) La 3d, (b) O 1s, (c) W 4f, (d) Mo 3d of W doped LAMOX samples treated in air. The Mo 3d and W core level show the natural splitting of the peak indicating the presence of a single 6+ oxidation state.

Table 4-4 La 3d_{3/2} and 3d_{5/2} binding energy difference values of W doped LAMOX compositions sintered in air and Ar/H₂ atmosphere.

W content	La 3d_{3/2} (eV)	La 3d_{5/2} (eV)	ΔE_j(air) (eV)	La 3d_{3/2} (eV)	La 3d_{5/2} (eV)	ΔE_j (Ar- H₂) (eV)
0.25	851.61	834.76	16.85	850.56	833.83	16.73
0.50	851.35	834.51	16.84	850.95	834.19	16.76
0.75	851.43	834.63	16.80	851.24	834.30	16.94
1.00	851.16	834.62	16.84	851.35	834.16	16.84
1.25	851.18	834.50	16.68	851.27	834.57	16.78
1.5	851.24	834.63	16.64	851.02	834.37	16.90
1.75	850.81	834.13	16.68	850.02	834.22	16.80
2.0	851.23	834.59	16.64	851.27	834.56	16.71

4.4.3 Study of O 1s, Mo 3d, and W 4f Spectra

The O 1s spectra for W doped LAMOX compositions sintered in air have been acquired and analysed as shown in figure 4-15 (b). The various peaks of O 1s spectra are found at 530.5 eV. But the positions of various O 1s peaks do not overlap with each other. As the W content increases in LAMOX, the O 1s peak can be noticed to shift towards the lower binding energy values, which is helpful in predicting the nature of bonding of W doped LAMOX compositions. As far as figure 4-16 is concerned, one can conclude that with increasing W content, the nature of bonding varies from semi covalent oxide (SCO) to normal ionic oxide (NIO) type for air sintered LAMOX samples. Whereas, for Ar-H₂ treated samples, the nature of bonding changes from very ionic oxide (VIO) to normal ionic in nature (NIO) with increasing W content. The nomenclature of various bonding nature mentioned above has been done with respect to the O 1s peak binding energy level and is described elsewhere in detail [Pawlak et al., 2002]. The binding energies of O 1s peaks for both the conditions are listed in table 4-5.

Table 4-5 Binding energies of O 1s peak of air and Ar-H₂ sintered W doped LAMOX compositions.

x (W mole fraction)	O 1s (eV) air sintered	O 1s (eV) Ar-H ₂ sintered
0.25	530.46	529.45
0.50	530.24	529.75
0.75	530.21	530.07
1.00	530.14	529.93
1.25	529.90	530.09
1.5	530.26	530.21
1.75	529.84	530.07
2.00	530.21	530.21

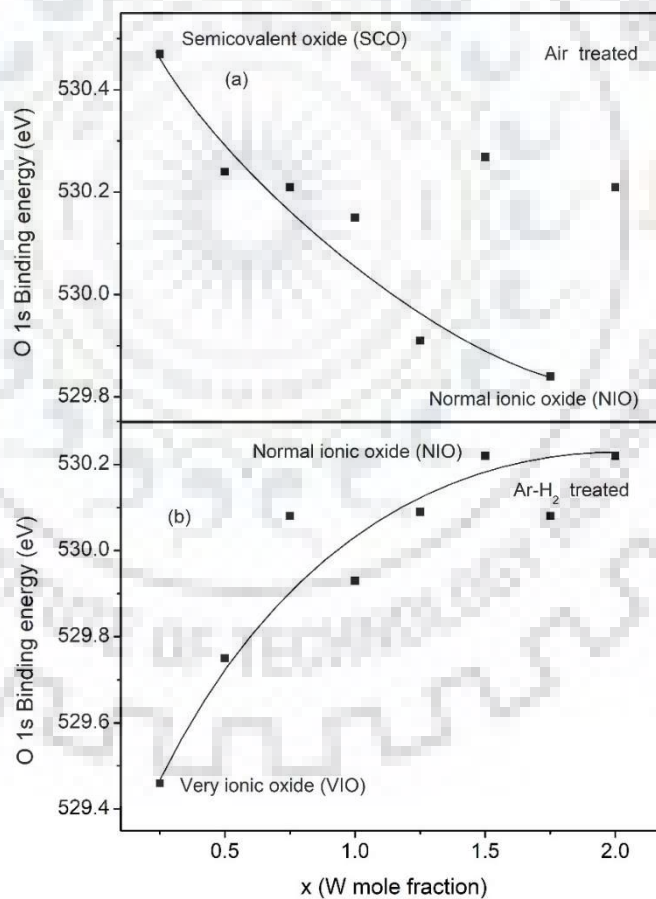


Figure 4-16 Nature of bonding based on O 1s peak values for (a) air treated and (b) Ar-H₂ treated W doped LAMOX samples in the W doping range of 0 to 2.

The Mo 3d and W 4f core-level spectra in figure 4-15 (c) and (d) indicate no splitting apart from their natural splitting, which is at 232.5 eV and 235.8 eV for Mo 3d_{5/2} and 3d_{3/2}. Whereas, for W 4f the peaks are centred around 35.46 eV and 37.6 eV for 4f_{7/2} and 4f_{5/2} respectively [Moulder 1995]. Therefore, one can conclude that air sintered compositions do not have much effect on the chemical states of the compound.

4.4.4 X-ray photoelectron spectroscopy (XPS) of reduced W doped LAMOX samples

This section deals with the spectroscopic studies of Ar-H₂ sintered W doped LAMOX compositions. Results obtained here are in agreement with the data analysed by XRD of W doped samples sintered under reducing conditions.

Figure 4-17 shows the core level analysis of La 3d, Mo 3d, W 4f, and O 1s core level acquired at 11.750 eV pass energy for better resolution. Likewise, as of the air treated sample, the La 3d spectrum in figure 4-17 (a) shows a similar peak shape. This suggests that reductive atmosphere has no significant effect on La 3d spectrum. But the slight shifting of the peak from their standard positions suggests some shifting of the core level electrons and valence electrons of La ion. If the difference between the 3d_{5/2} and 3d_{3/2} peaks is increasing, then core level electrons have moved closer to nucleus and valence electrons have moved further away and vice versa if the difference of 3d_{5/2} and 3d_{3/2} peak is decreasing as can be seen in air sintered samples [Khaled et al., 2012]. All the values have been listed in table 4-4. The W 4f peak in figure 4-17(c) after deconvolution shows only natural splitting same as the air treated sample. Therefore, the reductive atmosphere has no effect on W 4f spectrum as verified by XPS.

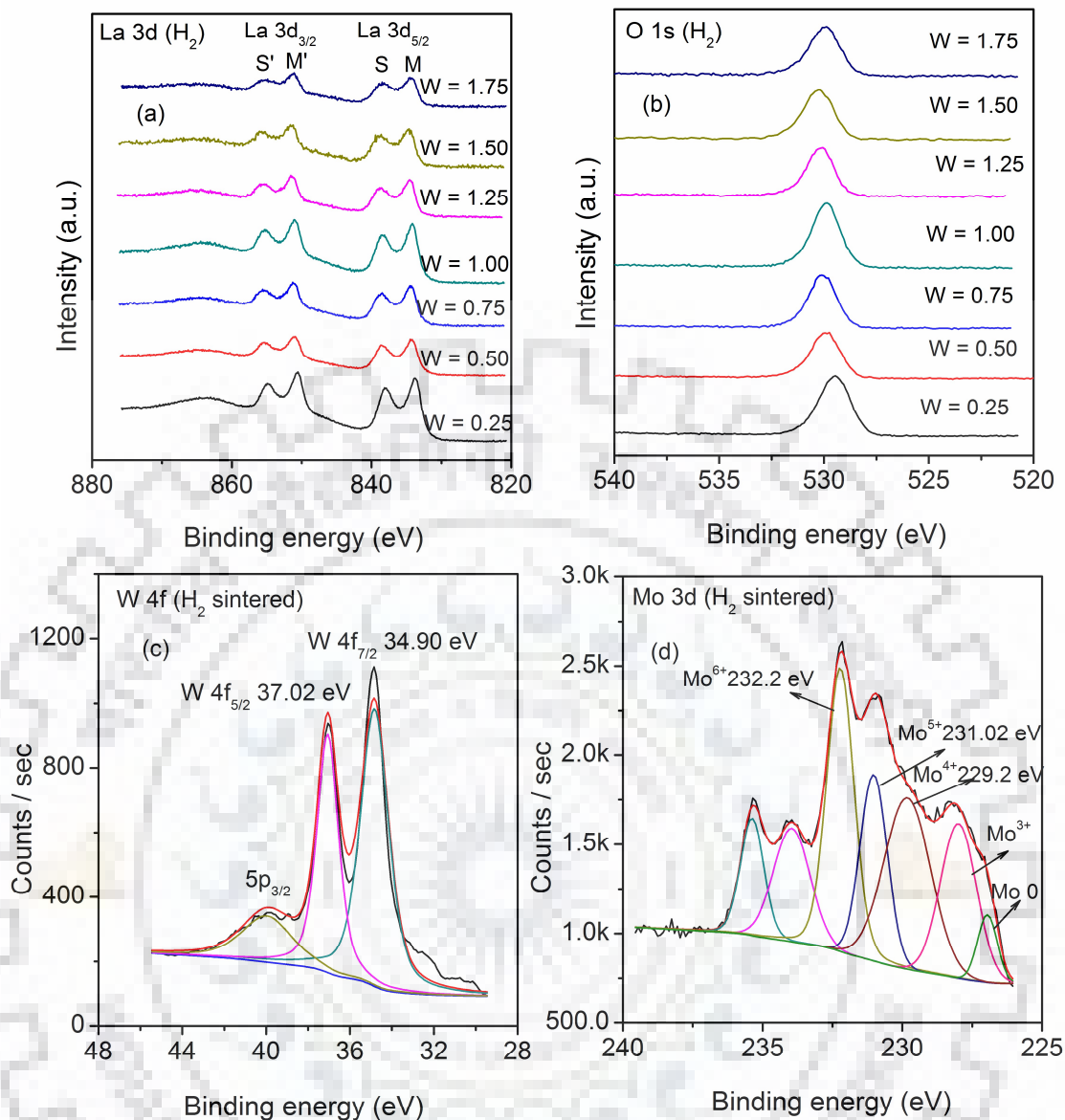


Figure 4-17 Core level spectra of W doped $\text{La}_2\text{Mo}_2\text{O}_9$ (a) La 3d (b) O 1s (c) W 4f and (d) Mo 3d of W doped LAMOX samples treated in Ar- H_2 conditions. The Mo 3d core level shows the splitting of the spectrum, indicating the presence of multiple oxidation states of Mo.

Figure 4-17(d) shows the core level spectrum and its deconvolution of Mo 3d peak sintered in reducing atmosphere. The most concerned region of analysis is Mo 3d spectrum because of its reducing nature in Ar- H_2 atmosphere. The core level analysis of Mo 3d peak clearly reveals the multiple splitting of its 3d core level peak on lower binding energy (B.E.) scale corresponding to various oxidation states of Mo. The reason for the Mo reduction has already been explained in the previous section of XRD analysis. In the complete series of W-LAMOX; the Mo 3d peak of $W = 0.25$ -mole fraction doped was analysed and it was found that W doping only partially

suppresses the Mo reduction but cannot fully eliminate it. The reason for the reducing nature of Mo in W doped LAMOX is its high reduction potential among all the elements (cations), which makes it highly susceptible to reduction [Bard 1985]. According to Kuo and co-workers, the evidence of H_xMoO_3 bronzes can also be explained by XPS analysis of Ar- H_2 treated W-LAMOX which shows the Mo $3d_{5/2}$ peak at 232.5-232.8 eV. In figure 4-17(d), the Mo^{6+} peak of W doped LAMOX and Mo $3d$ peak of H_xMoO_3 bronzes overlap with each other at 232.2 eV, thereby making the analysis of H_xMoO_3 structures difficult. But the XPS study done on W doped LAMOX in Ar- H_2 atmosphere gives a signature of H_xMoO_3 bronze structures. The reduction mechanism of Pt-based H_xMoO_3 bronzes has been done in detail [Kuo et al., 2008; Borgschulte et al., 2017].

The amount of reduced Mo^{6+} to lower oxidation states can be seen in figure 4-18, which has been plotted as atomic concentration % vs. W content. It is evident from the graph that up to W 50 mol %, the Mo^{6+} content decreases. After W = 50 mol % doping, Mo^{6+} content starts to increase but cannot be fully stabilised to the Mo^{6+} oxidation state. The atomic concentration values of different valence states are listed in table 4-6.

Table 4-6 Concentration values for Mo oxidation states obtained by heat-treated in Ar- H_2 atmosphere at 900 °C for 4 hours.

x	0.25	0.5	0.75	1.0	1.25	1.5	1.75
Mo states	Atomic conc %						
6+	27.854	33.244	19.814	15.49	28.876	35.404	41.324
5+	15.094	15.234	36.014	41.72	27.986	31.164	28.114
4+	33.564	31.98	17.394	15.32	15.176	14.204	9.264
3+	14.144	10.304	11.394	19.2	21.466	14.384	12.994
0	9.344	9.234	8.304	8.27	6.496	4.124	8.304

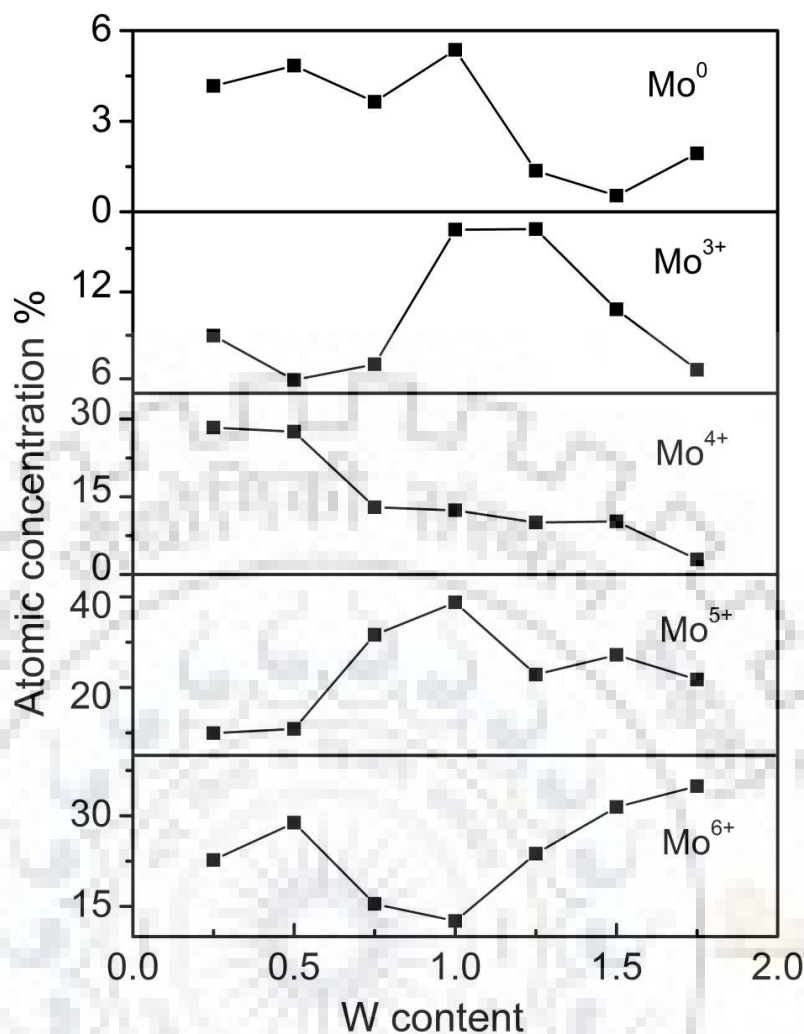


Figure 4-18 Plot of atomic concentration of various oxidation states of Mo in W doped LAMOX with varying concentrations. The graph clearly reveals that Mo⁶⁺ content has not been fully stabilised by W doping.

From XPS analysis, it can be concluded that the W doping over the entire range in LAMOX has only partially stabilised the Mo⁶⁺ from reduction to lower states in the compound. This reduction of Mo in Ar-H₂ atmosphere gives rise to electronic conductivity, which is not desirable in the fuel cell operation. No other elements in the LAMOX structure are reduced as observed from the data of air and diluted H₂ treated samples.

4.5 Oxide ion diffusion studies in LAMOX

The effect of W doping in LAMOX lattice has been discussed in the previous section. It is clear from the Rietveld analysis that upon W doping La-O bond length has an average decreasing trend which produces a regular trend of the oxide ions around the Mo ions. According to the difference in ionic radii for Mo⁶⁺ (0.59Å) and La³⁺ (1.032Å), the Mo-O polyhedron is usually smaller than

La-O polyhedron. Since O(1) site is highly localised, therefore, it does not take part in conduction. Oxygen atoms at O(2) and O(3) sites are delocalised and hence contribute to conduction part. The occupancy of the various oxygen atoms has been shown in figure 4-4(b). Since the W doped LAMOX structure is similar to β -LAMOX consisting of one O1, 3La and one Mo atoms forming a tetrahedral unit. According to the literature [Tealdi 2008] these tetrahedral units which are joined at La edges by the formula goes through tilt/rotation which opens up a pathway for the O(2) and O(3) ions to pass through tunnels created by tilt/rotation of these [O1La3Mo] tetrahedral units. This tilt can be calculated by the formula in equation 4.5

$$\tan(\delta) = \sqrt{\frac{8\left(\frac{d_{11}}{a}\right)^2}{3}} - 1 \quad 4.5$$

where d_{11} represents the distance between two adjacent La ions representing the edge of the tetrahedral unit, a is the lattice constant and δ is the tilting of the tetrahedral unit.

This tilt/rotation of the tetrahedral unit favours the migration of O^{2-} ions (O2 and O3) through the bottleneck opening/closing process of [O1 La3 Mo] tetrahedral units. Another plausible explanation by Hou et al., [2007] suggests that one O ion moves easily inside Mo–O polyhedron from O(2) to O(3) site and at the same time another O ion moves inside another Mo–O polyhedron or vice versa. O(2) and O(3) ions are mobile due to their less site occupancies and move in a concerted way but do not diffuse along with Mo–O polyhedron network.

From the explanation suggested by C Tealdi et al., [2008], the tilting of these tetrahedral units opens up the gate for oxide ions, which are at O(2) and O(3) site. Higher the tilting, greater is the movement of oxide ions. It has been confirmed from the Rietveld analysis that O(3) and O(2) sites are less occupied for W content up to 1.25 and correspondingly facilitating the oxide ion migration from one site to another very easily, thereby giving enhanced conductivity.

4.6 Ion dynamics and conductivity study of W = 0.25 doped LAMOX

The alternating current (ac) conduction in ionic oxides has got great importance in studying the ion dynamics and relaxation studies of dipoles. The Impedance spectroscopy (IS) study of doped electrolyte materials over a wide frequency range gives an opportunity to study the motion of the oxide ions at a very wide range of time scales corresponding to the frequency range 1 Hz - 1 MHz. Funke and Cramer [1997] defined the ac conduction a very powerful tool for ion dynamics. The ion dynamics and conductivity studies of W doped LAMOX are presented in this section.

The frequency dispersion graph of the real part of ac conductivity of air treated W = 0.5 doped LAMOX is shown in figure 4-19 (c and d). The graph can be analysed in two parts. The first part as a low-frequency region corresponds to d.c. conductivity and second region as high-frequency dispersive part corresponds to a.c. conductivity. The Low-frequency is a region where dipoles can align or respond to the applied electric field. In contrast, the high frequency is a region where dipoles virtually produce no polarisation because they cannot follow the rapid field (ac) variation. Also, figure 4-19(e) shows the imaginary part of modulus formalism, which is helpful in analysing the dielectric behaviour of the W doped LAMOX composition. This concept was introduced by Macedo et al., [1972] and is given as reciprocal of the complex dielectric permittivity:

$$M^* = 1/\epsilon^* = M' + iM'' \quad 4.6$$

The modulus formalism is also known as electric modulus, is a very efficient approach to study the behaviour of dipoles under the effect of alternate current (a.c.) conduction mechanism. Basically, it provides an in-depth information of various electrical transport mechanisms such as relaxation times, jump rate of conducting (oxide) ions. The detailed information of modulus formalism studies is obtained from modulus spectroscopy. The real part of modulus M' contributes to the electrical conduction. Whereas, the imaginary part of the modulus deals with the long and short-range of ion transportation and also the crossover from long-range to short-range hopping. From figure 4-19(e), the imaginary part of the modulus curve has peak nature at two different temperatures. The graph shows a flat or constant trend over the frequency range of 1 Hz to 1 kHz for both temperature profiles. Beyond 1 kHz the graph shows a steep increase in the values up to 3 MHz. The peak of the curve (blue) corresponding to higher frequency shows hopping of oxide ions to shorter distance, whereas the peak of the black curve corresponds to lower frequency favours the long-range hopping of oxide ions in the structure [Shamim et al., 2017].

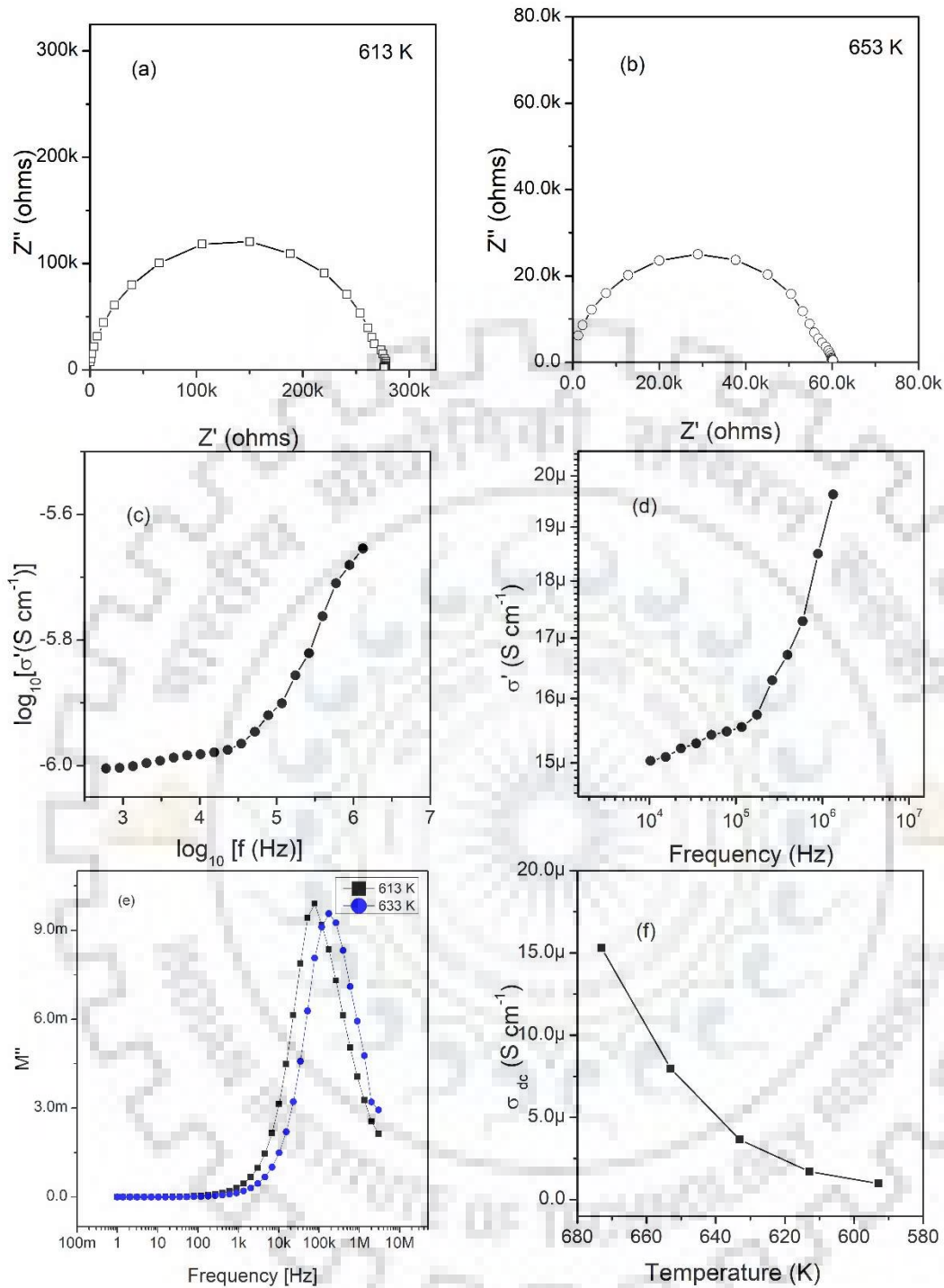


Figure 4-19 Complex impedance plot of $\text{La}_2\text{Mo}_{1.5}\text{W}_{0.5}\text{O}_9$ at (a) 613 K and (b) 653 K. (c) log-log plot of σ_{ac} vs. frequency at 593 K. (d) Frequency dispersion of real part of conductivity at 633 K, (e). Imaginary part of modulus of $\text{La}_2\text{Mo}_{1.5}\text{W}_{0.5}\text{O}_9$ at 633 K (blue) and 613 K (black). (f) Temperature dependence plot of dc conductivity σ_{dc} at various temperatures.

From the figure 4-19(e), the M'' shifts slightly towards the high frequency as the temperature is increased from 613 K to 633 K. The modulus formalism study done in the present case is limited up to 3 MHz. According to the literature Shamim et al., 2017, the higher temperature modulus

formalism curve show peak at higher frequency side as compared to the low-temperature plot. This shift on the frequency scale suggests the distribution of the attempt or jump frequencies (vibrational frequency $\nu_0 = 10^{13}$ Hz of mobile ion within the potential cage or mean positions) for the barrier cross over (E_a) by the oxide ions from one to another site. The peak of the modulus formalism implies the transition from long-range hopping to short-range hopping of the ions with increasing frequency. The peak of the modulus formalism curve gives information about the relaxation frequency and time required for ions to migrate from one site to another. With the increase in temperature, the peak of the imaginary part of the modulus formalism curve shows shift on the higher frequency side. This implies that at the higher temperature (corresponds to the high thermal energy of ions), the time required for oxide ion to migrate from one site to another is less as compared to low-temperature modulus values.

If the charges of the opposite sign are placed on the opposite faces of an ionic conductor, then there will be a rise in the electrical field which will eventually decay to zero due to the migration of the ions. This decay in the time domain may be defined as

$$E(t) = E(0) \phi(t) \quad 4.7$$

where $\phi(t)$, a decay function described by Kohlrausch-Williams-Watts (KWW) can be written as

$$\phi(t) = \exp[-(t/\tau)^\beta] \quad 4.8$$

where τ is the temperature-dependent relaxation time constant and β is the Kohlrausch exponent. The exponent term can be used to characterise the stretch of M'' peak. Smaller the value of β , larger is the peak stretch and larger is the deviation from Debye type relaxation.

The conductivity behaviour of the ionic conductors has been found to follow the universal power law given by the equation [Dyre 1991]:

$$\sigma' = \sigma(0) + A(\omega)^s \quad 4.9$$

where $\sigma(0)$ is the dc conductivity and s is the power-law exponent. This behaviour is called a universal dielectric response (UDR). The $\sigma_{ac}(\omega)$ obeys the Almond-West universal power law in the form of

$$\sigma_{ac}(\omega) = A(\omega)^s \quad 4.10$$

The value of s lies in between 0.3 and 0.7 or more general 0 to 1. $s = 1$ corresponds to pure ac conductivity.

The β value can be calculated as $1-s$, whereas s can be calculated from the slope of $\log\sigma_{ac}(\omega)$ vs $\log f$ plot as shown in figure 4-20(a). The value of s is found to be 0.23 at temperature 593 K. From the value of s , the β was calculated as 0.7637 which is in agreement with power-law equation stated above.

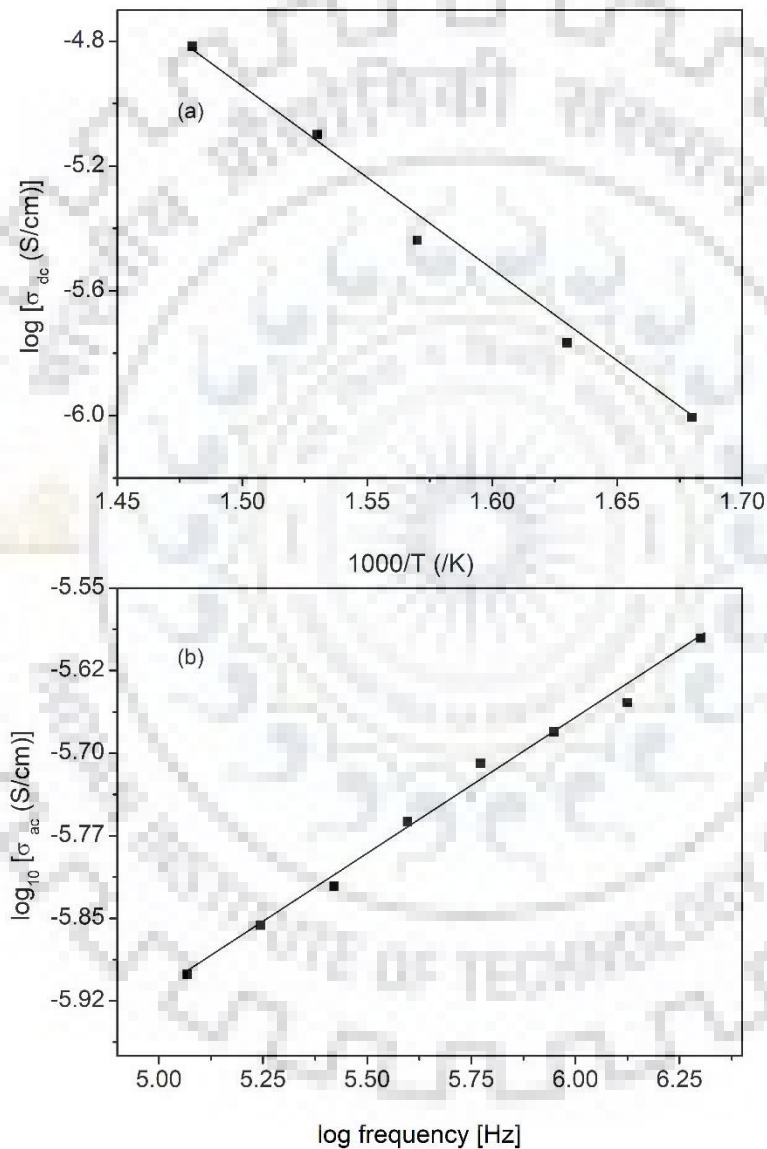


Figure 4-20 (a) Plot of σ_{dc} as a function of temperature ($1/T$). The slope of the graph yields activation energy (E_a) and follows the Arrhenius equation. (b) Plot of $\log\sigma_{ac}$ vs. \log frequency. The slope of the straight line gives the value of s , which represents the frequency-dependent ac conductivity, which follows the universal power law.

The impedance plots at various temperatures have been made in the form of Nyquist plot in figure 4-19(a) and (b). The presence of a broad semi-circle indicates the presence of non-debye type relaxation. The variation of dc conductivity for the bulk and grain boundary can be defined as

$$\sigma_{dc} = \sigma_0 \exp\left(-\frac{E}{kT}\right) \quad 4.11$$

where σ_0 is the pre-exponential factor, E is the activation energy, k is the Boltzmann constant and T is the absolute temperature.

The d.c. conductivity of W 0.5 doped LAMOX at various temperatures has been plotted as a function of temperature (T) as well as $1/T$ in figure 4-20(b). The log plot of the above dc conductivity vs. $1/T$ is a straight line for which the negative slope gives the activation energy value (E) and the intercept on the y-axis gives the value of σ_0 . The σ_{dc} is obtained from the impedance plot where the semi-circle intercepts the x-axis on the lower frequency side.

The activation energy E is found to be ~ 0.6 eV and pre-exponential factor obtained as 2.14×10^{-5} . The σ_{dc} measured here is at temperature up to 400°C . This conductivity may further increase to the order of 3 as the temperature increases. Therefore, to conclude, the ion dynamics has been studied in terms of frequency dispersion of the conductivity. The value of s was in agreement with universal power law, and also β value suggests that the relaxation phenomenon is slightly shifted towards the Debye type behaviour. The present results obtained here are comparable to values (viz. 0.69) for alkaline earth doped LAMOX, as reported by Basu et al., [2000].

4.7 Effect of K doping at La site in $\text{La}_2\text{Mo}_2\text{O}_9$

4.7.1 Introduction

In the previous section of this chapter, the effect of W doping in LAMOX has been studied and it was found that the cubic phase of the pure LAMOX has been stabilised at room temperature, but the reduction of W doped LAMOX compositions have not been entirely suppressed. Few research papers regarding K doping have investigated the effect on conductivity. But they have not shown any study related to stabilisation caused due to suppression of Mo in reductive atmosphere by K doping.

In this section effect of K doping at La site in LAMOX has been investigated by x-ray diffraction, scanning electron microscopy, and photoelectron spectroscopy. K = 5 mol % and 10 mol % at La site have been doped, and the effects were analysed. The main focus has been given

on chemical state analysis and structural stability of $\text{La}_{1.8}\text{K}_{0.2}\text{Mo}_2\text{O}_{9-\delta}$ and $\text{La}_{1.9}\text{K}_{0.1}\text{Mo}_2\text{O}_{9-\delta}$, which were studied by means of x-ray photoelectron spectroscopy (XPS) and x-ray diffraction.

4.7.2 Structural study of K doped $\text{La}_2\text{Mo}_2\text{O}_9$ by x-ray diffraction

Figure 4-21 shows the diffraction pattern of 5 mol % and 10 mol % K doped LAMOX at La site in the 2θ range of $15-70^\circ$. From the preliminary analysis of the XRD pattern, it is concluded that peaks are well-positioned and very distinctive in nature. For both K doped compositions, K_2O as an additional phase of cubic symmetry (JCPDS file no. 98-006-0489) along with cubic $\text{La}_{0.9}\text{K}_{0.1}\text{Mo}_2\text{O}_{9-\delta}$ phase (JCPDS file no. 98-024-5811 and space group $\text{P}2_13$) is found. Further phase analysis has been done by Rietveld method with X'pert high score plus software, and the results are presented in figure 4-22. Crystallographic information file (CIF) number 1533392 is used as a reference for the refining of the parameters. The reason for the appearance of K_2O phase is the solubility limit of K ions at La site, which is maximum up to 3 mol %. This restricted solubility may be attributed to large ionic radius of K^{1+} (1.34 Å) as compared to La^{3+} (1.032 Å) [Shannon 1976; Ravella 2012].

As it was already shown in the previous section that W doping at Mo site in LAMOX brings the high-temperature cubic phase at room temperature, but the structure was distorted by the doping, same effect has been occurred by K doping at La site in the host lattice. A slight distortion was observed, as seen in figure 4-22 inset. The (321) peak is slightly asymmetric in nature which suggests that K doping has introduced slight distortion in the host lattice site. The overall cubic structure of the β -LAMOX has been retained upon K doping with 5 mol %. The XRD analysis of K = 10 mol % doped LAMOX shows the shifting of the XRD pattern to the lower side of 2θ two theta side which implies a larger lattice constant as compared to that of K = 5 mol % doped LAMOX. The lattice parameter for K = 5 mol % LAMOX is found to be 7.15 Å as calculated by X'pert high score plus software. The solubility limit of K at La site is ~3 mol % and maximum doping of 7.5 mol % for dielectric relaxation study and doping level of 2.5 mol % for XRD study has been done by few researchers and mentioned elsewhere in detail [Tealdi et al., 2004; Wang et al., 2005]. Insufficient information is available about K = 10 mol % doping in the existing literature, restricts the XRD analysis in detail. Therefore, a detailed analysis has been done for K = 5 mol% doped LAMOX in the present study.

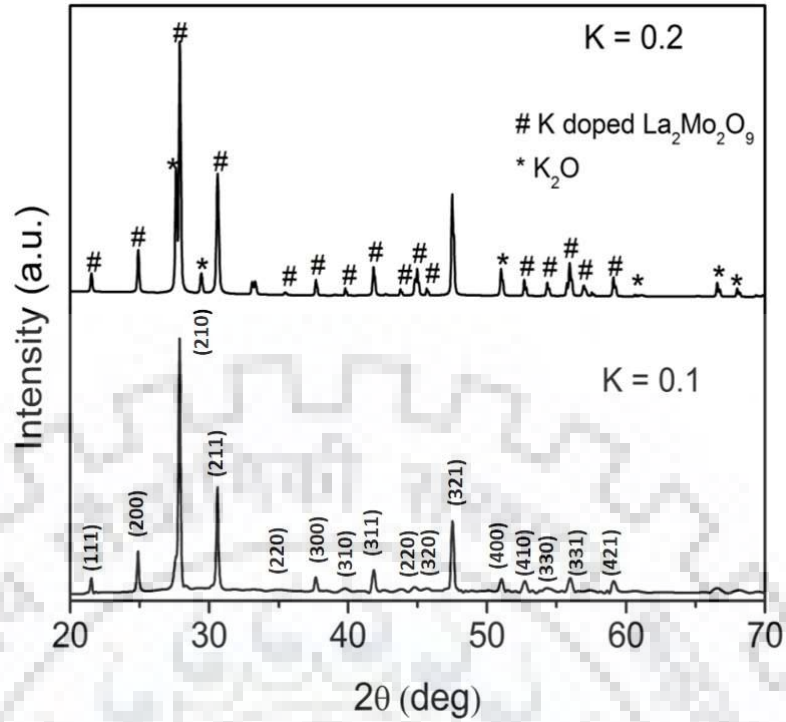


Figure 4-21 X-ray diffraction pattern for 5 mol % ($x = 0.1$) and 10 mol % ($x = 0.2$) for K doped $\text{La}_2\text{Mo}_2\text{O}_9$ obtained at room temperature. The appearance of K_2O as an additional phase is observed in both K doped LAMOX compositions.

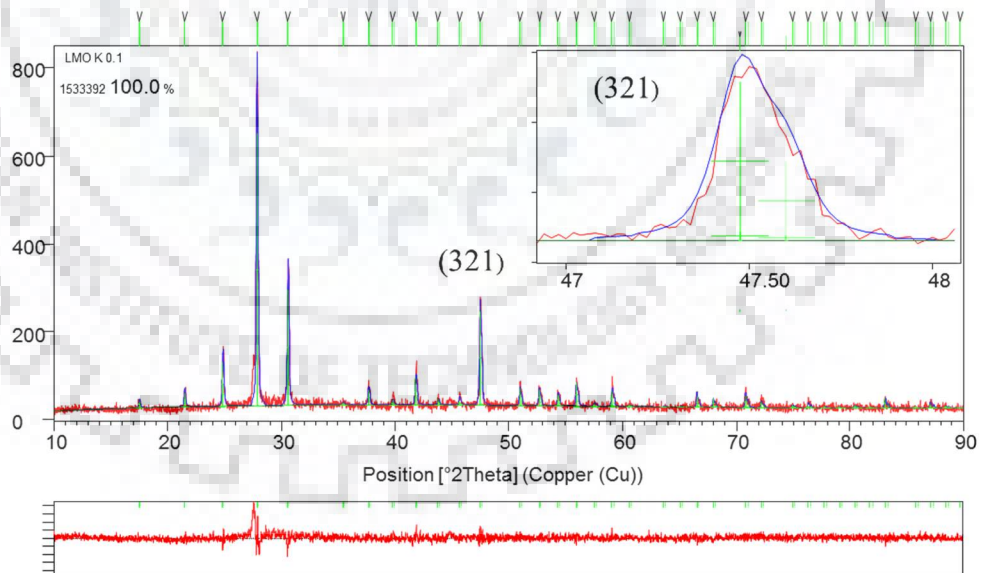


Figure 4-22 Rietveld refinement of $x = 0.1$ mole fraction K doped $\text{La}_2\text{Mo}_2\text{O}_9$. Inset shows the (321) peak, singlet in nature, confirming the cubic nature of the composition.

The reason for the stabilisation of the cubic structure at room temperature on K doping may be expressed as follows. The low-temperature phase of LAMOX has an ordered oxide ion and

vacancy sublattices which are responsible for low conductivity. Upon the temperature increase, this ordering of oxide ion and vacancy sub-lattice goes in the disordered form, thereby increasing the conductivity. These dopants prevent low-temperature ordering of vacancy/oxide ions (or cation/vacancy ordering). The literature shows that the compounds having disordered vacancy state has the larger conductivity. Therefore, the high-temperature form of LAMOX is retained even at low temperatures by doping. [Georges et al., 2006].

A large number of parameters are refined in this case to obtain a good fit are listed in table 4-7. The goodness of fit (G.O.F) or χ^2 value is found to be < 2 , indicating a good fit of the experimental profile. From the difference Fourier analysis, the position of the unoccupied oxygen atom has also been calculated along with their neighbouring atoms and is listed in table 4-8. Whereas table 4-9 presents the bond lengths of $\text{La}_{1.9}\text{K}_{0.1}\text{Mo}_2\text{O}_{9-\delta}$ constituent atoms obtained from refinement and compared with the β - LAMOX mentioned elsewhere [Wang 2008]. The respective bond lengths of La-O and Mo-O in $\text{La}_{1.9}\text{K}_{0.1}\text{Mo}_2\text{O}_9$ are not very much different from the β - LAMOX structure as evident from table 4-9, which suggests that introduction of K in the host structure stabilises the high-temperature β -LAMOX phase with nominal structural distortion of the unit cell.

Table 4-7 Refined crystal structure parameters (sp. gp P 2₁3) of La_{1.9}K_{0.1}Mo₂WO₉ from XRD.

x	K 0.1 (5 mol %)
a (Å)	7.159(3)
La (4a)	x 0.402(9)
	Occupancy 0.95
	B _{iso} 0.5
Mo(4a)	x 0.085(2)
	Occupancy 1.00
	B _{iso} 0.5
K	x 0.186(4)
	Occupancy 0.005
	B _{iso} 0.5
O(1) (4a)	x 0.917(3)
	Occupancy 1.0
	B _{iso} 10.00
O(2) (12b)	x 0.137(6)
	y 0.568(4)
	z 0.242(9)
	Occupancy 0.78
	B _{iso} 0.5
O(3)(12b)	x 0.105(3)
	y 0.161(4)
	z 0.301(1)
	Occupancy 0.38
	B _{iso} 0.5
R_{exp}	16.3979
R_{wp}	22.520
GOF	1.886

Table 4-8 Determination of missing oxygen atom coordinates from difference Fourier analysis of $\text{La}_{1.9}\text{K}_{0.1}\text{Mo}_2\text{O}_9$.

x	0.1
Unoccupied O atom	O(2) / O(3)
x(Å)	0.391(3)
y(Å)	0.391(3)
z(Å)	0.391(3)
Wyckoff position	12b
Electron density	1.011
Closest atoms	2 K: 0.010, 3 La 0.109

Table 4-9 Calculated bond lengths between various elements in K = 5 mol% doped $\text{La}_2\text{Mo}_2\text{O}_9$ compositions by Rietveld analysis. The standard uncertainty for bond lengths and lattice parameter has been shown in parenthesis.

Constituent atoms	Bond length (Å)
La-O1	2.673(4)
La-O2	2.492(7)
La-O3	2.776(2)
K-La	3.127(9)
K-O1	2.622(5)
O1-O2	2.792(5)
O2-O3	2.947(1)

Table 4-10 Comparison of bond length of K doped LAMOX with β -LAMOX (Source; Goutenoire et al., 2000).

Constituent atoms	β -LAMOX	K-LAMOX (K= 0.10)
La-O(1)	2.71(2)	2.673(4)
La-O(2)	2.40(3)	2.492(7)
La-O(3)	2.66(4)	2.776(2)
Mo-O(1)	1.83(2)	1.823(1)
Mo-O(2)	1.77(3)	1.742(2)
Mo-O(3)	1.73(4)	1.696(5)
Lattice parameters	7.2014(7)	7.159(3)

From the x-ray diffraction analysis, it can be concluded that high-temperature cubic phase of LAMOX is successfully stabilised by the K doping at La site. This was one of the drawbacks of pure LAMOX to be utilised as an electrolyte because of change in volume expansion, which could lead to failure of this compound as an electrolyte in the fuel cell systems.

4.8 Microstructural study by field emission scanning electron microscope of K doped $\text{La}_2\text{Mo}_2\text{O}_9$ composition sintered in air and Ar- H_2 atmosphere

In the previous section, the XRD analysis of K doped LAMOX, the high-temperature cubic phase, was successfully stabilised. The XRD study of reduced K doped samples has not been done in the present study. But the microscopy and x-ray photoelectron spectroscopy analyses have been done in detail. The microstructural details of K doped LAMOX have been investigated by FE-SEM. Figure 4-23 shows the FE-SEM images of the air sintered and Ar- H_2 sintered K doped pellets at 900 °C. The FE-SEM images clearly reveal that the air sintered sample has a good packing density of the grains, whereas the Ar- H_2 sintered samples show pores in the composition, which may be due to incomplete sintering of the samples which intensifies in Ar- H_2 atmosphere.

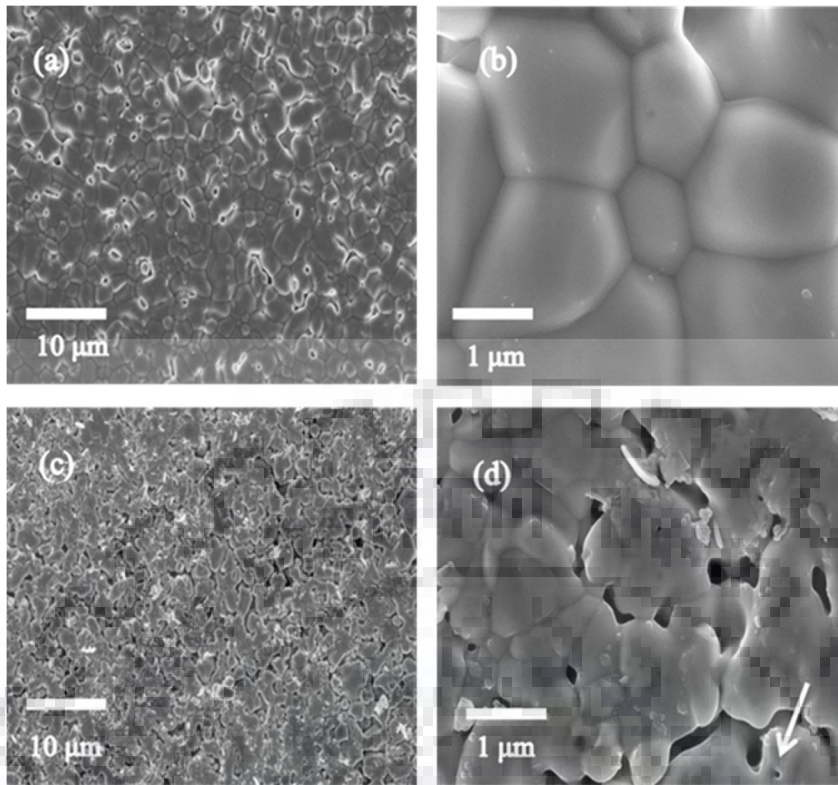


Figure 4-23 Microstructures of $\text{La}_{1.9}\text{K}_{0.1}\text{Mo}_2\text{O}_9$ sintered in air (a) low magnification (b) high magnification, Ar-H_2 sintered (c) low magnification and (d) high magnification. Pore formation due to incomplete sintering in Ar-H_2 is indicated by the arrow.

4.9 Chemical state analysis of air sintered and Ar-H_2 -reduced samples by x-ray photoelectron spectroscopy (XPS)

Likewise, in the previous section of W doped LAMOX analysis, this section presents the XPS analysis of air sintered and Ar-H_2 treated K doped samples. The XPS data are plotted together at the same binding energy level that gives the ease of analysis by comparison of various plots of the same core level of the respective elements.

4.9.1 Survey spectra analysis

Figure 4-24(a) shows the survey spectrum of $\text{K} = 5 \text{ mol } \%$ doped LAMOX along with the core level of the various constituent elements. Survey spectra over the range from 0 to 1100 eV at pass energy of 187.5 eV of the K doped compositions are taken in order to identify the elements present in the sample. Along with the core level photoelectron peaks, some auger peaks are also present in the spectrum as shown in figure 4-24(a). As mentioned in the experimental chapter, the C 1s reference has been taken as 284.5 eV for binding energy shift correction [Moulder 1995].

4.9.2 Core level analysis of K = 5 mol % doped La₂Mo₂O₉ in air and Ar-H₂ atmosphere (K 2p, O 1s, La 3d, Mo 3d)

The core level analysis of the La 3d, Mo 3d, K 2p and O 1s are represented in figure 4-24 (b to f). The K 2p peak is plotted in figure 4-24(b) due to the low level of doping; the noise signal is dominant in the spectrum. But the splitting of the peaks can be seen clearly. As evident from the figure the spectra have no further splitting of the peaks which suggests there is no reduction of the K 2p spectra.

The O 1s peak of K = 5 mol % doped LAMOX in figure 4-24(c) of air sintered shifts to lower binding energy side as compared to Ar-H₂ sintered composition. This arises due to the nature of the bonding changes from semi covalent oxide to normal ionic oxide. It means that Ar-H₂ treated sample is slightly ionic in nature as compared to air sintered samples.

The La 3d spectrum in figure 4-24(d) of air and Ar-H₂ sintered samples show no change in the peak shape. An inference may be drawn that La has no reducing effect on its spectrum. The binding energy value for La 3d peak is 834.23 eV. The spectrum shows main and satellite peaks, and the reason for this type of spectrum nature has been discussed in section 3.3.3 of chapter III.

The Mo 3d core level analysis in figure 4-24(e) and 4-24(f) shows the peak shape and curve-fitting profile. From figure 4-24(f) it can be noticed that peak shape of Mo 3d is almost similar to that of as-sintered K = 0.1 doped air treated sample. Upon curve fitting, the spectra shows some amount of reduced Mo⁵⁺ and Mo⁴⁺ oxidation states. The quantitative estimation has been listed in table 4-11. As compared to W doped LAMOX, the compositions of K doped LAMOX have shown more stability under reducing conditions. The systematic XPS analysis of K doped LAMOX material has not been reported so far by any authors.

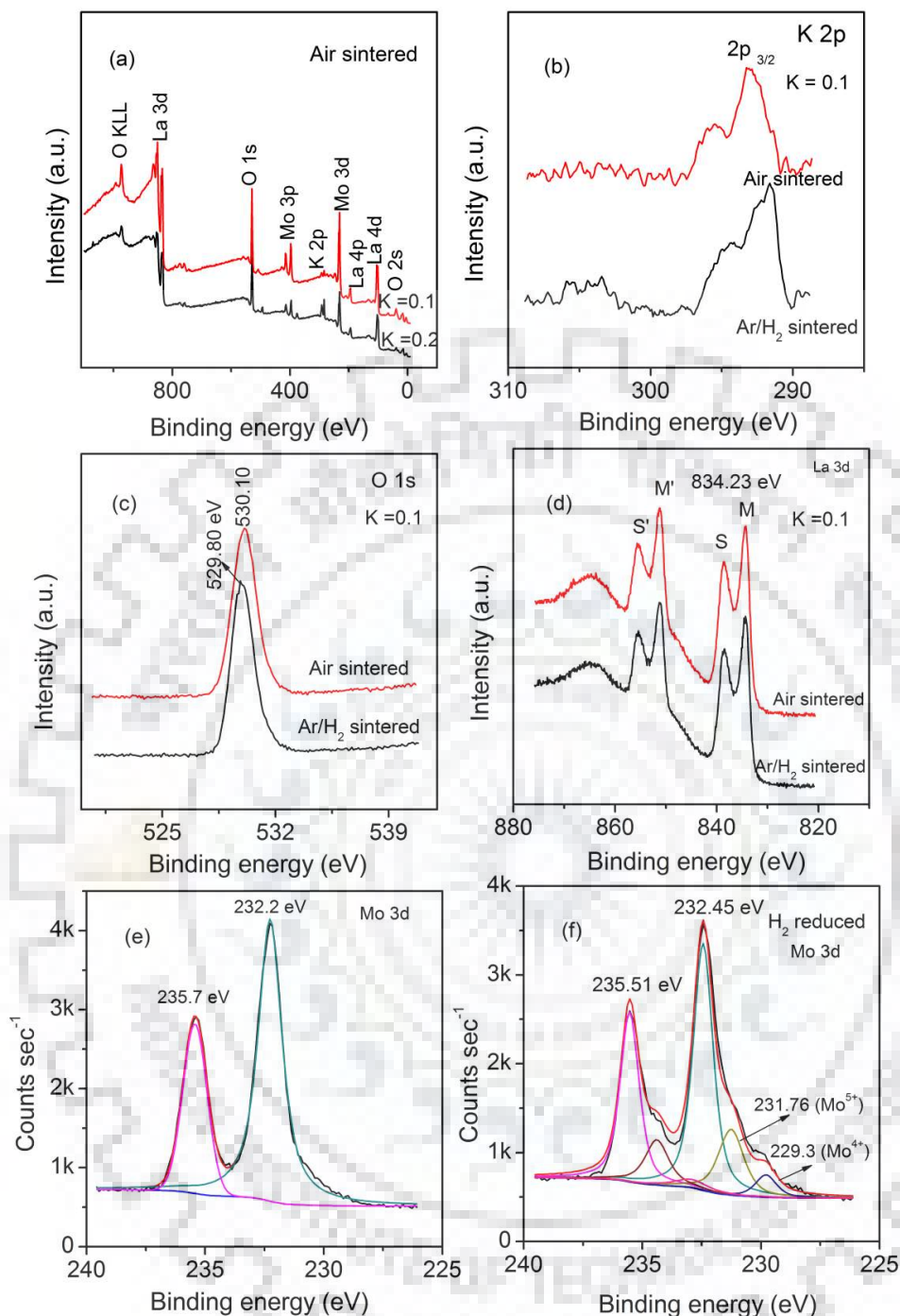


Figure 4-24 XPS spectra of K = 5 mol % ($x = 0.1$) doped LAMOX (a) survey and core-level spectra of air sintered and Ar-H₂ sintered reducing atmospheres (b) K 2p, (c) La 3d, (d) O 1s, (e) Mo 3d and (f) Mo 3d reduced. The data have been collected at room temperature.

4.9.3 Core level analysis of K = 10 mol % doped LAMOX (La 3d, Mo 3d, K 2p, O 1s)

K = 5 mol % doped LAMOX sample shows good stability under reducing conditions. Now K = 10 mol % doped LAMOX composition is analysed and presented. Figure 4-25 shows the core level spectra of La 3d, Mo 3d O 1s, and K 2p elements.

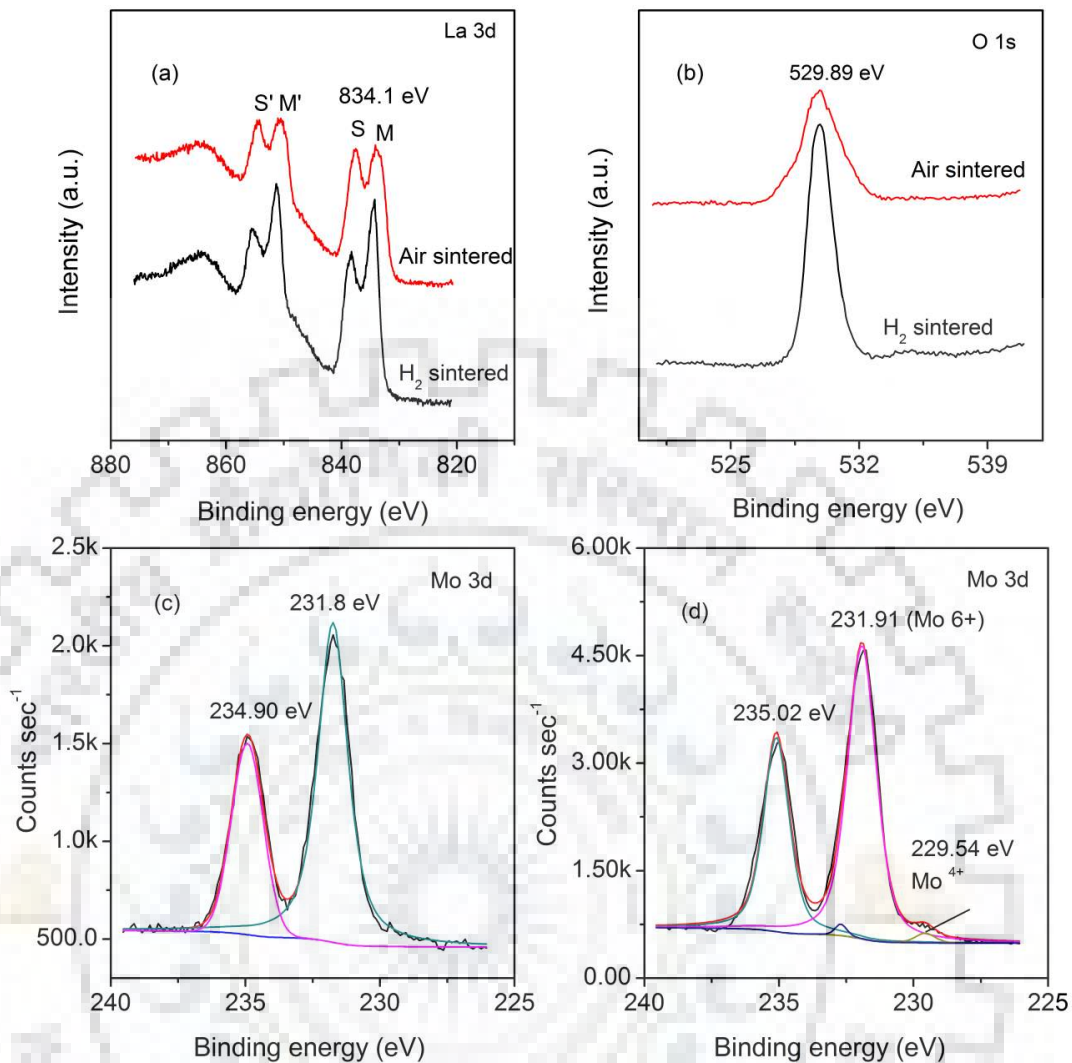


Figure 4-25 XPS spectra of K = 10 mol % doped LAMOX. Core level spectra of air sintered and Ar-H₂ reduced sample (a) La 3d (b) O 1s, (c) Mo 3d air sintered and (d) Mo 3d Ar-H₂ treated. All the spectra have been collected at room temperature.

As evident from figure 4-25(a), the La 3d spectrum has retained its natural peak shape in air as well as in reducing atmosphere, suggesting that no effect of H₂ atmosphere on La 3d spectrum. Whereas, the O 1s in figure 4-25(b) peak shows a negligible shift of the binding energy values when the sample is treated in air and Ar-H₂ atmosphere. Like in the previous section of K = 5 mol % doping, the XPS pattern of O 1s pattern is found similar. This excludes any effect of K doping on O 1s peak.

The Mo 3d spectra presented in figure 4-25(c) and (d) are of interesting nature. When both compared (air sintered and Ar-H₂ composition), the nature of Ar-H₂ sintered spectrum of Mo 3d was found to be very much similar to that of the air-sintered spectrum. This suggests that Mo 3d

in K = 10 mol % doped LAMOX has been stabilised under reducing condition at 900 °C. Furthermore, to confirm the results, deconvolution of the spectrum was done and it was found that a very trace amount of Mo⁴⁺ oxidation state has been formed. This confirms and completes the aim of doping in LAMOX in order to stabilise Mo under reducing atmosphere. The reason of the suppression of Mo reduction by K doping in the lattice might be due to the prohibition of intercalation of hydrogen in between the Mo-O polyhedral, which tend to form H_xMoO₃ structure leading to the formation of lower Mo states. The K doping in LAMOX has been reported earlier but the photoelectron spectroscopic studies were not done in the literature reported so far. Table 4-11 shows the quantitative analysis of Mo 3d content both in K doped LAMOX.

Table 4-11 Quantification of Mo⁶⁺ and lower valance states of Mo in K = 5 mol % and 10 mol % doped LAMOX.

x	Mo ⁶⁺ (atomic %)	Mo ⁵⁺ (atomic %)	Mo ⁴⁺ (atomic %)
K (5 mol%)	69.33	23.87	6.80
K (10 mol %)	97.77	--	2.23

4.10 Raman spectroscopy study of K = 10 mol % doped LAMOX

The Raman spectroscopy and analysis of La_{1.8}K_{0.2}Mo₂O_{9-δ} is shown in figure 4-26. The spectra were collected at room temperature over a range of 200 – 1000 cm⁻¹. The peak situated at around 866 cm⁻¹ indicated as band 1 corresponds to oxygen vacancies oscillation, and the peak at around 901 cm⁻¹ as band 2 corresponds to Mo = O oscillations. The peak around 342 cm⁻¹ indicates the existence of La – O bond.

From figure 4-26 it is evident that there is a noticeable change in the Band 1 intensity, which corresponds to a structural phase change in the two compositions [Liu et al., 2015; Zhou et al., 2007]. Thus, the phase change and the existence of oxygen vacancies in the two compositions have been further confirmed successfully.

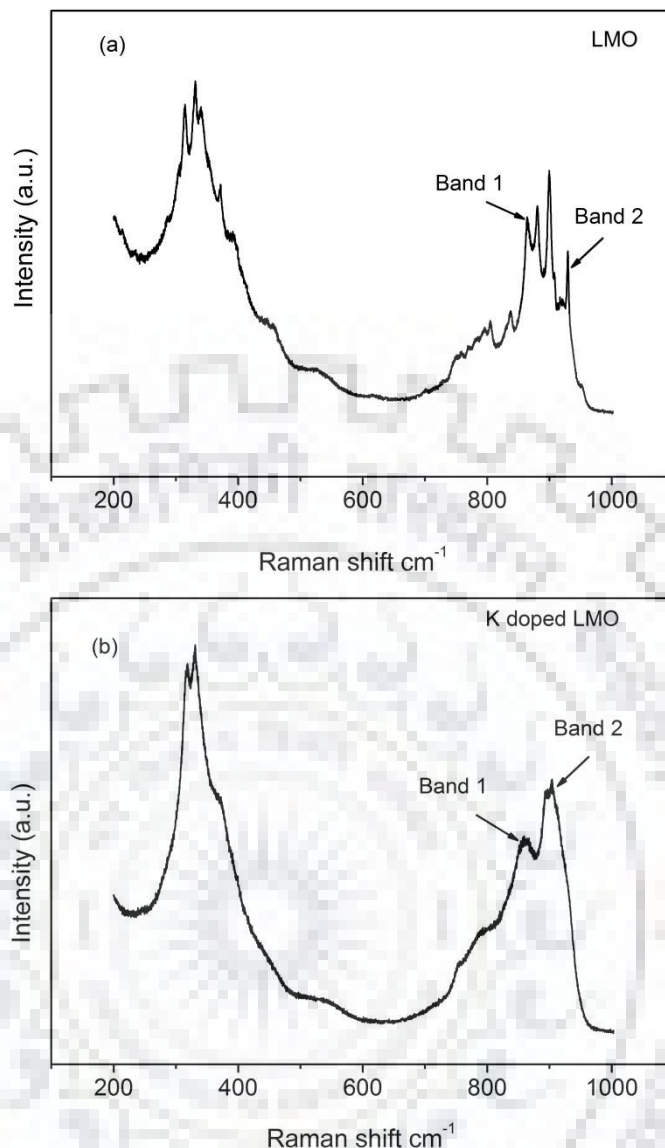


Figure 4-26 Raman spectra of (a) LAMOX and (b) K = 0.2 doped LAMOX. The difference in the intensities of band 1 and band 2 indicates the difference in crystallographic structure from monoclinic in LMO to cubic phase in K doped $\text{La}_2\text{Mo}_2\text{O}_9$.

4.11 Conductivity studies of air sintered K = 10 mol % doped $\text{La}_2\text{Mo}_2\text{O}_9$

This section deals with the conductivity behaviour of K doped LAMOX at different temperatures. Figure 4-27 shows the complex impedance plot of K = 10 mol % doped LAMOX at various temperatures. The figure shows broad semi-circular plots implying the presence of non-debye relaxation type phenomenon described in section 3.3.5 of chapter 3.

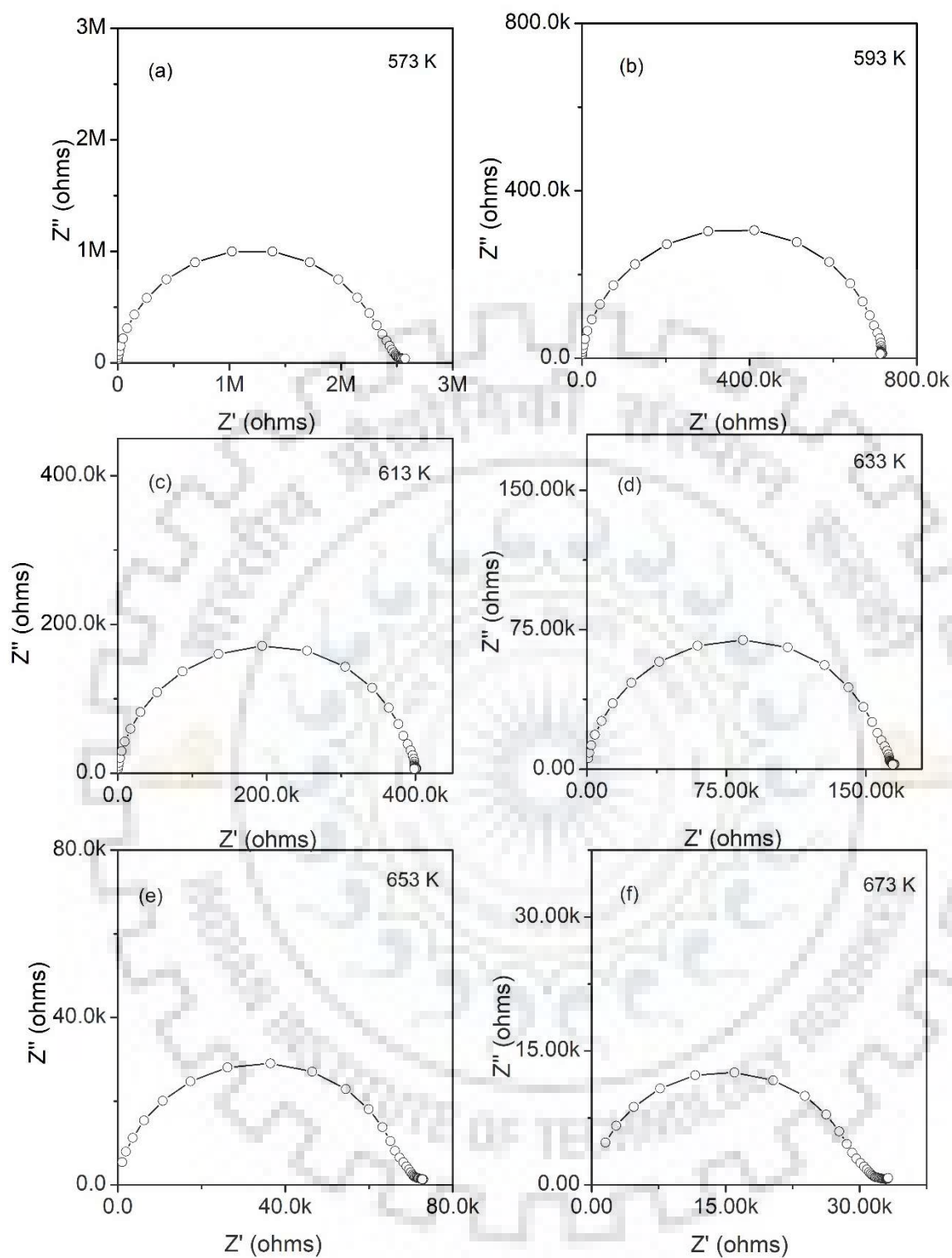


Figure 4-27 Complex impedance plot of $\text{La}_{1.8}\text{K}_{0.2}\text{Mo}_2\text{O}_9$ at (a) 573 K (300 °C) and (b) 593 K (320 °C) (c) 613 K (340 °C) (d) 633 K (360 °C) (e) 653 K (380 °C) and (f) 673 K (400 °C). The broad semi-circle represents a non-debye type relaxation phenomenon.

As seen in the figure, the real part of the impedance can be found by the intersection of the semicircle on the x-axis. The x-intercept gives the real part of the impedance, which accounts for

the bulk resistance. The conductivity value can be estimated by the formula $\sigma = l / R (t / A)$, where R is the real part of the impedance, t is the thickness of the pellet, and A is the cross-section area of the pellet. The value of conductivity obtained here is termed as dc conductivity and has been plotted in figure 4-28 along with the log plot of the dc conductivity.

Since the LAMOX structure has an intrinsically higher number of oxygen vacancies in the structure, the K doping has to be in a specific amount to achieve a significant increase in the electrical properties. According to Tealdi et al., [2004] doping above K = 5 mol% has a small enhancement in the conductivity. Though, the K doping suppresses the cubic to monoclinic transition of the LAMOX structure but do not enhance the conductivity. The reason for this may be attributed to large ionic radius of K⁺ ion (1.54 Å) as compared to La³⁺ ion (1.032 Å). On the structural level the large ionic radius of K creates difficulty in oxide ion migration through the vacancies. According to the literature by Wang et al., [2005], the maximum conductivity is obtained for doping of K = 2.5 mol % and higher than this level the electrical conductivity decreases. Also, the chemical affinity of K for oxygen is more as compared to La³⁺ ion, which shows the stronger bond between potassium and oxygen. These two effects will dominate over the oxide ion migration through the vacancies resulting in low ionic conductivity. The calculated value of activation energy is in agreement with the above explanation. The E_a value is found 0.68 eV which is greater than that of W doped LAMOX (0.59 eV). Therefore K doping in the LAMOX structure, which was supposed to enhance the dc ionic conductivity, has ultimately resulted in a decreased value after a certain doping level.

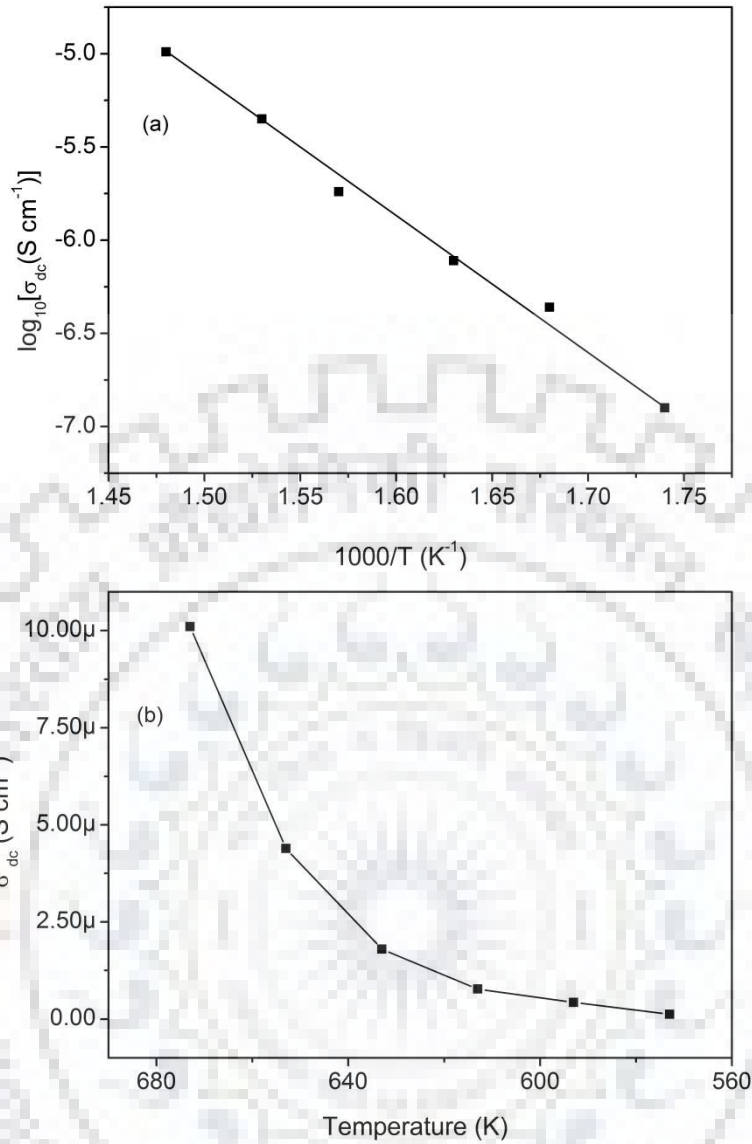


Figure 4-28 (a) log dc conductivity (Arrhenius) plot for LAMOX vs. $1/T$ (b) dc conductivity variation with temperature.

The d.c. conductivity can be written as

$$\sigma_{dc} = \sigma_0 \exp\left(-\frac{E}{kT}\right) \quad 4.12$$

where σ_0 is the pre-exponential factor, E is the activation energy, k is the Boltzmann constant and T is the absolute temperature.

Taking \log_{10} on both sides, the equation becomes,

$$\log \sigma_{dc} = \log \sigma_0 - \left(\frac{E}{k}\right) \frac{1}{T} \quad 4.13$$

From the log plot of the dc conductivity the value of activation energy was calculated from the slope of the graph using the straight-line equation $y = mx + c$. Here m represents the negative slope and c being the pre-exponential factor.

The value of σ_{dc} at 400 °C is found to be 1.2×10^{-5} S/cm and the value of E_a , i.e. activation energy is found to be 0.68 eV. This, when compared to W doped LMO, the value obtained, was 0.59 eV. The E_a value obtained here is slightly higher than that of W doped LAMOX suggesting less facilitation of ionic conductivity. The energy required for hopping of the oxide ion from one vacant site to another is more as compared to W doped LAMOX, thereby causing a reduction in the ionic conductivity of K doped LAMOX.

4.12 Relaxation dispersion studies and ionic conductivity in pristine and K doped LAMOX

This section deals with the relaxation frequency dispersion nature of pristine and doped LAMOX in response to an alternating electric field. Figure 4-29 shows the frequency dependence of the imaginary part of the impedance Z'' for K doped LAMOX, LAMOX air treated sample and Ar-H₂ treated sample. Similar type of study was conducted by Basu and co-workers on Ba doped La₂Mo₂O₉ [Basu et al., 2004]. From the figure 4-29, it is evident that the effect of the grain and grain boundary contribution can be seen at temperatures 573 K and 673 K. The dielectric relaxation process arises due to diffusional polarisation of short-range oxide ion vacancies which oscillate between anion sites parallel to the applied electric field. Random walk model reveals the process of jumping off an atom from its site to a nearby site with equal probability [Liu 2011; Chiang 1997; Orliukas 1994]. The thermally activated jumps (jump distance ' d ') in the random walk model theory, the diffusion coefficient of oxygen vacancies D_v are related to the relaxation frequency ω_r by the equation

$$D_v = \frac{1}{6} \gamma d^2 \omega_r \quad 4.14$$

where D_v [$\text{m}^2 \text{sec}^{-1}$] is the lattice diffusion coefficient of oxide ion vacancies, d^2 is the mean square jump distance between the anion sites in the crystal lattice, γ is the correlation factor and the probability population of the jump vectors, $1/6$ is the geometric factor for the cubic site symmetry and ω_r can be assumed as the jump rate between two successive oxide ion vacancy sites. For the yttria stabilised-zirconia single crystals, it has been derived that: $\gamma d^2 = 0.35a^2$ [Orliukas et al., 1994; Abelard 1982]. It has also been mentioned that geometric factor and the jump distance do not change dramatically for different crystal structures. Therefore, the diffusion

coefficients are largely dependent upon factors like availability of the neighbouring sites, migration energy, temperature, etc. This diffusional polarisation helps in calculating the diffusion coefficients and oxide ions mobility. The relaxation process, in general, is associated with a system returning from its perturbed state to equilibrium state. The relaxation process is defined by a relaxation time; in the form of $\exp(t/\tau)$, where τ is the relaxation time of the system. The inverse of this relaxation time constant is known as relaxation frequency denoted by f_r or ω_r . From the Z'' vs. frequency graph, the maximum of Z'' value the corresponding value of frequency is obtained as relaxation frequency and is written as $\omega_r \cdot \tau = 1$.

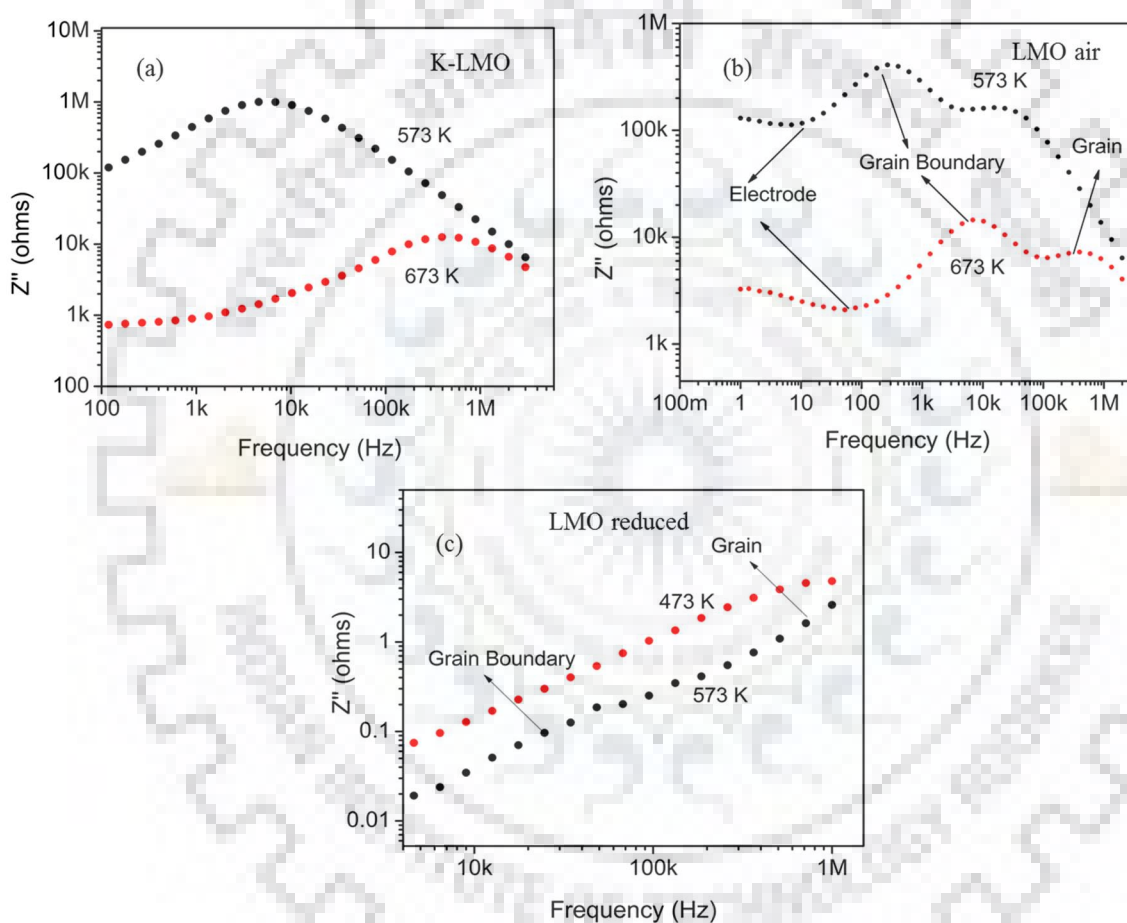


Figure 4-29 Frequency dependence of imaginary part (Z'') of the complex impedance of (a) K doped LAMOX (b) LAMOX treated in air and (c) LAMOX treated in Ar-H₂ at 900 °C.

The application of an alternating electric field leads the oxide ions to diffuse to several atomic distances. This, in turn, takes a finite amount of time for new charge distribution to establish itself after the application of the electric field. When compared to atomic and ionic polarisation processes, the diffusional polarisation and depolarisation processes are relatively slow and very much temperature-dependent.

Figure 4-30 shows the diffusional polarisation process after the atomic and ionic polarisation process upon the application of the field. If P_d is diffusional polarisation and P_{ds} is its final static value, then the rate of diffusional polarisation develops is proportional to $P_{ds} - P_d(t)$ and can be written as

$$\frac{dP_d}{dt} = \frac{1}{\tau} [P_{ds} - P_d(t)] \quad 4.15$$

where $\frac{1}{\tau}$ is proportionality constant. Integrating the above equation with initial condition $P_d = 0$ at $t = 0$ gives

$$P_d = P_{ds} \left\{ 1 - \exp\left(-\frac{t}{\tau}\right) \right\} \quad 4.16$$

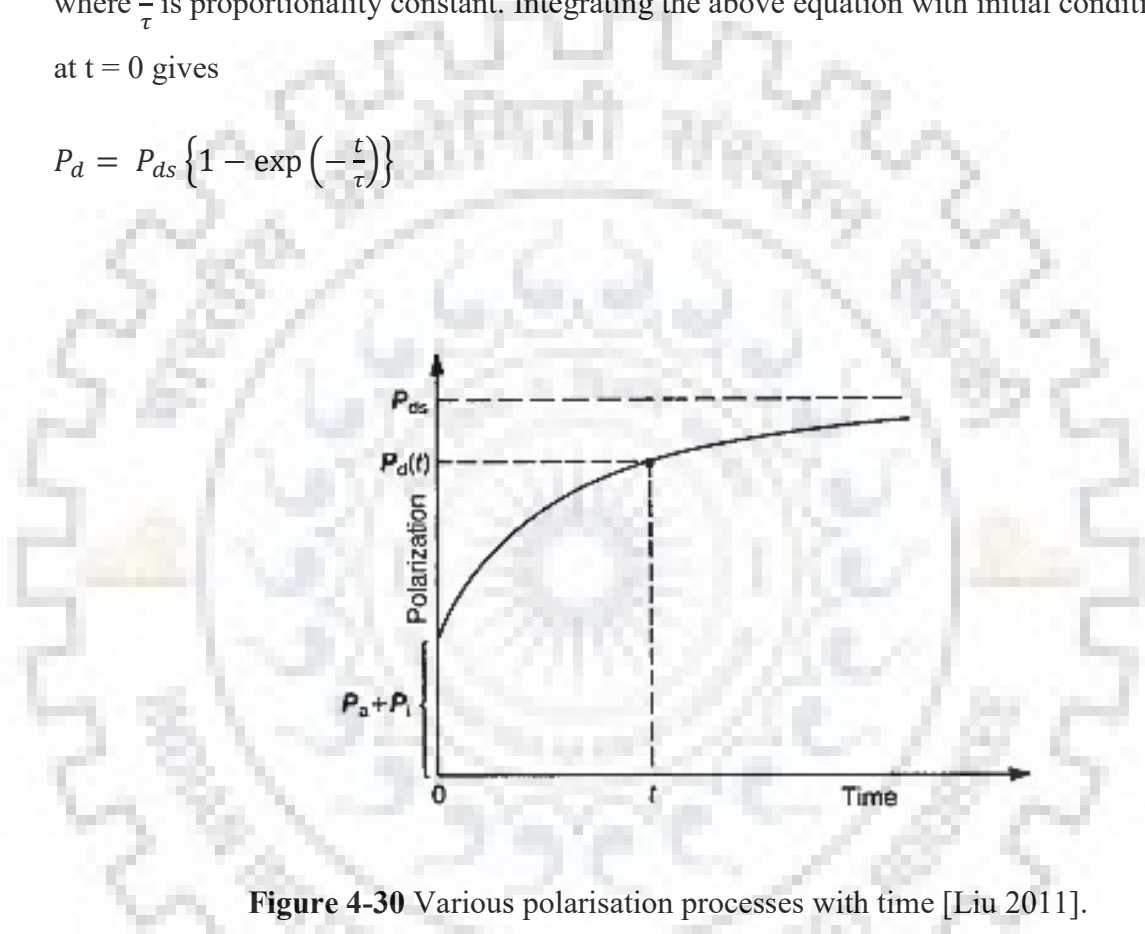


Figure 4-30 Various polarisation processes with time [Liu 2011].

The two conditions required for atomic diffusion are (i) availability of jump sites and (ii), the atom must have sufficient energy to break the bond with its neighbours and migrate to the next site which is called as the activation energy of diffusion. This has been shown in figure 4-31. The energy barrier is dependent upon the nearest atoms which need to relocate to let the diffusion happens. This process occurs more quickly at high temperatures when the atoms vibrate more at their mean positions. The temperature dependence of the diffusion process can be expressed as

$$D(t) = D_o \exp\left(-\frac{E_a}{RT}\right) \quad 4.17$$

where D_o is the constant and E_a activation energy.

The temperature dependence of the jump rate of the oxygen vacancies can be expressed by the formula

$$\omega = \omega_o \exp\left(-\frac{E_a}{kT}\right) \quad 4.18$$

where ω_o is the phonon frequency of the lattice vibration. The activation energy E_a is similar to activation energy of diffusion.

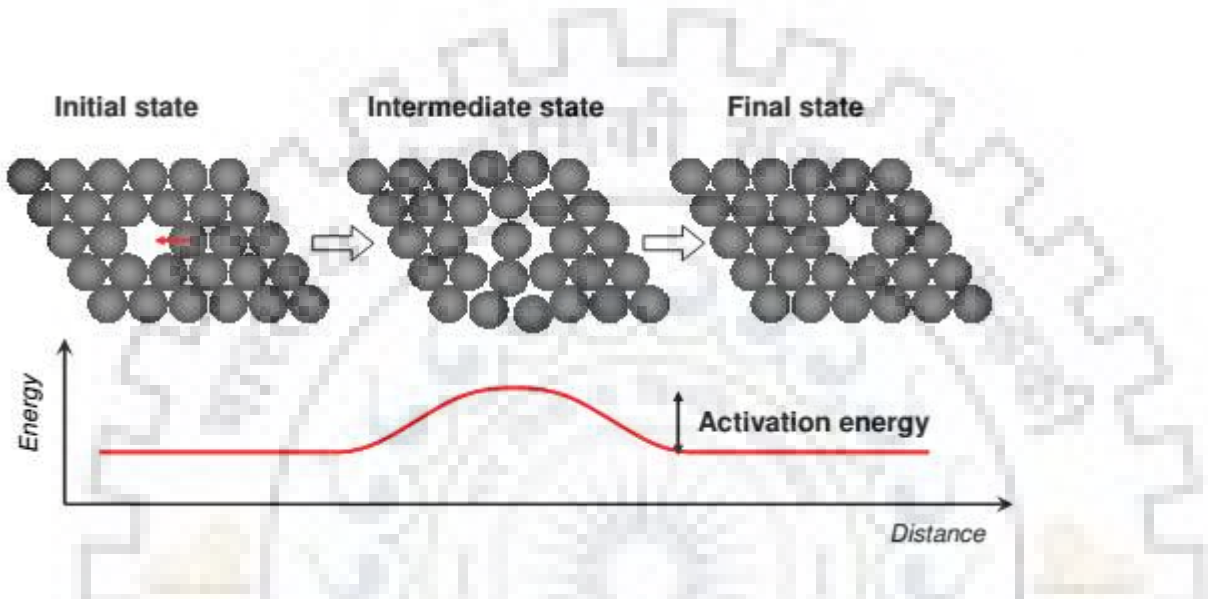


Figure 4-31 Thermally activated diffusion process and energy barrier during migration of ions [Liu 2011].

The ionic conductivity of cubic LAMOX and doped LAMOX may be defined as the product of the total number of oxide ion vacancies n , their mobility μ [$\text{m}^2/\text{V}\cdot\text{sec}$] and electric charge $z \cdot e$ [Amp \cdot sec]

$$\sigma = \mu n z e \quad 4.19$$

The mobility of the oxide ions is related by the diffusion coefficient of mobile oxide ion vacancies by the Nernst-Einstein equation

$$D_v = \mu kT / z e \quad 4.20$$

where k is the Boltzmann constant ($8.617 \cdot 10^{-5}$ eV / K), T is the absolute temperature in K, n is the concentration of oxide ion vacancies in m^{-3} , e is the electron charge, and z is the valence of oxygen vacancies.

The total number of extrinsic oxide ion vacancies created by the substitution of an atom other than host atoms may be calculated according to the formula

$$n_o = 4x/a^3$$

4.21

where a is the lattice parameter of the cubic unit cell and x is the number of oxygen vacancies per unit cell.

While using the above theory and postulations, all the formulae have been focussed on cubic yttria-stabilised zirconia. Here the same model has been adapted for cubic LMO and its doped cubic members. Therefore, to get an insight of how dipoles are responding in an external electric field of high and low frequencies, the same model of cubic YSZ was used to analyse the dielectric relaxation behaviour of doped and un-doped LAMOX.

From figure 4-29, relaxation frequency and corresponding relaxation time are calculated from maximum value of Z'' in the graph shown. The diffusion coefficient of oxygen vacancies has been calculated from equation 4.20. From equation 4.19, with the known value of oxide ion d.c. conductivity, the mobility of oxide ions is calculated and correspondingly, the total volume of mobile oxide ion vacancies was calculated and listed in table 4-12. The data are obtained at 380 °C and 400 °C.

Table 4-12 Various relaxation parameters for LAMOX air sintered and K - LAMOX composition.

Composition	Parameters						
	ω_R (rad s ⁻¹)	τ_R (sec)	μ (m ² /V.s)	D_v (m ² /s)	n (m ⁻³)	n_o (m ⁻³)	E_a (eV)
LAMOX	1.66 x10 ⁶	6x10 ⁻⁷	5x10 ⁻¹³	5x10 ⁻¹⁴	1x10 ²⁵	--	1.0
K- LAMOX	2.756 x10 ⁶	3x10 ⁻⁷	1x10 ⁻¹¹	8x10 ⁻¹⁴	2x10 ²⁵	1.5x10 ²⁸	0.68

From the table, it is evident that mobility of oxide ions for air sintered α - La₂Mo₂O₉ is lower than the value of K doped LAMOX. It may be attributed to the ordering of oxide ion/vacancy pair at low temperatures in LAMOX as compared to K = 10 mol % doped LAMOX which has a disordered pair of oxide ion/vacancy and also has a low activation energy barrier as compared to α - La₂Mo₂O₉.

4.13 Inter-atomic potentials, thermal energy and their relation to conductivity: A theoretical estimate

A lattice is usually represented by a set of ions or charged atoms. The short-range interactions of these ions are represented by interatomic pair potentials. According to Fumi and Tosi, these short-range potential can be described by the equation:

$$V_{Re-O} = A \exp \left[\frac{r_{Re} + r_o}{\rho} \right] \exp(-r/\rho)$$

where r_{Re} and r_o are the ionic radii of the rare earth cation and oxide ion respectively. Only A and ρ are required to compute the potential.

The thermal energy given to system can be defined as kT , where k is the Boltzmann constant and T is the temperature in Kelvin. When this energy is supplied to a system, the thermodynamic entropy of that system increases. According to the Arrhenius representation, the ionic conductivity can be written as:

$$\sigma T = A' \exp(-E_a/kT)$$

where σ is the ionic conductivity, T is the temperature in Kelvin, E_a is the activation energy and A' is the pre-exponential constant given by

$$A' = C\gamma(Z^2e^2/k)a_o^2v_o \exp(\Delta S_m/k)$$

where C is the concentration of charge carriers, γ is a geometrical factor; Ze is the charge of the carriers, a_o is the jump distance, v_o is the jump attempt frequency, and ΔS_m is the entropy of migration. The term E_a/kT represents the amount of entropy per mole. The E_a is similar to ΔH_m , enthalpy of migration. The concentration of charge carriers C can be calculated by the number of oxide ions able to exchange with oxygen vacancies, i.e. by

$$C = N_o[V_{\ddot{O}}](1 - [V_{\ddot{O}}])$$

where N_o is the number of anion sites per unit volume and $[V_{\ddot{O}}]$ is the concentration of oxygen vacancies expressed as site fraction. For small values of oxygen vacancies the above equation can be approximated as

$$C \approx N_o[V_{\ddot{O}}]$$

kT at room temperature corresponds to 0.02568 eV. According to the Born-Mayer equation, the short-range component of two body potential can be described as

$$V(r) = A \exp(-r/\rho) - Cr^{-6}$$

where C is in $\text{\AA}^{(+6)}$ eV. The value of A , ρ and C are 22764.3eV, 0.1490 \AA and 27.88 $\text{\AA}^{(+6)}$ respectively.

By using the Born Mayer equation one can determine the interatomic potential between oxide ions in the short-range which is 2×10^{-4} and less than the value of $1 kT$. This shows that even at the room temperature there is sufficient energy that can overcome the interatomic potential of oxide ions contributing to ionic conductivity [Kilner 1982; 2000].

4.14 Effect of multiple doping at La and Mo site in LAMOX

The main purpose of this section is to stabilise the Mo^{6+} state in reducing atmosphere. In this context, K and W doping in LAMOX were considered. Simultaneous doping at La and Mo sites by rare earth elements and W at respective sites are studied in this section by XPS analysis.

T.Y Jin [2007] and his co-workers reported the stabilisation of the Mo^{6+} state by Dy and W doping at La and W site, respectively. However, the results obtained are not in agreement with the authors' results, which will be shown in the subsequent section of this chapter. The study has been done by means of x-ray photoelectron spectroscopy through which the chemical states of the respective elements have been studied.

4.14.1 Microstructural study of rare-earth (Eu) doped and W doped LAMOX in Ar-H₂ atmosphere

This section is devoted to the preliminary confirmation of the existence of electronic conductivity in the Eu and W doped samples treated in Ar-H₂ atmosphere for 4 hours at 900 °C. The microstructural images in figure 4-32 were captured without any conductive coating on the sample. This implies that the sample is conductive since the electron charging effect is less. Further confirmation about electronic conductivity due to Mo reduction has been shown in the next section of the XPS analysis.

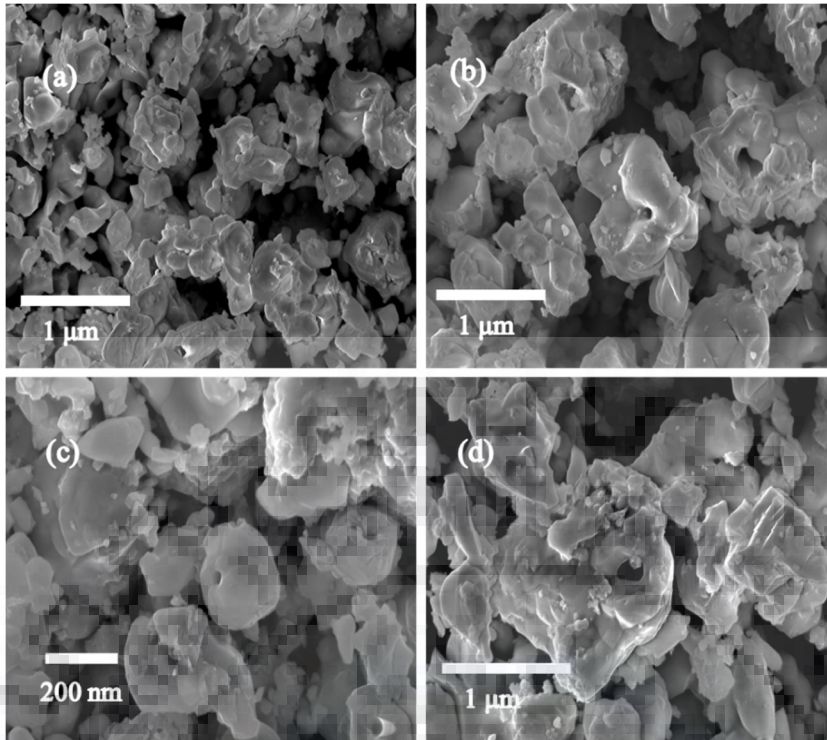
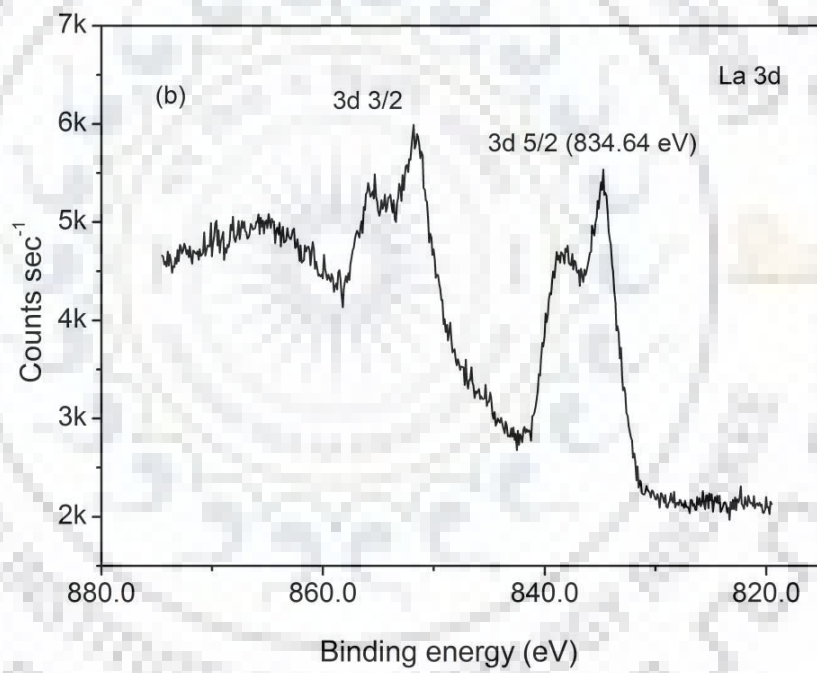
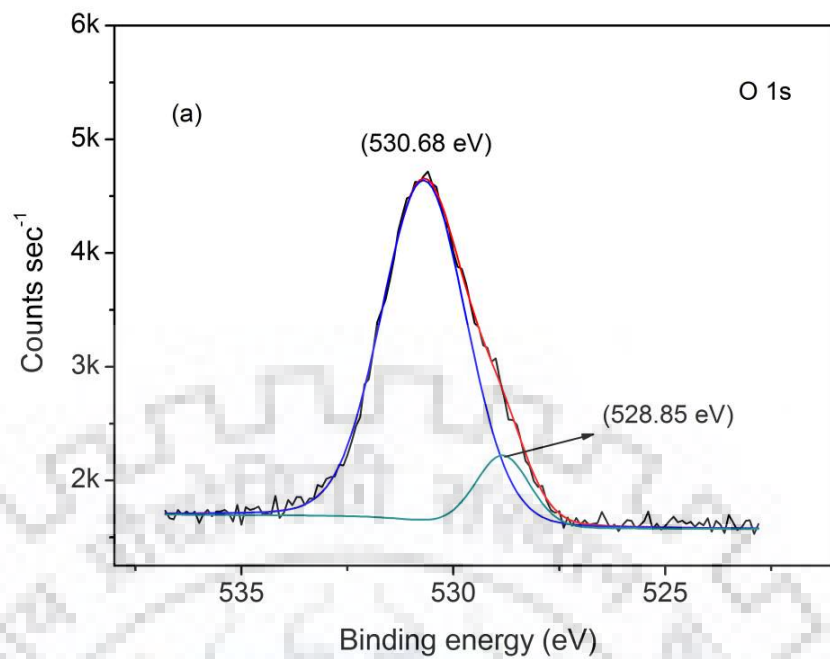
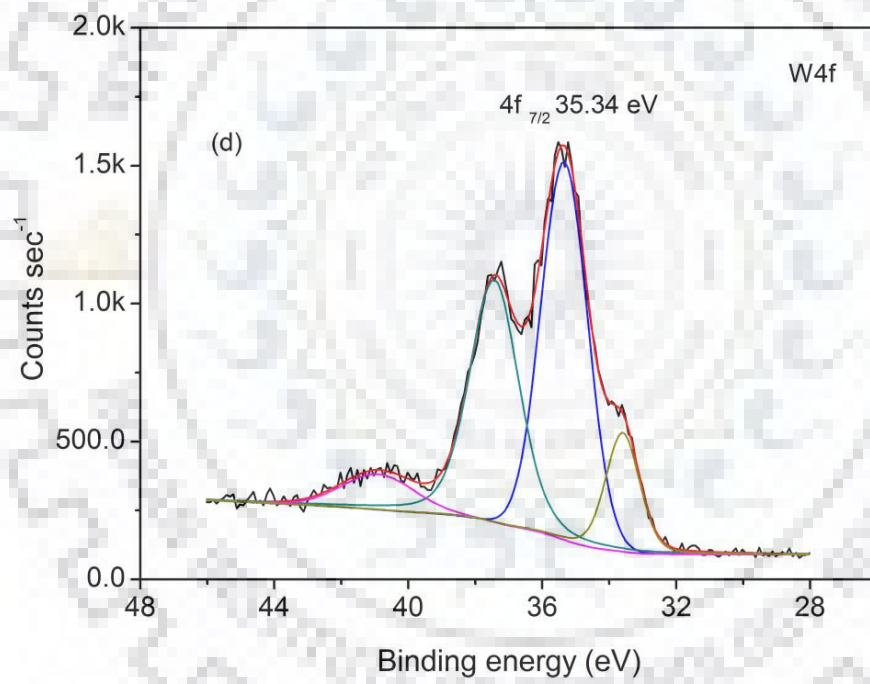
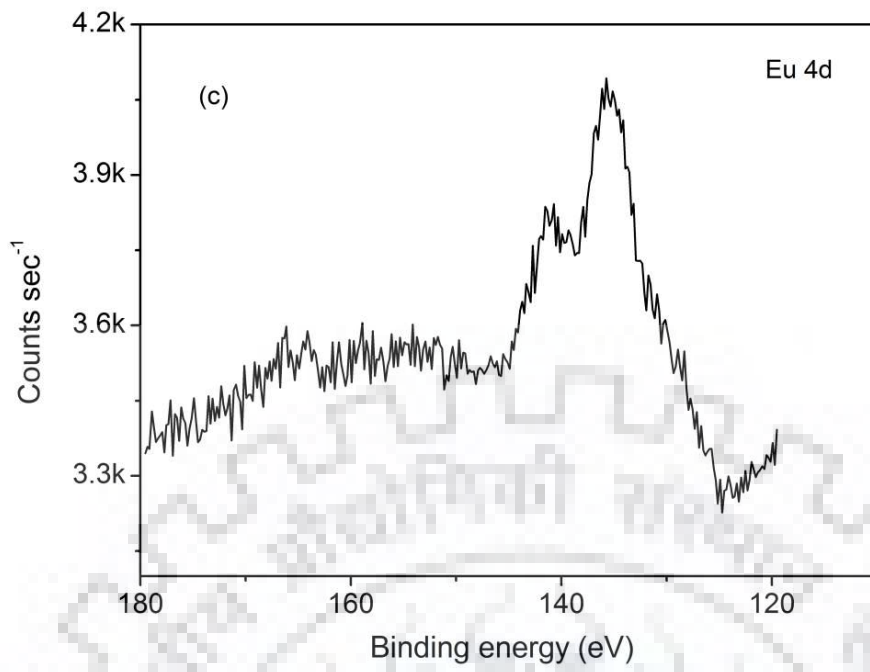


Figure 4-32 FE-SEM images of Eu and W doped $\text{La}_2\text{Mo}_2\text{O}_9$. Intra-granular pores are visible without carbon coating on the specimen due to reduction in Ar- H_2 atmosphere.

4.14.2 XPS study of rare-earth-doped ($\text{La}_{1.8}\text{X}_{0.2}\text{Mo}_1\text{W}_1\text{O}_9$) (X = Eu, Sm, Tm, Y) in reductive atmosphere

Figure 4-33 to 4-36 shows the core level spectra of rare-earth: Eu, Sm, Tm, and Y doped LAMOX for 10 mol % and W = 50 mol % at La and Mo site in LAMOX respectively. Some of the elemental spectra recorded have more noise interference because of its low atomic concentration.





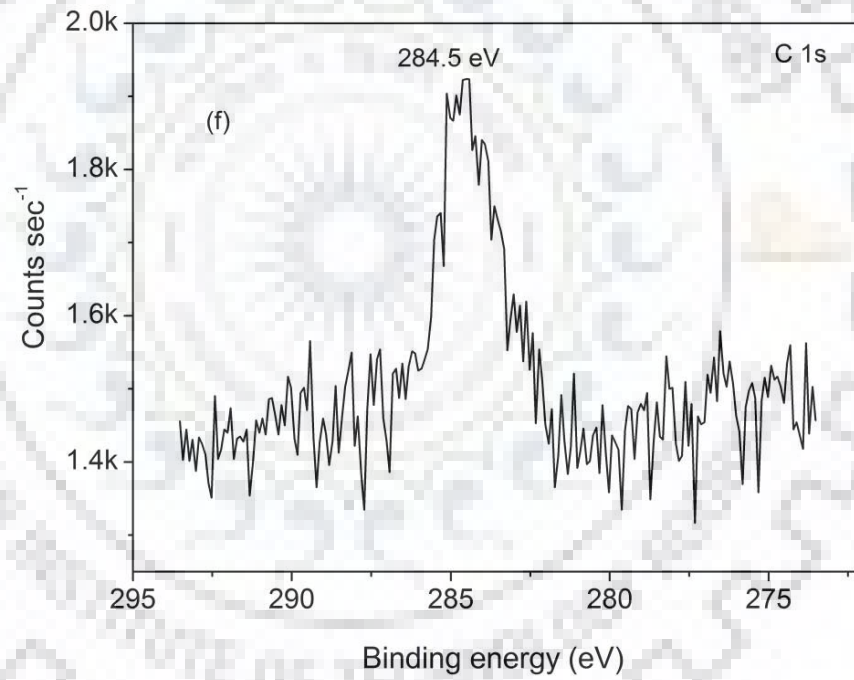
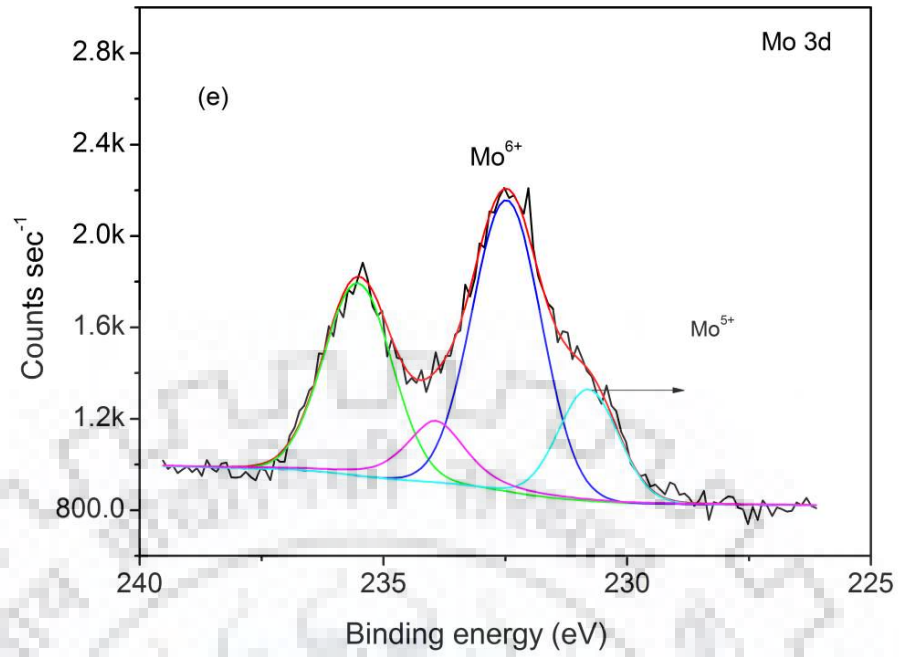
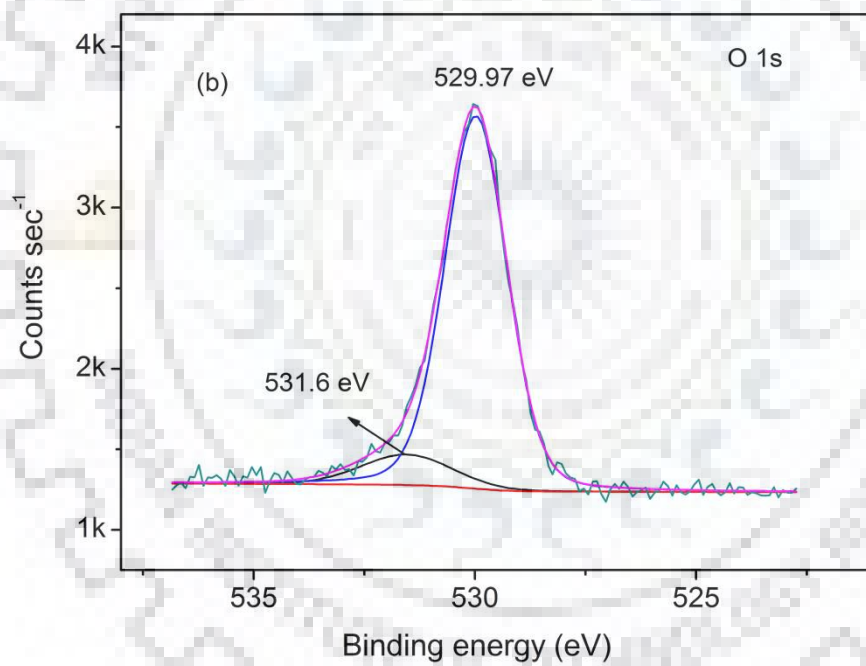
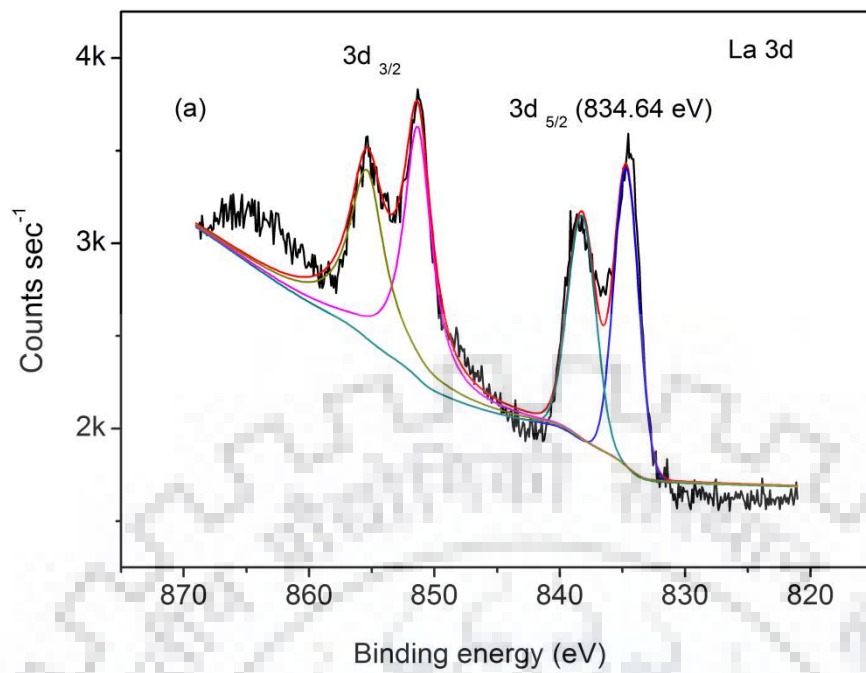
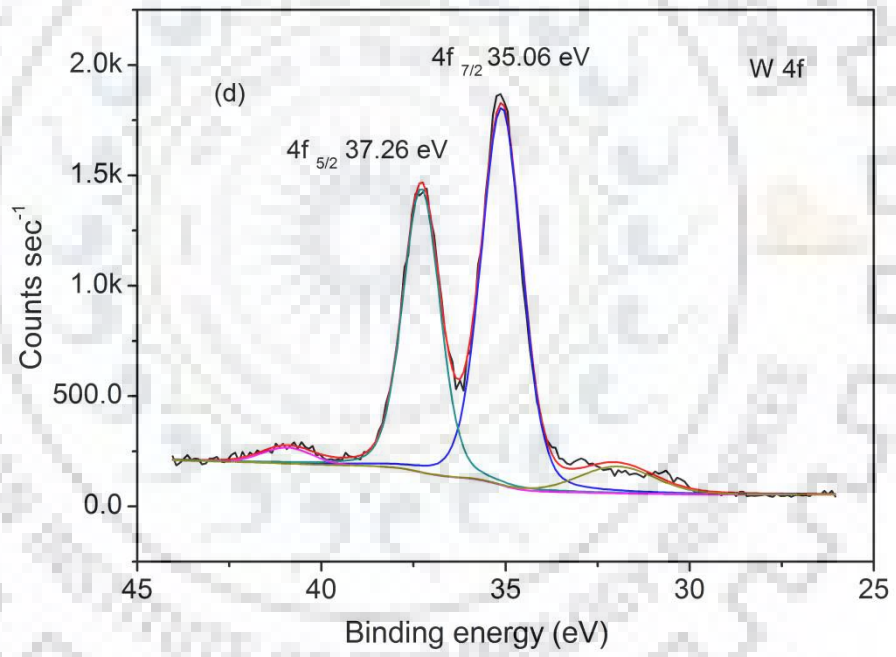
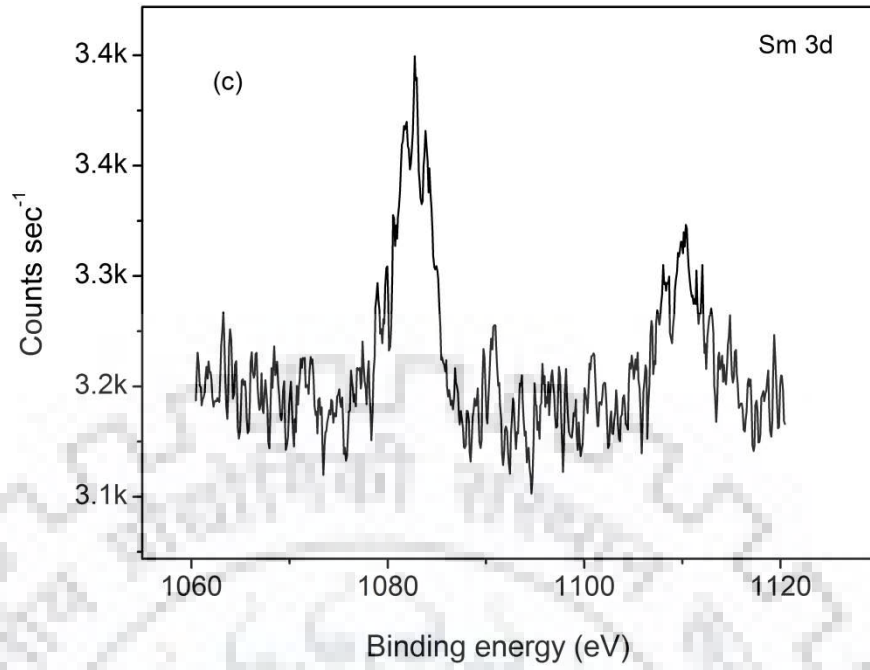


Figure 4-33 Core level spectra of respective elements of Eu 10 mol % and W 50 mol % doped LAMOX treated in reductive atmosphere. (a) O 1s (b) La 3d(c) Eu 4d (d) W 4f (e) Mo 3d and (f) C 1s.





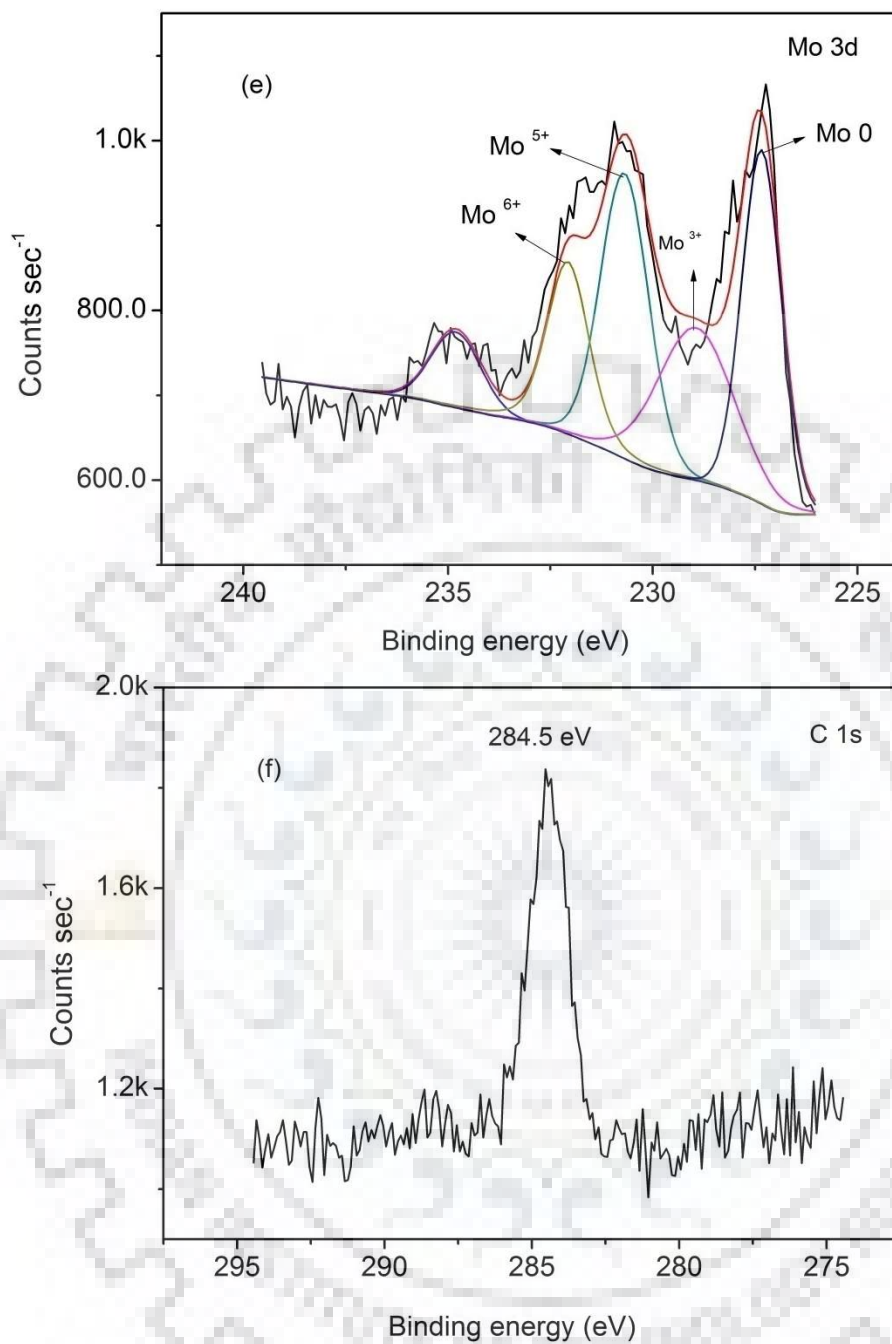
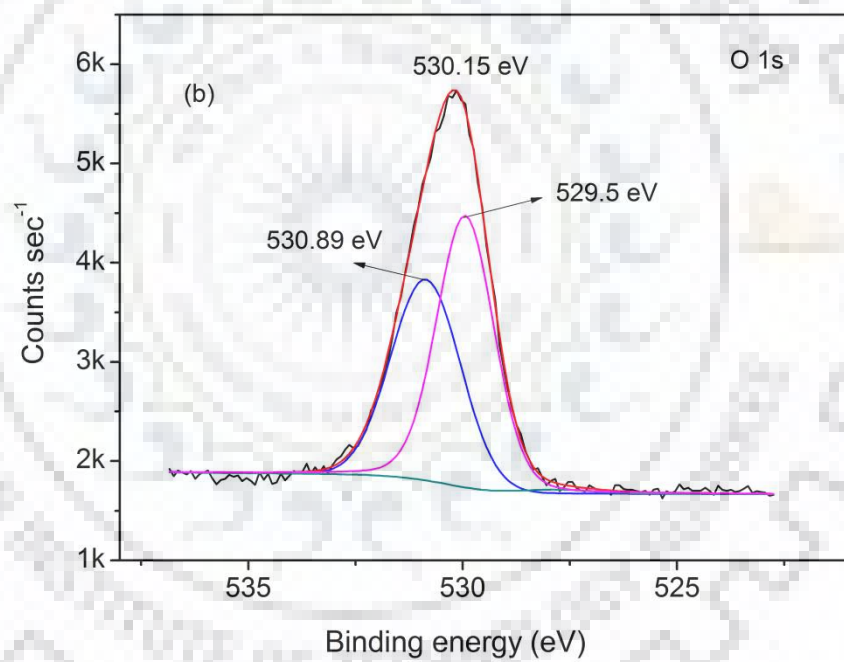
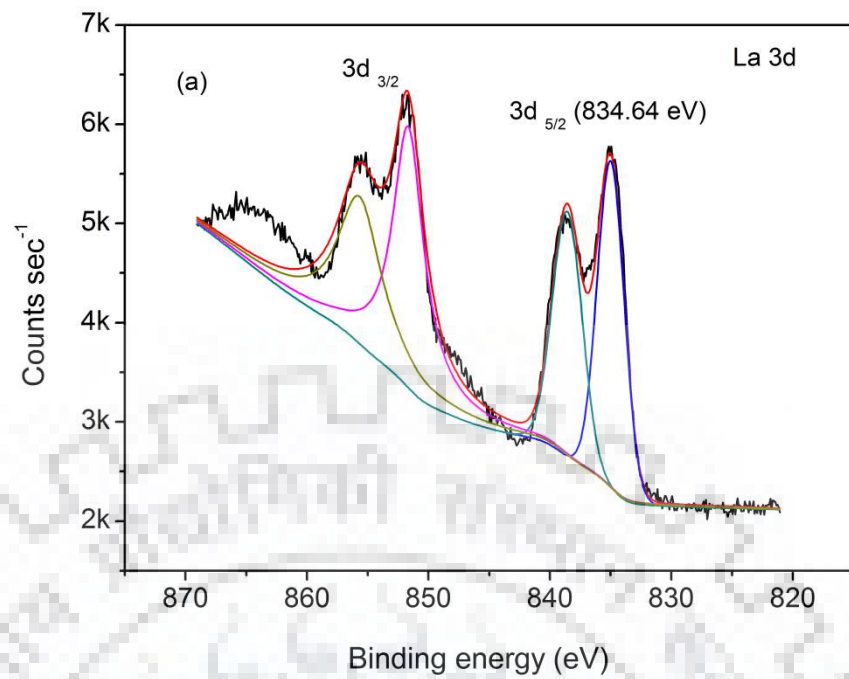
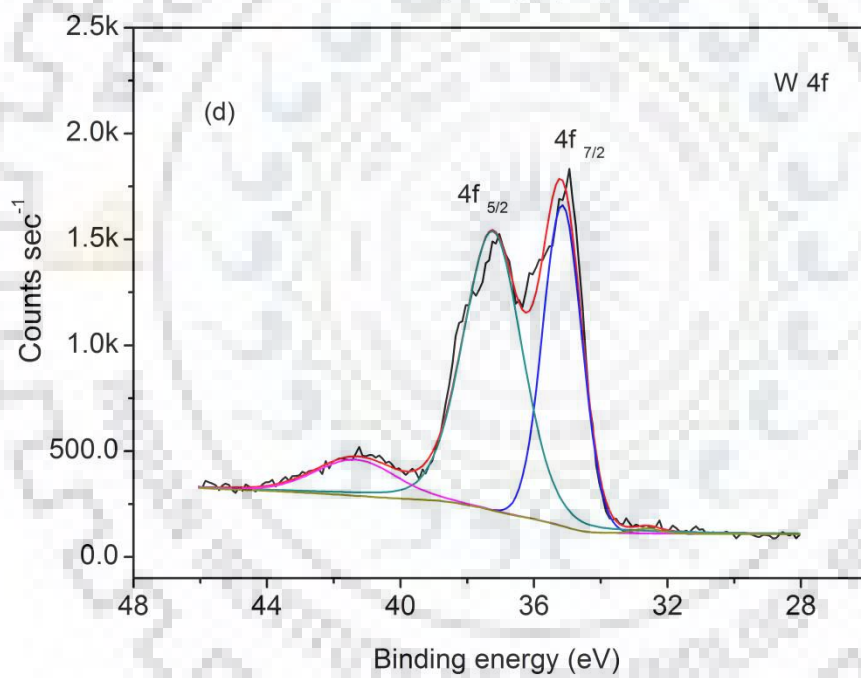
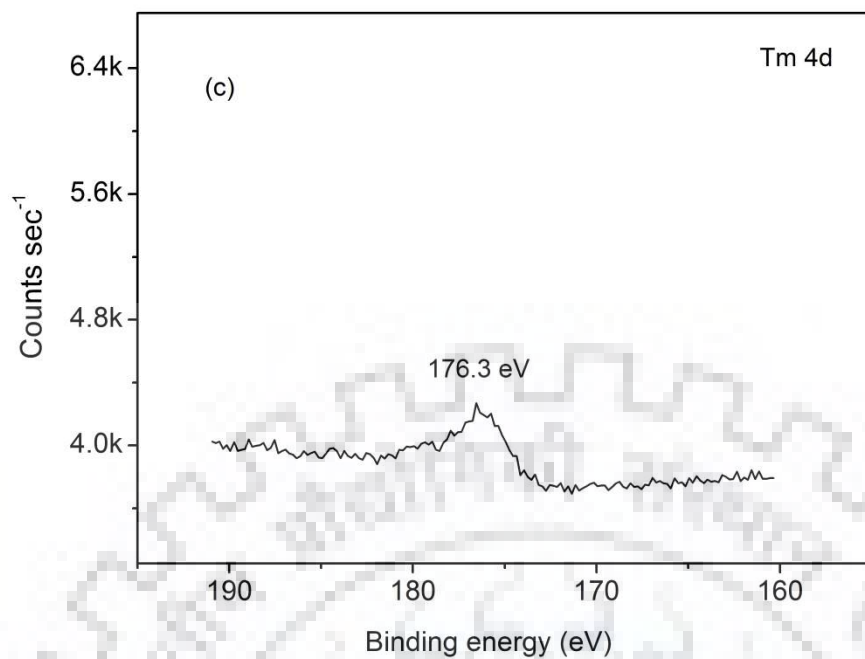


Figure 4-34 Core level spectra of respective elements of Sm 10 mol % and W 50 mol % doped LAMOX treated in reductive atmosphere. (a) La 3d (b) O 1s (c) Sm 3d (d) W 4f (e) Mo 3d and (f) C 1s.





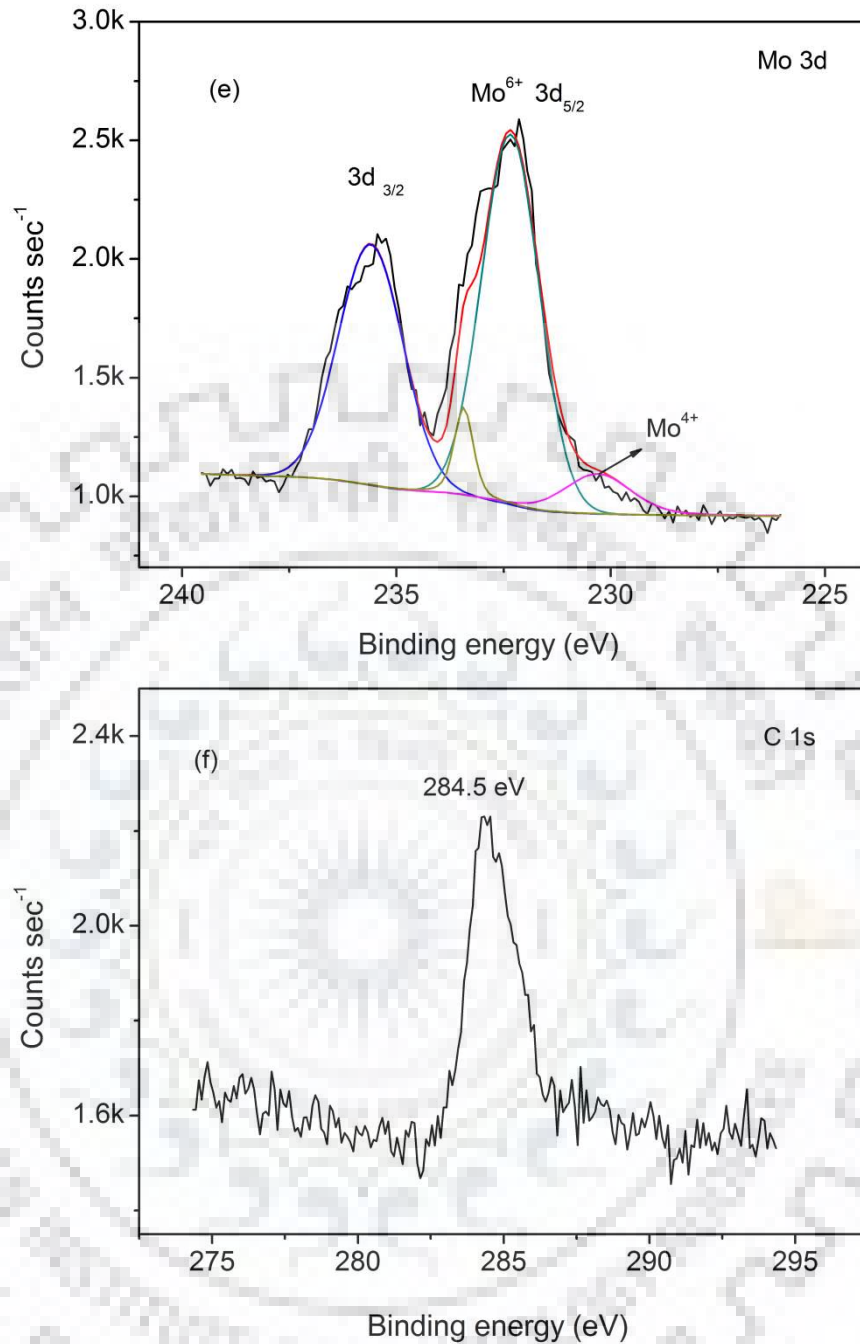
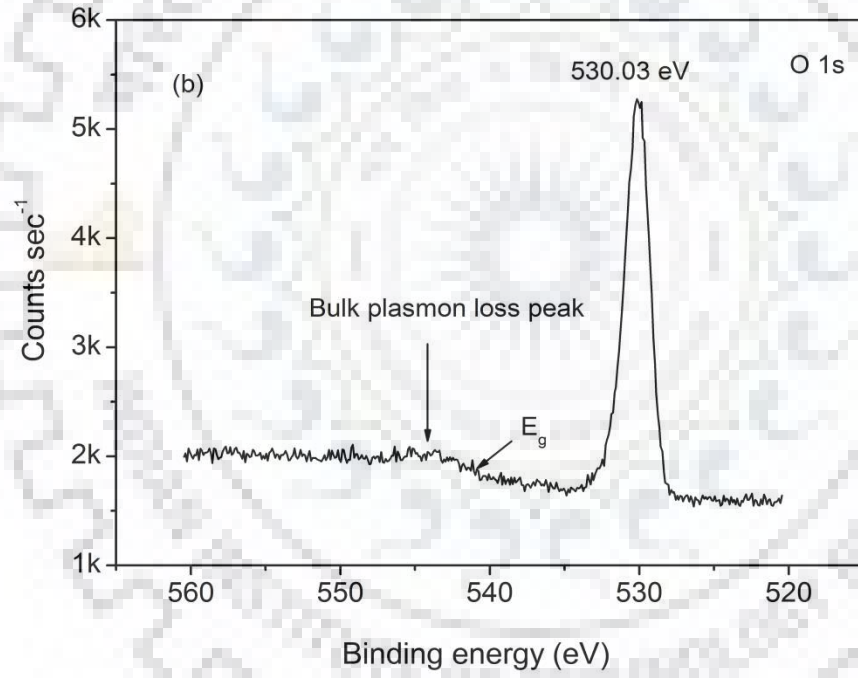
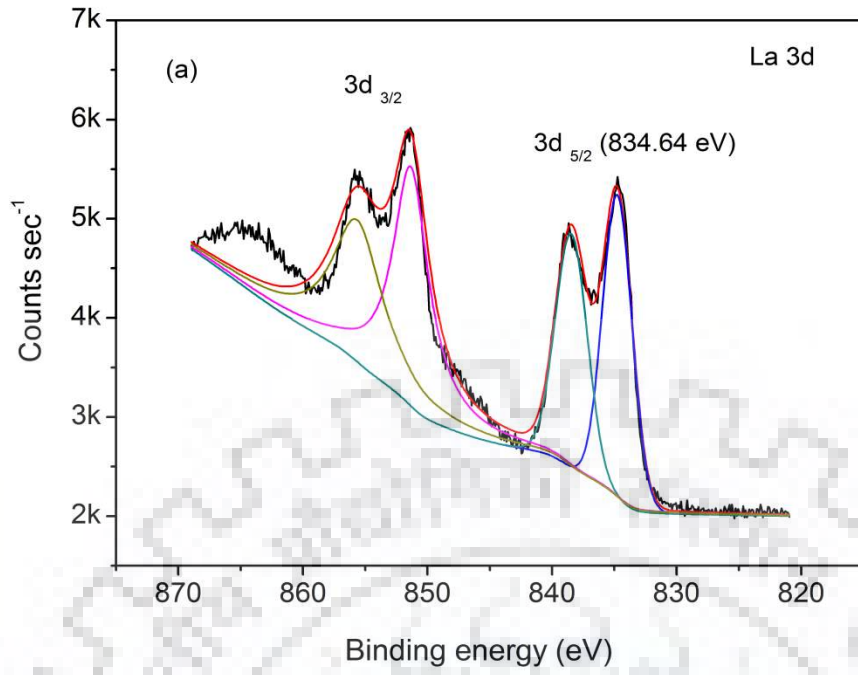
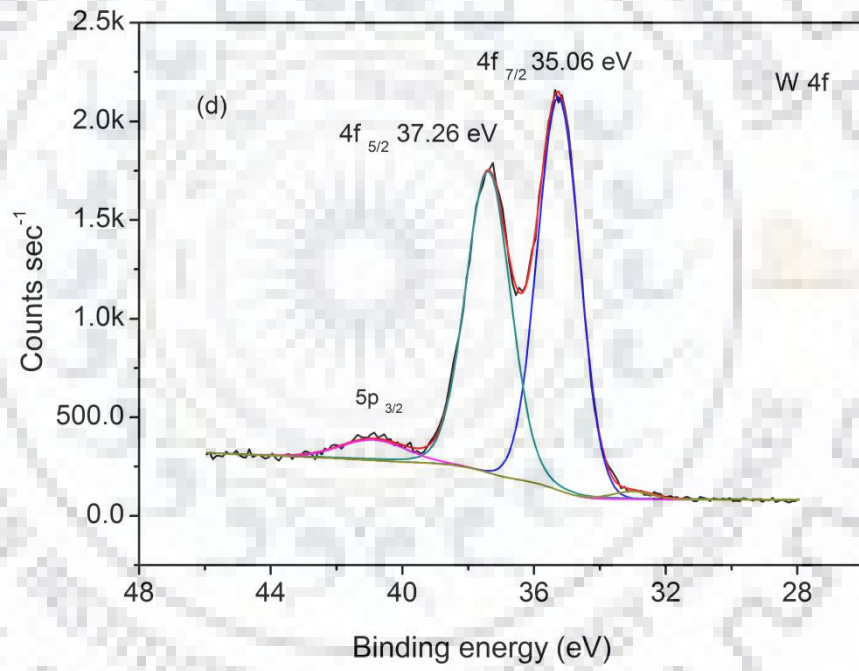
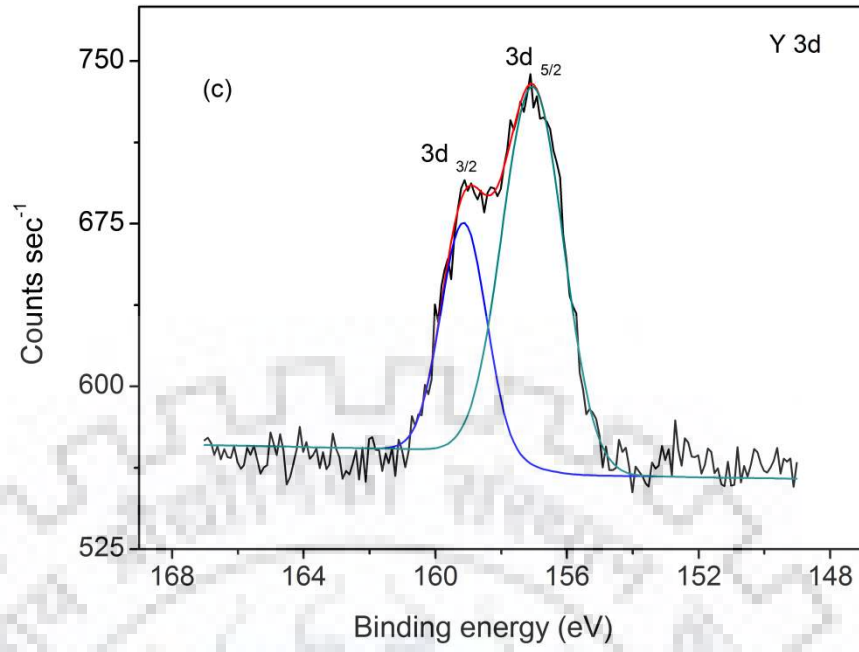


Figure 4-35 Core level spectra of respective elements of Tm 10 mol % and W 50 mol % doped LAMOX treated in reductive atmosphere. (a) La 3d (b) O 1s (c) Tm 4d (d) W 4f (e) Mo 3d and (f) C 1s.





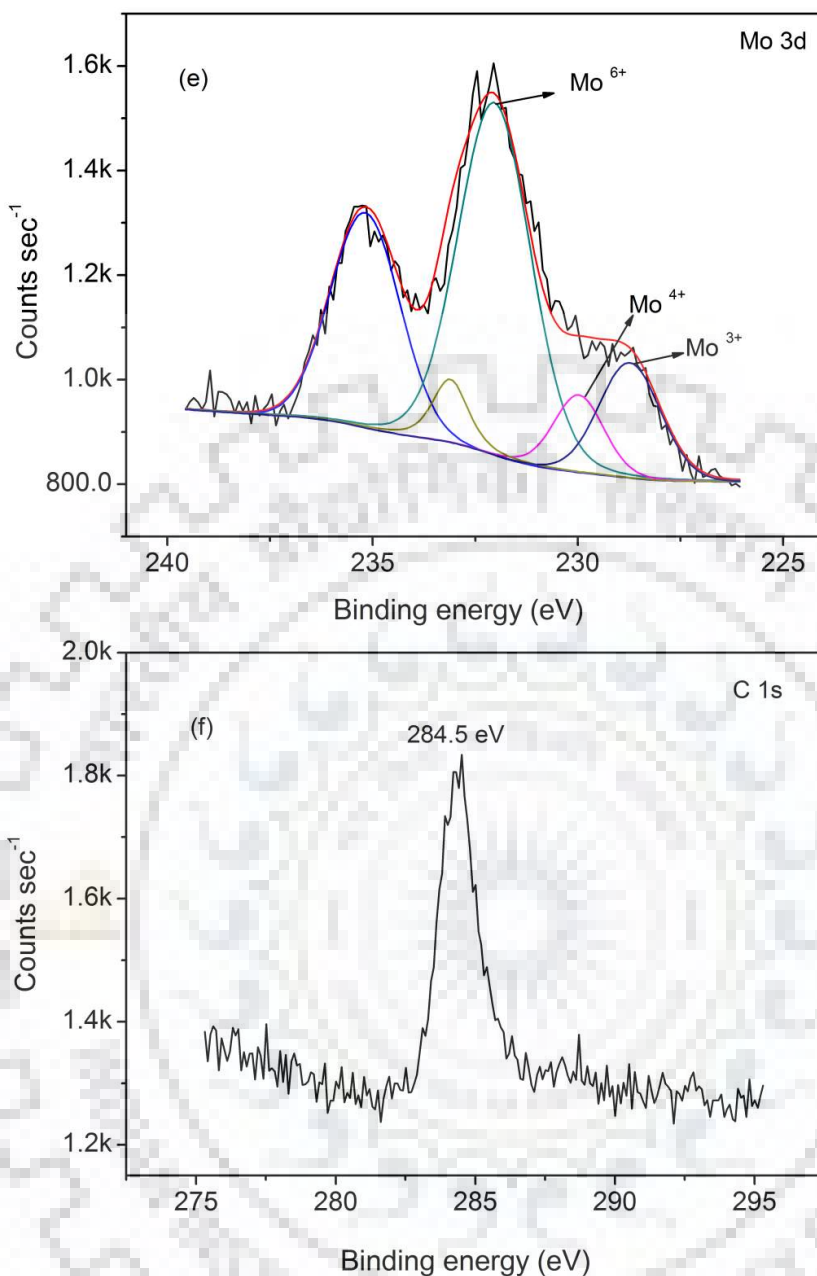


Figure 4-36 Core level spectra of respective elements of Y 10 mol % and W 50 mol % doped LAMOX treated in reductive atmosphere. (a) La 3d (b) O 1s (c) Y 3d (d) W 4f (e) Mo 3d and (f) C 1s.

As evident from figure 4-33 to 4-36, when the rare earth element and W doped LAMOX compositions treated at 900 °C in reducing atmosphere, the only element affected was Mo. It has been shown earlier also that Mo 3d is most susceptible to reduction. In every XPS plot of Mo 3d spectrum presence of multiple peaks upon deconvolution of the original peak confirms the presence of lower oxidation states of Mo. Apart from Mo 3d peak, La 3d, C 1s, and W 4f peaks are not affected in reducing atmosphere. The O 1s peak exhibits the presence of multiple peaks

composed of various metal oxides. Rare-earth doped elements show not exactly the same nature of the peaks. This may be due to overlap of auger peaks and other shallow core level peaks of other elements. But the peaks lie in the vicinity of the values as reported in the XPS literature [Moulder 1995]. This result obtained is not totally in agreement with the results of T.Y. Jin and co-workers.

4.15 Summary

In this chapter, the effect of various doping in LAMOX has been studied in order to overcome the disadvantages of pristine LAMOX like Mo reduction, thermal expansion coefficient mismatch due to phase change at ~ 600 °C and low ionic conductivity at room temperature. The first section of the chapter deals with W doping at Mo site which has a solubility limit of ~ 80 mol % at Mo site. The structural, morphological, x-ray photoelectron spectroscopy (XPS) and ion dynamics along with conductivity measurements of $\text{La}_2\text{Mo}_{2-x}\text{W}_x\text{O}_9$ ($0.25 \leq x \leq 1.5$) both in air and reductive atmospheres have been presented and discussed. Though the W doping in LAMOX successfully stabilises the cubic phase at room temperature, it was not able to fully suppress the Mo^{6+} reduction as clearly revealed by comprehensive FE-SEM and x-ray photoelectron spectroscopic studies. No other elements in the doped LAMOX compositions were reduced.

The microscopic study shows the presence of pores in the grains, which indicate the interaction of gas and solid particles leading to the formation of intra-granular pores. The reduction of Mo in Ar- H_2 atmosphere gives rise to electronic conductivity, which is not desirable in the fuel cell operation. The electrical conductivity measurement of the doped LAMOX samples treated in Ar- H_2 atmosphere has not been done in the present study; however, the conductivity values are reported elsewhere by Jacquens et al., [2010].

With the help of ion dynamics study it was shown that ac conductivity follows the universal power law. $\log \sigma_{dc}$ vs. $1/T$ curve follows the Arrhenius type behaviour of conductivity rise with the temperature. The imaginary part of modulus at different temperatures show peak shift towards the right side on frequency scale suggesting the presence of multiple jump frequencies of the oxide ions for energy barrier crossover. The parameter β is known as Kohlrausch exponent used to characterise the stretch of peak M'' and is related to power-law exponent by $\beta = 1-s$. The dc ionic conductivity calculated for W = 0.25 doped LAMOX follows the Arrhenius equation. The complex impedance plot shows a broad and depressed semi-circle suggesting a non-debye type relaxation. The activation energy value was found to be ~ 0.59 eV which is higher than that

of O-O bonding energy of the order of 10×10^{-4} eV. Thus the oxide ion conductivity occurs at room temperature and increases with temperature as evident from the log plot of the conductivity. Phase transition has been successfully addressed by W doping, but Mo reduction was not fully eliminated.

The second section of the chapter presents the effect of K doping in LAMOX. The composition $\text{La}_{1.9}\text{K}_{0.1}\text{Mo}_2\text{O}_{9-\delta}$ shows the stabilisation of high-temperature cubic phase of $\text{La}_2\text{Mo}_2\text{O}_9$ at room temperature, as confirmed by XRD and Rietveld analysis along with K_2O . $\text{La}_{1.8}\text{K}_{0.2}\text{Mo}_2\text{O}_{9-\delta}$ composition shows the formation of K doped LAMOX phase with the appearance of K_2O as a secondary phase. The microstructural analysis also reveals some intra-granular pores suggesting incomplete sintering in Ar- H_2 atmosphere of the doped compositions. X-ray photoelectron spectroscopic study has been done and shows the Mo^{6+} stability in the reductive atmosphere. $\text{La}_{1.8}\text{K}_{0.2}\text{Mo}_2\text{O}_{9-\delta}$ has more tolerance towards reducing atmospheres as compared to $\text{La}_{1.9}\text{K}_{0.1}\text{Mo}_2\text{O}_{9-\delta}$ composition. Furthermore, the complex impedance spectroscopy was also performed on $\text{La}_{1.8}\text{K}_{0.2}\text{Mo}_2\text{O}_{9-\delta}$ in order to investigate the electrical conductivity. From the log conductivity plot, the value of activation energy was found to be 0.68 eV. The activation energy of W doped LAMOX obtained was 0.59 eV. The increased value of activation energy is attributed to large ionic radius of K^+ ion as compared to La^{3+} ions, which suppresses the effect of oxide ion migration through vacancies. Also, the affinity of K^+ ions towards oxide ions is greater as compared to La^{3+} ions which restrict the movement of oxide ions through the vacancies in the structure.

The third and last part of the chapter shows the effect of simultaneous rare earth elements and W doping simultaneously in LAMOX at La and W site, respectively. The x-ray photoelectron spectroscopy study shows very slight Mo^{6+} stabilisation has occurred in the reductive atmosphere. Therefore, in a nutshell, the K doping at Mo site and La site respectively have been successful in stabilising Mo from reduction in Ar- H_2 atmosphere and may have a potential application at intermediate temperature fuel cell operation.

Chapter 5

Compatibility studies of $\text{La}_2\text{NiO}_{4+\delta}$ and $\text{La}_2\text{Mo}_{1.5}\text{W}_{0.5}\text{O}_9$ based electrode/ electrolyte for fuel cell application.

5.1 Introduction

The previous chapters dealt with the study of LAMOX and its derivatives as electrolytes and overcoming their drawbacks such as phase transition and Mo reduction in Ar- H_2 atmosphere. The problems associated with the LAMOX electrolytes have been sorted out, and it has been shown that Mo reduction could be suppressed by K doping at the La site. But, in order to exploit the electrolyte in actual cell application, compatible electrodes need to be identified to give a more meaningful finding.

This chapter deals with the compatibility study of $\text{La}_2\text{NiO}_{4+\delta}$ (LN) and $\text{La}_2\text{Mo}_{1.5}\text{W}_{0.5}\text{O}_9$ based electrode (cathode) / electrolyte and NiWO_4 (NW) / $\text{La}_2\text{Mo}_2\text{O}_9$ as anode/electrolyte material for fuel cell application. Various characterisation such as x-ray diffraction, microstructural analysis by scanning electron microscopy, and x-ray photoelectron spectroscopy both in air as well as in Ar- H_2 atmosphere treated samples was done to investigate the compatibility of two systems in the respective atmosphere for SOFC application. So far, only the structural study of $\text{La}_2\text{NiO}_{4+\delta}$ / α - LAMOX was described and reported elsewhere [Corbel and Lacorre 2006]. The present part of the work may be treated as a continuation of work done by the above author, who studied the compatibility of LN with LAMOX. So far, the compatibility of NiWO_4 has been tested only with YSZ based electrolytes and described elsewhere [Sabolsky et al., 2013]. The Mo reduction studies in reductive atmosphere based on XPS results on LAMOX with NiWO_4 has been carried out in this chapter.

A few researchers have studied the compatibility of conventional perovskite cathode materials such as $\text{La}_{0.6}\text{Sr}_{0.4}\text{Co}_{0.2}\text{Fe}_{0.8}\text{O}_{3-\delta}$ (LSCF), $\text{La}_{0.8}\text{Sr}_{0.2}\text{MnO}_{3-\delta}$ (LSM) with $\text{La}_2\text{Mo}_2\text{O}_9$ electrolyte. The $\text{La}_{0.75}\text{Sr}_{0.25}\text{Cr}_{0.5}\text{Mn}_{0.5}\text{O}_{3-\delta}$ (LSCM) and LMO at 600 °C show the appearance of new impurity phases of SrMoO_4 (Scheelite) and La_2MoO_6 . This is clearly evident that Sr and Mo diffuse into each other, making the respective compounds of Sr and Mo deficient. Hence, it makes them unsuitable for electrode and electrolyte applications in the fuel cell. A similar case was observed with the LSM and LCF electrode materials [Corbel and Lacorre 2006].

G. Corbel and P. Lacorre [2006] have reported the study on $\text{La}_2\text{Mo}_2\text{O}_9$ with a new kind of cathode material $\text{La}_2\text{NiO}_{4+\delta}$ which is considered to be good cathode material both in terms of electrical

conductivity ($76-95 \text{ S cm}^{-1}$ over $600 \text{ }^\circ\text{C} - 800 \text{ }^\circ\text{C}$) and electro-catalytic activity. The cathode material lanthanum nickelate shows a moderate thermal expansion coefficient along with high oxygen diffusion and oxygen exchange at gas/solid interfaces [Huang et al., 2008].

The reaction of LN and LAMOX at temperature of about $1000 \text{ }^\circ\text{C}$ forms the chemical compounds NiO and La_2MoO_6 on the cathode side of which NiO has a poor electrical conductivity of about $10^{-13} \text{ S cm}^{-1}$ at room temperature. The NiO has a cubic structure which is classified in the category of Mott-Hubbard insulator having a negative impact on electrochemical properties [Niu et al., 2013]. Therefore, it can be concluded that NiO either as the main product or as by-product on the anodic/cathodic side does not play a suitable role in electrode application of SOFCs.

In the present study, the chemical reactivity study for $\text{La}_2\text{NiO}_{4+\delta}$ and $\text{La}_2\text{Mo}_{1.5}\text{W}_{0.5}\text{O}_9$ was done by taking the equimolar amounts of respective compounds. The respective oxides under study were mixed thoroughly using an agate mortar and pestle in acetone medium. The equimolar mixture of LN / W-LAMOX and NW / LAMOX was compacted into pellets of 10 mm diameter using a hydraulic press. The pellets prepared were fired in air at $500 \text{ }^\circ\text{C}$ and $600 \text{ }^\circ\text{C}$ in air and at $500 \text{ }^\circ\text{C}$ in Ar- H_2 (Ar 90 % and H_2 10 %) atmosphere respectively for 5 hours. The prepared materials were subjected to x-ray diffraction and XPS studies, respectively.

5.2 X-ray diffraction studies of LN/W- LAMOX system

Figure 5-1 (left side) shows the room temperature XRD patterns of LN/W-LAMOX samples calcined at two different temperatures of $500 \text{ }^\circ\text{C}$ and $600 \text{ }^\circ\text{C}$ in air atmosphere. The diffraction data were collected over the 2θ range of $15-70^\circ$ and the patterns were analysed using PCPDFWIN and X'pert high score plus. The analysis shows the existence of five phases: $\text{La}_2\text{NiO}_{4+\delta}$ (JCPDS no. 81-2413), $\text{La}_2\text{Mo}_{1.5}\text{W}_{0.5}\text{O}_9$ (space group, $P2_13$, CIF no. 4000585), NiWO_4 (JCPDS file no. 15-0755), NiO (ICSD No. 98-006-1324) and $\text{La}_{1.77}\text{Mo}_{1.77}\text{O}_{8.001}$ (ICSD No. 98-008-9964). The formation of new phases can be explained due to the cationic diffusion from LN lattice site into W- LAMOX lattice to form new phases. This new phase was formed by the cationic diffusion of Ni from $\text{La}_2\text{NiO}_{4+\delta}$ lattice into $\text{La}_2\text{Mo}_{1.5}\text{W}_{0.5}\text{O}_9$ lattice site and reacts with W and O to form the respective phase. According to the literature, this monoclinic phase of NiWO_4 shows an excellent catalytic property of hydrodesulphurisation of crude oil [Bi et al., 2010]. Still, its compatibility with LAMOX and its derivatives has not been tested so far.

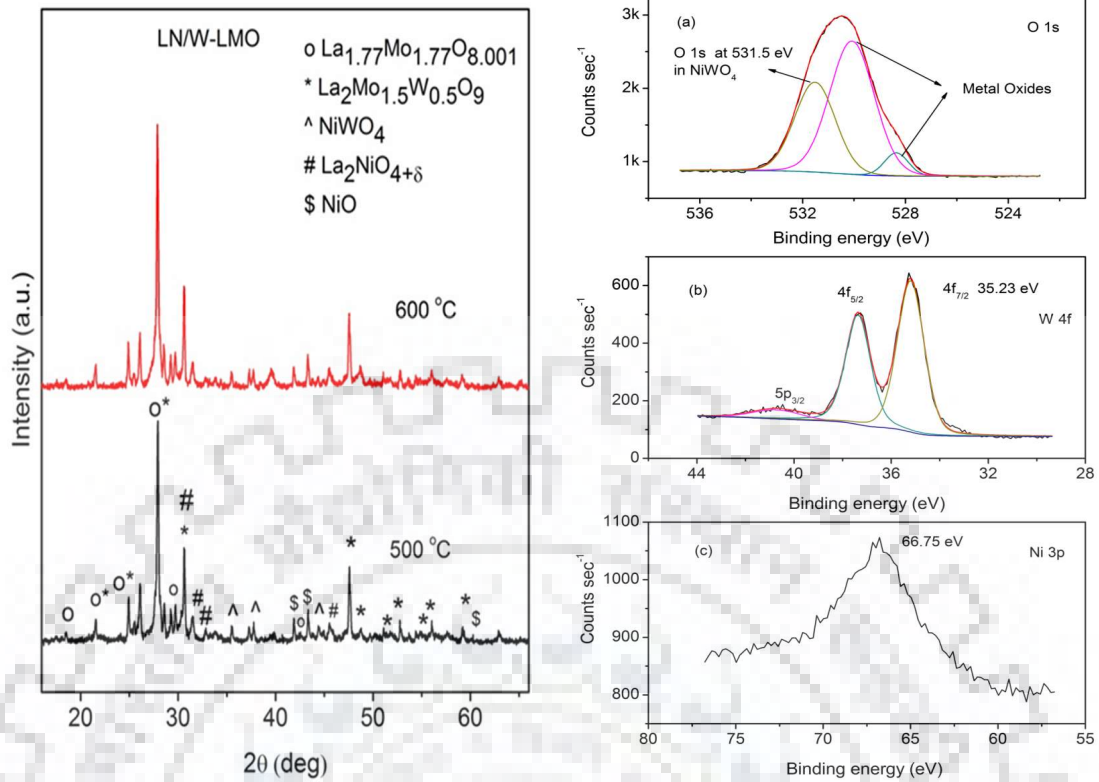


Figure 5-1 (Left side): Room temperature diffraction patterns of equimolar mixtures of $\text{La}_2\text{Mo}_{1.5}\text{W}_{0.5}\text{O}_9$ and $\text{La}_2\text{NiO}_{4+\delta}$ calcined in air at 500 °C and 600 °C respectively. The pattern shows the formation of new NiWO_4 phase along with the parent phase, **(Right side):** Deconvoluted core level spectra of (a) O 1s peak (b) W 4f peak and (c) Ni 3p peak sintered at 600 °C for 4 hours for LN/W-LAMOX.

In the fuel cell operation, the cathode side is fed with air or oxygen, and the formation of nickel tungstate (NiWO_4) as a by-product is a stable one which may cause no harm to the fuel cell performance. But the small amount of NiO formation, as evidenced by XRD analysis, may degrade the overall conductivity at the cathode side [Corbel and Lacorre 2006].

According to literature, the sulphur in the form of H_2S and CO have an adverse effect on fuel cell performance if sulphur content is greater than 20 ppm broadly. The sulphur poisoning of the SOFC components operating at intermediate temperatures of 700-850 °C are irreversible whereas SOFCs operating at high temperatures (> 900 °C) have reversible sulphur poisoning effect. But the operating cost of IT-SOFCs being economically favourable due to its low-cost inter-metallic connects (metal based) and more cheaper component materials as compared to HT-SOFCs (perovskite based interconnects). But they are most likely to be affected by the sulphur poisoning at the anode side through the fuel contamination. In solid oxide fuel cells (SOFCs) the H_2S concentration of even one ppm may result in a sudden performance drop of the cell. However,

this drop or loss in the performance may soon be stabilised into linear degradation. Sulphur, as a contamination in the fuel destroys the active sites for catalytic reactions. This effect is much more enhanced when nickel or iron compounds are a part of electrodes. According to data available in literatures the sulphur content up to 3000 ppm may be tolerable in high-temperature planar SOFCs [Williams 2004].

Here, the NiWO_4 formed as an additional phase can be a potential anode candidate for SOFCs application because of its excellent catalytic property, desulphurisation properties. The application of NiWO_4 as anode material and for desulphurisation have been so far tested in crude oils, gasoline and in yttria-stabilised zirconia (YSZ) in SOFC application in terms of both ionic and electronic conductivity described elsewhere [Scheffer et al., 1989; Sabolsky et al., 2013; Doudin et al., 2017]. As far as the formation of this new phase NiWO_4 is concerned, its importance is increased when the oxidant itself has a contamination of sulphur in any form. This will not only desulphurise the oxidant but also negate the degradation of the fuel cell.

Regarding NiWO_4 as an anode material, E.M. Sabolsky and co-workers [2013] have studied the in situ reduction study of NiWO_4 and yttria-stabilised zirconia (YSZ) at 1000°C . In the presence of H_2 fuel at 1000°C , the NiWO_4 was reduced to $\text{Ni} / \text{WO}_{3-x}$ cermet with mixed ionic and electronic conductivity (MIEC), which again proves it as a potential SOFC anode. Furthermore, the stability of NiWO_4 in H_2 fuel environment containing PH_3 as impurity has been tested and described elsewhere [Sabolsky et al., 2013]. Few other studies have shown that WO_x and tungsten carbide (WC) based compounds as a substitute for Ni-based electrodes since the WO_x based compounds can also be used as a catalyst for dehydrogenation and hydrodesulphurisation. The Ni-based cermets as anode materials in the presence of H_2 fuel has a negative impact on thermomechanical and electrochemical properties in SOFC application [Wang et al., 2009; Yates and Winnick 1999; Torabi and Etsell 2012a; 2012b; Antolini and Gonzalez 2010; Fruhberger et al., 1996].

5.3 X-ray photoelectron spectroscopy study of $\text{La}_2\text{NiO}_{4+\delta} / \text{La}_2\text{Mo}_{1.5}\text{W}_{0.5}\text{O}_9$ system

To confirm the presence of NiWO_4 compound, the $\text{La}_2\text{NiO}_{4+\delta} / \text{La}_2\text{Mo}_{1.5}\text{W}_{0.5}\text{O}_9$ system was treated at 600°C in air atmosphere, and the XPS data were collected at room temperature and plotted as shown in figure 5-1 (right side). As discussed earlier in chapter III and IV, the air treated LAMOX samples have no effect on La 3d, Mo 3d, W 4f and O 1s spectrum. Therefore, to confirm the presence of NiWO_4 , the Ni 3p peak is analysed instead of Ni 2p core level peak. This is because of the overlapping of La 3d and Ni 2p core-level spectrum in the binding energy

range of 820 to 880 eV [Moulder 1995]. The La 3d spectrum has been analysed in the XPS section of previous chapters of the thesis.

From figure 5-1 (right side) (a), it can be seen that deconvoluted O 1s peak shows the signature of NiWO₄. Figure 5-1 (right side) (b) and (c) also show the W 4f core level peak and Ni 3p peak at 66.75 eV, confirming the presence of NiWO₄. The binding energy values of obtained data and that of references have been summarised in table 5-1. Though, the values of the binding energy values are not exactly matched with the reference values but vary within the resolution range of the instrument. The binding energy shift correction has been done with respect to the C 1s spectrum [Moulder 1995, Kumar et al., 2017].

Table 5-1 Binding energy values of NiWO₄ components and their reference values.

Core level lines	Binding energy (eV)	Reference value	Reference
Ni 2p _{3/2} in NiWO ₄	858.16	857.7	Present work
Ni 3p	66.75	--	Present work
W 4f	35.23	35.4	Present work
O 1s	531.5	--	Present work

5.4 X-ray photoelectron spectroscopy study of NiWO₄ (anode) / La₂Mo₂O₉ (electrolyte) system in reductive atmosphere

The formation of NiWO₄ as a secondary phase in La₂NiO_{4+δ} / La₂Mo_{1.5}W_{0.5}O₉ as anode/electrolyte system has been considered as a fine catalyst and desulphurising agent according to the various literature [Scheffer et al., 1989, Sabolsky et al., 2013]. Therefore, in this subsection the NiWO₄ / La₂Mo₂O₉ system has been treated in Ar-H₂ atmosphere at 600 °C for 4 hours to study the effect of H₂ on the NW/LAMOX system in the initial stages of cell operation. Figure 5-2 (left side) shows the XPS spectra of O 1s, Ni 3p, Mo 3d, and La 3d, respectively. As evident from figure 5-2(c) (left side), only Mo in the presence of diluted H₂ atmosphere is reduced to its lower valence states. The majority of Mo is retained in Mo⁶⁺ (70 at. %) states, and rest are reduced to Mo⁵⁺ (20 at. %) and Mo⁴⁺ (10 at. %) states. No other elements were found to be reduced to lower oxidation states as evident from figure 5-2 (left side) (a), (b), and (d). Therefore, it can be concluded that even NiWO₄ as an anode material is not able to suppress the Mo

reduction to lower valence states. The Mo reduction suppression has been studied in detail in the previous chapters by suitable doping agents.

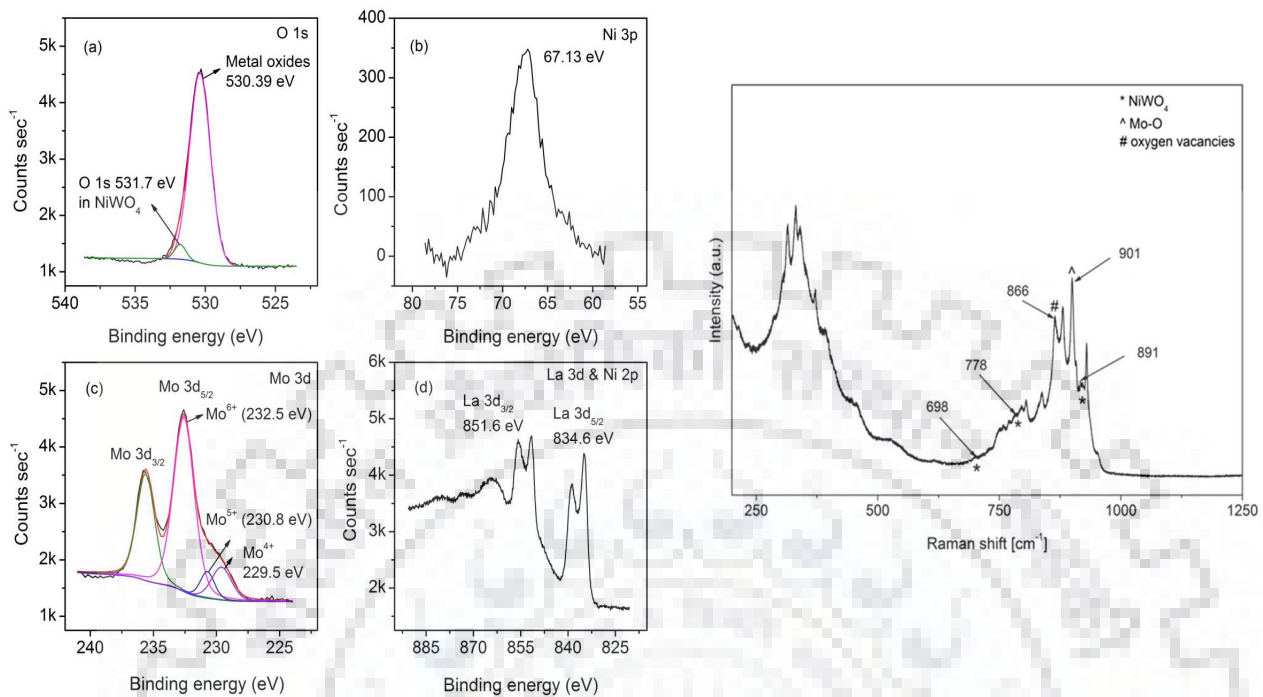


Figure 5-2 (Left side: a-d): Deconvoluted core level spectra of (a) O 1s peak (b) Ni 3p (c) Mo 3d peak and (d) La 3d and Ni 2p sintered at 600 °C of NW/LAMOX system for 4 hours, **(Right side):** Raman spectrum of LN / W-LMO showing the presence of NiWO₄ peaks along with Mo-O bonding and oxygen vacancies existence.

5.5 Raman spectroscopy study of La₂NiO_{4+δ} / La₂Mo_{1.5}W_{0.5}O₉ system

To further validate the presence of NiWO₄, the Raman spectroscopy is done, and the spectrum of La₂NiO_{4+δ}/La₂Mo_{1.5}W_{0.5}O₉ is plotted in figure 5-2 (right side). The spectrum was collected at room temperature over the wavenumber range of 200 – 1250 cm⁻¹. The peak situated at around 866 cm⁻¹ indicates oxygen vacancies (corresponding to W-LAMOX) and the peak at about 901 cm⁻¹ corresponds to Mo - O oscillation. The presence of NiWO₄ can be verified by the peaks observed at 698, 778, and 891 cm⁻¹ [Liu et al., 2015; Murni et al., 2013].

The formation of NiWO₄ and NiO is inter-cationic diffusion, which occurs as a result of thermal process like sintering, grain growth, and densification in solid-state reaction process. This phenomenon is observed at the interface of the two solid particles. When these cations are diffused in the host crystal lattice, it modifies the ideal interface of the electrode/electrolyte interface by bringing the chemical composition changes. However, as mentioned here, the

NiWO₄ product formed due to the cationic diffusion may not be treated as a negative result. The effect of oxygen blocking as a result of the by-product formed has not been tested here which can deteriorate the cell performance.

The equation describing the inter-diffusion process in one dimension can be written as

$$\frac{\partial c(x,t)}{\partial t} = \frac{\partial}{\partial x} \left(\widehat{D}[c(x,t)] \frac{\partial c(x,t)}{\partial x} \right) \quad 5.1$$

where c is the concentration or the density of the diffusing material at location x and time t . \widehat{D} is the collective diffusion coefficient represented here in the form of concentration-dependent interdiffusion matrix \widehat{D} . This interdiffusion process is often limited by electrical polarisation of the cations which have different size and valance states [Liu 2009; Hu et al., 2014].

According to the literature, this monoclinic phase of NiWO₄ shows an excellent catalytic property of hydrodesulphurisation of crude oil [Scheffer 1989], but its compatibility with LAMOX and its derivatives has not been studied so far. But it might show the similar kind of catalytic properties of desulphurisation in fuel gases containing sulphur.

5.6 Summary

The study shows that the reactivity of La₂NiO_{4+δ} and W-LAMOX at relatively lower annealing temperatures (500 and 600 °C) leading to the formation of NiWO₄ along with NiO, La_{1.77}Mo_{1.77}O_{8.001}. NiWO₄, according to the literature is an excellent catalyst and a desulphurising agent. NiWO₄ shows conductivity higher than NiO, because the latter being a Mott-Hubbard insulator having electrical conductivity of 10⁻¹³ S / cm. The XPS core level analysis of LN / W-LAMOX system confirms the presence of NiWO₄. The presence of NiO is also confirmed from XRD analysis. NiO being an insulator, may have a negative impact on overall fuel cell performance. Therefore, La₂NiO_{4+δ} may be considered as a potential cathode material which can be compatible with W doped LAMOX, although it has not shown a good compatibility with pure α-La₂Mo₂O₉.

Further investigations are required to check the impact of NiO on W doped LAMOX based electrolytes which are not conducted in the present study. NiWO₄ may serve as useful anode material since Ni-based cermet faces a compatibility problem either with the by-products formed or, with the reducibility of Mo in reducing atmosphere. The study of NiWO₄/La₂Mo₂O₉ system as anode/electrolyte has also shown the reduction of Mo⁶⁺ to lower valence states. It suggests that NiWO₄ alone is not sufficient to suppress the effect of H₂ on the Mo reduction. The effect of

sulphur poisoning or PH_3 effect in the presence of NiWO_4 as anode has not been carried out in the present study, but the literature supports the electro-catalytic and desulphurising properties of NiWO_4 . The operating temperature, in this case, might restrict the conductivity value of the electrolyte because, at these intermediate temperatures, electrolyte resistance may play an important role in overall fuel cell operation. But a trade-off must be achieved between these two parameters to achieve the optimum performance of the cell.



Chapter 6

Concluding remarks and future work scope

The well-known oxide ion conductor $\text{La}_2\text{Mo}_2\text{O}_9$ (LAMOX/LMO) and its derivatives in SOFC electrolyte application (or as an anode material) have been investigated and discussed here in this thesis. The LAMOX undergoes a structural phase transformation at around 580°C or above. The room temperature monoclinic phase $\text{P}2_1$ is a low conducting phase and exposure to reducing atmosphere causes the Mo reduction, ultimately leading to the generation of electronic conductivity and impairment of the fuel cell. The high thermal expansion coefficient of LAMOX and the above features are the main drawbacks of LAMOX which restrict its potential application as fuel cell electrolyte. This thesis explores the possibilities of utilising the LAMOX as an electrolyte to be exploited to its full potential by suitable dopants. The development of compatible parts viz. electrodes and other interconnects is also a challenge for commercialisation of the SOFC technology.

6.1 Concluding remarks on pristine LAMOX electrolyte

After analysing the demerits of the pristine LAMOX and instrumentation details in chapter I and II, respectively, the subsequent chapters show the study of LAMOX and its derivatives. The III chapter of the thesis validates some experimental work done in the present study and are in agreement with the previously published results. The room temperature phase of LAMOX as confirmed by XRD analysis, and Mo reduction in the presence of diluted hydrogen atmosphere, has been studied in detail by FE-SEM and XPS analysis which were scarcely reported earlier. This Mo reduction which ultimately leads to loss of oxygen from the host lattice leads to generation of electronic conductivity in the electrolyte which has been further shown by impedance spectroscopy of reduced LAMOX. The FE-SEM analysis of Ar- H_2 treated samples of LAMOX shows a colour change along with intra-granular pores at high magnification. These porous Ar- H_2 treated LAMOX samples can very well be exploited in anodic applications as they are sulphur tolerant according to the literature. The XPS analysis confirms the degradation of $\text{Mo}^{6+} \sim 75$ atomic percent to lower oxidation states in reducing atmosphere at 900°C . Also, the electrical conductivity shows a three orders of enhancement from 16×10^{-6} to 3×10^{-3} S/cm when the same was treated in air and Ar- H_2 conditions at 900°C . The appearance of electronic conductivity during the fuel cell operation is highly undesirable for fuel cell operation.

6.2 Concluding remarks on doped LAMOX

The fourth chapter of the thesis was devoted to the study of doped LAMOX compounds. It can also be termed as tailoring the properties of LAMOX by suitable doping. W^{6+} (0.6 Å) doping at Mo site having a similar ionic radius as that of Mo^{6+} (0.59 Å) has a good solid solubility of around 80 percent. At 75 mol % doping and above $\alpha-La_2W_2O_9$ (LWO) phase was formed in addition to the β -LAMOX phase. The lower doping compositions of W content less than 75 mol % shows stabilisation of the β -LAMOX phase at room temperature. The FE-SEM study has shown the formation of pores in the grains as well as on the grain boundaries. Some of the images were captured and analysed without the conductive coating on the samples indicating the presence of electronic conductivity in the compound. The images captured were of good quality except in the cases of high W doping where Mo^{6+} reduction has been suppressed and W content is dominant. The XPS analysis shows that the reduction of Mo^{6+} in W-LAMOX has not been fully eliminated. Therefore, the problem still remains of fully eliminating the electronic conductivity generated by the reduction of Mo which in turn causes oxygen loss from the LAMOX lattice. The d.c. ionic conductivity of W doped LAMOX at 400 °C is 15 μ S/cm which is expected to increase as the operating temperature is increased.

The next section of this chapter has provided some insight into Mo stabilisation in Ar- H_2 atmosphere. The K doping was done at La site in LAMOX to study the effect Ar- H_2 atmosphere and its consequences on ionic conductivity. The maximum solubility limit of K in LAMOX is about 3-5 mol %. The K doped LAMOX composition has stabilised the high-temperature cubic phase P 2₁₃ at room temperature, as confirmed by XRD and Rietveld analysis. The FE-SEM and XPS analysis confirmed the elemental composition, and through core level analysis it was very well proved that by K doping in LAMOX ~ 95 atomic % of Mo^{6+} is stabilised when the K = 10 mol % doped LAMOX was treated at 900 °C in Ar- H_2 atmosphere. The dc conductivity measurement shows the value of σ_{dc} is about 10 μ S/cm at 673 K. This value is slightly less than the value obtained for W doped LAMOX (15 μ S/cm). The decreased value of ionic conductivity is attributed to the large ionic radius of K^+ ions as compared to La^{3+} ions which suppress the effect of oxide ion migration through vacancies. Also, the affinity of K^+ ions towards oxide ions is greater as compared to La^{3+} ions which restrict the movement of oxide ions through the vacancies in the structure.

The Raman analysis throws some light to support the evidence of enhanced oxide ion vacancies and structural phase change as confirmed by the intensity of band one and band two in the spectrum.

The relaxation studies for K doped LAMOX and pristine LAMOX were done and parameters like mobility (μ), diffusion coefficient (D_v), relaxation frequency ω_r , and the total number of oxide ion vacancies (n_o) were calculated.

After doping at respective individual sites in LAMOX, the next section of chapter IV reveals the effect of the reductive atmosphere on Mo^{6+} in the presence of rare earth elements and W doping at La and Mo site simultaneously by XPS analysis. The Mo peak after treatment in reductive atmosphere does not show complete stabilisation of Mo^{6+} in Ar- H_2 atmosphere as proposed by T.Y. Jin et al., 2007.

6.3 Concluding remarks on $\text{La}_2\text{NiO}_{4+\delta}$ (LN) and $\text{La}_2\text{Mo}_{1.5}\text{W}_{0.5}\text{O}_9$ (W-LAMOX) based electrode/electrolyte

The fifth chapter deals with the compatibility studies of $\text{La}_2\text{NiO}_{4+\delta}$ / $\text{La}_2\text{Mo}_{1.5}\text{W}_{0.5}\text{O}_9$ based cathode/electrolyte and NiWO_4 / $\text{La}_2\text{Mo}_{1.5}\text{W}_{0.5}\text{O}_9$ as anode/electrolyte for fuel cell application. The equimolar mixture of the two compounds was treated in air and reductive conditions at 500 °C and 600 °C for 4 hours and then analysed by XRD and XPS. The XRD analysis shows the formation of a new phase NiWO_4 is formed with LN/W-LAMOX. The new phase (NiWO_4) was confirmed by XPS analysis by O 1s and Ni 3p core-level peaks. The Mo core level peak after deconvolution shows some amount of Mo^{4+} and Mo^{5+} contents in reductive atmosphere. This new NiWO_4 phase formed is a potential dehydrosulphurising agent and fine catalyst according to literature which can negate the effect of sulphur from the fuel and ultimately enhancing the operation cycle of fuel cell system.

6.4 Overall concluding remarks

The LAMOX based electrolytes for IT-SOFCs application has been studied and presented in this thesis. Limitations viz. phase transformation (monoclinic to cubic at 580 °C), abrupt volume change, Mo reduction in Ar- H_2 atmosphere, the appearance of electronic conductivity restrict the potential application of the LAMOX as a SOFC electrolyte. The doped and pristine LAMOX samples were synthesised by the solid-state route in the present study. Various characterisation viz. XRD, FE-SEM, XPS, and EIS have been done to study the properties of LAMOX in air and reductive (Ar- H_2) atmosphere. Previous literature shows the Mo reduction to lower oxidation states, which contributes to the electronic conductivity in the LAMOX compound but no detailed work regarding Mo reduction is reported. The core contribution of the present research work focuses on the Mo stabilisation by W and K doping in the LAMOX structure by XPS analysis.

The pristine and W, K doped LAMOX compound treated in air and Ar-H₂ atmosphere have been studied to a great depth. The stabilisation of Mo reduction to lower valence states along with high-temperature cubic phase stabilisation has been achieved by W and K doping. The stabilisation of Mo to 6+ state is of great importance from an electrolyte point of view, which results in the suppression of electronic conductivity. The detailed oxidation state study of various LAMOX constituent elements has also been done in the thesis. The compatibility of La₂NiO_{4+δ} and NiWO₄ as cathode and anode material have also been investigated in the thesis. The NiWO₄ may be utilised as anode material in LAMOX based SOFCs due to its dehydrosulphurisation property. LAMOX as an electrolyte material has a potential application in IT-SOFCs, which will help in reducing the overall cost of fuel cell operation.

6.5 Future scope of the work

The following points present the future scope of the work based on the present study:

1. Electrochemical impedance study for doped La₂Mo₂O₉ compositions under reductive atmospheres can be further investigated at higher temperatures.
2. Complete stabilisation of Mo⁶⁺ in reductive atmosphere can be investigated at elevated temperatures by suitable doping.
3. Sulphur tolerance, along with hydrogen atmosphere, can be investigated for electrolytes and electrode compositions.
4. New electrode materials can be investigated which are compatible with the LAMOX electrolyte.
5. Synthesis of nanocrystalline thin films for achieving higher performance can be investigated by inexpensive methods like the sol-gel route.
6. Suitable interconnects, and sealants for proper design can be investigated for making commercial use.

Bibliography

Abelard P., 1982, Study of the dc and ac electrical properties of an yttria-stabilized zirconia single crystal [(Zr_{0.2}) (Y_{0.88}O₃)_{0.12}] Phys. Rev. B. 26, 1005-1017.

Adham K. El., Hammou A., 1983, 'Grain Boundary Effect' on Ceria Based Solid Solutions Solid State Ionics, 9&10, 905–912.

Agarwal B.K., 1979, X-ray spectroscopy: An introduction, 121-179.

Andersson D.A., Simak S.I, Skorodumova N.V., Abirkosov I.A., Johansson B., 2005, Optimization of ionic conductivity in doped ceria, Proc. Natl. Acad. Sci. 103, 3518-3521.

Analyticaltechniques.com. 10th annual world congress on mass spectrometry and analytical techniques.

Annual Energy Review, 2001, Energy Information Administration Office of Energy Markets and End Use U.S. Department of Energy Washington, D.C., 20585.

Annual Energy Review, 2011, Energy Information Administration Office of Energy Markets and End Use U.S. Department of Energy Washington, DC 20585.

Annual Energy Outlook, 2019, Energy Information Administration Office of Energy Markets and End Use U.S. Department of Energy Washington, DC 20585.

Antolini E., Gonzalez E. R., 2010, Tungsten-based materials for fuel cell applications Appl. Catal. B Environ., 96, 245-266.

Arai H., 1992, Oxygen ion conductor and its application, J. Bull. Ceram Soc. Japan, 27, 100-104.

Arulraj A., Goutenoire F., Tabellout M., Bohnke O., Lacorre P., 2002, Synthesis and Characterization of the Anionic Conductor System La₂Mo₂O_{9-0.5x}F_x (x = 0.02–0.30) Chem. Mater., 14, 2492-2498.

Bail L., A, Duroy H., Fourquet J.L., 1988, Ab-initio structure determination of LiSbWO₆ by X-ray powder diffraction. Mater. Res. Bull, 23, 447-452.

Badwal S. P. S., Foger K., 1996, Solid Oxide fuel cell review, Ceram. International, 22, 257-265.

Badwal S. P. S., Ciachhi F., Milosevic T., 2000, Scandia–zirconia electrolytes for intermediate temperature solid oxide fuel cell operation, *Solid State Ionics* 5, 136-137.

Bard A. J., Parsons R., Jordan, J. 1985, *Standard Potentials in Aqueous Solutions*, Marcel Dekker, New York.

Basu S., Devi P. S., Maiti H. S., Nb-Doped $\text{La}_2\text{Mo}_2\text{O}_9$: 2005, A New Material with High Ionic Conductivity, *Journal of the Electrochemical Society*, 152, A2143- A2147.

Basu S., Devi P. S., Maiti H. S., Lee Y., Hanson J. C., 2006, Lanthanum molybdenum oxide: Low-temperature synthesis and characterization, *Journal of Materials Research* 21, 1133-1140.

Basu S., Maiti H.S., 2010, Ion dynamics in Ba-, Sr-, and Ca-doped $\text{La}_2\text{Mo}_2\text{O}_9$ from analysis of ac impedance, *Journal of Solid State Electrochemistry*, 14, 1021-1025.

Basu S., Maiti H.S., 2009, Ion Dynamics Study of Nb^{+5} Substituted $\text{La}_2\text{Mo}_2\text{O}_9$ by A.C. Impedance Spectroscopy, *Journal of the Electrochemical Society*, 156, P114-P116.

Basu S., Maiti H.S., 2010, Ion dynamics study of $\text{La}_2\text{Mo}_2\text{O}_9$, *Ionics*, 16, 111-115.

Baurele J. E. 1969, Study of solid electrolyte polarization by a complex admittance method *J. Phys. and Chem. of Solids*, 30, 2657-2670.

Bezian J.J., 1998, Report from the Centre d'Energetique de l'Ecole des Mines de Paris, October pp 1–44.

Bhowmik A., Malik R., Prakash S., Sarkar T., Bhardwaj M.D., Aich S., Ghosh S., 2015, Classical molecular dynamics and quantum ab-initio studies on lithium-intercalation in interconnected hollow spherical nanospheres of amorphous silicon, *J. Alloys and Compounds*, 665, 165.

Bi Y., Nie H., Li D., Seng S., Yang Q., Li M., 2010, NiWO_4 nanoparticles: promising catalyst for hydrodesulfurization, *Chem. Commun.* 46, 7430-7432.

Bo Q. B., Feng J., Wang H. Y., Meng J., 2003, Synthesis of new solid solutions on neodymium-stabilized $\text{La}_2\text{Mo}_2\text{O}_9$, *Chinese Chemical Letters*, 14, 197-200.

Borgschulte A., Sambalova O., Delmelle R., Jenatsch S., 2017, Hydrogen reduction of molybdenum oxide at room temperature, 7, 40761 1-9.

Bottcher C. J. F., Bordewijk P., 1978, Theory of Electric Polarization, Vol. II: Dielectrics in Time Dependent Fields (Elsevier, Amsterdam/Oxford/New York,).

Buvat G., Sellimi H., Ravella U. K., Barre M., Coste S., Corbel G., Lacorre P., 2016, Reduction Kinetics of $\text{La}_2\text{Mo}_2\text{O}_9$ and Phase Evolution during Reduction and Re-oxidation *Inorg. Chem.* 55, 2522–2533.

Caglioti G., Paoletti A., Ricci F.P., 1958, Nucl. Choice of collimators for a crystal spectrometer for neutron diffraction *Inst.* 3, 223 – 228.

Calderwood J.H., 1992, The interpretation of debye relaxation by means of a classical vibrational model, *IEEE*, 249-252.

Castillo J. V., Mogni L., Corbel G., Lacorre P., Caneiro A., 2010, On the thermodynamic stability of $\text{La}_2\text{Mo}_2\text{O}_{9-\delta}$ oxide-ion conductor, *International Journal of Hydrogen Energy*, 35, 5890-5894.

Chalk. S., 2002, Progress Report for Hydrogen, Fuel Cells, and Infrastructure Technologies Program, U.S. Department of Energy, Washington.

Chiang Y M., Birnie D. P., Kingery W. D., 1997, *Physical Ceramics: Principles for Ceramic Science and Engineering.*, New York; Chichester: John Wiley.

Chiodelli G., Malavasi L., Electrochemical open circuit voltage (OCV) characterization of SOFC materials, 2013, 19, 1135-1144.

Choudhury A., Barbora L., Arya D., Lal B., Subudhi S., Mohan S.V., Ahammad S.Z., Verma, A., 2017, Effect of electrode surface properties on enhanced electron transfer activity in microbial fuel cells. *Engineering in Life Sciences*, 17,186-192.

Chusuei C.C., Goodman D.W., 2002, X-ray photoelectron spectroscopy, *Encyclopedia of Physical Science and Technology*, 3rd edition, 17, 921.

Cohen J.B., Fine M. E., 1962, Some aspects of short range order, *Nuclear Magnetic Resonance*, 10, 749-762.

Collado J. A., Aranda M. A. G., Cabeza A., Pastor P. Olivera, Bruque S., 2002, Synthesis, Structures, and Thermal Expansion of the $\text{La}_2\text{W}_{2-x}\text{Mo}_x\text{O}_9$ Series, *Journal of Solid State Chemistry*, 167, 80-85.

Corbel G., Mestiri S.; Lacorre P., 2005, Physio-chemical compatibility of CGO fluorite, LSM and LSCF perovskite electrode materials with $\text{La}_2\text{Mo}_2\text{O}_9$ fast oxide-ion conductor *Solid State Sciences*, 7, 1216-1224.

Corbel G., Laligant Y., Goutenoire F., Suard E., Lacorre P., 2005, Effects of Partial Substitution of Mo^{6+} by Cr^{6+} and W^{6+} on the Crystal Structure of the Fast Oxide-Ion Conductor Structural Effects of W^{6+} , *Chemistry of Materials*, 17, 4678-4684.

Corbel G., Lacorre P., 2006, Compatibility evaluation between $\text{La}_2\text{Mo}_2\text{O}_9$ fast oxide-ion conductor and Ni-based materials, *Journal of Solid State Chemistry*, 179, 1339-1344.

Corbel G., Chevereau E., Kodjikian S., Lacorre P., 2007, Topological Metastability and Oxide Ionic Conduction in $\text{La}_{2-x}\text{Eu}_x\text{Mo}_2\text{O}_9$, *Inorganic Chem.*, 46, 6395-6404.

Corbel G., Durand P., Lacorre P., 2009, Comprehensive survey of Nd^{3+} substitution in $\text{La}_2\text{Mo}_2\text{O}_9$ oxide-ion conductor, *J. of Solid State Chemistry*, 182, 1009-1016.

Crippa, M., Oreggioni, G., Guizzardi D., Muntean M., Schaaf E., Lo Vullo E., Solazzo E., Monforti-Ferrario F., Olivier J.G.J., Vignati E. 2019, JRC science for policy report: Fossil CO_2 and GHG emissions of all world countries, 1-15.

Demirskyi D, Borodianska H., Agrawal D., Ragulya A., Sakka Y., Vasylykiv O., 2012, Peculiarities of the neck growth process during initial stage of spark-plasma, microwave and conventional sintering of WC spheres, *J Alloys and Compounds* 523, 1-10.

Debye P. 1912, Summary in polar molecules, *Phys. Z.* 13, 97.

Doudin N., Pomp S., Blatnik M., Resel R., Vorokhta M., Goniakowski J., Noguera C., Netzer F. P., Surnev S., 2017, Epitaxial NiWO_4 films on Ni (110): Experimental and theoretical study of surface stability *Surf. Sci.*, 659, 20-30.

Dutta V., Rao A. R., 2004, Hexagonal Cd-Te nanorods in spray deposited CdTe nanoparticle thin films, *Physica State Solidi*, 201, R72-74.

Dyre J.C., 1991, Some remarks on ac conduction in disordered solids, *J. Non-Crystalline Solids*, 135, 219-226.

Emery J., Massiot D., Lacorre P., Laligant Y., Conder K., 2005, Magnetic Resonance in Chemistry O NMR in room temperature phase of $\text{La}_2\text{Mo}_2\text{O}_9$ fast oxide ionic conductor, 43, 366-371.

Eguchi K., Setoguchi T., Inoue T., Arai H., 1992, Electrical properties of ceria-based oxides and their application to solid oxide fuel cells *Solid State Ionics* 52, 165-172.

Eurobarometer, 2017, Report on Climate change, 459.

Evans I. R., Howard J. A. K., Evans J. S. O., 2005, The Crystal Structure of $\alpha\text{-La}_2\text{Mo}_2\text{O}_9$ and the Structural Origin of the Oxide Ion Migration Pathway, *Chem. Mater.*, 17, 4074-4077.

Fang Q. F., Wang X. P., Zhang G. G., Yi Z. G., 2003, Damping mechanism in the novel $\text{La}_2\text{Mo}_2\text{O}_9$ -based oxide-ion conductors *Journal of Alloys and Compounds*, 355, 177-182.

Fang Q. F., Wang X. R., Li Z. S., Zhang G. G., Yi Z. G., 2004, Relaxation peaks associated with the oxygen-ion diffusion in $\text{La}_{2-x}\text{Bi}_x\text{Mo}_2\text{O}_9$ oxide-ion conductors, *Structural Materials Properties Microstructure and Processing*, 370, 365-369.

Fang Q. F., Zhuang Z., Wang X. P., Li D., Wang J. X., 2008, Phase Transition and Oxygen Ion Diffusion in $(\text{La}_{1-x}\text{Ln}_x)_2\text{Mo}_2\text{O}_9$ ($\text{Ln} = \text{Nd}, \text{Gd}, x = 0.05 - 0.25$) Using Dielectric Relaxation Method, *Chinese Journal of Chemical Physics*, 21, 270-274.

Fournier J.P., Fournier J., Kohlmuller R., 1970, Etude des systèmes $\text{La}_2\text{O}_3\text{-MoO}_3$, *Bull. Soc. Chim. Fr.*, 4277.

Fruhberger B., Grunze M., Dwyer D. J., 1996, Surface chemistry of H_2S -sensitive tungsten oxide film, *Sens. Actuators B. Chem.*, 31, 167-174.

Fuel cell materials by Nextech materials. August 2001.

Funke K., Cramer C., 1997, Conductivity Spectroscopy, *Current Opinion in Solid State and Materials*, 2, 483-490.

Galdo J., Bologna H.Q, 2001, United States Department of Energy, Conference on fuel cells, Italy. May 31 –June 01.

Georges S., Goutenoire F., Lalignat Y. and Lacorre P., 2002, Proceedings of the 5th European SOFC Forum, Luzern, Switzerland, Joep H, pp. 671–678.

Georges S., Goutenoire F., Altorfer F., Sheptyakov D., Fauth F., Suard E., Lacorre P., 2003, Thermal, structural and transport properties of the fast oxide-ion conductors $\text{La}_{2-x}\text{R}_x\text{Mo}_2\text{O}_9$ (R = Nd, Gd, Y) *Solid State Ionics*, 161, 231-241.

Georges S., Goutenoire F., Lalignat Y., Lacorre P., 2003, Reducibility of fast oxide-ion conductors $\text{La}_{2-x}\text{R}_x\text{Mo}_{2-y}\text{W}_y\text{O}_9$ (R = Nd, Gd) *J. Mater. Chem.*, 13, 2317-2321.

Georges S., Goutenoire F., Lacorre P., Steil M. C., 2005, Sintering and electrical conductivity in fast oxide ion conductors $\text{La}_{2-x}\text{R}_x\text{Mo}_{2-y}\text{W}_y\text{O}_9$ (R: Nd, Gd, Y), *J. European Ceramic Society*, 25, 3619-3627.

Georges S., Bohnke O., Goutenoire F., Lalignat Y., Foullet J., Lacorre P., 2006, Effects of tungsten substitution on the transport properties and mechanism of fast oxide-ion conduction in $\text{La}_2\text{Mo}_2\text{O}_9$ *Solid State Ionics*, 177, 1715-1720.

Georges S., Rocha R.A., Djurado E., 2008, Microstructure related conductivity in $\text{La}_2\text{Mo}_2\text{O}_9$ ceramics, *J. Phys. Chem. C*, 112, 3194-3202.

Gerck, C., Willert-Porada, M. 1999, Innovative Materials in Advanced Energy Technologies; Advances in Science and Technology; Techna: Faenza, Italy, Vol. 24, 71-78.

Gerhardt R., Nowick A. S., Mochel M. E., Dumler I. 1986, Grain-Boundary Effect in Ceria Doped with Trivalent Cations: II, Microstructure and Microanalysis, *J. Am. Ceram. Soc.*, 69, 647–651.

Ghosh A., Shukla S., Khosla G.S., Lochab B., Mitra S., 2016, Sustainable sulfur-rich copolymer/graphene composite as lithium-sulfur battery cathode with excellent electrochemical performance. *Nature Scientific reports*, 6, 25207.

Goel, M., Djurado, E., Georges, S., 2011. Reducibility of $\text{La}_2\text{Mo}_2\text{O}_9$ based ceramics versus porosity. *Solid State Ionics*, 204, 97-103.

- Goff J.P., Hayes W., Hutchings M.T., Claussen K.N., 1999, Defect structure of yttria-stabilized zirconia and its influence on the ionic conductivity at elevated temperatures, *Phys. Rev. B.*, 59, 14202-14219.
- Goodenough J.B., Diaz J.E., 1990, Oxide-ion conduction in $\text{Ba}_2\text{In}_2\text{O}_5$ and $\text{Ba}_3\text{In}_2\text{MO}_8$ (M = Ce, Hf, or Zr), *Solid State Ionics*, 44, 21-31, 1990.
- Goutenoire F., Lacoore P., 2003, Compounds derived from $\text{La}_2\text{Mo}_2\text{O}_9$ and their use as ionic conductors, U.S. patent US 2003/0160216 A1.
- Goutenoire F., Retoux R., Suard E., Lacorre P., 1999, *Ab Initio* Determination of the Novel Perovskite-Related Structure of $\text{La}_7\text{Mo}_7\text{O}_{30}$ from Powder Diffraction *Journal of Solid State Chemistry*, 142, 228-235.
- Goutenoire F., Isnard O., Retoux R., Lacorre P., 2000, Crystal Structure of $\text{La}_2\text{Mo}_2\text{O}_9$, a New Fast Oxide-Ion Conductor, *Chem. Mater.*, 12, 2575-2580.
- Goutenoire F.; Isnard O., 2001, Structural and transport characteristics of the LAMOX family of fast oxide-ion conductors, based on lanthanum molybdenum oxide $\text{La}_2\text{Mo}_2\text{O}_9$ *J. Mater. Chem.* 11, 119-124.
- Grove W.R., 1839, On voltaic series and the combination of gases by platinum, *Philos Mag.* 14, 127-130.
- Guha S., 1997, Materials aspects of amorphous silicon solar cells, *Current Opinion in Solid State and Materials Science*, 2, 425-429.
- Guo X., 1995, Physical origin of the grain boundary resistivity of stabilized zirconia: Role of space-charge layers *Solid State Ionics*, 81, 235-242.
- Guo X., 2001, Size Dependent Grain-Boundary Conductivity in Doped Zirconia *Comput. Mater. Sci.*, 20 168-176.
- Guo X., Maier J., 2001, Grain Boundary Blocking Effect in Zirconia: A Schottky Barrier Analysis *J. Electrochem. Soc.*, 148, E121-E126.
- Guo X., Sigle W., Maier J., 2003, Blocking Grain Boundaries in Yttria-Doped and Undoped Ceria Ceramics of High Purity *J. Am. Ceram. Soc.*, 86, 77-87.

Guo X., and Waser R., 2006, Electrical properties of the grain boundaries of oxygen ion conductors: acceptor-doped zirconia and ceria. *Prog. Mater. Sci.*, 51, 151-210.

Hayward S. A., Redfern S. A. T., 2004, Thermodynamic nature of and spontaneous strain below the cubic–monoclinic phase transition in $\text{La}_2\text{Mo}_2\text{O}_9$, *Journal of Physics-Condensed Matter*, 16, 3571-3583.

He T. M., Huang Y. L., He Q., Ji Y., Pei L., Liu J., Lu Z., 2005, The effects on the structures and properties in the oxide-ion conductor $\text{La}_2\text{Mo}_2\text{O}_9$ by partial substituting Ba for La, *Journal of Alloys and Compounds*, 388, 145-152.

Hirschenhofer J.H, Stauffer D.B, Engleman R.R., Klett M.G., 1998, U.S. Department of Energy, Fuel cell hand book, fourth edition, pp 42.

Horita T., Ishikawa M., Yamaji K., Sakai N., Yokokawa H., Dokiya M., 1998, Cation diffusion in $(\text{La,Ca})\text{CrO}_3$ perovskite by SIMS, *Solid State Ionics*, 108, 383-390.

Hou C.J., Zhang X., Liu C.S., Wang X.P., Fang Q.F., 2008, Crystal structure of $\beta\text{-La}_2\text{Mo}_2\text{O}_9$ from first principle calculation, *Chin. Phys. Lett.*, 25, 3342-3345.

Hou C.J., Li Y.D., Wang P.J., Liu C.S., Wang X.P., Fang Q.F., Sun D.Y., 2007, Oxygen-ion arrangements and concerted motion in $\beta\text{-La}_2\text{Mo}_2\text{O}_9$, *Phys. Rev. B*, 76, 014104 1-6.

Hu J.M., Liang L., Ji Y., Hong Y., Gerdes K., Chen L.Q., 2014, Interdiffusion across solid electrolyte-electrode interface, *Appl. Phys. Lett.*, 104, 213907 1-6.

Huang D. P., Xu Q., Chen W., Zhang F, Liu H. X., 2008, Sintering, microstructure and conductivity of $\text{La}_2\text{NiO}_{4+\delta}$ ceramic *Ceram. International*, 34, 651-655.

Islam M.S., Tolchard J.R., Slater P.R., 2003, An apatite for fast ion conduction, *Chem. Commun.*, 13, 1486-1487.

IPCC, 2018: Global Warming of 1.5 °C. An IPCC Special Report on the impacts of global warming. ipcc.ch/site/assets.

Jacobson A.J., 2010, Materials for Solid Oxide Fuel Cells, *Chem. Mater.* 22, 660-674.

Jacquens J., Stabilité, réactivité et Performances de conducteurs par ions oxyde de la famille LAMOX comme éléments de cœur de pile à combustible SOFC mono-chambre. Université du Maine, Le Mans, 2010.

Jacquens J., Farruseng D., Georges S., Viricelle J. P., Gaudillere C., Corbel G. and Lacorre P., 2010, Tests for the Use of $\text{La}_2\text{Mo}_2\text{O}_9$ -based Oxides as Multipurpose SOFC Core Materials Fuel Cells, 10, 433-439.

Jana K.K., Srivastava A., Parkash O., Avasthi, D.K., Rana D., Shahi V.K., Maiti, P., 2016, Nanoclay and swift heavy ions induced piezoelectric and conducting nano-channel based polymeric membrane for fuel cell, J. Power Sources, 301, 338-347.

Jana K.K., Prakash O., Shahi V.K., Avasthi D.K., Maiti, P., 2017, Poly(vinylidene fluoride-co-chlorotrifluoro ethylene) Nanohybrid Membrane for Fuel Cell, ACS Omega, 3, 917-928.

Jana K.K., Tiwari V.K., Avasthi D.K., Paine T.K., Maiti P., 2017, New generation fuel cell membrane using swift heavy ions, Chemistry Select, 2, 6413-6437.

Janakiraman S., Surendran A., Ghosh S., Anandhan S., Venimadhav A., A new strategy of PVDF based Li-salt polymer electrolyte through electrospinning for lithium battery application, 2018, 6, 035303.

Jos G.J. Olivier, Greet Janssens-Maenhout, Marilena M., Jeroen A.H.W. Peters, 2015, Trends in global CO_2 emissions, 1-80.

Jin T. Y., Rao M.V.M., Cheng C.L., Tsai D.S., Hung M.H., 2007, Structural stability and ion conductivity of the Dy and W substituted $\text{La}_2\text{Mo}_2\text{O}_9$, Solid State Ionics, 178, 367-374.

Karle J., 1991, Direct calculation of atomic coordinates from diffraction intensities: Space group P1, Proc. Natl. Acad. Sci. USA, 88, 10099-10103.

Karlsruhe ICSD (F12), 2004.

Khadashva Z. S., Venskivskii N. U., Safronenko M. G., Mosunov A. V., Politova E.D., Stefanovich S. Y., 2002, Synthesis and properties of $\text{La}_2(\text{Mo}_{1-x}\text{M}_x)_2\text{O}_9$ (M = Nb, Ta) ionic conductors, Inorganic Mater., 38, 1168-1171.

Khaled A., Pireaux J.J., Khelili S., 2012, Synthesis and Characterization of Ca and Ba Doped LAMOX Materials and Surface Study by X-ray Photoelectron Spectroscopy, *Acta. Chim. Slov.*, 59, 766-768.

Keep C. W., Baker, R. T. K., France J. A., 1977, Origin of filamentous carbon formation from the reaction of propane over nickel *J. Catal. B.*, 47, 232–238.

Kendrak E., Islam M., 2007, Developing apatites for solid oxide fuel cells: insight into structural, transport and doping properties, *J Mater Chem.* 17, 3104-3111.

Kenneth A. Burke, 2003, First International Energy Conversion Engineering Conference, pp. 1-15 August 17–21.

Kilner J.A., 2000, Fast oxygen transport in acceptor doped oxides, *Solid state ionics*, 129, 13-23.

Kilner J.A., 1982, A study of oxygen ion conductivity in doped non stoichiometric oxides. *Solid State Ionics*, 6, 237-252.

Kishimoto H., Sakai N., Horita T., Yamaji K., Brito M. E., Yokokawa H., 2007, Cation transport behavior in SOFC cathode materials of $\text{La}_{0.8}\text{Sr}_{0.2}\text{CoO}_3$ and $\text{La}_{0.8}\text{Sr}_{0.2}\text{FeO}_3$ with perovskite structure, *Solid State Ionics*, 178, 1317-1325.

Kramer S., Spears M., Tuller H. L., 1994, Conduction in titanate pyrochlores: Role of dopants, *Solid State Ionics*, 72, 59-66.

Kumar M., Chakraborty J., Das P. K., 2018, Inter-diffusion across Electrode-Electrolyte Interface in Solid Oxide Fuel Cell Incorporating the Finite Size Effect of the Ions, *J. Electrochem. Soc.*, 165, F1184-F1191.

Kumar R., Bhuvana T., Sharma A., 2017, Nickel tungstate–graphene nanocomposite for simultaneous electrochemical detection of heavy metal ions with application to complex aqueous media, *RSC Advances*, 7, 42146-42158.

Kuo C.W., Sivakumar C., Wen T. C., 2008 Nanoparticles of Pt/ H_xMoO_3 electrodeposited in poly (3,4 – ethylenedioxythiophene)-poly (styrene sulfonic acid) as the electrocatalyst for methanol oxidation, *J. Power Sources*, 185, 807-814.

- Lacorre P., Retoux R., 1997, First Direct Synthesis by High Energy Ball Milling of a New Lanthanum Molybdate, *J. Solid State Chem.*, 132, 443-446.
- Lacorre P., 2000, The LPS concept, a new way to look at anionic conductors, *Solid State Sci.*, 2, 755-758.
- Lacorre P., Goutenoire F., Bohnke O., Retoux R., Lalignat Y., 2000, Designing fast oxide-ion conductors based on $\text{La}_2\text{Mo}_2\text{O}_9$ *Nature*, 404, 856-858.
- Lacorre P., Altorfer F., Sheptyakov D., Fauth F., Suard E., 2003, *Advances in Science and Technology*, 33, (10th International Ceramic Congress-part C), pp 737-747.
- Lacorre P., Selmi A., Corbel G. Boulard B., 2006, On the Flexibility of the Structural Framework of Cubic LAMOX Compounds, in Relationship with Their Anionic Conduction Properties *Inorganic Chemistry*, 45, 627-635.
- Le M.V., Tsai D.S., Nguyen T.A., 2018, BSCF/GDC as a refined cathode to the single-chamber solid oxide fuel cell based on a LAMOX electrolyte, *Ceram. Int.*, 44, 1726-1730.
- Li C., Wang X. P., Wang J. X., Li D., Zhuang Z., Fang Q. F., 2007, Study on the electrical conductivity and oxygen diffusion of oxide-ion conductors $\text{La}_2\text{Mo}_{2-x}\text{T}_x\text{O}_{9-\delta}$ (T = Al, Fe, Mn, Nb, V), *Materials Research Bulletin*, 42, 1077-1084.
- Li D., Wang X. P., Zhuang Z., Fang Q. F., 2009, Dielectric relaxation studies of Ba-doping effects on the oxygen-ion diffusion and phase transition in $\text{La}_2\text{Mo}_{2-y}\text{W}_y\text{O}_9$ ceramics, *Physica B-Condensed Matter*, 404, 1757- 1760.
- Li D., Wang X. P., Fang Q. F., Wang J. X., Li C., Zhuang Z., 2007, Phase transition associated with the variation of oxygen vacancy/ion distribution in the oxide-ion conductor, *Physica Status Solidi a-Applications and Materials Science*, 204, 2270-2278.
- Li D., Wang X. P., Zhuang Z., Wang J. X., Li C., Fang Q. F., 2009, Reducibility study of oxide-ion conductors $\text{La}_{2-x}\text{Ba}_x\text{Mo}_{2-y}\text{A}_y\text{O}_{9-\delta}$ (A = W, Al, Ga) assessed by impedance spectroscopy, *Materials Research Bulletin*, 44, 446-450.

Li M. R., Kuang X. J., Chong S. Y., Xu Z. L., Thomas C. I., Niu H. J., Claridge J. B., Rosseinsky M. J., 2010, Interstitial Oxide Ion Order and Conductivity in $\text{La}_{1.64}\text{Ca}_{0.36}\text{Ga}_3\text{O}_{7.32}$ Melilite *Angewandte Chemie-International Edition*, 49, 2362-2366.

Li X., Yang Z. P., Guan L., Liu C., Li P. L., 2008, Luminescent properties of Eu^{3+} -doped $\text{La}_2\text{Mo}_2\text{O}_9$ red phosphor by the flux method, *Journal of Crystal Growth*, 310, 3117-3120.

Liang F. J., Wang X. P., Fang Q. F., Wang J. X., Li C., Li D., Zhuang Z., 2006, Internal friction studies of $\text{La}_{2-x}\text{Ba}_x\text{Mo}_2\text{O}_{9-\delta}$ oxide-ion conductors, *Phys. Rev. B*, 74, 014112-1- 014112-5.

Lilley E., Strutt J. E., 1979, Bulk and Grain Boundary Ionic Conductivity in Polycrystalline β "-Alumina *Phys. Stat. Sol. (a)* 54, 639-650.

Lin Y, Fang S, Su D, Brinkman K S, Chen F., 2015, Enhancing grain boundary ionic conductivity in mixed ionic–electronic conductors *Nature Comm.*, 6 1-9.

Liu J., 2011, Mass Transport and Electrochemical Properties of $\text{La}_2\text{Mo}_2\text{O}_9$ as a Fast Ionic Conductor Ph.D thesis, Imperial College London, London.

Liu W., Pan W., Luo J., Godfrey A., Ou G, Wu H., Zhang W., 2015, Suppressed phase transition and giant ionic conductivity in $\text{La}_2\text{Mo}_2\text{O}_9$ nanowires *Nature*, 6:8534, 1-8.

Loganathan A., Gandhi A.S., 2017, Toughness evolution in Gd-and Y-stabilized zirconia thermal barrier materials upon high-temperature exposure, *J. Mater. Sci.*, 52, 7199-7206.

Lopez D. Marrero, Nunez P., Abril M., Lavin V., Mendoza Rodriguez U. R., Rodriguez V. D., 2004, Synthesis, electrical properties, and optical characterization of Eu^{3+} doped $\text{La}_2\text{Mo}_2\text{O}_9$ nano-crystalline phosphors *Journal of Non-Crystalline Solids*, 345, 377-381.

Lopez D. Marrero, Morales J.C.Ruiz., Coll D. P., Nunez P., Abrantes J.C.C., Frade J.R., 2004, Stability and transport properties of $\text{La}_2\text{Mo}_2\text{O}_9$, *Solid state electrochem.*, 8, 638-643.

Lopez D. Marrero, Vazquez J. Canales, Morales J. C. Ruiz, Rodriguez A., Irvine J. T. S., Nunez P., 2005, Synthesis, sinterability and ionic conductivity of nano-crystalline $\text{La}_2\text{Mo}_2\text{O}_9$ powders, *Solid State Ionics*, 176, 1807-1816.

Lopez D. Marrero, Vazquez J. Canales, Morales J. C. Ruiz, Irvine J. T. S, Nunez P., 2005, Electrical conductivity and redox stability of $\text{La}_2\text{Mo}_{2-x}\text{W}_x\text{O}_9$ materials *Electrochimica Acta* 50, 4385-4395.

Lopez D. M., Zhou W., Vazquez J. C., Irvine J. T. S., Nunez P., 2006, Structural studies on W^{6+} and Nd^{3+} substituted $La_2Mo_2O_9$ materials, *J. Solid State Chem.* 179 278-288.

Lopez D. Marrero, Martinez J. Pena, Morales J. C. Ruiz, Coll D. Perez, Martin-Sedeno M. C., Nunez P., 2007, Applicability of $La_2Mo_{2-y}W_yO_9$ materials as solid electrolyte for SOFCs, *Solid State Ionics*, 178, 1366-1378.

Lopez D. Marrero, Coll D. Perez, Morales J. C. Ruiz, Vazquez J. Canales, Sedeno M. C. Martin, Nunez P., 2007, Synthesis and transport properties in $La_{2-x}A_xMo_2O_{9-\delta}$ ($A = Ca^{2+}, Sr^{2+}, Ba^{2+}, K^+$) series, *Electrochimica Acta*, 52, 5219-5231.

Lu X.C., Zhu J. H., 2008, Amorphous Ceramic Material as Sulfur-Tolerant Anode for SOFC, *Journal of The Electrochemical Society*, 155, B1053-B1057.

Macdonald J. R., 1987, Impedance spectroscopy: emphasizing solid materials and systems / edited by J. Ross Macdonald.

Macedo P.B., Moynihan C.T., Bose R., 1972, The role of ionic diffusion in polarization in vitreous ionic solids, *Phys. Chem. Glasses* 13, 171-179.

Malavasi L., Kim H., Billinge S. J. L., Proffen T., Tealdi C., Flor G., 2007, Nature of the Monoclinic to Cubic Phase Transition in the Fast Oxygen Ion Conductor $La_2Mo_2O_9$ (LAMO), *Journal of the American Chemical Society*, 129, 6903-6907.

Malik K., Singh S., Basu S., Verma, A., 2017, Electrochemical reduction of CO_2 for synthesis of green fuel. *Wiley Interdisciplinary Reviews: Energy and Environment*, 6, 244.

Marozau I. P., Shaula A. L., Kharton V. V., Vyshatko N. P., Viskup A. P., Frade J. R., Marques F. M. B., 2005, Transport properties and thermal expansion of $La_2Mo_2O_9$ -based solid electrolytes, *Mater. Res. Bull.*, 40, 361-371.

Martin M. C., Mecartney M. L., 2003, Grain boundary ionic conductivity of yttrium stabilized zirconia as a function of silica content and grain size 2003 *Solid State Ionics*. 161, 67-79.

Mei, B.A., Munteshari, O., Lau, J., Dunn, B. and Pilon, L., 2017, Physical interpretations of Nyquist plots for EDLC electrodes and devices, *J. Phy. Chem. C*, 122, 194-206.

Minh Q N. 1993, Ceramic fuel cells. *J of Amer. Ceram. Soc.* 76, 563-588.

Moulder J.F., Stickle W.F.D., Sobol P.E., Bomben K.D, 1995, Handbook of X- ray photoelectron spectroscopy. Edited by J. Chastain and R.C. King Jr. Published by ULVAC-PHI, Inc. Japan. pp 10.

Muniz A. R., Meyyappan M., Maroudas D., On the hydrogen storage capacity of carbon nanotube bundles, *Appl. Phys. Lett.* 95, 163111, 2009.

Muniz A. R., Singh T., Maroudas D., 2009, Effects of hydrogen chemisorption on the structure and deformation of single-walled carbon nanotubes, *Appl. Phys. Lett.* 94, 103108.

Murni S., Zawawi M., Yahya R, Hassan A., Ekramul H. N. M., Daud M. N., 2013, Structural and optical characterization of metal tungstates ($MAWO_4$; M=Ni, Ba, Bi) synthesized by a sucrose-templated method. *Chemistry Central Journal*, 7, 1-11.

Murray E. P., Tsai T, Barnett S. A., 1999, A direct-methane fuel cell with a ceria-based anode *Nature*, 400, 649– 651.

Nakayama S., Aono H., Sadaoka Y., 1995, Ionic Conductivity of $Ln_{10}(SiO_4)_6O_3$ ($Ln = La, Nd, Sm, Gd$ and Dy) *Chem. Lett.*, 6, 431–432.

National Centre for Atmospheric Research. News release, July 2001.

Nernst N., 1899, The theory of lead-acid batteries 46-52.

Niu L., Li Z., Xu Y., Sun J., Hong W., Liu X., Wang J., Yang S., 2013, Simple Synthesis of Amorphous $NiWO_4$ Nanostructure and Its Application as a Novel Cathode Material for Asymmetric Supercapacitors, *Appl. Mater. Interfaces*, 5, 8044-8052.

Orliukas A., Bohac P., Sasaki K., Gauckler J.L., 1994, The relaxation dispersion of the ionic conductivity in cubic zirconias, *Solid State Ionics*, 72, 35-38.

Palacio Loyola de, Busquin P., 2003, Hydrogen energy and fuel cells- A vision of our future. Directorate General of energy and transport, EUR 20719 EN, pp. 1-35.

Park J. Y., Levenspiel O., 1975, The crackling core model for the reaction of solid particles *Chem. Engineering Science*, 30, 1207-1214.

Paul T., Ghosh A., 2014, Ionic conductivity and dielectric relaxation in Y doped $La_2Mo_2O_9$ oxide-ion conductors, *J. Appl. Phys.* 116, 1-6.

Pawlak D.A., Ito M., Oku M., Shimamura K., Fukuda T., 2002, Interpretation of XPS O (1s) in Mixed Oxides Proved on Mixed Perovskite Crystals, *J. Phys. Chem. B*, 106, 504-507.

Pechini M.P., 1967, Method of preparing lead and alkaline earth titanates and niobates and coating method using the same to form a capacitor, US Patent, 3330697A.

[phi.com/XPS images/](http://phi.com/XPS_images/).

Pinet P., Fouletier J., Georges S., 2007, Conductivity of reduced $\text{La}_2\text{Mo}_2\text{O}_9$ based oxides: The effect of tungsten substitution, *Mater. Res. Bull.*, 42, 935-942.

Pornprasertsuk R., Cheng J., Huang H., Prinz F. B., 2007, Electrochemical impedance analysis of solid oxide fuel cell electrolyte using kinetic Monte Carlo technique, *Solid State Ionics*, 178, 195-205.

Pratt R.H., Ron A., Tseng H.K., 1973, Atomic photoelectric effect above 10 keV, *Rev. Mod. Phys.* 45, 273.

Predith A., Ceder G., Wolverton C., Persson K., Mueller T., 2008, Ab initio prediction of ordered ground-state structures in $\text{ZrO}_2\text{-Y}_2\text{O}_3$, *Phys. Rev. B.*, 77, 144104-1 – 144104-7.

Rahaman M.N., Jhonghe L.C., 2003, *Handbook of Advanced Ceramics*, Ch. 4. pp 187.

Rao T. S. R. P., Turaga U.T., 2003, Opportunities and challenges for fuel cells in India, *Am. Chem. Soc., Div. Fuel Chem.*, 48, 795-796.

Ravella. U.K. 2012, Thermal stability of potential fuel cell core materials $\text{La}_2\text{Mo}_{2-y}\text{O}_9$ ($0 \leq y \leq 2$) under air and reducing atmospheres, and in contact with a Sr containing cathode material. Ph.D thesis, 24-25 Ph.D. Thesis,.

Report on fuel cell development in India, Appendix VI, Ministry of New and Renewable Energy, Government of India, New Delhi, 2016.

Rietveld H.M., 1967, Line profiles of neutron powder-diffraction peaks for structure refinement, *Acta. Crystallogr.* 22, 151–152.

Rigaku.com/en/products/xrd.

Robert. T. Watson, 2001 Intergovernmental Panel on Climate Change, Sixth Conference of Parties to the United Nations Framework Convention on Climate Change, pp. 1-11.

Rocha R. A., Muccillo E. N. S., 2005, Characterisation of La_2MoO_6 prepared by complex cation technique, *J. Alloys and Comp.*, 400, 83-87.

Russ J. C., 1984, *Fundamentals of Energy Dispersive X-ray Analysis*, Butterworths. London.

Sabolsky E. M., Gansor P., Çiftyürek E., Sabolsky K., Xu C., Zondlo J. W., 2013, In situ formation of a solid oxide fuel cell (SOFC) cermet anode by NiWO_4 reduction *J. Power Sources*, 237, 33-40.

Sammes N.M., Cai Z., 1997, Ionic conductivity of ceria/yttria stabilized zirconia electrolyte materials, *Solid State Ionics*, 100, 39-44.

Sandler V. A., Yakushkin E. D., 2010, Dielectric properties, ionic conductivity and phase transitions in $\text{La}_2\text{Mo}_2\text{O}_9$ ceramics, *Bull. Russian Acad. Sci.*, 74 1245–1248.

Satyapal S., 2018, Hydrogen and fuel cell Technologies Office, U.S. Department of Energy, Office of Energy Efficiency and Renewable Energy, Washinton D.C., 1-30.

Scheffer B., Molhoek P., Mouljin J. A., 1989, Temperature-programmed reduction of $\text{NiO-WO}_3/\text{Al}_2\text{O}_3$ Hydrodesulphurization catalysts *Appl. Catalysis.*, 46, 11-30.

Schulmeyer W. V., Ortner H.M., 2001, Mechanism of the hydrogen reduction of molybdenum oxide 15th international Plansee Seminar Vol 3, Eds Kneringer G., Rodhammer P. and Wildner H., Plansee Holding AG, Reutte.

Selmi A., Corbel G., Lacorre P., 2006, Evidence of metastability and demixion/recombination process in fast oxide-ion conductor $\text{La}_{1.92}\text{Ca}_{0.08}\text{Mo}_2\text{O}_{8.96}$, *Solid State Ionics*, 177, 3051-3055.

Selmi A., Galven C., Corbel G., Lacorre P., 2010, Thermal stability of alkali and alkaline-earth substituted LAMOX oxide-ion conductors, *Dalton Trans*, 1, 93-102.

Shamim K. M., Sharma S., Sinha S., Nasreen E., 2017 Dielectric relaxation and modulus spectroscopy analysis of $(\text{Na}_{0.47}\text{K}_{0.47}\text{Li}_{0.06})\text{NbO}_3$ ceramics, *J. Adv. Dielectrics*, 7, 1750020-1-1750020-11.

Shannon R. D., 1976, Revised effective ionic radii and systematic studies of inter-atomic distances in halides and chalcogenides, *Acta. Crystallogr. Sect. A*, 32, 751-767.

- Singhal S.C., 2000, Advances in solid oxide fuel cell technology, *Solid State Ionics*, 135, 305-313.
- Smith E., Dent G., 2005 *Modern Raman Spectroscopy- A practical approach*, John Wiley and sons Ltd., pp 4.
- Sloczynski J., 2002, Kinetics and Mechanism of MoO₃ Reduction. Comments on “In Situ XAS and XRD Studies on the Formation of Mo Sub-oxides during Reduction of MoO₃” *J. Phys. Chem. B* 106, 7718-7718.
- Stambouli A.B, Traversa E, 2002, Solid oxide fuel cells: A review of an environmentally clean and efficient source of energy *Renewable and Sustainable Energy Reviews* 6, 433-455.
- Steele B. C. H., Heinzl A., 2001, Materials for fuel-cell technologies, *Nature* 414, 345-352.
- Steele B. C. H., 2001, Material science and engineering: The enabling technology for the commercialisation of fuel cell systems, *J. Mater Sci.* 36, 1053-1068.
- Steil M. C., Thevenot F., and Kliez M., 1997, Densification of yttria stabilized zirconia impedance spectroscopy analysis *J. Electrochem. Soc.*, 144, 390-398.
- Subasri R., Matusch D., Nafe H., Aldinger F., 2004, Synthesis and characterization of (La_{1-x}M_x)₂Mo₂O_{9-δ}; M = Ca²⁺, Sr²⁺ or Ba²⁺ *Journal of the European Ceramic Society*, 24, 129-137.
- Subasri R., Nafe H., Aldinger, F., 2003, On the electronic and ionic transport properties of La₂Mo₂O₉, *Materials Research Bulletin* 38,1965-1977.
- Swami S. K., Chaturvedi N., kumar A., Dutta V., 2016, Effects of electric field during deposition on spray deposited indium-doped zinc oxide films, *Prog. Photovolt: Res. Appl.* 24, 74–82.
- Taimatsu H., Wada K., Kaneko H., Yamamura H., 1992, Mechanism of Reaction between Lanthanum Manganite and Yttria-Stabilized Zirconia, *J. Amer. Ceram. Soc.*, 75, 401-405.
- Takahashi T, Iwahara H., 1972, High oxide ion conduction in sintered Bi₂O₃ containing SrO, CaO or La₂O₃, *J. Appl. Electrochem.* 2, 97-104.
- Takahashi T, Iwahara H, J., Arao T, 1975, High oxide ion conduction in sintered oxides of the system Bi₂O₃-Y₂O₃, *J. Appl. Electrochem.* 5 187-195.

Tealdi C., Chiodelli G., Malavasi L., Flor G., 2004, Effect of alkaline-doping on the properties of $\text{La}_2\text{Mo}_2\text{O}_9$ fast oxygen ion conductor, *J. Mater. Chem.*, 14, 3553- 3557.

Tealdi C., Chiodelli G., Flor G., Leonardi S., 2010, Electrode stability and electrochemical performance of LAMOX electrolytes under fuel cell conditions, *Solid State Ionics*, 181, 1456-1461.

Teitz F., 2008, Solid oxide fuel cells, Reference Module in Materials Science and Materials Engineering, 1-8.

Torabi A., Etsell T. H., Semagina N., Sarkar P., 2012, Electrochemical behaviour of tungsten carbide-based materials as candidate anodes for solid oxide fuel cells *Electrochim. Acta*, 67, 172-180.

Torabi A., Etsell T. H., 2012, Ni Modified WC-Based Anode Materials for Direct Methane Solid Oxide Fuel Cells *J. Electrochem. Soc.*, 159, B714-B722.

Tripathi A.M., Mitra S., 2014, Ecofriendly approach to making graphene-tin/tin oxide nanocomposite electrodes for energy storage. *Chem. Electro. Chem.*, 1,1327-1337.

Tsai D. S., Hsieh M. J., Tseng J. C., Lee H. Y., 2005, Ionic conductivities and phase transitions of lanthanide rare-earth substituted $\text{La}_2\text{Mo}_2\text{O}_9$, *J. European Ceramic Society*, 25, 481-487.

Turik A. V., Vogatin A.S., Andreev E.V., 2011, Relaxation process in non-debye dielectrics, *Physics of the solid state*, 53, 2421-2423.

[https://www.usatoday.com/story/money/2019/07/14/china-us-countries-that-produce-the-most-CO₂-emissions/39548763/](https://www.usatoday.com/story/money/2019/07/14/china-us-countries-that-produce-the-most-CO2-emissions/39548763/)

Vollman M., Waser R., 1994, Grain Boundary Defect Chemistry of Acceptor Doped Titanates: Space Charge Layer Width *J. Am. Ceram. Soc.*, 77, 235-245.

Voronkova V., Kharitonova E., Krasilnikova A., 2009, Phase transitions and electrical conductivity of Bi-doped $\text{La}_2\text{Mo}_2\text{O}_9$ oxide ion conductors, *physica status solidi (a)*, 206, 2564-2568.

- Voronkova V., Kharitonova E., Krasilnikova A., 2010, Specific features of phase transitions and the conduction of $\text{La}_2\text{Mo}_2\text{O}_9$ oxide-ion conducting compound doped with vanadium, *Crystallography Reports*, 55, 276-282.
- Voronkova V., Kharitonova E., Krasilnikova A., Kononkova N. N., 2008, Phase transition peculiarities in LAMOX single crystals, *J. of Phys: Cond. Matter*, 20, 195210.
- Wang J., Wang Q., Wang X., 2008, Synthesis and Characterization of Fine Grained High Density $\text{La}_2\text{Mo}_2\text{O}_9$ -based Oxide-ion Conductors, *J.Mater. Sci. Technol.*, 24, 761-768.
- Wang J. X., Wang X.P., Liang F.J., Cheng Z.J., Fang Q.F., 2006, Enhancement of conductivity in $\text{La}_2\text{Mo}_2\text{O}_9$ ceramics fabricated by a novel three-stage thermal processing method, *Solid State Ionics*, 177, 1437-1442.
- Wang S., Iraba H., Tagwa H., 1997, Non-stoichiometry of $\text{Ce}_{0.8}\text{Gd}_{0.2}\text{O}_{1.9-x}$, *J. Electrochem. Soc.*, 144, 4076-4080.
- Wang S., He Y., Zo J., Wang Y., Huang H., 2009, Growth of single-crystal W whiskers during humid H_2/N_2 reduction of Ni, Fe – Ni, and Co – Ni doped tungsten oxide, *J. Alloys Compd.*, 482, 61-66.
- Wang X. P., Fang Q. F., 2001, Low-frequency internal friction study of oxide-ion conductor $\text{La}_2\text{Mo}_2\text{O}_9$ *J. Physics-Condens. Matter*, 13, 1641-1651.
- Wang S, Koboyashi T, Dokiya M., 2000, Electrical and Ionic Conductivity of Gd-Doped Ceria, *J of Electrochem Soc.* 147, 3606-3609.
- Wang X. P., Fang Q. F., Effects of Ca doping on the oxygen ion diffusion and phase transition in oxide ion conductor $\text{La}_2\text{Mo}_2\text{O}_9$, *Solid State Ionics*, 146, 185-193, 2002.
- Wang X. P., Cheng Z. J., Fang Q. F., 2005, Influence of potassium doping on the oxygen-ion diffusion and ionic conduction in the $\text{La}_2\text{Mo}_2\text{O}_9$ oxide-ion conductors, *Solid State Ionics*, 176, 761-765.
- Wang X. P., Li D., Fang Q. F., Cheng Z. J., Corbel G., Lacorre P., 2006, Phase transition process in oxide-ion conductor $\beta\text{-La}_2\text{Mo}_{2-x}\text{W}_x\text{O}_9$ assessed by internal friction method, *Applied Physics Letters*, 89, 021904-1 021904-3.

Wang X.P., Fang Q.F., Li S.Z., Yi G.Z., 2002, Dielectric relaxation studies of Bi-doping effects on the oxygen-ion diffusion in $\text{La}_{2-x}\text{Bi}_x\text{Mo}_2\text{O}_9$ oxide-ion conductors, *Appl. Phys. Lett.* 81, 3434-3436.

Warshay M., Prokopius P.R., 1989, *The Fuel Cell in Space: Yesterday, Today and Tomorrow*, Fuel Cell Symposium (Grove 1839 - 1989), London, Great Britain.

Williams M. C., 2004, *Fuel Cell Handbook*, Chapter 7 National Energy Technology Laboratory (Seventh Edition) By EG&G Technical Services, Inc., November 7.1 -7.49.

Xia R., Oldman R., Catlow R., 2009, Computational Modeling Study of Bulk and Surface of Yttria-Stabilized Cubic Zirconia, *Chem. Mater.*, 21, 3576-3585.

Yang J. H., Gu Z. H., Wen Z. Y., Yan D. S., 2005, Preparation and characterization of solid electrolytes $\text{La}_{2-x}\text{A}_x\text{Mo}_{2-y}\text{W}_y\text{O}_9$ (A = Sm, Bi), *Solid State Ionics*, 176, 523-530.

Yates C., Winnick J., 1999, Anode Materials for a Hydrogen Sulfide Solid Oxide Fuel Cell *J. Electrochem. Soc.*, 146, 2841-2844.

Yoo K. S., Jacobson A. J., 2005, Effects of Sr and Cr doping on properties of $\text{La}_2\text{Mo}_2\text{O}_9$ electrolytes, *Journal of Materials Science*, 40, 4431-4434.

Zeiss.com/microscopy/int/products/scanning-electron-microscopes.html.

Zhang G. G., Fang Q. F., Wang X. P.; Yi Z. G., 2003, A.C. impedance and dielectric relaxation study on the effects of the excess Pb introduced in $\text{La}_2\text{Mo}_2\text{O}_9$ oxide-ion conductors, *Physica Status Solidi a-Applied Research*, 199, 329-334.

Zhou D.F., Synthesis, 2007, Characterization and electrical properties of solid state electrolyte materials $\text{La}_{2-x}\text{Ca}_x\text{Mo}_{1.7}\text{W}_{0.3}\text{O}_{9-\delta}$ ($0 \leq x \leq 2$) *Chin. J. Inorg. Chem*, 1, 81-85.